UCGE Reports
Number 20260

Department of Geomatics Engineering

The Torus-Based Semi-Analytical Approach in Spaceborne Gravimetry

(URL: http://www.geomatics.ucalgary.ca/research/publications/GradTheses.html)

by

Chen Xu

January 2008

THE UNIVERSITY OF CALGARY

The Torus-Based Semi-Analytical Approach in Spaceborne Gravimetry

by

Chen Xu

A THESIS

SUBMITTED TO THE FACULTY OF GRADUATE STUDIES

IN PARTIAL FULFILLMENT OF THE REQUIREMENTS FOR THE

DEGREE OF DOCTOR OF PHILOSOPHY

DEPARTMENT OF GEOMATICS ENGINEERING

CALGARY, ALBERTA

January, 2008

Abstract

THE main objective of this research is to present a complete and comprehensive analysis of the torus-based semi-analytical approach of gravity field determination from spaceborne gravimetry observations. The focus is placed on the torus-based approach because it theoretically saves computational time and memory storage as a result of using both a two-dimensional fast *Fourier* transform (2D FFT) technique and the block-diagonal structured normal matrix in least-squares adjustment. However, the full implementation of this approach for practical applications has never been done.

Starting with an introduction of the theoretical and mathematical backgrounds of several state-of-art gravity field determination approaches, namely the direct, space-wise, time-wise, and torus-based semi-analytical approaches, the strengths and weaknesses of each approach are discussed. A complete and detailed calculating flow chart of the torus-based approach is developed. Under the assumption of a nominal orbit, the approach basically recovers the Earth's global gravity field in three major steps. In the first step, the *in situ* contaminated satellite observations, such as the disturbing potential data from the CHAMP mission or the gravity gradient tensor components from the GOCE mission, are reduced and interpolated onto a nominal torus grid. The second step is to calculate the pseudo-observables, the lumped coefficients A_{mk}, using a 2D FFT technique. In the final step, spherical harmonic coefficients are estimated separately for the individual orders by least-squares adjustment. Several critical issues involved in the calculations have to be investigated. These issues are: filtering observations contaminated by colored noise, reducing height and inclination variations onto a nominal orbit, interpolating a torus grid, analyzing the aliasing problems in both spatial and spectral domains, calculating a weight matrix from an error power spectral density (PSD) model, investigating the regularization techniques in a nearly ill-posed problem of the normal matrix, determining the optimal weighting factors for the combined solution, and iterating the estimated solution.

Several case studies on the processing of satellite observations using the complete calculating flow are described and analyzed. The comparisons between the direct and torus-based approach show that the latter achieves the same accuracy level as the former with

only 1% of the calculating time. Two groups of solutions, namely the stand-alone and the combined solutions, are obtained. The disturbing potential data from CHAMP and GRACE are able to recover the gravity field up to $L = 70$. However, the gravity field determined from the GRACE-type line-of-sight (LOS) gradiometry data is not successful because the ≈ 220 km inter-satellite baseline of GRACE breaks the assumption that the baseline should be sufficiently small. In addition, the solutions of the gravity gradient tensor data from GOCE do not provide enough accuracy because the interpolation errors reach 3% of the original values. It is very easy to combine different types of observations or data sets using the torus-based approach. The combined (overall) solutions using the optimal weights determined by the variance components approach are better than the individual stand-alone solutions or equal-weighted overall solutions.

Finally, a summarized and comprehensive calculating procedure for the general applications of gravity field determination from satellite missions is proposed.

Acknowledgements

I would like to express my sincere gratitude to my distinguished supervisors, Professor Dr. Michael G. Sideris and Professor Dr. Nico Sneeuw, for their guidance, support, encouragement, and advice in every stage of my graduate study. Their knowledge, kindness, patience, open-mindedness, and vision have provided me with lifetime benefits. The other member of my supervisory committee, Professor Dr. Yang Gao, is acknowledged also for answering various questions throughout my studies at the University of Calgary.

I am grateful to the other members of my examining committee, Dr. Ming Wei from Intermap Technologies Corp. and Dr. Alan Hildebrand in the Department of Geosciences, for their valuable comments and suggestions, and enlightening discussions on the dissertation drafts. I also would like to thank all faculty members at the Department of Geomatics Engineering, the University of Calgary, for providing a wonderful academic environment. Special thanks to Dr. J. A. Rod Blais, Dr. Patrick Wu, Dr. Naser El-Sheimy, and Dr. Gérard Lachapelle for their guidance in my courses and several independent projects that have expanded my vision.

I am also very thankful to Professor Dr. Jiexian Wang at the Tongji University, who brought me to the world of satellite geodesy. I would like to thank deeply Dr. Alexander Braun and Dr. Georgia Fotopoulos for their constructive discussions and assistance. I would like to express my special thanks to Professor Dr. C. K. Shum at the Ohio State University for his advice and recommendations on my research. Dr. Martin Wermuth from TU Munich is gratefully acknowledged for his valuable discussions and suggestions. Dr. Xinyu Xu is also thanked for providing the simulated GOCE data.

My memories of graduate studies in Calgary can never be complete without mentioning my fellow graduate students in the gravity field and geodynamics group. I would like to thank Matthias Weigelt and Mohamed El-Habiby for our great friendship. We stayed four amazing years in the same office with countless discussions, and we helped each other and shared our happiness and success. I would like to acknowledge Wouter van der Wal for reading and editing my dissertation draft. I was very glad to work in the group with Elena Rangelova, Raymond Tsoi, Balaji Devaraju, Vidyavathy Renganathan, Bihter Erol, and

Rossen Grebenitcharsky. I also would like to thank Qiaoping Zhang, Haiying Hou, Xiaoji Niu, Changlin Ma, Wuji Yang, Zhizhao Liu, Kongzhe Chen, Li Sheng, to name only a few, for their great helps during my lives and studies in Calgary.

Funding for my PhD studies was provided from numerous sources, including NSERC, GEOIDE, C. F. Gauss Award, F. R. Helmert Award, Robert B. Paugh Memorial Scholarship in Engineering, Graduate Research Scholarship Award, and Graduate Travel Grant.

I am deeply grateful to my dear wife, Siyue Chen. My PhD dream could not be fulfilled without her love, encouragement, support, and sacrifice. Thank life for letting me know her and marry her in Calgary. I feel so privileged to share my life with her. My beautiful baby boy, Jackson Jiachen Xu, every day is new and meaningful to me because of you. Your smile is the fuel that drives me. My beloved parents, I can not say any words other than thanks to you. Thank you, mom, for your patience and sacrifice. Thank you, dad, for your care and encouragement toward the pursuit of excellence. I know that you are watching and blessing our family from Heaven. I also would like to thank my dear sister. I dedicate this dissertation to my family.

谨以此博士论文献给

我的父母, 爸爸（**1950-2000**）和妈妈

我的爱人, 思越

我的宝贝, 壮壮

Table of Contents

List of Tables

List of Figures

List of abbreviations

1D	....	One Dimensional
2D	....	Two Dimensional
3D	....	Three Dimensional
AIC	....	Akaike Information Criterion
ARMA	....	Auto-Regressive (AR) and Moving Average (MA)
CHAMP	....	CHAllenging Mini satellite Payload
CPR	....	Cycles Per Revolution
DSG	....	Dynamic Satellite Geodesy
FFT	....	Fast *Fourier* Transform
GAST	....	*Greenwich* Apparent Sidereal Time
GCV	....	Generalized Cross-Validation
GFZ	....	GeoForschungsZentrum Potsdam
GNSS	....	Global Navigation Satellite System
GOCE	....	Gravity field and steady-state Ocean Circulation Explorer
GPS	....	Global Positioning System
GRACE	....	Gravity Recovery and Climate Experiment
HE	....	*Hill* Equations
IFFT	....	Inverse Fast *Fourier* Transform
IMU	....	Inertial Measuring Unit
INS	....	Inertial Navigation System
LEO	....	Low Earth Orbiter
LOS	....	Line of Sight
LPE	....	*Lagrange*'s Planetary Equations
LSA	....	Least Squares Adjustment
LSC	....	Least Squares Collocation
MBW	....	Measurement Band-Width
PG	....	Pocket Guide
PC	....	Parametric Covariance
PCGMA	....	Preconditioned Conjugated Gradient Multiple Adjustment

RMS	....	Root Mean Square
RMSE	....	Root Mean Square Error
SAR	....	Synthetic Aperture Radar
SFF	....	Satellite Formation Flying
SGG	....	Satellite Gravity Gradiometry
SH	....	Spherical Harmonics
SNR	....	Signal-to-Noise Ratio
SST	....	Satellite-to-Satellite Tracking
STD	....	Standard Deviation
TUM	....	Technische Universität München
TSVD	....	Truncated Singular Value Decomposition
VC	....	Variance Components

List of symbols

Coordinates

X, Y, Z	Cartesian coordinates in the inertial frame:
	vernal equinox, completeness of right-handed frame, north pole
x, y, z	Cartesian coordinates in the local orbital frame:
	along-track, cross-track, radial direction
ϕ, λ, r	spherical coordinates:
	latitude, longitude, radius
u, Λ	torus coordinates:
	argument of latitude, longitude of ascending node

Functions

$\bar{Y}_{lm}(\phi, \lambda)$	complex normalized spherical harmonic
$\bar{P}_{lm}(\sin\phi)$	normalized associated *Legendre* function
$\bar{F}_{lmk}(I)$	normalized inclination function
$\bar{F}^*_{lmk}(I)$	normalized cross-track inclination function

Coefficients

$\bar{K}_{lm}$	normalized complex-valued SH coefficient
$\bar{C}_{lm}, \bar{S}_{lm}$	normalized real-valued SH coefficient
A_{mk}	lumped coefficient
H_{lmk}	transfer coefficient, sensitivity coefficient
ψ_{mk}, ψ_n	orbital frequency

Chapter 1

Introduction

Absolute space, in its own nature, without regard to any thing external, remains always similar and immovable... So far I have explained the phenomena by the force of gravity...

Sir Isaac Newton (1643-1727)

1.1 Background and motivation

AFTER THE first artificial satellite (the SPUTNIK mission in 1957) demonstrated the value of the Earth's flatting J_2, the way of employing spaceborne technologies has been widely adopted to improve the knowledge of the Earth's dynamic processes. The major technological developments relevant to spaceborne gravity field determination are the continuous orbit tracking by global navigation satellite systems (GNSS) and the onboard accelerometers (Rummel, 1986), from which three basic concepts are derived: the satellite-to-satellite tracking in high-low mode (SST-hl), satellite-to-satellite tracking in low-low mode (SST-ll), and satellite gravity gradiometry (SGG). These three concepts are realized by three dedicated gravity field satellite missions: CHAMP, GRACE, and GOCE (ESA, 1999; Balmino, 2001; Rummel et al., 2002), respectively. In general, these three gravity field satellite missions can be referred to as "spaceborne gravimetry." However, none of these missions are able to measure the Earth's gravity field directly, because an orbiting spacecraft and all its contents are in free fall. Therefore, the gravity field information in terms of a series of spherical harmonic coefficients can be derived only indirectly from the *in situ* observations by making use of both the onboard GNSS receivers and precise accelerometers.

Gravity field determination from spaceborne gravimetry has the following characteristics: on the one hand, numerous observations are available in a global and homogeneous quality as a result of the longer mission duration and denser sampling rate; on the other hand, the effect of increasing the maximum resolvable degree L of spherical harmonics enlarges the number of the spherical harmonic unknowns quadratically, and the size of the normal matrix is changed correspondingly to $(L+1)^2 \times (L+1)^2$ in least-squares adjustment for coefficient estimation.

Two main approaches are available for gravity field determination. They are the numerical way and the (semi-)analytical way. The former yields the direct (brute-force) approach, which is based on orbit perturbation theory (Reigber, 1989; Rummel et al., 2004). Theoretically, the direct approach is the most robust and accurate solution, and it can be applied in any projection domain, i.e., a sphere, an orbit, or a torus. However, it is not preferable for spaceborne gravimetry observations because of its intrinsic limitations in the computational time and storage memory requirement. Rummel et al. (1993) summarized two (semi-)analytical approaches: the space-wise and time-wise approaches. The space-wise approach projects the observations as a function of location on a spherical domain, and the time-wise approach treats the observations as a time series in an orbital domain. Under certain approximations and assumptions, a fast numerical algorithm can be applied in both the space-wise (Colombo, 1981) and time-wise approaches (Colombo, 1984, 1989). In addition, the normal matrix in least-squares adjustment leads to an m-wise (m order of spherical harmonics) block-diagonal structure, in which the maximum size is $(L+1) \times (L+1)$ for $m = 0$, and the minimum size is only 1×1 for $m = L$ (Koop, 1993). These two approaches have been employed widely in gravity field determination from the CHAMP and GRACE missions, and they are also proposed in the framework of the high level processing facility to determine the gravity field from the GOCE mission. For the space-wise approach, see e.g., Albertella et al. (2000), Tscherning et al. (2000), and Migliaccio et al. (2004); and for the time-wise approach, see e.g., Koop et al. (2000), Klees et al. (2000), Pail and Plank (2002), and Pail et al. (2005).

As an extended version of the time-wise approach in the frequency (*Fourier*) domain, Sneeuw (2000a,b) proposed a torus-based semi-analytical approach for gravity field determination. By making use of two orbital coordinates, argument of latitude u and right ascension of ascending node Λ, this approach projects naturally the spaceborne gravimetry observations on a torus domain. It has the following advantages:

- ▶ A regular grid on the torus allows the application of a two dimensional (2D) fast *Fourier* transform (FFT) technique to obtain the so-called "lumped coefficient" as a pseudo-observable (Schrama, 1989, 1990).

- An assumption of a nominal orbit with constant radius and constant height yields a block-diagonal structured normal matrix in least-squares adjustment for estimating the spherical harmonic coefficients.
- A weight matrix is able to be derived from the *a-priori* error information in terms of the power spectral density (PSD) in the stochastic model.
- A collection of the so-called "transfer coefficients" shows the feasibility of dealing with any geopotential functional (Rummel et al., 1993).
- In addition, by applying interpolation, this approach is not affected by a repeat orbit assumption, data gaps, or polar gaps.

Sneeuw (2000b) and Sneeuw et al. (2002) concluded that the torus-based semi-analytical approach is a flexible and powerful pre-mission error assessment and validation tool based on the analysis of the simulated observation errors. Karrer (2000) tested this approach in the presence of the GOCE simulated gravity gradient tensor data, and Sneeuw et al. (2005b) employed it in the determination of monthly gravity field solutions from the CHAMP disturbing potential data. In addition, from the one-dimensional repeat orbit perspective, Pail and Plank (2004), and Pail et al. (2007) illustrated that the semi-analytical approach can be used as a quick-look tool for the purpose of a fast analysis of the GOCE input data. However, none of the studies mentioned above provided a complete processing flow chart of the torus-based approach for gravity field determination from satellite observations. Therefore, the main motivation of this research is to present a complete and detailed analysis of the torus-based semi-analytical approach in spaceborne gravimetry. This work will be focused on the implementation, refinement, and investigation of each corresponding processing step to achieve a final solution of spherical harmonic coefficients as accurate as possible, compared to a reference gravity field model.

The general calculating flow of gravity field determination using the torus-based approach has been discussed in Sneeuw (2000a). However, there are still several open questions to be investigated:

- How to filter the satellite observations contaminated by colored noise in the pre-processing stage.
- How to reduce the measurements onto a nominal torus with constant height and constant inclination.
- How to determinate the partial and cross derivatives of the observations with respect to height and inclination in a gravity field synthesis procedure.
- How to create a torus grid with a sufficient increment size and estimate the gridding errors.
- How to incorporate the weight matrix from the error PSD model in the order-wise least-squares adjustment.
- How to solve the (nearly) singular normal matrix.
- How to combine different types of observations and data sets for a joint solution.
- How to improve the least-squares estimation to compensate for assumptions and approximations.

1.2 Thesis objectives

The main objective in this thesis is to study in detail the torus-based semi-analytical approach for gravity field determination from spaceborne gravimetry observations. Specifically, all the critical issues in the calculating procedure will be discussed in the context of the processing of the different satellite observations. The objectives can be grouped into three domains:

From the *in situ* observations to the lumped coefficients

- Implementation of the design of an ARMA (Auto-Regressive and Moving Average) filter for the colored noise contaminated observations as a pre-processing stage. Analysis of the error PSD model before and after filtering.

- ► Derivation of a multi-parametric *Taylor* expansion series for the reductions of the height and inclination variations.

- ► Development of the torus-based gravity field synthesis procedure, specifically for the first and second order partial and cross derivatives of geo-potential observables with respect to height and inclination.

- ► Investigation of the deterministic and geo-statistical interpolation methods for both the isotropic and anisotropic observables. Evaluation of the error budget for the spherical harmonics estimation.

- ► Discussion on the aliasing problems in spatial/temporal and frequency domains. Investigation of a re-sampling tool for the aliasing effects caused by the variant ground track patterns.

Estimation of spherical harmonics from the pseudo-observables

- ► Development of a weight matrix of the observations for the order-wise least-squares adjustment from the error PSD model.

- ► Investigation of regularization techniques in nearly ill-posed problems, including the analysis of the characteristics of regularization matrices and determination of regularization factors.

- ► Assessment of the optimal weighting determination methods for distinct orders in the combined solutions from different types of observations or data sets.

- ► Development of a torus-based iteration procedure for the corrections of the nominal orbit assumption and interpolation errors.

Studies of the processing of the CHAMP, GRACE, and GOCE observations

- ► Comparison between the direct approach and the torus-based approach.

- ► Evaluation of the stand-alone and combined solutions from disturbing potential, line-of-sight (LOS) gradiometry, and gravity gradient tensor observables.

1.3 Thesis outline

THE analysis and results of this research are presented in Chapters 2 through 7. An outline of the essential structure of this thesis is given below.

Chapter 2 starts with a brief introduction of physical geodesy and dynamic satellite geodesy. The concepts of the three spaceborne gravimetry technologies are presented, with their realization in the dedicated gravity field missions. The satellite data in the individual missions are described. Furthermore, with the high-accuracy and high-resolution gravity field models derived from spaceborne gravimetry, the corresponding impacts on the geo-scientific applications are discussed.

Beginning with the representations of disturbing potential on a sphere, Chapter 3 presents an overview of the state-of-art gravity field determination approaches, namely the direct, space-wise, time-wise, and torus-based semi-analytical approaches. Their mathematical derivations, the corresponding projection domains, and the relationship among these approaches are introduced on the basis of spherical harmonics representation. The strengths and weaknesses of each approach also are highlighted for the purpose of theoretical comparison. In particular, a detailed calculating flow chart of torus-based approach is completed, and the relevant open questions in the individual steps are pointed out.

The error representations in both the spectral and spatial domains are introduced first in Chapter 4. Then, the filtering technique is studied as a pre-processing tool for the colored noise contaminated observations. The *in situ* observations are reduced to a nominal torus by a multi-parametric *Taylor* expansion series. The partial derivatives of the observables with respect to orbital height and inclination are calculated from a developed torus-based synthesis procedure. The methodologies of the deterministic and geo-statistical interpolation methods are studied to create a torus grid from the reduced observations. Aliasing problems are discussed in the spatial/temproal and frequency domains. In particular, the effects of the ground track patterns caused by the varying orbital heights are presented.

In Chapter 5, the focus is placed on the estimation of spherical harmonic coefficients from the pseudo-observables, the lumped coefficients, by the order-wise least-squares adjustment. Determination of the weight matrix from the error PSD model is studied. The characteristics of the regularization matrices and the regularization factor determination approaches are discussed. The performances of the optimal weighting methods are investigated. Finally, an iteration scheme is sketched to improve the least-squares estimations.

Chapter 6 focuses on the applications of the complete torus-based semi-analytical gravity field recovery in spaceborne gravimetry. The results of numerous case studies are described and analyzed. Two groups of solutions are achieved, namely the stand-alone and the combined solutions. In the former group, the processed satellite data cover disturbing potential from CHAMP and GRACE, GRACE-type line-of-sight (LOS) gradiometry, and gravity gradient tensor from GOCE. Different combination scenarios are investigated in the latter group.

Finally, Chapter 7 outlines the main achievements of this research and draws conclusions on the major contributions. It provides several recommendations for using the torus-based approach in gravity field determination. In addition, future development in this area is also presented.

Chapter 2

Dedicated satellite gravity field missions and data description

THE Earth's gravity field and its variations, which are integrated by various dynamic processes, reflect the Earth's mass transport and mass distribution, such as ocean circulation and transport, ice mass balance, and hydrologic cycles. Purely defined by gravity, the geoid is needed as a reference surface for all topographic features. However, classical gravity field information does not have a sufficient accuracy and spatial resolution in a global scale. Employing space techniques, global, regular, and dense data sets with high and homogeneous quality are achievable. The concept of spaceborne gravimetry is realized by three actual space methods: satellite-to-satellite tracking in the high-low mode (SST-hl), satellite-to-satellite tracking in the low-low mode (SST-ll), and satellite gravity gradiometry (SGG) (ESA, 1999; Rummel et al., 2002). These three concepts are implemented by three dedicated satellite missions: CHAMP, GRACE, and GOCE, respectively. The mission concepts and characteristics, the transformation from the direct measurements to the corresponding geo-potential functionals, and the description on the different level products of the data are addressed in Sections 2.2, 2.3, and 2.4 for the three satellite missions, respectively. Different types of data sets, which will be processed in this thesis, also are described in the corresponding sections. Section 2.5 lists the impacts on several geo-scientific applications of the gravity field models derived from the satellite missions.

2.1 From physical geodesy to dynamics satellite geodesy

Geodesy is a discipline that deals with measurements and representation of the Earth, including its gravity field, in a 3D time varying space.

Vaníček and Krakiwsky (1986)

As a sub-branch of geodesy, physical geodesy aims at the determination of the physical shape of the Earth. It is concerned with the physical properties of the Earth's gravity field and their geodetic applications. The Earth's gravity plays an essential role in understanding the interior and exterior mass balances of the Earth, because it is an integrated signal of Earth's mass transport and distribution. Changes in gravity over time occur as a result of ocean circulation, tectonics, earthquakes, ice melting, and so on. The geoid (i.e., the equipotential surface at mean sea level of a hypothetical ocean surface at rest, in the absence of tides and currents) serves as the reference surface for all topographic features. Figure 2.1 demonstrates the relations among gravity, geoid, and mass balance of the Earth's system, which will be discussed in detail in the context of the dedicated gravity field satellite missions in Section 2.5.

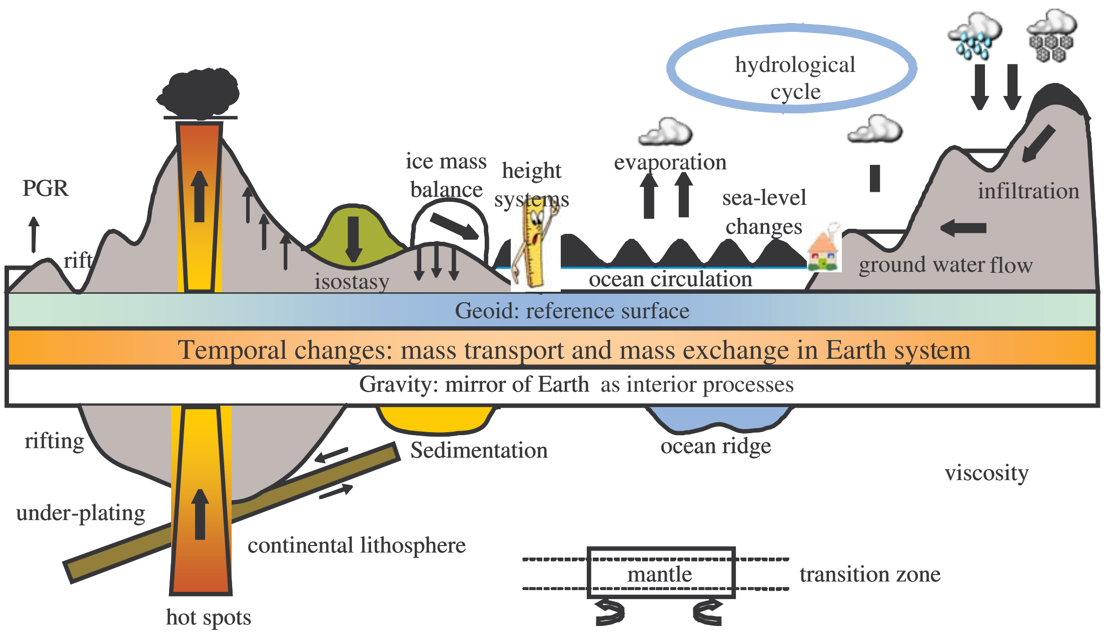

Figure 2.1: Relationship among the gravity, geoid, and mass balance of the Earth's system (ESA, 1999)

Before the dedicated gravity field satellite missions were launched, three types of gravity data were available (Rummel et al., 2002):

- mean gravity anomalies derived from terrestrial gravimetry in combination with precise height measurements and from ship-borne gravimetry. These data are inhomogeneous and inconsistent. A global map of mean gravity anomalies available in 1997 is shown in Figure 2.2.

- satellite altimetry, which provides the sea surface topography and is regarded as a direct geoid measuring technique in ocean areas only. However, the resulting stationary sea surface still deviates from the geoid because of ocean dynamics.

- satellite orbit analysis, which yielded geo-potential models in the long wavelength part of the spectrum from short-arc measurements only, such as the GRIM-4S gravity field model (Schwintzer et al., 1997).

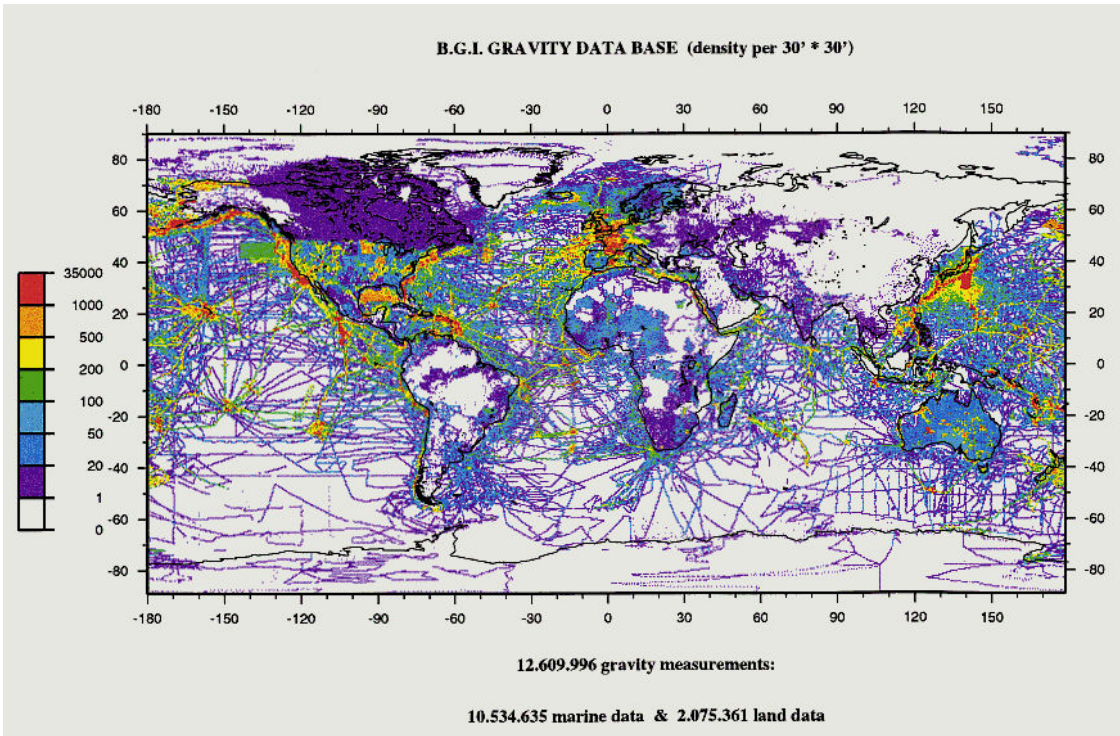

Figure 2.2: **Distribution of available measurements of gravity in 1997, from the database of the Bureau Gravimétrique International (BGI)**

The traditional techniques of gravity field determination have reached their intrinsic limits in terms of accuracy and spatial resolution from a global perspective. The global spatial resolution is expressed by the half wavelength:

$$\frac{\lambda}{2} = \frac{20,000\,\mathrm{km}}{L}, \tag{2.1}$$

with L the maximum degree of spherical harmonics; see Equation (3.1).

An advance has been brought about by space techniques because they provide global, regular, and dense data sets of high and homogeneous quality (ESA, 1999; Rummel et al., 2002).

Dynamic satellite geodesy is the application of celestial mechanics to geodesy. It aims in particular at describing satellite orbits under the influence of gravitational and non - gravitational forces.

Sneeuw (2000b)

Satellite geodesy is geodesy by means of satellites. The gravitational and non-gravitational forces lead to motions of flying satellites in a dynamic sense. However, gravity cannot be measured directly in space, and can be derived only indirectly from enormous spaceborne observations, such as position, velocity, and acceleration data. With continuous tracking by global navigation satellite systems (GNSS) and the precise accelerometers on board, spaceborne gravimetry is able to determine the Earth's gravity field. The concept of spaceborne gravimetry is implemented by three methods. These are

- satellite-to-satellite tracking in high-low mode (SST-hl),
- satellite-to-satellite tracking in low-low mode (SST-ll), and
- satellite gravity gradiometry (SGG).

2.2 Satellite-to-satellite tracking in high-low mode (SST-hl)

2.2.1 Concept of the SST-hl mode

SST-hl mode means that a low Earth orbiter (LEO) spacecraft is flying at an altitude of a few hundred kilometers and the onboard GPS receivers are continuously tracking high orbiting GNSS satellites. Simultaneously, the non-gravitational forces acting on the low orbiter are measured by on-board accelerometers (Figure 2.3). When the spacecraft is flying over a mass anomaly on the Earth, changes of gravitational attraction result in a corresponding disturbance of the satellite orbit. Then, the gravity field can be derived based on the orbital perturbations (Visser et al., 2002).

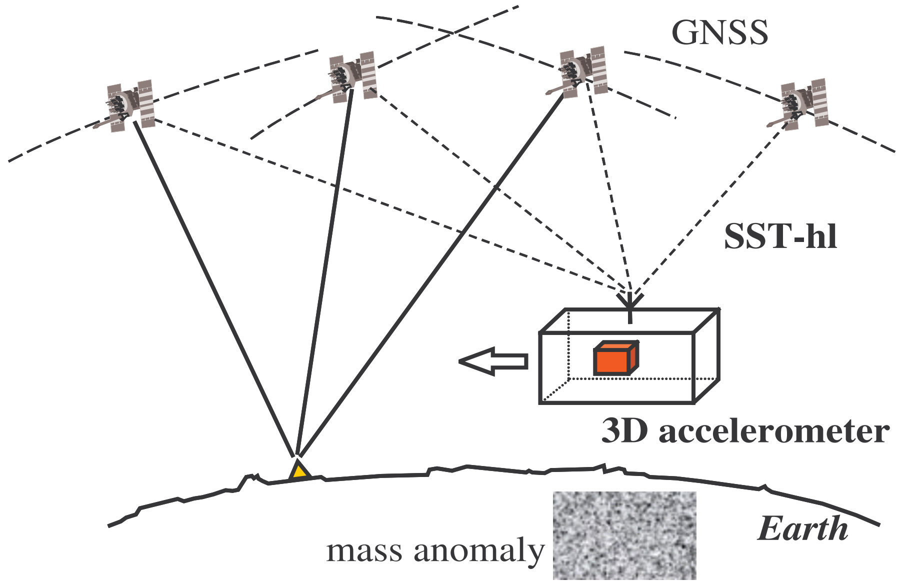

Figure 2.3: **Concept of the SST-hl mode (Seeber, 2003)**

The basic observables from the SST in the high-low mode are precise positions, velocities, and accelerations, from which the disturbing potential data along the orbit can be derived. One traditional way is the numerical integration method, which includes all parameters in a huge system and is not feasible for satellite missions. An alternative way is applying the energy balance approach, which has been comprehensively discussed in the literature of gravity field determination from satellite gravity field missions (Jekeli, 1999; Sneeuw et al., 2003; Weigelt, 2006). Therefore, only the basic idea is introduced here.

The energy balance approach, also referred to as the energy integral approach, is based on the law of energy conservation. It has been introduced in gravity field determination since the early stage of the satellite era (O'Keefe, 1975). Derived from the equation of motion in a rotating frame, the energy integral can be written as follows (Jekeli, 1999):

$$V + c = E_{\mathrm{kin}} - U - Z - \int f \cdot \mathrm{d}r. \tag{2.2}$$

The quantities at the left side are the disturbing potential and an unknown constant. All terms at the right are provided from SST-hl data and existing gravity field models:

c = *Jacobi* integral; is an integration constant

V = disturbing potential to be determined

$E_{\text{kin}} = \frac{1}{2}\dot{r}\dot{r}$ = kinematic energy; requires satellite velocities $\dot{r}$

U = normal gravitational potential; requires satellite positions r and an *a-priori* gravity field model

Z = centrifugal potential at satellite's location; requires satellite positions r

$\int f \cdot \mathrm{d}r$ = dissipative energy integrated along the satellite orbit from dissipative force f

The derived and validated disturbing potential will be treated as the input observable and will be processed to determine the Earth's gravity field model; see gravity field recovery approaches in Section 3.2.

2.2.2 The CHAMP mission and data description

As a realization for SST high-low tracking, the CHAMP (CHAllenging Mini-satellite Payload) satellite mission exploits for the first time highly precise gravity and magnetic field measurements simultaneously. It was launched in 2000 into a near polar ($I = 87°$), near circular ($e = 0.004$), 454 km initial altitude orbit (CHAMP website). Since the CHAMP mission is not an air-drag compensated mission, the satellite orbit decay was considerably fast over the mission life time. In order to avoid the mission being finished earlier than expected, two orbit change manoeuvres were performed to boost the orbital altitude in June and December 2002, respectively (Figure 2.4). The importance of mentioning the orbit changes is that the satellite passed through a number of repeat cycles more than once. A repeat orbit mode is a critical issue for gravity field determination because of the ground track patterns, which will be discussed in Section 4.5.

The CHAMP level-0 data (raw data) are stored in the science operation system at GFZ Potsdam. The standard science products are tagged from level-1 to level-4 according to the number of processing steps applied to the level-0 data. Decoding of level-0 data results in level-1 products. Level-2 data are preprocessed, edited and calibrated experiment data supplemented with necessary satellite housekeeping data and arranged in daily files. Level-3 products comprise the operational rapid products and fine processed data. Finally, level-4

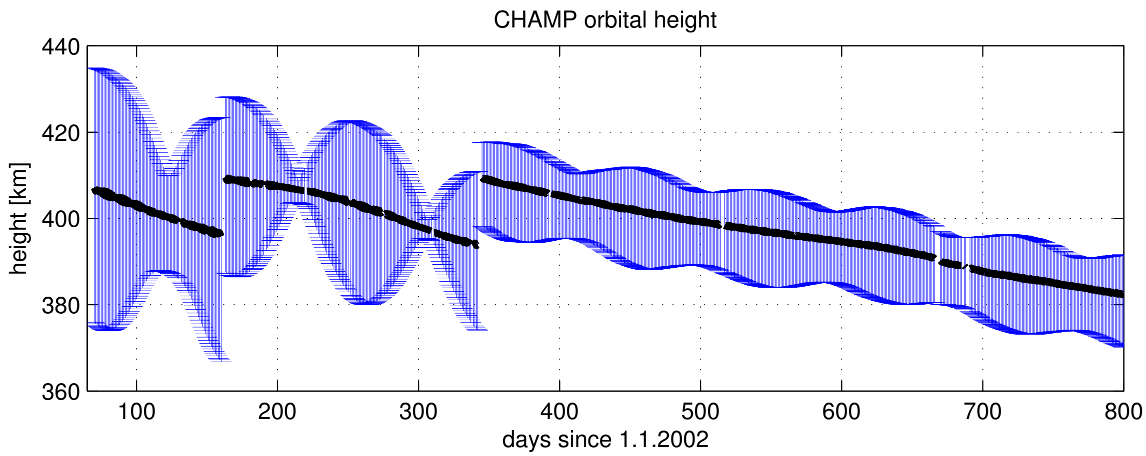

Figure 2.4: Variant and mean orbital heights of the CHAMP mission from April 2002 to February 2004

data provide geo-scientific models for different fields of research and applications. For the orbit and gravity field processing system, they are described as follows (CHAMP website):

- level-1: GPS satellite-to-satellite phase and code tracking observations from the CHAMP satellite and ground stations;
- level-2: preprocessed accelerometer observations annotated with calibration parameters, attitude information, and thruster firing time events;
- level-3: rapid science orbits of the CHAMP and GPS satellites;
- level-4: post-processed precise orbits of the CHAMP and GPS satellites, global gravity field model represented by the adjusted coefficients of a spherical harmonic expansion.

In this thesis, disturbing potential data along the orbit are derived from post-processed precise orbit information of CHAMP level-4 data. This procedure is done by the energy balance approach given in Weigelt (2006). The time span is from April 2002 to February 2004. The period includes the two orbit manoeuvres mentioned above (Figure 2.4). The sampling rate is 30 s and the data have interruptions due to missing information. Monthly solutions will be first determined for individual months and the overall solution will be merged using the multi-observable model discussed in Section 5.2. For the processing, this data set is denoted as "CHAMP data set."

2.3 Satellite-to-satellite tracking in low-low mode (SST-ll)

2.3.1 Concept of the SST-ll mode

SST-ll mode means two LEOs fly in the same orbit over the Earth. The inter-satellite range is continuously tracked by an accurate ranging instrument; at the same time, the precise positions and velocities of these twin orbiters are determined in a SST-hl mode by the GNSS system (Figure 2.5). As the gravity field changes beneath the satellites because of changes in mass and topography of the surface beneath, the orbital motion of each satellite is changed. This change in orbital motion causes the distance between the satellites to expand or contract and can be measured very precisely using the ranging system. From this measurement, the fluctuations in the Earth's gravity field can be determined (Jekeli, 1999; Balmino, 2003). One advantage of the SST-ll over the pure SST-hl is that differentiation of observables provides a much higher sensitivity. For instance, the K-band microwave is able to detect the inter-satellite range changes with a resolution of 10μm (the width of a human hair). Because of the precise relative relation between the two satellites, this differentiation observable will be more sensitive to the time-variable gravity field compared to the observables in the SST-hl mode.

Beside the precise range, range rate, and range acceleration information between the two satellites, each satellite can be treated individually as a single CHAMP-like satellite with the SST-hl concept. Therefore, disturbing potential of each satellite can be determined by the energy balance approach from the satellite position, velocity, and acceleration data as described above. Other treatments are differential gravimetry and line-of-sight (LOS) gradiometry, which will be discussed in Section 5.1.

2.3.2 The GRACE mission and data description

The SST-ll concept has been realized by the GRACE (Gravity Recovery And Climate Experiment) mission, which was launched in 2002. The characteristic orbit is almost polar ($I = 89^\circ$) and near circular ($e < 0.005$) starting with an initial altitude at 485 km (GRACE

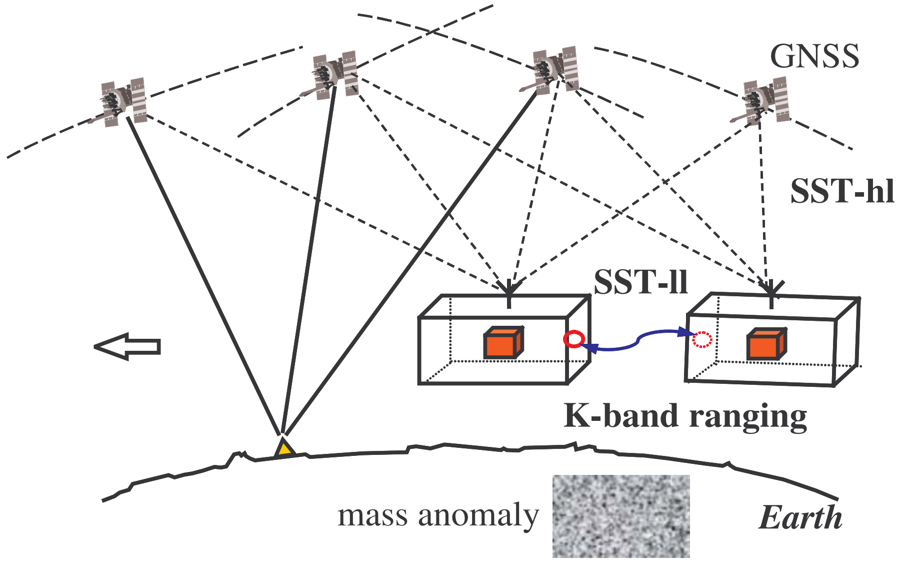

Figure 2.5: Concept of the SST-ll mode (Seeber, 2003)

website). The twin satellites are separated by approximately 220 ± 50 km in the along-track direction.

Different levels of the data products from GRACE are described as follows (Case et al., 2004):

- level-0: raw data which are separated into the science instrument and spacecraft housekeeping data streams;
- level-1A: sensor calibration factors which are applied to convert the data to engineering units with the quality flags;
- level-1B: scientific data products, such as K-band ranging data and GPS data;
- level-2: the precise orbits for the GRACE satellites and the estimations of spherical harmonic coefficients.

The K-band range ρ and range acceleration $\ddot{\rho}$ data with a sampling rate of 30 s from level-1B products were collected from September 2003 to October 2003. Under certain approximations, their ratio $\ddot{\rho}/\rho$ is treated as a similar quantity to the gravity gradient tensor along-track component V_{xx} (Sharifi, 2004); see Sneeuw (2000b) and Section 5.1. This data set is labelled "GRACE data set I."

Since the *in situ* range acceleration from the GRACE mission is very noisy, the simulated GRACE data by the Institut für Theoretische Geodäsie, Universität Bonn [1], will be employed for theoretical validation and various comparisons. Choosing the EGM96 gravity field model as the specified reference model (pseudo-real model), the data set includes the position, velocity, and acceleration measurements. These simulated data cover a time span of 30 days with a sampling rate of 5 s for both satellites, GRACEA and GRACEB. The simulation scenarios are simplified by using errorless position, velocity, and acceleration observations of the GPS satellites and the two GRACE satellites. Therefore, the errorless inter-satellite range and range acceleration can be easily calculated from the simulated position, velocity, and acceleration data. Then, the range and range acceleration data will be used to derive the pseudo LOS gradiometry observations (Section 5.1). The simulated data set is tagged "GRACE data set II."

In addition, monthly disturbing potential data for both satellites are calculated from the position, velocity, and acceleration level-1B products from August 2002 to February 2004 using the energy balance approach done by Weigelt (2006). In this case, the twin satellites are treated as two CHAMP-like satellites in the SST-hl mode. The collected data are named "GRACE data set III."

2.4 Satellite gravity gradiometry (SGG)

2.4.1 Concept of the SGG

A gradiometer is a sensor that can measure the differences of the accelerations in space, i.e., the gravity gradient tensor, which consists of the second order derivatives of the gravitational potential $V_{ij} = \frac{\partial^2 V}{\partial i \partial j}$. The tensor V_{ij} is symmetric. The *Laplace* condition is $\Delta V = V_{xx} + V_{yy} + V_{zz} = 0$.

$$V_{ij} = \begin{bmatrix} V_{xx} & V_{xy} & V_{xz} \\ V_{yx} & V_{yy} & V_{yz} \\ V_{zx} & V_{zy} & V_{zz} \end{bmatrix}. \tag{2.3}$$

[1] ftp : //geo@atlas.geod.uni – bonn.de/pub/SC7_SimulationScenarios/GRACE/

Satellite gravity gradiometry consists of three pairs of highly sensitive accelerometers in a diamond configuration, located in close vicinity to the satellite's center of mass (Seeber, 2003). Differences in the acceleration are measured in the *Eötvös* unit ($1\,Eötvös = 1\,\mathrm{E} \triangleq 10^{-9}\,\mathrm{s}^{-2}$). Equipped with the GNSS receivers, the disturbed orbit of the LEO can be precisely determined by SST-hl mode in a sensor fusion technique (Figure 2.6).

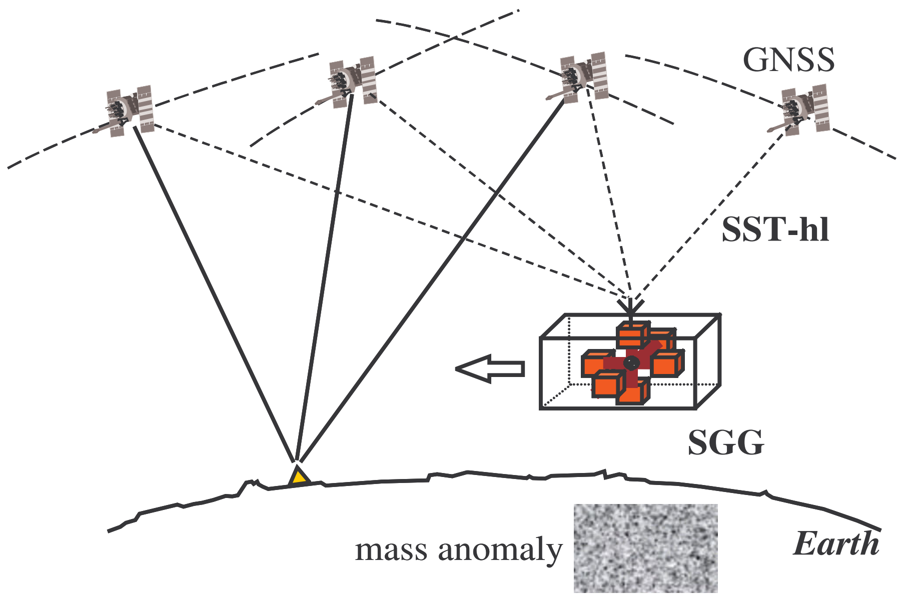

Figure 2.6: Concept of the SGG mode (Seeber, 2003)

The SGG observable, i.e., the gravity gradient tensor V_{ij}, is obtained from the accelerometer difference observation Γ after removing centrifugal acceleration $\Omega\Omega$ (Ω the angular velocity) and angular acceleration $\dot{\Omega}$ component, which are caused by the measurement in a moving frame fixed to the satellite (Rummel, 1986):

$$V_{ij} = \Gamma - \Omega\Omega - \dot{\Omega}. \tag{2.4}$$

2.4.2 The GOCE mission and data description

The GOCE (Gravity field and steady-state Ocean Circulation Explorer) mission is dedicated to measuring the static gravity field. It is scheduled for launch in spring 2008. The orbit will be sun-synchronous with an exact inclination of 96°.6. It is drag-free as low as about 250 km (GOCE website). The flight altitude is selected as a compromise between gravity attenuation and the influence of the atmosphere (ESA, 1999). The GOCE mission is unique in meeting four fundamental criteria for high accuracy and high resolution gravity field determination:

- three dimensional continuous tracking,
- compensation for the effect of non-gravitational forces such as air-drag and solar radiation pressure,
- sensing a strong gravity signal because of a low flying altitude, and
- employing the satellite gravity gradiometry (SGG) technique to counteract the gravity-field attenuation at altitude; see the *Meissl* scheme in Figure 5.1.

Similar to GRACE, the GOCE data products are categorized as follows (ESA, 1999):

- level-0: the time-ordered science and housekeeping raw data;
- level-1A: reformatted data for respective instrument packets;
- level-1B: the time series instrument and satellite data along the orbit, including calibrated and corrected gravity gradient tensors, satellite positions and velocities, satellite attitude and angular rates, and so forth;
- level-2: rapid and precise orbits, gravity field solutions and the variance-covariance matrix.

The GOCE mission is able to provide the gravity gradient tensor observations with a measuring accuracy of the order of $3 \times 10^{-3}\,\mathrm{E}/\sqrt{\mathrm{Hz}}$ within the gradiometer measurement bandwidth from 0.005 Hz to 0.1 Hz. In addition, with the implementation of the SST-hl concept, the disturbing potential observations of the GOCE mission can be derived from the position, velocity, and acceleration measurements also using the energy balance approach.

Design studies and simulations concerning the GOCE mission have been taking place in a consortium called SID. A software tool was designed to build a simulated mission in a near realistic scenario. For instance, the gradiometric measurement accuracy, the environmental disturbances, the spacecraft dynamics, and the gravity field impact are all considered in the simulation flow. In this end-to-end simulator (Figure 2.7), the gravity gradient

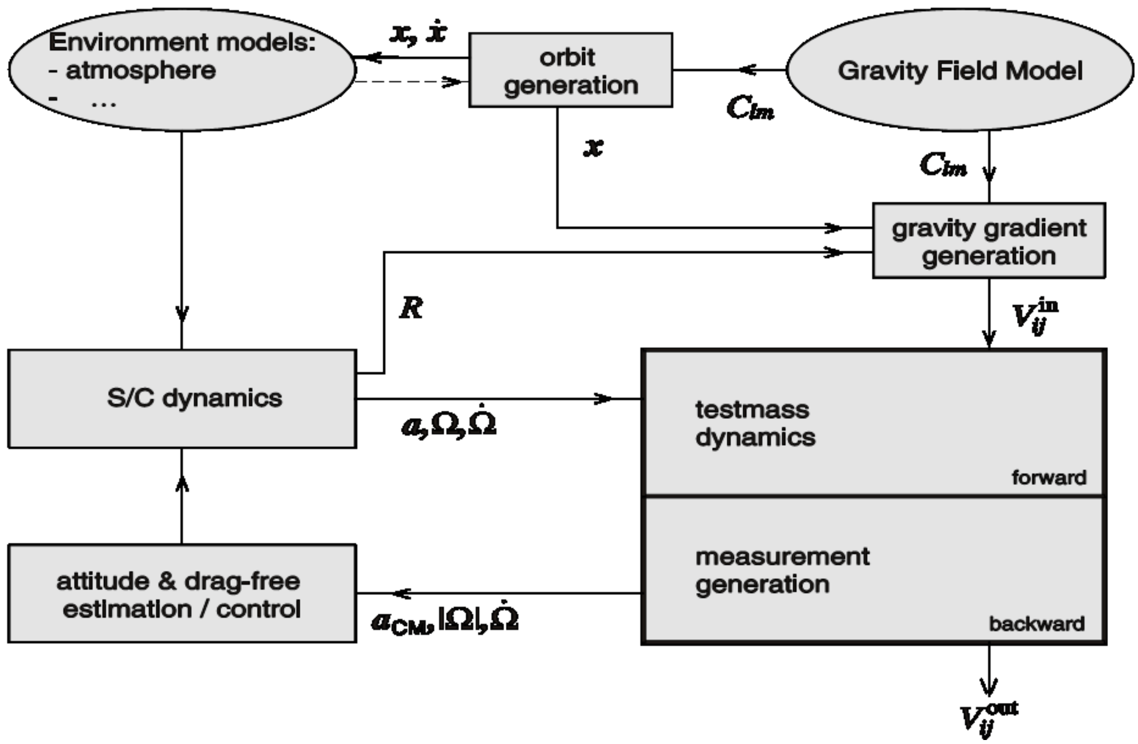

Figure 2.7: **Flow chart of the GOCE gravity gradient tensor simulator (SID, 2000)**

tensor observations are simulated. Starting from an input gravity field model (OSU91A model), a simulated orbit is integrated. Along the orbit, gravity gradients (forward box) are calculated as the input to the core of the simulator. The contaminated gravity gradient tensors (backward box) are simulated as measurements from positions (perturbed orbit), input gravity gradients, orientation (attitude errors), and disturbing forces (SID, 2000). Only the main diagonal elements of the gravity gradient tensor observables are available for analysis in this thesis. These components are simulated based on the OSU91A gravity field up to degree $L = 180$ with the normal field removed. The satellite is in a 10-day, sun-synchronous orbit (inclination $I = 96^\circ.6$) at an altitude of 246.6 km. The measurement error spectrum of the gravity gradient tensor components stays below $3\,\mathrm{mE}/\sqrt{\mathrm{Hz}}$ in terms of the power spectrum density (PSD) inside the measurement bandwidth (MBW), which is the criterion for the mission expected measurement error spectrum budget in Figure 2.8 (ESA, 1999). This data set is named “GOCE data set I.”

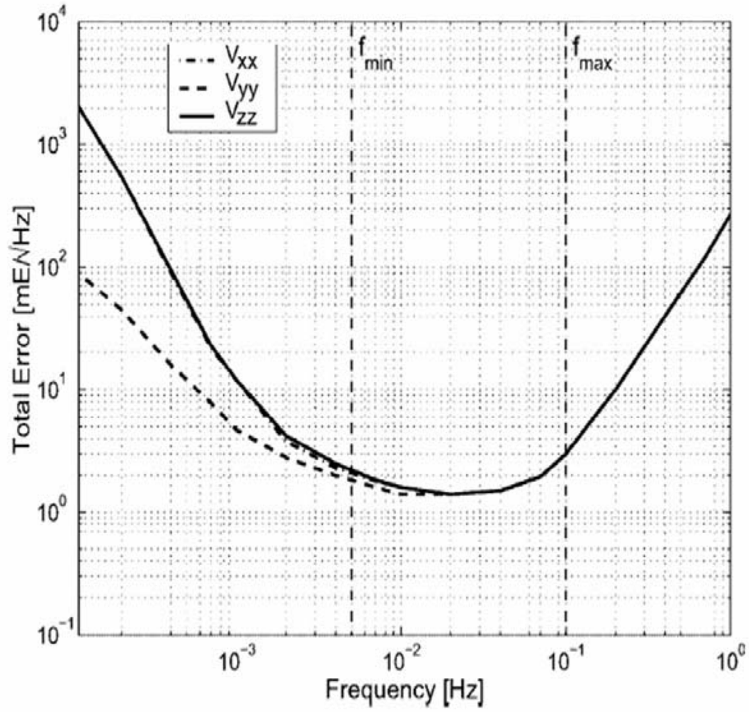

Figure 2.8: Spectra of the gravity gradient measurement error budget of GOCE with MBW of $0.005\,\mathrm{Hz} \leq f \leq 0.1\,\mathrm{Hz}$

The second simulated GOCE data set has been created by a research group at Universität Bonn [2]. The generated measurements are satellite position, velocity, and acceleration in the inertial frame and the full gravity gradient tensor components in a satellite local frame with x-axis the along-track, y-axis the cross-track, and z-axis the radial direction (Figure 3.2). The *a-priori* gravity field is the EGM96 model up to degree 300. The noise model contains external noise because of spurious forces acting on the accelerometers and internal noise caused by the position measurement of the test masses. This data set is called "GOCE data set II."

2.5 Impacts of spaceborne gravimetry on geosciences

As demonstrated in Figure 2.1, the Earth's gravity field plays a special role in geosciences because it is the only way to monitor the Earth's mass transport and mass distribution, such

[2] ftp : //geo@atlas.geod.uni – bonn.de/pub/SC7_SimulationScenarios/GOCE/

as ocean circulation and transport, and ice mass balance, on a global scale. The quantitative requirements for the different geo-scientific applications expressed in terms of the geoid height and gravity anomaly accuracies are shown in Table 2.1 (ESA, 1999; Visser et al., 2002).

Table 2.1: Gravity field requirement for sciences, expressed in terms of geoid height and gravity anomaly accuracies (Rummel et al., 2002)

Application	Accuracy		Resolution
	Geoid (cm)	Gravity (mGal)	($\lambda/2$ in km)
Oceanography			
short-scale	1–2		100
basin-scale	0.1–0.2		1 000
Ice sheets			
rock basement		1–5	50–100
ice vertical movements	2		100–1 000
Solid Earth			
lithosphere density		1–2	100
tectonic motions		1–2	50–100
Geodesy			
levelling by GPS	1		100–1 000
height systems	1		100–20 000
INS accelerometer		1–5	100–1 000
orbit determination		1–3	100–1 000
Sea level change	many of above applications		

As a result of the measurement principles and the mission implementations discussed above, the CHAMP mission is dedicated to resolving the long wavelength part of the Earth's gravity field, the GRACE mission is sensitive to medium to long wavelengths, and the GOCE mission is able to recover the short wavelengths of the static gravity field. The characteristics are summarized in Table 2.2. In addition, the extremely accurate K-band ranging system of the GRACE mission enables, for the first time, the detection of temporal variations of mass transport and distribution on a global scale with a geoid height accuracy of $2 \sim 3$ mm at a spatial resolution as small as 400 km (Tapley et al., 2004). The global, homogeneous, high-resolution, high-accuracy static gravity field and its variations with time from spaceborne gravimetry will have significant impacts on several geo-scientific objectives, which are highlighted below.

Table 2.2: Gravity field characteristics of the CHAMP, GRACE & GOCE missions

	CHAMP	GRACE	GOCE
gravity field model	EIGEN-3P	GGM02S	N/A
spatial resolution [km]	350	285	< 100
gravity accuracy [mGal]	1	1	1
geoid accuracy [cm]	10	1	$1-2$
reference resource	Reigber et al. (2005)	Tapley et al. (2005)	Rummel et al. (2002)

Ocean dynamics. Satellite altimetry missions such as the TOPEX/Poseidon and JASON-1 mission, provide accurate sea surface height (Fu et al., 1994). With the combination of the high precise geoid model derived from the gravity field missions as a reference surface, the dynamic sea surface topography can be obtained. Fenoglio-Marc et al. (2006) assessed the ability of the GRACE mission for recovering the seasonal seawater mass variation in semi-closed basins of the Mediterranean Sea with the knowledge of the satellite altimetry measurements and the oceanographic model. Morison et al. (2007) showed that the time variable gravity field from the GRACE mission is able to reveal a declining trend in the Arctic Ocean mass distribution.

Ice mass balance and sea level. Changes in the Antarctic and Greenland ice sheet mass balance have important consequences for global sea level change and climate change. In order to predict future sea level rising with more confidence, it is necessary to better understand the current evolution of continental ice masses, and to quantify their present mass balance. The time-variable gravity field from the GRACE mission is able to determine mass variations of the Antarctic ice sheet. Velicogna and Wahr (2006) found that the mass of the ice sheet decreased significantly during 2002 to 2005, at a rate of 152 ± 80 cubic kilometers of ice per year, which is equivalent to 0.4 ± 0.2 millimeters of global sea-level rise per year. Similar research was done to estimate the Greenland ice sheet melting using the monthly gravity field models from spaceborne gravimetry. The results show a consistent agreement with the estimation from independent remote sensing measurements (Luthcke et al., 2006;

Chen et al., 2006).

Solid Earth. Mass anomalies at the Earth's surface, in the crust and in the mantle, are both the cause and the result of various geodynamic processes such as plate tectonics and mantle convection. The instantaneous global gravity potential field may be used in combination with seismological and mineral physics data to refine global flow models with laterally varying viscosity, one of the key parameters of the Earth's interior (Chao et al., 2000). Temporal geoid variations may provide a data set that further constrains on mantle rheology and mantle flows (Swenson and Wahr, 2002).

Geodesy. Finally, geodesy will benefit from an improved global gravity field model in the following applications:

- GNSS/levelling. Differential GNSS provides precise ellipsoidal heights h at the GNSS stations. By subtracting precise geoid heights or geoid undulations N derived from satellite gravity field missions, orthometric heights H can be calculated very precisely, which are usually measured by the time-consuming spirit levelling (Schwarz et al., 1987). The principle of GNSS/levelling is illustrated in Figure 2.9.

$$H = h - N. \tag{2.5}$$

  The Canadian Geodetic Vertical Datum of 1928 does not satisfy needs of current users for precise height determination in terms of accuracy and accessibility. Discarding the traditional spirit levelling technique, the Geodetic Survey Division (GSD) of Natural Resources Canada recommended a redefinition of the vertical datum by adopting a gravimetric geoid model. By applying the principle of the GNSS/levelling, a new height network will allow users to access an accurate and uniform orthometric height datum everywhere across the Canadian territory (Véronneau et al., 2006).

- Unification of height systems. There are still a large number of unconnected height systems in use around the world. With the geoid precision achievable by spaceborne gravimetry, it will be possible to connect all height systems with cm-precision and few discontinuities between adjacent islands by one globally consistent height system

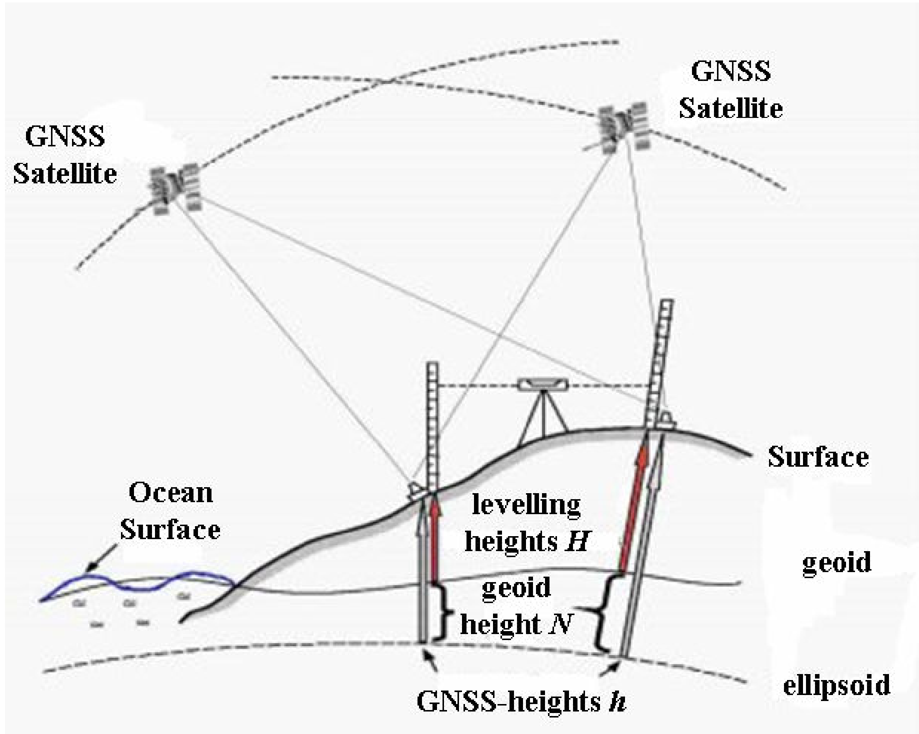

Figure 2.9: Principle of GNSS/levelling, from (GOCE website)

(Xu and Rummel, 1991). Arabelos and Tscherning (2001) assessed the improvement of the accuracy of vertical datum transfer because of the high accuracy and spatial resolution gravity field model that can be expected from the GOCE mission.

- Inertial navigation systems (INS). The core sensors of any inertial measuring unit (IMU) for performing navigation are a set of gyroscopes and accelerometers. The velocity and position of the vehicle can be obtained by single and double integrations, respectively, with respect to the accelerations measured by the accelerometers. The accelerometers measure not only the vehicle's motion, but also the gravity acceleration. Precise gravity information will serve to separate the gravimetric from the kinematic acceleration and reduce the errors significantly (Schwarz, 1981).

- Orbit determination. A high-accuracy gravity field model will provide a dramatic improvement in orbit computations for Earth orbiting satellites. Improvements in modelling orbit perturbations will lead to more accurate orbit predictions and enable near real-time operations.

Therefore, it is critically important to determine the gravity field from spaceborne gravimetry observations. The state-of-art approaches for gravity field recovery from spaceborne gravimetry will be addressed in the next chapter.

2.6 Summary

BECAUSE of continuous orbit tracking and spaceborne accelerometers, the dedicated satellite mission CHAMP, GRACE, and GOCE provide position, velocity, and acceleration data with high accuracy and homogeneous quality. These data can be transformed to geo-potential functionals and then the Earth's gravity field can be derived. Different types of geo-potential functionals related data set will be processed in this thesis, and there characteristics are summarized in Table 2.3.

Table 2.3: Summary of the data sets of satellite observations

characteristic	CHAMP	GRACE			GOCE	
	data set	data set I	data set II	data set III	data set I	data set II
orbit height (km)	454	485	407	485	246.6	257
inclination	87°	89°	89.5°	89°	96°.6	96°.6
time period (day)	729	607	30	607	10	30
sampling rate (s)	30	30	5	30	30	5
observable	V	$\rho\&\ddot{\rho}$	$\rho\&\ddot{\rho}$	V	V_{ij}	V_{ij}
product level	level-4	level-1B	N/A	level-1B	level-1B	level-1B
reference model	GGM02S	GGM02S	EGM96	GGM02S	OSU91A	EGM96
comments	orbit boosts	K-band	noiseless	GRACEA&B	MBW	MBW

With the high accuracy and high resolution models of the Earth's gravity field and its variations derived from spaceborne gravimetry, the knowledge of gravity related dynamic processes will be significantly improved.

Chapter 3

Overview of gravity field determination from spaceborne gravimetry

THE purpose of this chapter is to study different gravity field determination approaches from spaceborne gravimetry observations and present a review, in particular, of the torus-based semi-analytical approach. Section 3.1 starts with the spherical harmonic series of the disturbing potential on a sphere, which is a fundamental domain for the Earth's gravity representation. Next, two main branches for the purpose of spherical harmonic analysis are presented, namely the numerical and (semi-)analytical approaches. In Section 3.2, the theoretical and mathematical backgrounds of several gravity field determination approaches, which are the direct, space-wise, time-wise, and torus-based approaches, are introduced. In the different approaches, the spherical harmonic series is also transformed into different domains, i.e., a sphere, a repeat orbit, or a torus. The relations among these approaches are sketched in a family tree. The strengths and weaknesses of the different approaches are compared theoretically. In Section 3.3, a complete and comprehensive calculating flow chart is developed. It particularly provides a detailed insight into the practical implementation issues and the open questions to be answered in this thesis for the torus-based approach. A brief discussion on the corresponding solutions is presented before summarizing this chapter.

3.1 Representation of the Earth's gravity field on the Earth's surface

Since the first order shape of the Earth is approximately a sphere, any geo-potential observables on or above the Earth's surface can be projected onto this spherical domain with $\lambda \in [0, 2\pi)$ (longitude) and $\phi \in [-\pi/2, \pi/2)$ (latitude). A spherical harmonic series is a proper representation of a geo-potential functional because spherical harmonics have the following properties: orthogonality, global support, and harmonicity. Therefore, they are a natural base function solution of the *Laplace* equation.

The Earth's gravity field is expressed typically by the gravity potential W, which can be defined as the sum of a normal gravity potential U and a disturbing potential V, namely, $W = U + V$. Including the centrifugal potential caused by the Earth's rotation, the normal gravity potential U is the potential of a rotating ellipsoid approximating the Earth's shape and mass, which can be modelled analytically. Since the disturbing potential V is harmonic outside the masses and fulfills the *Laplace* equation, i.e., $\Delta V = 0$, where Δ is the *Laplace* operator, it can be represented globally as a series of spherical harmonic coefficients (Heiskanen and Moritz, 1967):

$$V(r,\phi,\lambda) = \frac{GM}{R}\sum_{l=0}^{L}\left(\frac{R}{r}\right)^{l+1}\sum_{m=0}^{l}(\bar{C}_{lm}\cos m\lambda + \bar{S}_{lm}\sin m\lambda)\bar{P}_{lm}(\sin\phi), \tag{3.1a}$$

$$= \frac{GM}{R}\sum_{l=0}^{L}\left(\frac{R}{r}\right)^{l+1}\sum_{m=-l}^{l}\bar{K}_{lm}\bar{Y}_{lm}(\phi,\lambda). \tag{3.1b}$$

in which

r,ϕ,λ	=	radius, latitude, longitude
R	=	the Earth's equatorial radius
GM	=	gravitational constant G and the Earth's mass M
$\bar{C}_{lm}$, $\bar{S}_{lm}$	=	normalized spherical harmonic coefficients of degree l and order m to the maximum resolvable degree L
$\bar{P}_{lm}(\sin\phi)$	=	normalized *Legendre* function as a function of latitude ϕ

The fully normalized quantities denoted by an over bar are defined in the way that the average square over the sphere for the individual quantity is unity (Heiskanen and Moritz, 1967). The corresponding normalization factor Ξ_{lm} is as follows:

$$\Xi_{lm} = \sqrt{(2-\delta_{m0})(2l+1)\frac{(l-m)!}{(l+m)!}}, \text{ for } \bar{C}_{lm}, \bar{S}_{lm}, \tag{3.2}$$

$$= (-1)^m\sqrt{(2l+1)\frac{(l-m)!}{(l+m)!}}, \text{ for } \bar{K}_{lm}, \tag{3.3}$$

with δ the *Kronecker* operator.

The complex-valued quantities $\bar{Y}_{lm}(\phi,\lambda)$ and $\bar{K}_{lm}$ make the expression more concise, and they are defined in the following way:

$$\bar{Y}_{lm}(\phi,\lambda) = \bar{P}_{lm}(\sin\phi)e^{jm\lambda} \tag{3.4a}$$

$$\bar{K}_{lm} = \begin{cases} \frac{1}{2}(\bar{C}_{lm} - j\bar{S}_{lm}) & ,m > 0 \\ \bar{C}_{lm} & ,m = 0 \\ \frac{1}{2}(\bar{C}_{lm} + j\bar{S}_{lm}) & ,m < 0 \end{cases} \tag{3.4b}$$

with "j" the imaginary unit and $\bar{K}_{lm} = (-1)^m \bar{K}^*_{l,-m}$. The superscript "$*$" denotes a complex conjugate value.

Similar to the disturbing potential V in Equation (3.1b), the related geo-potential functionals also can be expressed by means of spherical harmonic coefficients. For instance, the second order derivative of the disturbing potential with respect to the radius direction V_{rr} can be derived as

$$V_{rr}(r,\phi,\lambda) = \frac{GM}{R^3}\sum_{l=0}^{L}(l+1)(l+2)\left(\frac{R}{r}\right)^{l+3}\sum_{m=0}^{l}(\bar{C}_{lm}\cos m\lambda + \bar{S}_{lm}\sin m\lambda)\bar{P}_{lm}(\sin\phi), \tag{3.5a}$$

$$= \frac{GM}{R^3}\sum_{l=0}^{L}(l+1)(l+2)\left(\frac{R}{r}\right)^{l+3}\sum_{m=0}^{l}\bar{K}_{lm}\bar{Y}_{lm}(\phi,\lambda). \tag{3.5b}$$

By making use of geographical coordinates λ and ϕ, this type of spherical harmonic expression leads to a basic spherical projection ($2\pi \times \pi$) domain on the Earth's surface. Since spaceborne gravimetry provides continuous and global observations, which can be treated as a function of time t along the spacecraft's orbit, the *in situ* observations can be expressed as functionals of disturbing potential V both on the temporal sphere as a function of location and on the orbit trajectory as a time series. The corresponding mathematical representations for the time series of the disturbing potential on the orbital projection will be derived in the following sections.

3.2 State-of-art gravity field recovery approaches

Based on Equation (3.1), the forward computation of geo-potential functionals for a given series of spherical harmonic coefficients is know as synthesis. In contrast, the determination of the Earth's gravity field in terms of spherical harmonics form geo-potential observations is called gravity field analysis (Gauss, 1839; Colombo, 1981; Rummel et al., 1993). One of the main purposes of dynamic satellite geodesy is the determination of the Earth's gravity field from spaceborne gravimetry observations.

The historical evolution of the gravity field recovery approaches is presented. All currently available approaches are discussed in detail below.

Any analytical approach solving the problem of gravity field analysis relies only on explicit equations rather than numerical trial and error. Therefore, it is very detailed and accurate. Rooted in celestial mechanics, the analytical theories of satellite motion, such as the *Lagrange* planetary equations (LPE), were traditionally used in the early days of satellite geodesy when only relatively inaccurate measurements were available (Kaula, 1966). Special attention was devoted particularly to the resonance effects because only for those effects could the inaccurate measurements provide a reasonable signal-to-noise ratio (SNR) (Lelgemann and Cui, 2003). However, the analytical approach was mostly discarded because of its complicated derivations and limited applications for large data volume and quadratically increasing number of spherical harmonic coefficients with higher degrees.

With the availability of computer technology around 1970, numerical methods were widely employed under a good knowledge of initial state vectors. Derived by numerical integration of the variation equations, the brute-force numerical computation was the state-of-art approach in modelling satellite-only gravity field at that time (Wagner, 1983; Reigber, 1989). However, it has intrinsic limitations; for instance, it requires large computational efforts in terms of processing time and memory.

Therefore, as a compromise between the numerical and analytical approaches, the semi-analytical techniques got more attention. In literature, the space-wise and time-wise approaches are two typical methods for gravity field determination. In an analytical sense, such a semi-analytical approach explicitly links the observations with the geo-potential functionals in the spherical harmonic domain through the so-called "transfer coefficient". In a numerical sense, the Earth's gravity field can be numerically recovered by least-squares adjustment for the common over-determined problem. In general, the semi-analytical approaches have the following advantages:

- under certain assumptions and approximations, they can be formulated in a 1D or a 2D *Fourier* domain to utilize a fast *Fourier* transform (FFT) technique.

- with the same assumptions, the normal matrix in the least-squares adjustment leads to a block-diagonal structure for an individual spherical harmonic order m. Therefore, the computational time in the least-squares inversion will be quadratically decreased.

3.2.1 The brute-force approach

Treating the observations as they are, the brute-force approach, also known as the "direct" approach, makes use of well-determined orbits, an *a-priori* gravity field model, and observations from spaceborne gravimetry for setting up the linearized design equation based on orbit perturbation theory (Reigber, 1989). The spherical harmonic coefficients $\kappa = \{\bar{K}_{lm}\}$ are treated as unknown parameters on one side and the number of unknowns is $(L+1)^2$ with maximum resolvable degree L. The linear relation between geo-potential observations and unknown parameters is simply written as follows:

$$\underset{n\times 1}{y} = \underset{n\times(L+1)^2}{H} \; \underset{(L+1)^2\times 1}{\kappa}, \tag{3.6}$$

where n is the number of observations, y is the vector of observations, and H is the linearized design matrix, which contains partial derivatives of the observables with respect to every spherical harmonic coefficient. Based on this linear/linearized equation, the coefficients can be optimally estimated by a classical least-squares adjustment with the weight matrix P determined from *a-priori* information. The weight matrix is normally a diagonal matrix and the main diagonal elements are reciprocal to the value of observation variances.

$$\hat{\kappa} = (H^{\mathrm{T}}PH)^{-1}(H^{\mathrm{T}}Py). \tag{3.7}$$

Thus, the normal matrix is obtained by $N = (H^{\mathrm{T}}PH)$ with $(L+1)^4$ elements, and the estimated solution provides a fully populated *a-posteriori* variance-covariance matrix of $Q_{\hat{\kappa}} = N^{-1}$.

Theoretically, the brute-force approach is a domain independent approach. Therefore, it can be applied flexibly to any disturbing potential related functionals in any possible domain, e.g., a sphere, a repeat orbit, or a torus projection, which will be demonstrated in the relation tree in Figure 3.3.

3.2.2 The space-wise approach

Based on Equation (3.1), the word "space-wise" means an analytical function of the geographical location on the sphere. It has the advantage of the spatial correlation of the observations with a spherical projection on the Earth. Rummel et al. (1993) introduced the space-wise approach as a boundary value problem approach to physical geodesy. It transforms or interpolates the observations on a reference surface or in a spherical shell at satellite height, after which the spherical harmonic coefficients are retrieved from the disturbing potential or its derivatives. The computational data are usually given on a grid, which represents averages over grid cells. By dividing meridians in L equal intervals and parallels in $2L$ equal intervals, the $2L^2$ block averaged values of observations can be treated as quasi-observations to solve $(L+1)^2$ spherical harmonics unknowns in this over-determined situation ($L > 2$). The linear equation for a specific order m can be written as

$$\underset{n\times 1}{y} = \underset{n\times(L+1)^2}{H}\;\underset{(L+1)^2\times 1}{\kappa}, \tag{3.8}$$

with n the number of block averaged values, i.e., $n = 2L^2$.

In the subsequent least-squares adjustment, the normal matrix has the same size of $(L+1)^2 \times (L+1)^2$ as the one in the brute-force approach. For a larger L, the direct inversion would have difficulties. However, if the normal matrix is summed first along the parallels, a block-diagonal structure of the normal matrix can be achieved (Figure 3.1, where "e" means even l and "o" means odd l). The maximum size of the block is $\frac{1}{2}(L+1) \times \frac{1}{2}(L+1)$ if $m = 0$ and the minimum size is only 1×1 when $m = L$ (Colombo, 1986; Koop, 1993, Chap. 4). Under this circumstance, the inversion of the block-diagonal normal matrix is calculated easily by different blocks. Therefore, this simplification procedure leads to a semi-analytical approach.

3.2.3 The time-wise approach

The principles of the time-wise approach for the error analysis of gradiometer measurements have been developed by Colombo (1984, 1989). In this approach, the observations are formulated as a time series along the spacecraft trajectories. Subsequently, the spherical harmonics are rotated and transformed from the sphere to an orbital representation by in-

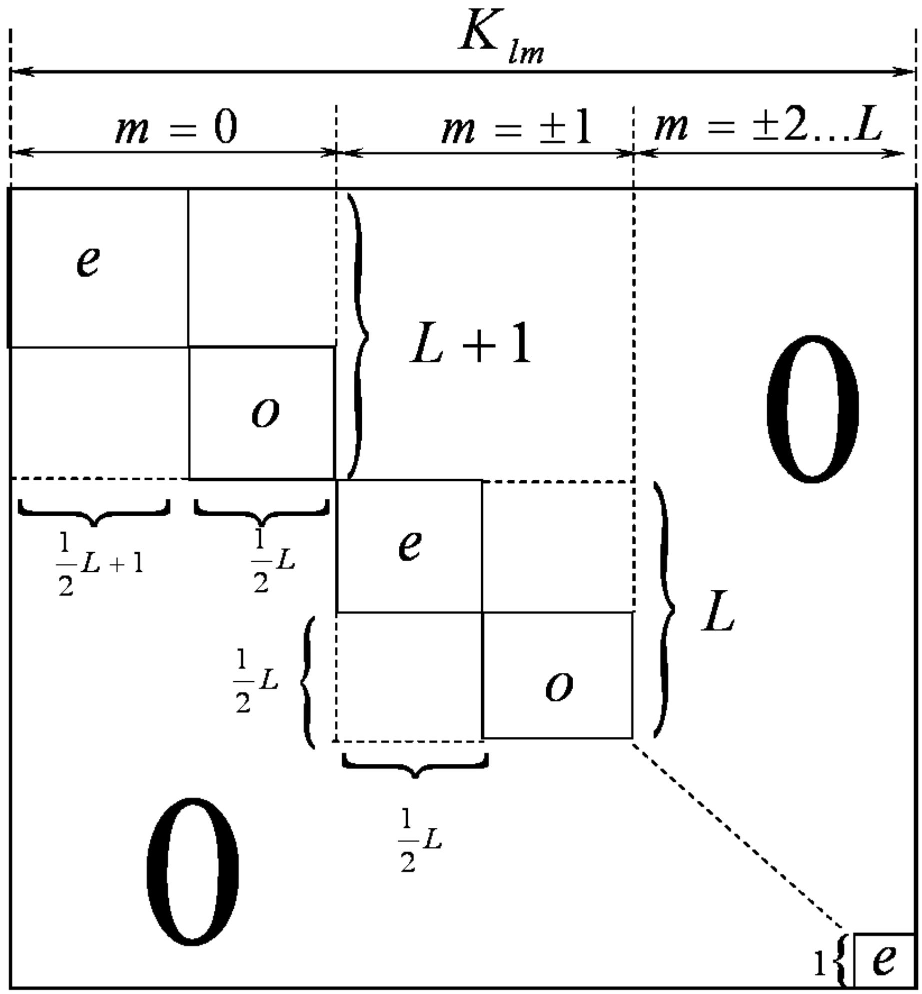

Figure 3.1: Block-diagonal structured normal matrix (Koop, 1993)

troducing the normalized complex-valued inclination function $\bar{F}_{lmk}(I)$ (Sneeuw, 1992). For instance, the gravitational disturbing potential in Equation (3.1b) can be expressed along the perturbed orbit as a function of the orbital frequency ψ:

$$V(r, I, \psi) = \frac{GM}{R} \sum_{l=0}^{L} \left(\frac{R}{r}\right)^{l+1} \sum_{m,k=-l}^{l} \bar{K}_{lm} \bar{F}_{lmk}(I) e^{j\psi(t)}, \tag{3.9}$$

in which

I	=	orbital inclination,
k	=	third index introduced by rotation and transformation,
$\bar{F}_{lmk}(I)$	=	normalized inclination function,
ψ	=	orbital spectrum as a function of time, calculated by Equation (3.16).

This time series expression is an exact representation, i.e., valid on an osculating orbit; that is, the spacecraft radius $r(t)$ and the orbital inclination $I(t)$ vary with time because of the perturbation forces acting on the spacecraft. Since the time series of observations are linearly related to the spherical harmonic coefficients, the unknown coefficients can be solved numerically by a least-squares adjustment in a similar way to the "brute-force" approach. Under a number of simplifying conditions, the normal matrix yields a block-diagonal structure identical to the one mentioned in the space-wise approach (Preimesberger and Pail, 2003). Therefore, the coefficients can be solved for individual order m. The assumptions are:

- uninterrupted observations are available;
- the sampling rate must be constant;
- the satellite orbit must have an exact repeat cycle, which means the number of nodal days N_e and the orbital revolutions N_o have to be relative primes. In other words, they do not have a common divisor; and
- the maximum solved degree L has to be less than $N_o/2$ because of the *Nyquist* theorem; see Section 4.5.

3.2.4 The time-wise semi-analytical approach in the frequency domain

As an important modification of the time-wise approach, Kaula (1983) and Wagner (1983) conceived the time-wise concept in the frequency domain for spherical harmonic analysis of SST data. Thus, the original time series is transformed to the spectral domain by the discrete *Fourier* transform. Compared to the aforementioned time-wise approach in the time domain, this approach is known as the time-wise approach in the frequency domain. Rummel et al. (1993) and Bouman (2000) proved that under the assumption of an uninterrupted data stream the time domain approach can be reduced to the frequency domain approach for an exact repeat orbit. The Fourier coefficients, which serve as pseudo-observations, represent linear combinations of spherical harmonic coefficients, and they are usually referred to as "lumped coefficients" (Gooding, 1971; Wagner and Klosko, 1977; Schrama, 1989).

Depending on the dimension of the *Fourier* transform, the lumped coefficients can be obtained by a 1D or a 2D fast *Fourier* transform (FFT), which will be discussed separately in detail below.

2D FFT based semi-analytical approach

Sneeuw (2000b) proposed the torus-based semi-analytical approach by identifying the lumped coefficients as a 2D Fourier spectrum of the gravity functional in the presence of two orbital parameters: the argument of latitude u and the longitude of ascending node Λ. Correspondingly, the disturbing potential in Equation (3.1b) can be expressed as follows (Sneeuw, 2000b):

$$V(r,I,u,\Lambda) = \frac{GM}{R}\sum_{l=0}^{L}\left(\frac{R}{r}\right)^{l+1}\sum_{m=-l}^{l}\sum_{k=-l}^{l}\bar{K}_{lm}\bar{F}_{lmk}(I)\mathrm{e}^{j(ku+m\Lambda)}, \tag{3.10}$$

in which

$$\begin{aligned} u &= \omega+\nu \\ \Lambda &= \Omega-\mathrm{GAST} \end{aligned}$$

where

$$\begin{aligned} \omega &= \text{argument of perigee} \\ \nu &= \text{true anomaly} \\ \Omega &= \text{right ascension of ascending node} \\ \mathrm{GAST} &= \textit{Greenwich}\ \text{apparent sidereal time} \end{aligned}$$

The orbital quantities are graphically explained in Figure 3.2, where X, Y, Z are the axes in the inertial frame, and x, y, z are the axes in the satellite local frame. The two orbital coordinates, u and Λ, attain values in the range of $[0,2\pi)$, and both are periodic. Topologically, the periodic product of $[0,2\pi)\times[0,2\pi)$ as two circles generates a torus, which is the proper domain of a two-dimensional *Fourier* series (Hofmann-Wellenhof and Moritz, 1986; Sneeuw and Bun, 1996).

In order to represent Equation (3.10) more clearly for a *Fourier* formulation, the following lumped coefficient A_{mk} and transfer coefficient H_{lmk} are used:

$$A^V_{mk} = \sum_{l=\max(|m|,|k|)}^{L} H^V_{lmk}\bar{K}_{lm}, \tag{3.11a}$$

$$H^V_{lmk} = \frac{GM}{R}\left(\frac{R}{r}\right)^{l+1}\bar{F}_{lmk}(I). \tag{3.11b}$$

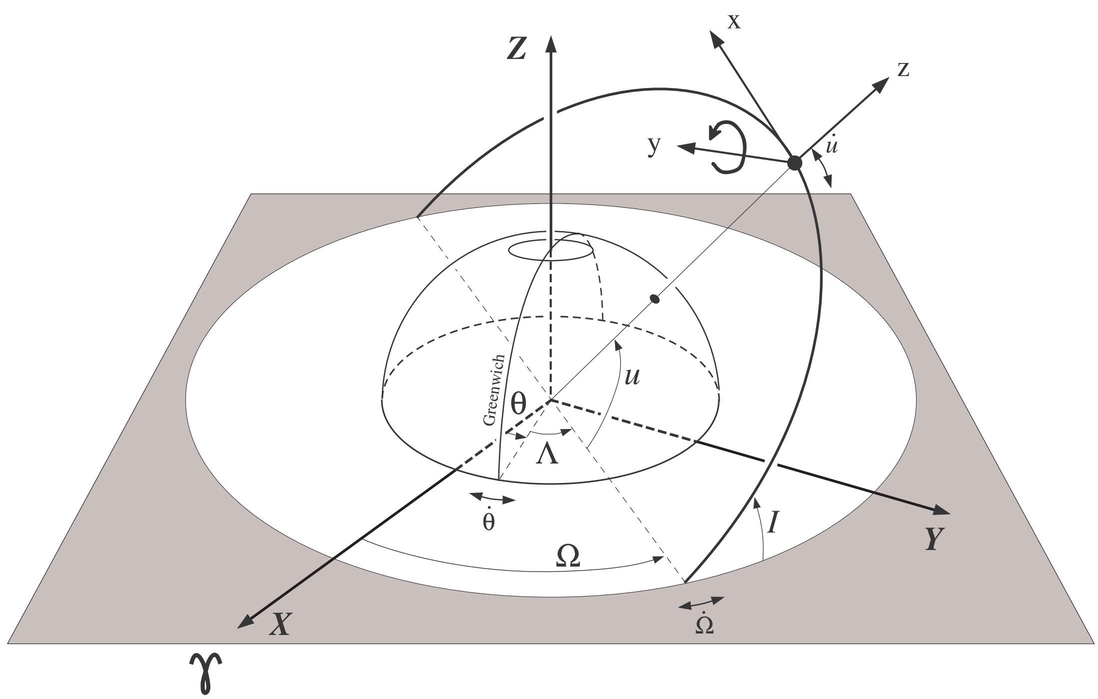

Figure 3.2: Orbit configuration (Sneeuw, 2000b)

where the superscript "^{V}" denotes disturbing potential specified quantities.

The "lumped coefficient" A^V_{mk} in terms of indices m and k are named after the linear combination of coefficients over degree l. The "transfer coefficient" H^V_{lmk} links the lumped coefficients in the frequency domain and the coefficients in the spherical harmonic domain. It is obtained by combining a dimensional factor, an upward continuation term, and an inclination function; see Section 5.1.

With these quantities (A^V_{mk} and H^V_{lmk}), the expression of the disturbing potential reduces to the following series:

$$V(r,I,u,\Lambda) \quad = \quad \sum_{m=-L}^{L} \sum_{k=-L}^{L} A^V_{mk} \mathrm{e}^{j(ku+m\Lambda)}. \tag{3.12}$$

Similar to the representation of the disturbing potential in the time-domain in Equation (3.9), the equations derived above (3.10, 3.11, and 3.12) are valid for any orbit, even in the case of the osculating orbital variables, e.g., $r(t)$, $I(t)$, as a function of time. However, it is not a full set of *Kepler* elements for an osculating orbit (eccentricity $e \neq 0$). If the orbit is an eccentric orbit, the expression has to be complemented by introducing the eccentricity function $G_{lkq}(e)$ (Kaula, 1966):

$$V(r,I,u,\Lambda,e) = \frac{GM}{R}\sum_{l=0}^{L}\left(\frac{R}{r}\right)^{l+1}\sum_{m=-l}^{l}\sum_{k=-l}^{l}\sum_{q=-\infty}^{\infty}\bar{K}_{lm}\bar{F}_{lmk}(I)G_{lkq}(e)\mathrm{e}^{j(k\omega+(k+q)M+m\Lambda)}, \tag{3.13}$$

with q an additional index and M the mean anomaly.

Although it is an exact expression containing all *Kepler* elements explicitly, the equation above becomes very complicated to be implemented, especially for a fast calculating algorithm. In addition, a 2D *Fourier* transform requires the observations to be given on a torus grid with a constant radius ($e = 0$) and a constant inclination (Figure 3.2). Therefore, a nominal orbit will be always assumed in the torus-based approach. The errors caused by this assumption can be corrected by an iteration procedure when variations in orbital eccentricity and inclination are very small, for example, $e < 4\cdot 10^{-3}$ and $\delta I < 0.01^\circ$ (Klees et al., 2000; Pail and Plank, 2002).

Sneeuw (2000b) discussed the generalized formulations of the torus-based semi-analytical approach for any geo-potential functionals. Therefore, not only the disturbing potential but also its functionals can be represented by a 2D *Fourier* series. Generally speaking, for a specific observable f, its spectral decomposition up to the maximum resolvable degree L is expressed in the following equations:

$$f(u,\Lambda) = \sum_{m=-L}^{L}\sum_{k=-L}^{L} A_{mk}\mathrm{e}^{j(ku+m\Lambda)}, \tag{3.14a}$$

$$A_{mk} = \sum_{l=\max(|m|,|k|)}^{L} H_{lmk}\bar{K}_{lm}. \tag{3.14b}$$

where the corresponding transfer coefficient H_{lmk} can be derived based on a proper differentiation technique and orbital perturbation theory; see Section 5.1 for more discussion on the derivations of different transfer coefficients.

If the lumped coefficient A_{mk} is determined, it can be treated as a pseudo-observable in the linear system of Equation (3.14b). The other components in the linear system are the transfer coefficient H_{lmk} as the design matrix and the spherical harmonic coefficients $\bar{K}_{lm}$ as unknown parameters. Under a nominal orbit assumption, the normal matrix shows a block-diagonal structure for each order m. The unknowns can be estimated by a least-squares adjustment for individual order m, which will be discussed in Section 5.2.

1D FFT based semi-analytical approach

In addition to the conditions listed in the time-wise approach in the time-domain, especially with a repeat orbit assumption, the 1D-FFT semi-analytical approach is set up based on a nominal orbit assumption as well. Similar to the lumped coefficient A_{mk} in the 2D *Fourier* coefficient expression, the lumped coefficients are reduced in an 1D expression A_n corresponding to the 1D *Fourier* transform. In this scenario, the disturbing potential in Equation (3.12) can be rewritten as a 1D *Fourier* series:

$$V(r, I, \psi_n) = \sum_{m,k=-L}^{L} A_n^V e^{j\psi_n}. \tag{3.15}$$

The orbital frequency ψ_n can be calculated by the orbital parameters u and Λ:

$$\psi_n = ku + m\Lambda. \tag{3.16}$$

Again, the pseudo-observable, the lumped coefficient A_n, can be easily obtained by a 1D FFT technique under a nominal orbit assumption.

Similar to the 2D FFT approach, the only difference of the 1D FFT approach is the way of obtaining the lumped coefficient. Since the transfer coefficient still linearly links the lumped coefficient and unknown parameters, the spherical harmonic coefficient can be determined by a least-squares adjustment in the same way as the method mentioned in the 2D semi-analytical case.

3.2.5 Characteristics of different approaches

Aiming at the same goal for spherical harmonic analysis, the aforementioned gravity field recovery approaches are categorized into two major branches: numerical and analytical (semi-analytical). The brute-force, space-wise, time-wise, and frequency domain approaches as well as their corresponding projection domains are sketched, for the first time, in a family tree, shown in Figure 3.3.

As indicated in this family tree, the brute-force approach is the numerically direct way without any approximations and assumptions. It has the following advantages:

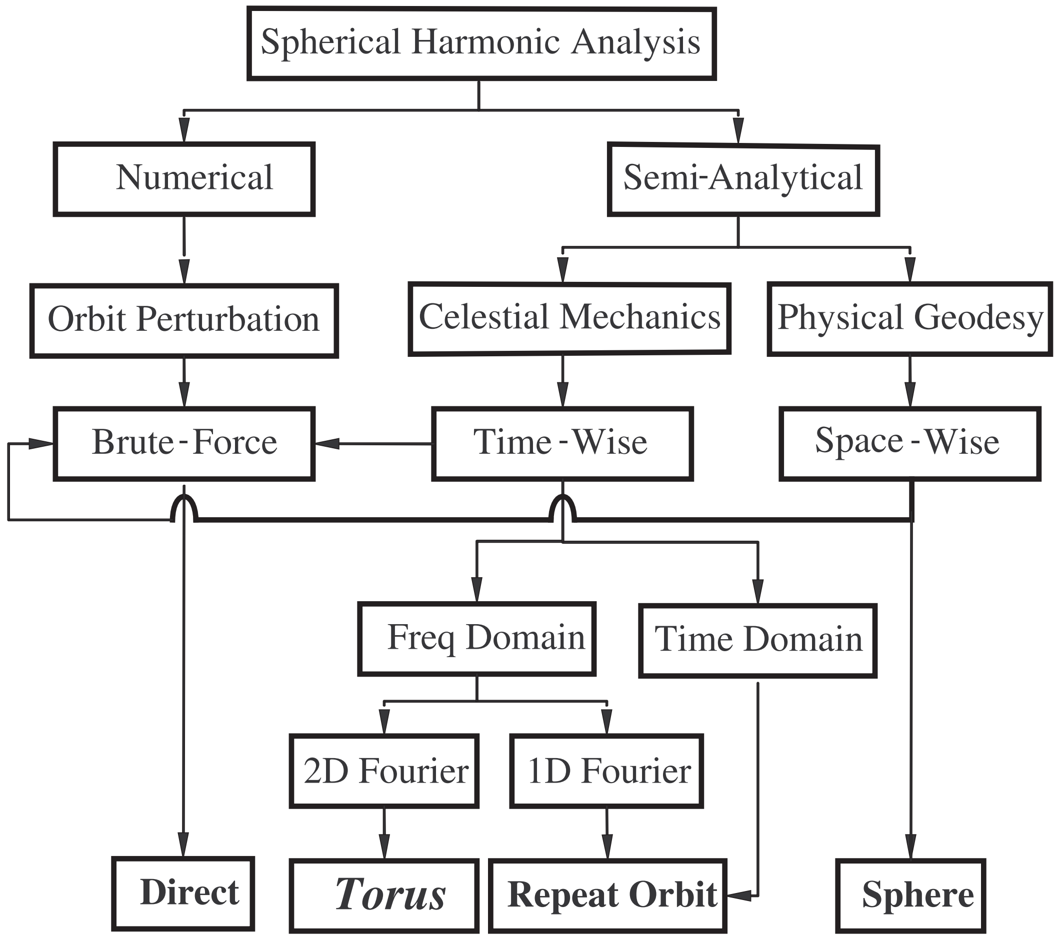

Figure 3.3: Relations among the gravity field recovery approaches

- theoretically, it is the most robust, and accurate solution without any data gap and data interruption problems, and
- it is the only approach that provides a fully populated *a-posteriori* variance-covariance matrix through the least-squares adjustment.

As a drawback, it demands an enormous computational time and very high memory storage, which are the common problems for all numerical approaches. The computational effort can be handled only by supercomputers or clusters for large degree L. For instance, by solving the spherical harmonic coefficients to $L = 100$ from about $450,000$ gravity gradient tensor data of one month measurements (30 s sampling rate), the size of the design matrix becomes $450\,000 \times 101^2$ and the corresponding normal matrix has a size of $101^2 \times$

101^2. A typical computational time for such a scenario is 48 h on a normal computer with 1 GB RAM for the brute-force method compared with only several hours for the other semi-analytical approaches (Wermuth et al., 2004). It is very difficult to solve the maximum degree up to 300 directly from the GOCE satellite mission by the brute-force approach.

Under the branch of the semi-analytical family, there are the space-wise, time-wise in time-domain, and time-wise in frequency domain with 1D FFT and 2D FFT approaches. Since the spherical harmonic coefficients can be transformed in any coordinate system, these approaches are naturally inter-connected. The domains for different representations in the semi-analytical approaches are visualized in Figure 3.4 (Sneeuw, 2000b).

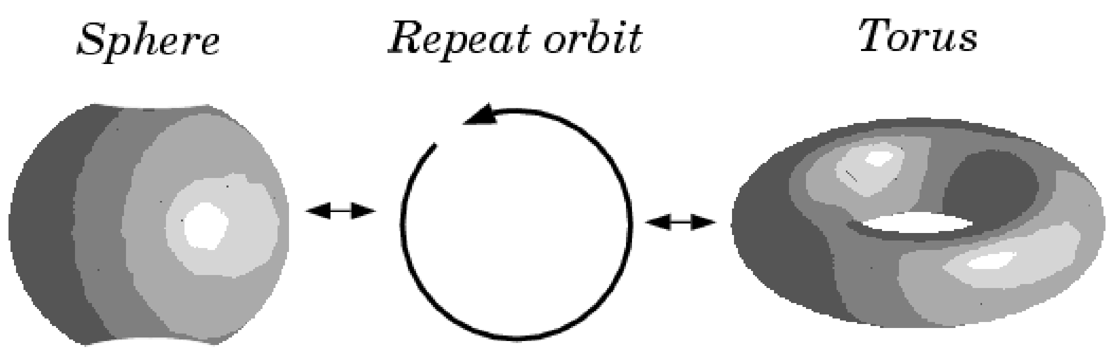

Figure 3.4: Different projection domains: sphere, repeat orbit, and torus

Rooted in physical geodesy, no assumptions about the orbit are required in the space-wise approach (Sneeuw, 2000a), and an immediate practical advantage is that it does not depend on a continuous data stream. For instance, data gaps, interruptions, and jumps do not pose a problem as long as the Earth's surface is covered sufficiently dense with data. Pail and Plank (2002) simulated missing data in the case of a large data gap of 30%, but the method still gave accurate results. Although the space-wise approach is independent on the orbital inclination, data gaps in the polar areas may cause a leakage problem. Migliaccio et al. (2004) proposed an enhanced space-wise simulation to deal with the polar gap effects, gridding effects, and noise propagation problem by least-squares collocation (LSC) and numerical integration. The conclusion is drawn that LSC and numerical integration are almost equivalent, and the collocation method is more robust. However, the space-wise approach obviously lacks any connection to the peculiarities of the orbit, its variation in heights, its resonance behavior, or its uncertainty (Rummel et al., 1993, Chapter 4). A further drawback may be the fact that the spectral stochastic model is highly complicated in terms of the error power spectral density (PSD) (Sneeuw, 2000a), which will be discussed in Section 5.3.

Apparently, the time-wise approach in the time domain is more closely related to the physics of a space experiment. All orbit features are naturally built in, therefore, it is able to incorporate error information in terms of PSD in the stochastic model in Equation (5.25); See Section 5.3. A practical disadvantage of the time-wise approach is its sensitivity to data gaps. Data interruptions will result in spectral leakage, i.e., in a smearing of the lumped coefficients. Additionally, it suffers from some assumptions involved in the fast calculating strategy. For instance, a repeat orbit is not always a realistic scenario of a mission life time, and data interruptions will result in a spectral leakage problem under an assumption of constant radius (Sneeuw, 2000a). Clearly, in addition to a nominal orbit assumption, the time-wise semi-analytical approach in the frequency domain using 1D FFT has the same problems mentioned above.

An interesting inter-relationship exists among the brute-force, space-wise, and time-wise approaches. Shown in Figure 3.3, the brute-force approach actually is inter-connected with both time-wise and space-wise approaches. When all unknown parameters involved in either time-wise or space-wise approaches are numerically solved in a whole linearized system like Equation (3.6) without any assumptions and approximations, it also can be considered as a direct approach and shares the advantages and disadvantages of the brute-force approach.

As an alternative approach, the torus-based semi-analytical approach shows the advantages of an interpolation surface with the spherical shell in the space-wise approach. At the same time, it shares the flexibility of observable type with the time-wise approach. Since this semi-analytical approach naturally yields lumped coefficients, a spectral error modelling by means of error PSD is allowed. Moreover, the orbit can be chosen freely and is not restricted to a repeat orbit.

To summarize the pros and cons for different gravity field recovery approaches, Sneeuw (2003) pointed out that the method of choice depends on practical considerations. These considerations are:

- the size of the normal matrix and its inverse in least-squares adjustment for the maximum resolvable degree L,
- the assumption of a repeat orbit for simplification,
- the influence of data gaps and polar gaps,
- the characteristics of observation noise in the spatial or in the spectral domain, and
- the ability of the interpolation methods to handle the isotropic (average over all azimuths) or anisotropic (non-isotropic) observables.

Under these considerations, the strengths and weaknesses of different approaches are summarized in Table 3.1.

Table 3.1: Strengths ($\surd$) and weaknesses ($\times$) of gravity field determination approaches

	brute-force	space-wise	time-wise	1D FFT	2D FFT
data type	$\times$	$\times$	$\surd$	$\surd$	$\surd$
repeat orbit	$\surd$	$\surd$	$\times$	$\times$	$\surd$
data gaps	$\surd$	$\surd$	$\times$	$\surd$	$\surd$
interpolation	$\surd$	$\times$	$\surd$	$\times$	$\times$
spectral analysis	$\times$	$\times$	$\surd$	$\surd$	$\surd$

3.3 The torus-based semi-analytical approach

The thesis will focus on the torus-based semi-analytical approach, which combines the strengths from both space-wise and time-wise approaches. Although Sneeuw (2000b) comprehensively discussed the theoretical background of this approach as well as various simulation scenarios for different kinds of geo-potential functionals, this gravity field analysis tool has never been implemented completely for real satellite missions, in which the situations are more complicated and observations are more noisy than the simulated scenarios. Therefore, the practical implementations of the torus-based semi-analytical approach will be studied for actual spaceborne gravimetry applications (Xu et al., 2006b).

3.3.1 Practical implementations

A complete and comprehensive calculating flow chart of the torus-based approach is developed in Figure 3.5. Under the assumption of a nominal orbit, it recovers the Earth's global gravity field in three main steps. In the first step, the observation noise is analyzed to examine if it processes white noise characteristics in order to achieve periodicity of the functional. Next, the *in situ* validated observations from spaceborne gravimetry, such as the disturbing potential data from the CHAMP mission or the gravity gradient tensor components from the GOCE mission, are reduced from the orbital variations by applying corrections with respect to both height and inclination. An *a-priori* gravity field model is used to calculate the reference values at the nominal orbit with constant height and constant inclination. The reduced irregular measurements along the satellite tracks are interpolated regularly onto a regular nominal torus grid by interpolation methods, such as least-squares collocation (LSC) or *Kriging*.

The second step is to calculate the pseudo-observable, the lumped coefficient A_{mk}, using the 2D FFT algorithm. The maximum resolvable degree L depends on the grid increment on the nominal torus and the number of mission revolutions for a repeat orbit based on the *Nyquist* criterion.

In the final step, spherical harmonic coefficients $\bar{K}_{lm}$ for distinct order m are solved separately by least-squares adjustment based on the linear system in Equation (3.11a). In addition, the error information of the estimated coefficients is provided. When an *a-priori* noise model provides observation error information in the form of power spectral density (PSD), this information is treated as stochastic input for least-squares adjustment and is propagated through the covariance matrix as output.

Several important issues involved in least squares adjustment also have to be included in the calculating flow chart. Regularization should be considered if an *a-priori* gravity field is introduced in the linear system to provide additional information or to avoid an ill-posed problem in the normal matrix inversion. To fully explore the gravity field information from several sensors, a sensor fusion concept is used. Observations from SST-hl are sensitive to the low-frequency part of the geo-potential, whereas SGG measurements will resolve the high frequencies. A better solution, however, can be achieved by combining both types of measurements. Optimal weighting methods provide relative weighting factors among different types of data sets. In addition, because of the nominal orbit assumption, this linear system is solved by least-squares adjustment from approximated initial values. This calculating scheme can be improved by iterating and updating the last estimated values, and it will stop at a certain convergence criterion.

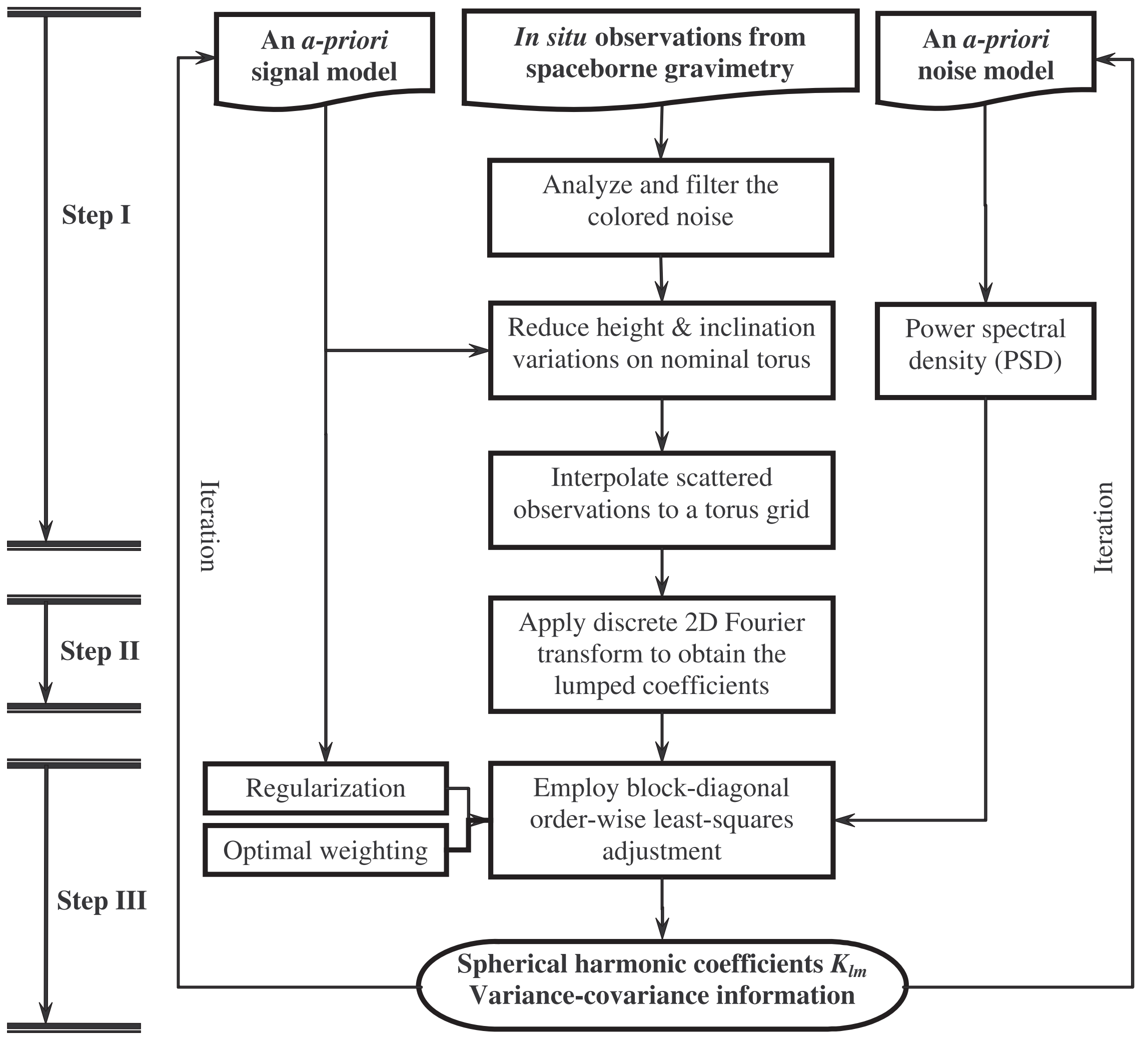

Figure 3.5: **Calculating flow chart of the torus-based semi-analytical approach of gravity field determination**

3.3.2 Open questions

The advantages of the torus-based semi-analytical approach, which are listed in Table 3.1, make it an alternative for data processing in spaceborne gravimetry. However, there are still several open questions to be investigated.

Observations are always contaminated by noise. Sometimes the noise is not a pure white-noise. Proper filters should be designed to whiten the observations before the observations are projected to the periodic torus and the least-squares adjustment can be applied (Section 4.2). The data will have to be corrected for height and inclination variations and to be reduced onto a nominal torus. A *Taylor* expansion series will be applied with the information from an *a-priori* gravity field model. The partial derivatives with respect to height $\partial^n/\partial h^n$ and inclination $\partial^n/\partial I^n$ have to be studied for a high enough order n. The calculation of the derivatives is actually a synthesis procedure and also can be implemented easily by the torus formulation. The height and inclination derivatives can be obtained by an inverse FFT with the corresponding transfer coefficients for the height and inclination derivatives (Section 4.3).

Interpolation methods have to be employed to obtain a regular torus on the nominal orbit (Section 4.4). Ordinary deterministic methods, such as linear and cubic interpolation, and geo-statistical methods, such as, the least-squares collocation (LSC) and *Kriging*, are investigated to interpolate observations (isotropic or anisotropic) from spaceborne gravimetry. Essential parameters in LSC and *Kriging* are the covariance function and the semi-variogram, respectively. Determining the suitable parameters in the covariance function or the semi-variogram from the observations is essential for the interpolation results. Empirical determination from the observation themselves and global analytical covariance models are two basic ways to reach this goal.

A 2D FFT is applied to obtain the lumped coefficients A_{mk} from regular grids. The aliasing problem will be investigated and it may be caused by several reasons, e.g., insufficient sampling in both the temporal and the spatial domains, omission errors in the signal, and effects of satellite ground track patterns caused by the orbital geometry (Section 4.5). Although the FFT algorithm is trivial, a real-valued formulation has to be derived before getting the lumped coefficients into the procedure of least squares adjustment (Section 4.6).

A pocket guide (PG) needs to be established with the transfer coefficients for the geopotential functionals in the torus-based semi-analytical approach (Section 5.1). Future satellite missions will most likely be designed in a special configuration by taking advantage of the concept of Satellite Formation Flying (SFF). The corresponding transfer coefficients for the specific observables should be studied.

Next, an order-wise least-squares adjustment (LSA) will be applied to solve the spherical harmonic coefficients (Section 5.2). Error information will be propagated through the normal matrix. The error information in terms of power spectrum density (PSD) will be converted to variance-covariance information, which will be implemented as the weight matrix in the least-squares inversion in Section 5.3. The downward continuation from satellite altitude to the surface of the Earth, which amplifies not only the signal but also noise, always causes instabilities. Therefore, regularization has to be considered for ill-posed problems in least-squares adjustment. Two aspects involved in regularization have to be studied: regularization matrix and optimal regularization factor determination (Section 5.4). In addition, the optimal weighting methods compute the relative weighting factors between different types of observations from SST and SGG. In order to achieve a better solution, the determination of an optimal weighting factor has to be investigated in Section 5.5.

One of the drawbacks of the torus-based semi-analytical approach is that it only provides an approximate solution as a result of the assumption of a nominal orbit and the errors in the interpolation computation. The estimated solution from least-squares adjustment can be improved by means of iteration. The calculating flow of the iterative scheme will be studied in Section 5.6.

3.4 Summary

GLOBAL spherical harmonic analysis determines the Earth's gravity field from spaceborne gravimetry. Numerical and (semi-)analytical approaches are the two main ways to achieve this goal. For the first time, the relations among these inter-connected approaches in different domains are summarized in a family tree. In the numerical direction, the direct approach is the most robust and accurate solution, and it is the only approach providing a fully populated *a-posteriori* variance-covariance matrix. In the analytical direction, depending on different projection domains, i.e., a sphere, a repeat orbit or a torus, the space-wise, time-wise, and torus-based approaches are described.

Each approach has strengths and weaknesses. The torus-based semi-analytical approach is the main one to be investigated in this thesis. A complete and comprehensive calculating flow chart is developed. Three major steps are needed in order to solve the spherical harmonic coefficients:

- ► in the first step, the *in situ* observations along the orbit have to be reduced onto a nominal torus grid;
- ► in the second step, the lumped coefficients are obtained as pseudo-observables by an fast numerical algorithm, i.e., the 2D FFT technique; and
- ► in the final step, the spherical harmonic coefficients are estimated from the lumped coefficients by an order-wise least-squared adjustment as a result of the block-diagonal structured normal matrix.

Several critical issues have been outlined and discussed briefly as an overview of the practical implementation of the torus-based semi-analytical approach for spaceborne gravimetry observations. These issues include: filtering technique, data reduction, interpolation, FFT technique, PG of the transfer coefficient, order-wise least-squares adjustment, regularization, optimal weights determination, and iterative solution.

Chapter 4

From *in situ* observations to pseudo-observables: lumped coefficients

THE direct input of the torus-based semi-analytical approach are the *in situ* geo-potential observations, such as the disturbing potential or its derivatives, along the orbital trajectories. However, these observations can not be used directly by the FFT technique obtaining the pseudo-observables, the lumped coefficients. Reduced and interpolated observations on a torus grid are required instead. The algorithms and methodologies of critical issues involved in the first two major steps, such as the type of filtering, data reductions, interpolation methods, and aliasing problems, will be investigated in this section. Section 4.1 starts with the error representations in both the spectral and spatial domains for the purpose of validation and comparison. As a pre-processing stage, Section 4.2 makes use of the filtering technique to filter the colored noise in the contaminated observations to get a white-noise series. A low order ARMA filter is found to work well for this purpose. Next, the calibrated observations are corrected for the height and inclination variations onto a nominal orbit in Section 4.3, where two topics will be covered. First, the multi-parametric *Taylor* expansion series is derived in Section 4.3.1, where a new expression of the derivative of inclination function $\bar{F}'_{lmk}(I)$ is developed. Second, height and inclination corrections are calculated by a developed torus-based synthesis procedure, which will be addressed in Section 4.3.2. In Section 4.4, the mathematical backgrounds of different interpolation methods are discussed, and their performances for interpolating a grid from isotropic and anisotropic satellite observations are also evaluated. In addition, the determination of the essential parameters involved in covariance function and semi-variogram is investigated. The aliasing problems, caused by the insufficient sampling rate in the spatial/temporal and frequency domains, omission errors, and the varying ground track patterns, are discussed in Section 4.5. A real-valued expression of the 2D FFT is presented in Section 4.6.

4.1 Error representations

Before studying the determination procedure from the *in situ* observations to the pseudo-observable, lumped coefficient A_{mk}, several error representation measures are defined in the spectral domain as well as in the spatial domain for the purpose of evaluating and visualizing the quality of the spherical harmonic solutions by the torus-based semi-analytical approach. Sometimes the error measures are represented with respect to a reference gravity field model from a relative perspective. The following error quantities will be employed extensively in the rest of the thesis.

4.1.1 Spectral error representation

Gravity field determination from spaceborne gravimetry provides the spherical harmonic coefficients as output. Simultaneously, the corresponding output error information can be obtained from least-squares adjustment; see Section 5.2. Correspondingly, this error information can be represented in the spectral domain in terms of spherical harmonics. Different types of 1D and 2D spectral error measures are derived next.

Two-dimensional (2D) error spectrum. The 2D error spectrum σ^2_{lm} for the spherical harmonic coefficients $\bar{K}_{lm}$ can be derived directly from the variances of the estimated coefficients $\hat{\bar{K}}_{lm}$, which are the main diagonal elements of the estimated cofactor matrix $Q_{\hat{\bar{K}}_{lm}}$ from least-squares adjustment (neglecting the correlations within m-blocks as a result of the block-diagonality property).

$$\sigma^2_{lm} = \mathrm{diag}(Q_{\hat{\bar{K}}_{lm}}). \tag{4.1}$$

Therefore, σ^2_{lm} represents a quality level for the results, i.e., the internal accuracy. Sometimes, in order to compare to another signal spectrum, e.g., a reference gravity field, the differences between two spherical harmonic spectra show the quality of the results in the context of the external accuracy.

$$\Delta_{lm} = \hat{\bar{K}}_{lm} - K^{\mathrm{ref}}_{lm}. \tag{4.2}$$

One-dimensional (1D) error spectrum. Considering the 2D error spectrum as a basic error measure, the corresponding 1D error spectra can be derived depending on different interests for either degree l or order m specific components. The error degree variance, which is used most, denotes the total error power of a certain degree l:

$$\sigma_l^2 = \sum_{m=-l}^{l} \sigma_{lm}^2. \tag{4.3}$$

Since the number of the coefficients per degree is $2l+1$ in Equation (4.3), the root-mean-square per degree (RMS_l) is derived from the error degree variance by taking the square root of the average value. Thus, it shows the average standard deviation to be expected for a single coefficient from the cofactor matrix $Q_{\hat{\bar{K}}_{lm}}$ in Equation (4.1).

$$\mathrm{RMS}_l = \sqrt{\frac{1}{2l+1}\sigma_l^2}. \tag{4.4}$$

The relative measure of the degree RMS in terms of the differences between the estimated spectral and the reference spectral is referred to as degree RMS error (RMSE):

$$\mathrm{RMSE}_l = \sqrt{\frac{1}{2l+1}\sum_{m=-l}^{l}\left(\hat{\bar{K}}_{lm} - \bar{K}_{lm}^{\mathrm{ref}}\right)^2}. \tag{4.5}$$

Commission error and omission error. Both error degree variance and degree RMS describe the error power of certain degree l. If these quantities are summed over a certain bandwidth, the cumulative error spectrum will be achieved for the total power up to a certain degree l. This is also called the commission error:

$$\mathrm{CUM}_l = \sqrt{\sum_{i=2}^{l}\sigma_i^2} = \sqrt{\sum_{i=2}^{l}\sum_{m=-i}^{i}\sigma_{im}^2}. \tag{4.6}$$

After removing the commission error spectrum from the entire gravity field spectrum, the remaining part is referred to as the omission error, which is caused by the truncation of the spectrum or by the unmodelled signal. Theoretically, it can be expressed by

$$\mathrm{OMI}_l = \sqrt{\sum_{i=l+1}^{+\infty}\sigma_i^2}. \tag{4.7}$$

Signal-to-noise ratio (SNR). Another relative error measure of importance is the ratio of the signal power to the noise power, which is called signal-to-noise ratio (SNR). The 2D SNR can be expressed in the following way:

$$\mathrm{SNR}_{lm} = \frac{|\hat{\hat{K}}_{lm}|}{\sigma_{lm}}. \tag{4.8}$$

The corresponding 1D degree SNR is denoted as the relative ratio for a certain degree l:

$$\mathrm{SNR}_{l} = \frac{\sqrt{(s_l)}}{\sigma_{l}}. \tag{4.9}$$

The quantity s_l in the numerator is the signal degree variance. It can either be obtained from a signal variance model such as *Kaula*'s rule of thumb in Equation (4.10) or be computed from the estimated spherical harmonic coefficients, e.g., $s_l = \sum_m (\hat{\hat{K}}_{lm})^2$.

$$s_l = \frac{1.6 \times 10^{-10}}{l^3}. \tag{4.10}$$

In addition, the base 10 logarithm of SNR represents the number of significant digits. This number is normally used to determine the resolution or the maximum resolvable degree L of a gravity field mission. If the ratio is equal to one, i.e., $\mathrm{SNR}_L = 1$, the signal curve crosses the noise curve and the corresponding degree is the maximum resolvable degree to be sought. However, this definition is weak because of the ambiguous boundaries between signal and noise. Sneeuw (2000b) discussed in detail the resolution determination from different *a-priori* signal models.

4.1.2 Spatial error representation

Since any geo-potential functional can be expressed in the form of a spherical harmonic series, the error information in the spherical harmonic spectral domain also can be propagated to the spatial domain. Therefore, complementary to the spectral error measures, the spatial error measures are of interest in terms of the corresponding physical meaning of the error information. For instance, the cumulative error in geoid height up to a certain degree l stands for the accuracy of the geoid determination over the sphere.

4.2 Noisy data pre-processing and the ARMA filtering technique

White noise is always preferred for a stationary process especially in the context of least-squares adjustment, because the spectral energy of white noise is independent of frequency over an infinite bandwidth. Under this circumstance, the noisy observations theoretically are uncorrelated. In addition, a periodic function with white noise is required to be projected on the torus for the employment of the *Fourier* transform. However, observations are always contaminated by different errors as a result of various noise sources, such as perturbation forces, satellite maneuvers, and measurement interruptions. Therefore, in a realistic scenario, the noise level is normally not white or is white only for certain bandwidths. In a word, it is colored noise. Therefore, noise analysis and pre-whitening should be performed as a pre-processing stage.

In the spatial or temporal domain, the auto-correlation function $R(\tau)$ is an efficient model for correlated observations. Given a time series of a signal or a noise $x(t)$, the continuous autocorrelation $R_{xx}(\tau)$ is most often defined as the continuous integral of $x(t)$ with itself, at the time lag τ.

$$R_{xx}(\tau) = \int_{-\infty}^{\infty} x(t)x(t+\tau)\mathrm{d}t. \tag{4.11}$$

The relation in the time domain can be transformed to the frequency domain in terms of the power spectral density (PSD), $S(f)$, which is the *Fourier* transform of the autocorrelation function if the random process is (weakly) stationary (Papoulis, 1965).

$$S(f) = \int_{-\infty}^{\infty} R(\tau)\mathrm{e}^{-j2\pi f\tau}\mathrm{d}\tau \Leftrightarrow R(\tau) = \int_{-\infty}^{\infty} S(f)\mathrm{e}^{j2\pi f\tau}\mathrm{d}f, \tag{4.12}$$

with f the frequency.

$S(f)$ describes how the power of a signal or a noise is distributed with frequency. According to *Parseval*'s theorem, the power computed in the spectral domain equals the power in the time domain. By analyzing the PSD characteristics of a noise process, it is easy to distinguish if the noise is a white noise or a colored noise. If the noise has a constant power density over all frequencies, it is white noise. In the torus-based approach, the orbital spectral power for certain m and k can be determined by the corresponding error variance σ_{mk}^2. The relationship between the variance and the PSD will be discussed in Section 5.3.

The theoretical background on de-noising and filtering techniques has been discussed comprehensively in Broersen (2006). The goal in this thesis is to de-correlate the colored noise in observations to achieve the white noise by using a proper filtering technique. Colored noise can always be interpreted as one realization of an autoregressive moving-average (ARMA) process, which is a linear invariant discrete system. This ARMA process $y(p,q)$ is expressed by a white noise process x with the model coefficients $\{a_m : m = 1,...,p\}$ and $\{b_n : n = 1,...,q\}$, and the pair (p,q) describes the order of the ARMA process.

$$y(k) = -\sum_{m=1}^{p} a_m y_{k-m} + \sum_{n=0}^{q} b_n x_{k-n}. \tag{4.13}$$

This differential equation can be separated into two special processes: namely, the autoregressive (AR) process of order p if $q = 0$ and the moving-average (MA) process of order q if $p = 0$. Schuh (2002) discussed the advantages and disadvantages of these three types of processes (AR, MA, and ARMA) in the context of the processing of the simulated GOCE SGG measurements. In general, the procedure of filtering the colored noise relies on an ARMA representation, which is usually obtained from a noise realization or model identification. Klees and Broersen (2002) discussed in detail the algorithms for building an optimal filter to handle colored noise in large least-squares problems. By applying the optimal filtering technique, Schuh (2003) showed that a low order ARMA filter, e.g., $p = 2$ and $q = 2$, is able to model the non-purely white process of the SGG behavior. Similarly, a simple ARMA$(2,1)$ model was design to filter the colored noise from contaminated SGG observations in Klees et al. (2003).

Therefore, a low order ARMA filter is designed and tested to whiten the colored noise as a pre-processing step in gravity field determination. For the noise model identification, the model coefficients of the ARMA filter are estimated empirically using the ARMASA toolbox developed by Broersen (2006). Then, the estimated filtering coefficients will be used as the reciprocal coefficients to design the decorrelation filter. This filter is called the inverse filter (Makhoul, 1975). The stability and causality of the inverse system is out of the scope of this thesis, and more details can be found in Grenier (1983). The following two examples demonstrate the feasibility and usefulness of the ARMA filtering technique for spaceborne gravimetry observations.

A one-day colored noise time-series of the gravity gradient tensor observations was simulated with a 1 s sampling rate. The analytical function of the noise power spectral density (PSD) is defined as follows (Ditmar et al., 2003b):

$$S(f) = \frac{S_0}{1 - e^{-\frac{f}{f_0}}}, \tag{4.14}$$

where $S_0 = 3.2\,\mathrm{mE}/\sqrt{\mathrm{Hz}}$ and $f_0 = 0.005\,\mathrm{Hz}$. This function is a smooth approximation of "$1/f$" behavior of the PSD when $f < f_0$ and is almost a constant when $f \geq f_0$ up to 0.1 Hz; See the PSD of the colored noise is plotted in Figure 4.1 (top). It clearly shows that the nearly constant measurement bandwidth (MBW) is located in the range of $0.01\,\mathrm{Hz} < f < 0.1\,\mathrm{Hz}$. Outside the MBW, the noise is colored noise.

Several lower order ARMA processes are tested, and an ARMA$(8,1)$ process is found to work well for the purpose of de-noising filtering. The bottom plot of Figure 4.1 shows that the PSD model of the noise after filtering are almost constant in the entire frequencies, therefore, the series of de-noised noise is very close to white noise.

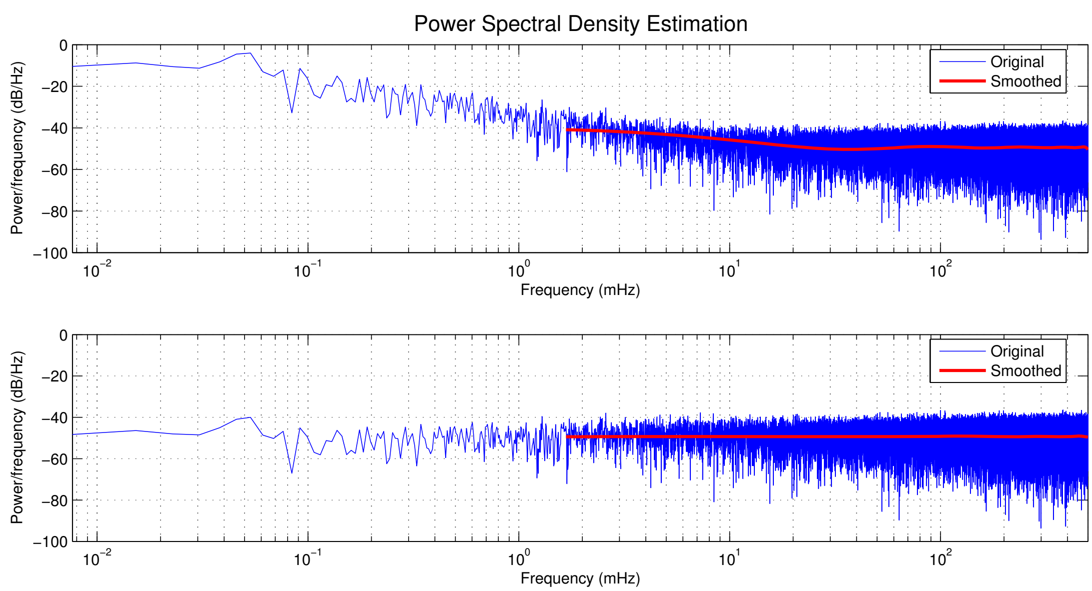

Figure 4.1: Error PSD from the simulated colored noise before and after the ARMA(8,1) filtering

Unfortunately, observation noise is normally unknown for spaceborne gravimetry observations; for instance, the *a-priori* noise model is not available. In this thesis, the differences between the noisy observations and synthesized corresponding values from a reference gravity field model are considered as the total observation errors. Spectral analysis of " GOCE data set I " with the sampling rate of 0.2 Hz (Section 2.4.2) is carried out in the second example. As a result of the measurement bandwidth (MBW), the simulated data are designed towards having colored noise, which is clearly shown in the top plot in Figure 4.2. The oscillations in the original PSD are caused by the randomness of the noise, and the red curves are the smoothed PSD. Again, a lower order ARMA$(8,1)$ process is found to work well to filter out the correlation, and the error power spectral is moving towards a white noise property with a smoothed red flat line (bottom plot).

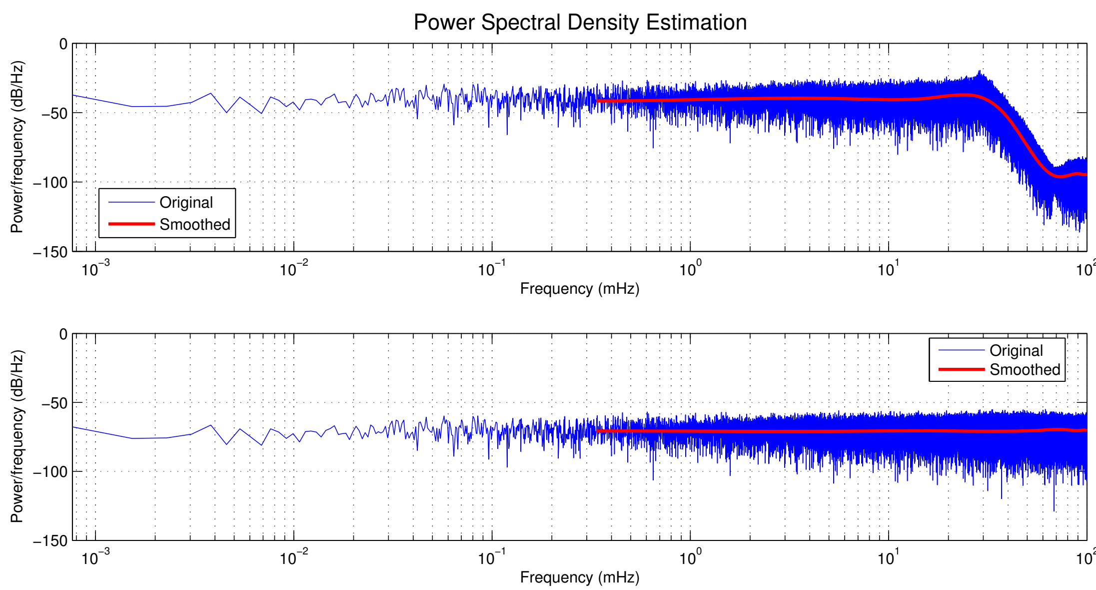

Figure 4.2: Error PSD from the GOCE gravity gradient tensor data before and after ARMA(8,1) filtering

The filtering examples show that the ARMA technique is able to filter out the colored noise from the contaminated observations. This technique should be applied to the observations with measurement bandwidth, e.g., the gravity gradient tensor components, as a pre-processing step before applying the torus-based approach. However, the assumed errors, which are calculated from the differences between the observations and the reference values, may not represent the real noise level in an actual satellite mission. Therefore, filtering will not be used in the processing of the disturbing potential data from the CHAMP and GRACE missions, where the observation noise is supposed to be a white noise.

4.3 Height and inclination variation reductions

A real satellite orbit is always influenced by disturbing forces, such as the Earth's oblateness effect, atmospheric drag, and solar radiation pressure. Figure 4.3 shows the orbital height and inclination variations of the CHAMP satellite orbit in June 2003. The orbital height varies in the range of $\pm 10\,\text{km}$, and the inclination changes by $\pm 0.006°$. Even if an orbit is not perturbed, e.g., perfect *Kepler* motion, eccentricity still introduces height variations. These variations have to be corrected to a nominal orbit with constant height and constant inclination before interpolating a grid and applying FFT.

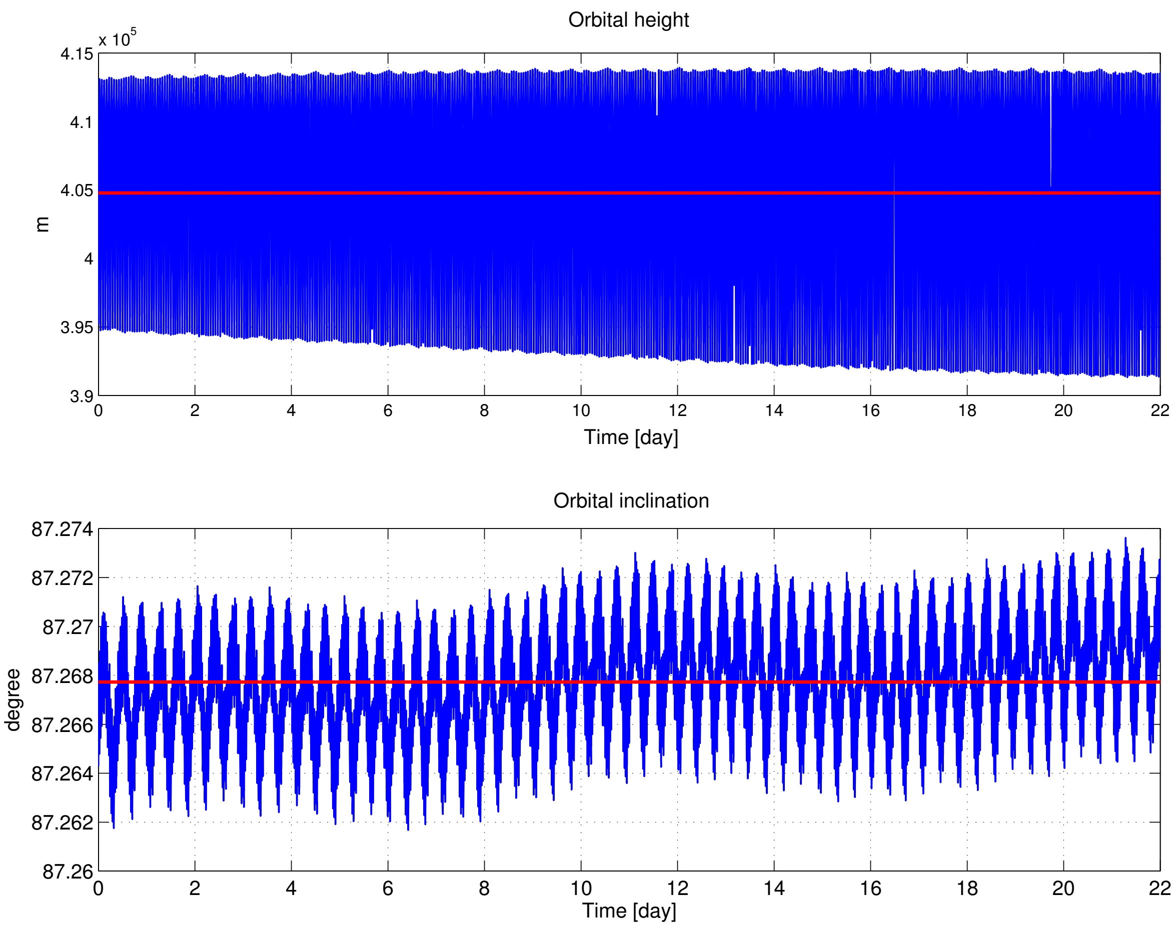

Figure 4.3: Orbital height and inclination variations of the CHAMP mission in June 2003

4.3.1 The multi-parametric *Taylor* expansion series

A typical *Taylor* expansion series is employed to reduce the in-situ observations downward or upward onto the nominal orbit in the presence of the height and inclination variations

(Figure 4.4). For instance, the *Taylor* series of disturbing potential V with respect to height h and inclination I expansions is derived as follows:

$$\begin{aligned} V(h,I) &= V(h_0,I_0) + \left.\frac{\partial V}{\partial h}\right|_{h_0,I_0} \cdot (h-h_0) + \left.\frac{\partial V}{\partial I}\right|_{h_0,I_0} \cdot (I-I_0) \\ &+ \left.\frac{1}{2}\frac{\partial^2 V}{\partial h^2}\right|_{h_0,I_0} \cdot (h-h_0)^2 + \left.\frac{1}{2}\frac{\partial^2 V}{\partial I^2}\right|_{h_0,I_0} \cdot (I-I_0)^2 \\ &+ \left.\frac{\partial^2 V}{\partial h \partial I}\right|_{h_0,I_0} \cdot (h-h_0)(I-I_0)\ldots \end{aligned} \tag{4.15}$$

where the subscript "0" means the corresponding values on the nominal torus.

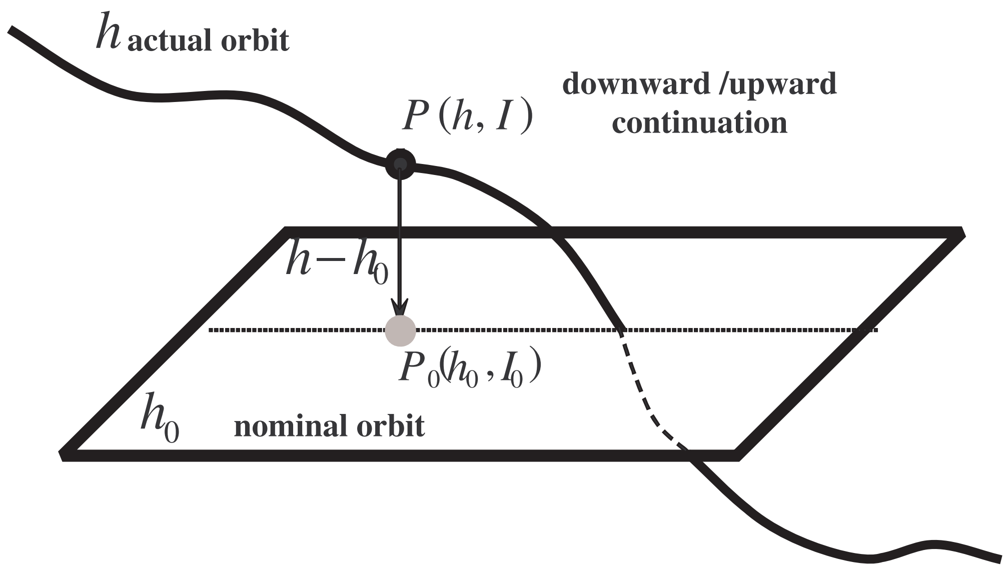

Figure 4.4: **Corrections along the radial direction onto a nominal orbit**

4.3.2 Development of the torus-based gravity field synthesis

If the gravity field analysis is defined as an inverse problem from observations to spherical harmonic coefficients, the gravity field synthesis is a simple forward problem determining the geo-potential observations from the spherical harmonics. The subscript "0" in Equation (4.15) refers to the values calculated from an *a-priori* gravity field model. It is actually a gravity field synthesis procedure to calculate the disturbing potential, and also its first and second order derivatives with respect to height and inclination. The torus-based approach is an efficient and powerful synthesis tool making use of an inverse FFT algorithm (IFFT) and the transfer coefficient collections of the PG.

The calculating procedure for the gravity field synthesis is demonstrated in Figure 4.5. Compared to the gravity field analysis procedure in Figure 3.5, the synthesis procedure is more straightforward. First, the spherical harmonic coefficient solution or the reference gravity field model is employed to obtain the pseudo-observables, the lumped coefficients, based on the linear system in Equation (3.14b). In the next step, the observations on a nominal torus grid can be quickly computed by the IFFT algorithm from Equation (3.14a). The *in situ* observations along the nominal orbit can be interpolated from the torus grid data. This step will introduce the interpolation errors in the on-orbit observations. In order to avoid the interpolation errors, the time series observations along the nominal orbit can be directly calculated by the superposition with respect to the indices m and k in Equation (3.14a). Although it is not as fast as the application of the IFFT algorithm, the superposition can be handled efficiently by a numerical vector operation without any computational problems. Computational time is partially saved because no interpolation is needed for the synthesis. If the observations along the disturbing orbit are needed, the corrections with respect to the height and the inclination have to be added on the nominal orbit using the *Taylor* expansion series in a reverse way.

The torus-based approach is certainly an alternative, useful, and powerful tool for the purpose of gravity field synthesis, because it is able to deal with any geo-potential functional and its partial derivatives. For instance, it would be very difficult to calculate the partial derivatives with respect to inclination directly from the direct approach using Equation (3.1) because the inclination is not an explicit parameter in the expression. Nevertheless, the explicit inclination function $\bar{F}_{lmk}(I)$ in Equation (3.10) makes this procedure much easier, because $\bar{F}_{lmk}(I)$ is the only quantity containing the inclination variable, while the dimensioning factor, the upward continuation part R/r, and the specific transfer term are considered constant with respect to inclination.

$$\frac{\partial V(r,I,u,\Lambda)}{\partial I} = \frac{GM}{R}\sum_{l=0}^{L}\left(\frac{R}{r}\right)^{l+1}\sum_{m=-l}^{l}\sum_{k=-l}^{l}\bar{K}_{lm}\bar{F}'_{lmk}(I)\mathrm{e}^{j(ku+m\Lambda)}, \tag{4.16}$$

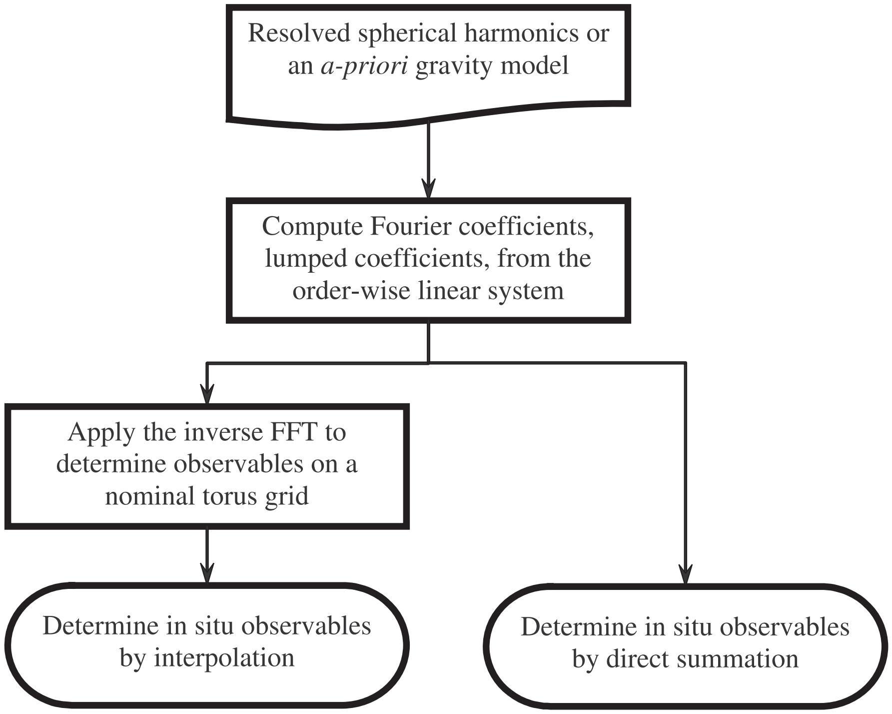

Figure 4.5: Calculating flow chart of the torus-based gravity field synthesis approach

Balmino et al. (1996) derived a twofold analytical expression of the first order derivative of the inclination function $\bar{F}'_{lmk}(I)$ by making use of the inclination function $\bar{F}_{lmk}(I)$ and the cross-track derivative of the inclination function with respect to the colatitude coordinate $(\theta = 90^\circ - \phi)$, denoted as $\bar{F}^*_{lmk}(I)$ (Sneeuw, 1992). In addition, by definition, the cross-track inclination function $\bar{F}^*_{lmk}(I)$ vanishes when $l-k$ is even, while the inclination function $\bar{F}_{lmk}(I)$ attains a zero value when $l-k$ is odd.

$$\bar{F}'_{lm,k-1}(I) = +\left(\frac{(k-1)\cos I - m}{\sin I}\right)\bar{F}_{lm,k-1}(I) - \bar{F}^*_{lmk}(I), \tag{4.17a}$$

$$\bar{F}'_{lm,k+1}(I) = -\left(\frac{(k+1)\cos I - m}{\sin I}\right)\bar{F}_{lm,k+1}(I) + \bar{F}^*_{lmk}(I). \tag{4.17b}$$

By replacing the index $k-1$ with k in Equation (4.17a) and the index $k+1$ with k in Equation (4.17b), $\bar{F}'_{lmk}(I)$ can be re-arranged and represented by the cross-track inclination function $\bar{F}^*_{lmk}(I)$ only:

$$\bar{F}'_{lmk}(I) = \frac{\bar{F}^*_{lm,k-1}(I) - \bar{F}^*_{lm,k+1}(I)}{2}. \tag{4.18}$$

In terms of the partial derivatives with respect to height, the inclination function is a constant term for height. The variant coefficients are the dimensioning term and the transfer factor, as well as the upward continuation part "R/r". For instance, in Equation (3.10), the disturbing potential V has these three terms with values of GM/R, 1, and $l+1$, respectively. When taking the partial derivative of the disturbing potential with respect to height ($\partial V/\partial r$), these three terms are derived as GM/R^2, $-(l+1)$, and $l+2$, respectively. Therefore, the cross-derivative term with respect to inclination and height can be derived as follows:

$$\frac{\partial^2 V(r,I,u,\Lambda)}{\partial I \partial r} = -(l+1)\frac{GM}{R^2}\sum_{l=0}^{L}\left(\frac{R}{r}\right)^{l+2}\sum_{m=-l}^{l}\sum_{k=-l}^{l}\bar{K}_{lm}\bar{F}'_{lmk}(I)\mathrm{e}^{j(ku+m\Lambda)}, \tag{4.19}$$

As an example, the *in situ* disturbing potential data from the CHAMP mission at satellite altitude in January 2004 are reduced to the nominal orbit by the *Taylor* expansion series. The first order (left) and the second order (right) height corrections are plotted in Figure 4.6. The first order inclination corrections (left) and the corrections of the cross-derivative (right) with respect to both height and inclination are plotted in Figure 4.7.

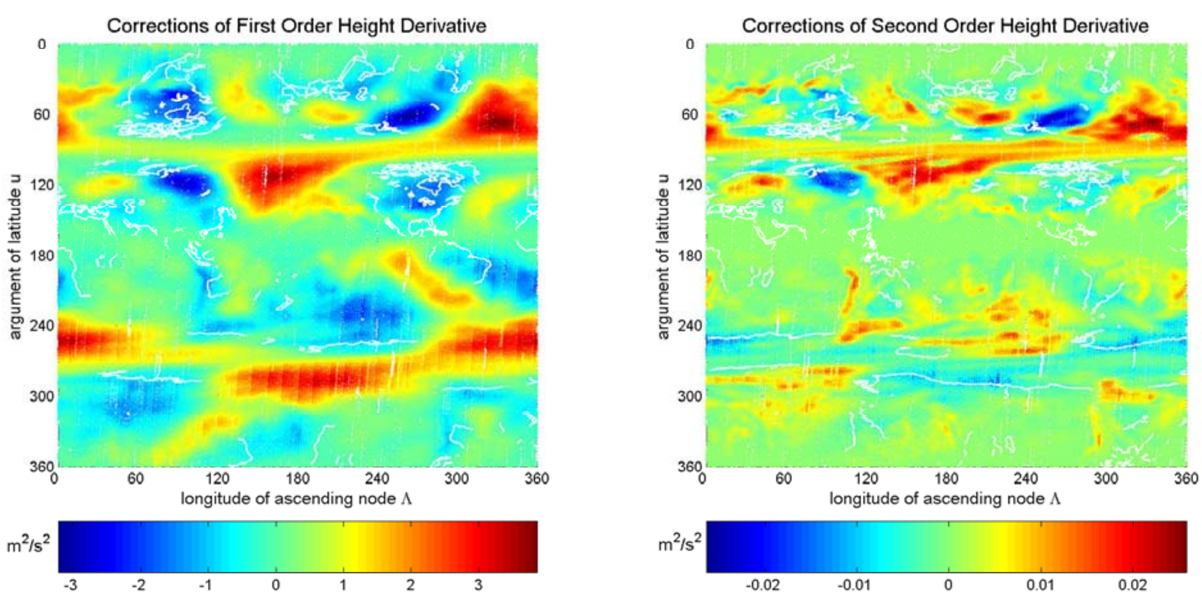

Figure 4.6: Corrections of height derivatives for the disturbing potential data

The range of the *in situ* disturbing potential data is $\pm 600\,\mathrm{m}^2/\mathrm{s}^2$. The reductions are calculated as the percentage of the original values for the purpose of comparison. Figure

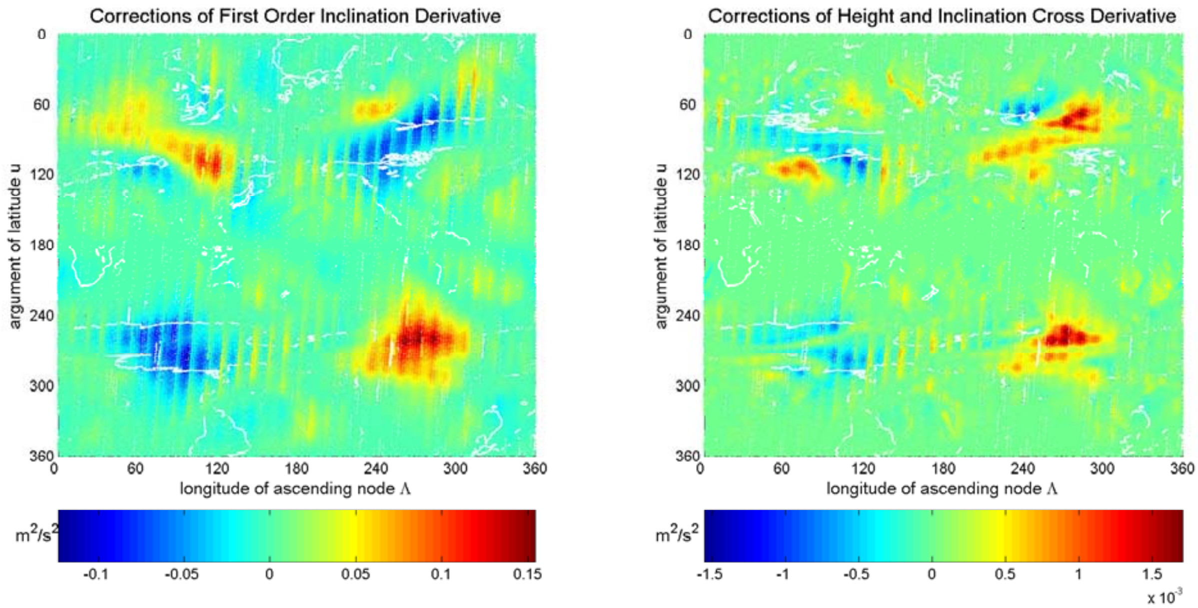

Figure 4.7: Corrections of inclination derivatives for the disturbing potential data

4.6 shows that the range of the first order height corrections is $\pm 3\,\mathrm{m}^2/\mathrm{s}^2$ ($\approx 0.50\%$), and the second order height corrections is $\pm 0.03\,\mathrm{m}^2/\mathrm{s}^2$ ($\approx 0.005\%$). Figure 4.7 shows that the first order inclination corrections is in the range of $\pm 0.15\,\mathrm{m}^2/\mathrm{s}^2$ ($\approx 0.025\%$), and the cross-derivative corrections have a maximum value of $\pm 0.0015\,\mathrm{m}^2/\mathrm{s}^2$ ($\approx 0.00025\%$).

Taking the percentage value at 0.005% ($\pm 0.03\,\mathrm{m}^2/\mathrm{s}^2$) as a threshold, the *Taylor* expansion series can be truncated at the second order of the height corrections and at the first order for the inclination corrections, and the cross-derivative corrections will be neglected because of their small values. Therefore, the final *Taylor* series is used as follows:

$$V(h_0,I_0) = V(h,I) - \left.\frac{\partial V}{\partial h}\right|_{h_0,I_0} \cdot (h-h_0) - \left.\frac{\partial V}{\partial I}\right|_{h_0,I_0} \cdot (I-I_0) - \frac{1}{2}\left.\frac{\partial^2 V}{\partial h^2}\right|_{h_0,I_0} \cdot (h-h_0)^2. \quad (4.20)$$

Figure 4.8 shows the difference between the *in situ* disturbing potential data and the reference values on the nominal torus before (left) and after (right) the height and inclination corrections. The standard deviations (STD) are $1.55\,\mathrm{m}^2/\mathrm{s}^2$ and $1.01\,\mathrm{m}^2/\mathrm{s}^2$, respectively. After the reduction procedure, the differences with respect to the reference gravity field are more homogeneous.

A similar comparison is carried out for the gravity gradient tensor in the radial direction V_{zz} component from “GOCE data set I,” shown in Figure 4.9. The large variations with a

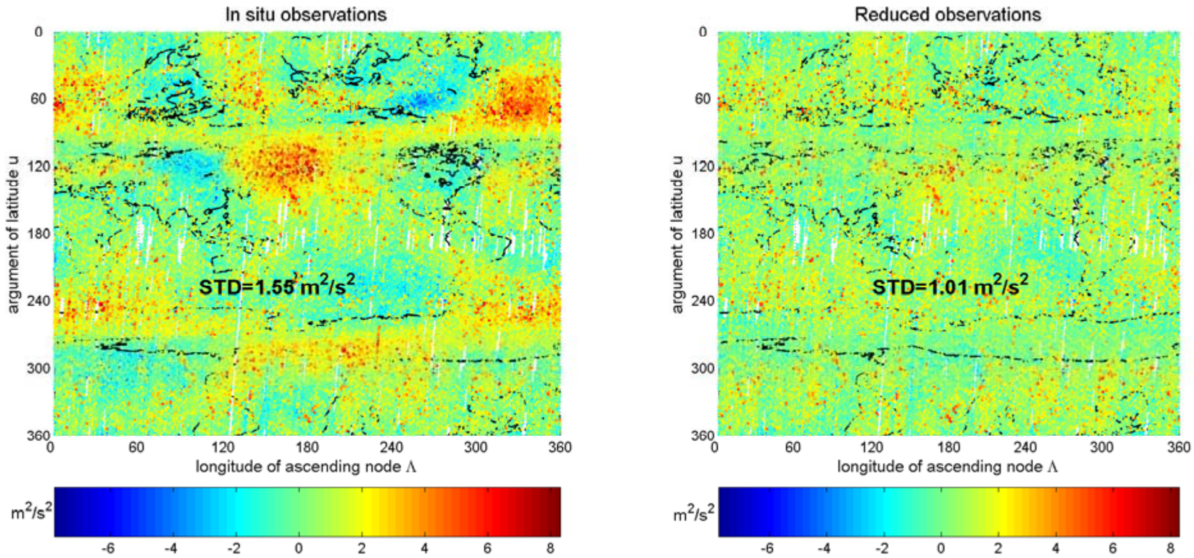

Figure 4.8: Comparison of disturbing potential before and after data reduction, the GGM02S model as reference

pattern in the along-track direction are removed by the data reduction. The values of STD are 7.16 E and 0.02 E before and after the inclination and height reductions. Since the magnitude of the disturbing part after removing the normal gravity field is about 1.0 E, the magnitude of the corrections ($\approx$ 15.0 E) shows that the reduction procedure is critically necessary for observations without the normal gravity field removed.

4.4 Evaluation of interpolation methods

The *in situ* observations from spaceborne gravimetry are obtained along the spacecraft orbital trajectories, and they are normally scattered and irregularly distributed when projected onto either the spherical Earth's surface or a torus. The situation sometimes becomes even worse if

- measurements are interrupted by data gaps caused by operating mechanic problems or calibration failure;
- the LEO flies in an exact repeat orbit mode, which means the number of nodal days N_e and the orbital revolutions N_o have to be relative primes. Therefore, the Earth surface or the torus surface cannot be covered densely by observations; and

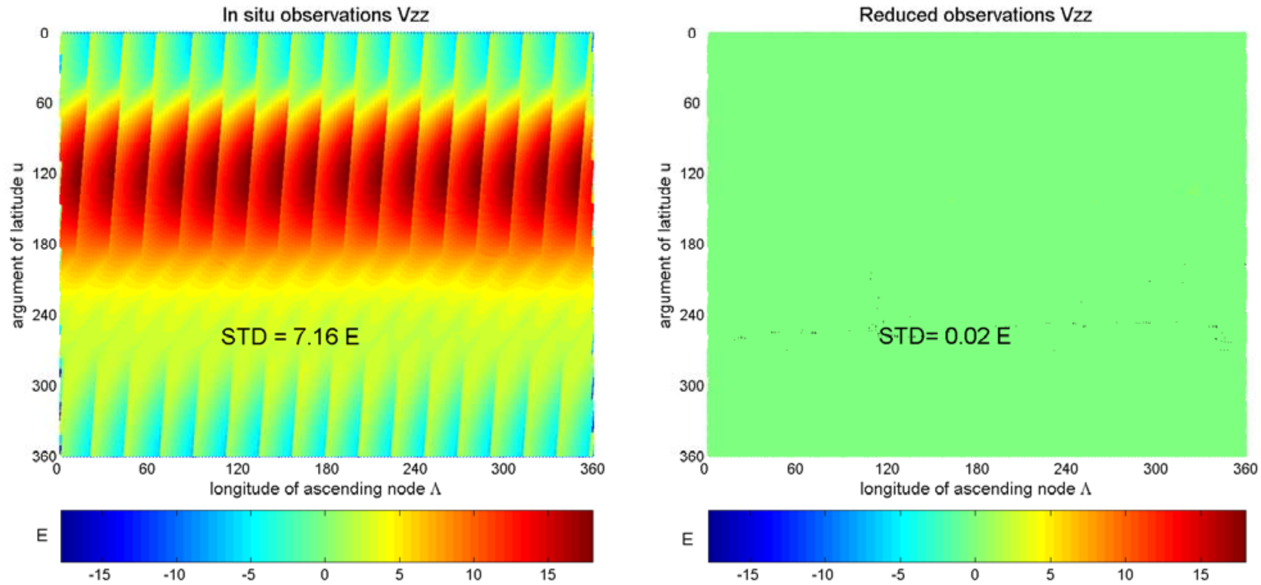

Figure 4.9: Comparison of gravity gradient tensor V_{zz} before and after data reduction, the OSU91A model as reference

- the orbital inclination is not always 90° for a non-polar orbit, e.g., in the case of a sun-synchronous orbit. There is no observation coverage in the two polar areas with $|90^\circ - I|$ gaps, which are called polar gaps (Sneeuw and van Gelderen, 1997).

All the problems mentioned above are demonstrated under one circumstance in Figure 4.10. It is an extreme scenario but it can happen in the real world. Note that naturally no polar gaps are shown in the torus projection Figure 4.10(b).

In addition, regular and dense data distribution is necessary and sometimes mandatory for geodetic applications when fast processing algorithms are employed; for instance, the 2D FFT technique in the torus-based semi-analytical approach requires the regularly distributed observations on a nominal torus grid.

As a result, interpolation becomes an essential and powerful tool for creating a regular grid from the irregular and sparse measurements. Several methods are available and are usually classified into two classes: deterministic approaches, e.g., the bi-linear method and spline method, and geo-statistical approaches, e.g., least-squares collocation (LSC) and the *Kriging* method.

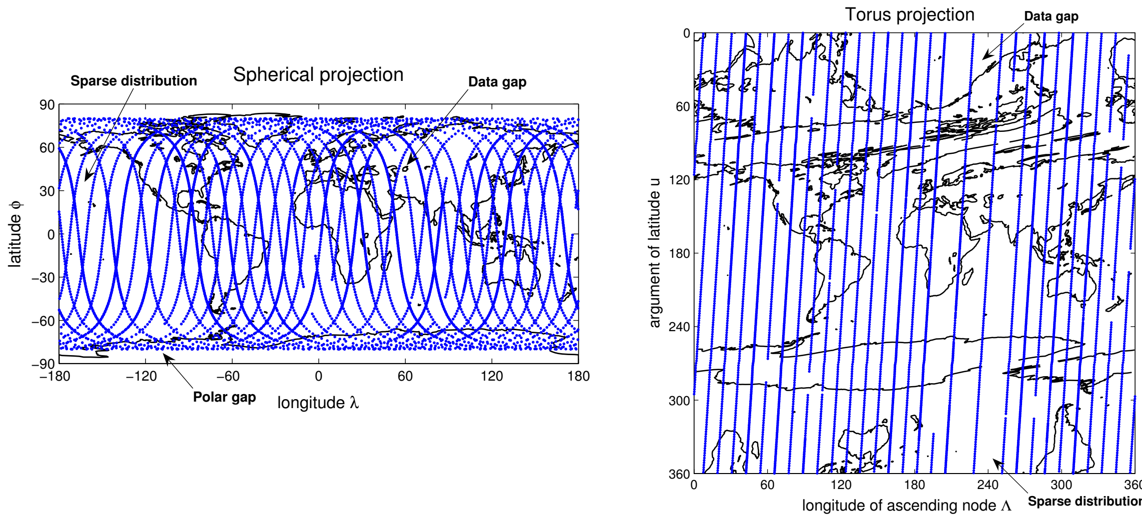

(a) Spherical projection

(b) Torus projection

Figure 4.10: Satellite observations with an irregular and sparse surface data coverage, and polar gaps

4.4.1 Deterministic methods

Because there are no height and inclination variations on the nominal orbit after data reduction, interpolation deals only with a 2D problem. The deterministic methods attempt to fit a surface from given measurements without assessing the interpolation errors. The two typical local interpolators are bi-linear and spline models.

Bi-linear interpolation. It is a 2D extension of linear interpolation. The unknown value $z(x,y)$ is interpolated by calculating a weighted average from the nearest 2 by 2 neighborhood observations. The idea is to perform a linear interpolation first in one direction, and then in the other direction. Alternatively, the calculating formula can be written in a polynomial format:

$$z(x,y) = a_1 + a_2 x + a_3 y + a_4 xy, \tag{4.21}$$

where the coefficients $a_i (i = 1 \ldots 4)$ are the weighting functions of the known points $s_i (i = 1 \ldots 4)$, which depend on the distances between the interpolated point and the known points; see Figure 4.11(a).

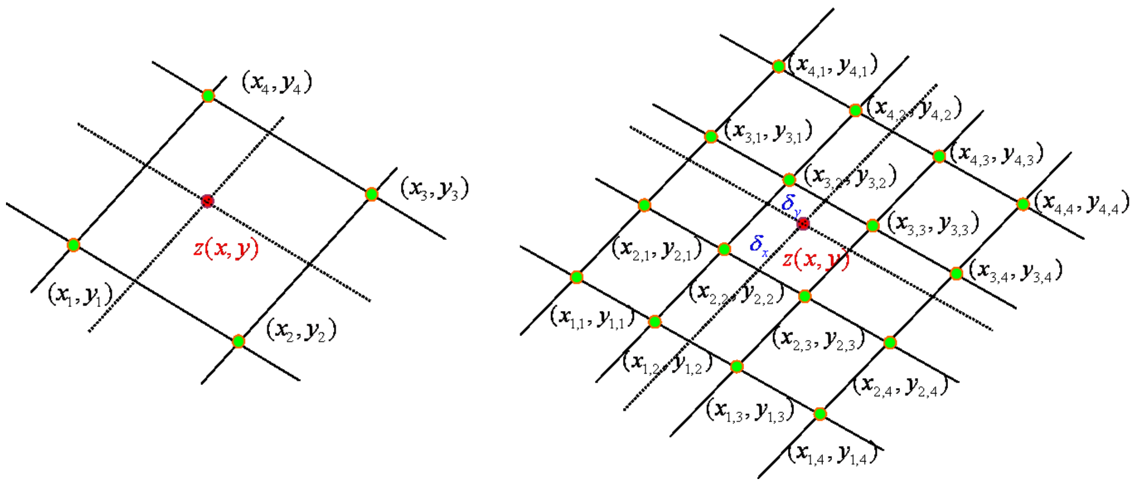

Figure 4.11: 2D deterministic interpolation: bi-linear (left) and *Overhauser* spline (right)

Spline interpolation. It is a form of interpolation where the interpolator is a special type of piece-wise polynomial called a spline. The *Overhauser* spline, sometimes called the "*Catmull-Rom*" spline, is a member of the cubic interpolating splines family (Overhauser, 1968; Catmull and Rom, 1974). In this type of 2D interpolation, the nearest 4 by 4 neighborhood points are used to determine the unknown value $z(x,y)$; see Figure 4.11(b):

$$z(x,y) = \sum_{i=1}^{4}\sum_{j=1}^{4} f_i(x_{i,j}-x) f_j(y_{i,j}-y) s(x_{i,j}, y_{i,j}), \tag{4.22}$$

where the weighting functions f_i and f_j depend on the distance parameters δ along the x and y direction, respectively. The cubic weighting kernel in either x or y dimension can be expressed in a matrix format (Hill et al., 1990):

$$f_i(x_{i,j}-x \,/\, y_{i,j}-y) = \begin{bmatrix} -\frac{1}{2} & \frac{3}{2} & -\frac{3}{2} & 2 \\ 1 & -\frac{5}{2} & -2 & -\frac{1}{2} \\ -\frac{1}{2} & 0 & \frac{1}{2} & 0 \\ 0 & 1 & 0 & 0 \end{bmatrix} \begin{bmatrix} \delta^3 \\ \delta^2 \\ \delta \\ 1 \end{bmatrix}. \tag{4.23}$$

By definition, the *Overhauser* spline has the following characteristics: it is an exact local interpolation method, and it is a smooth and continuous curve.

4.4.2 Least-squares collocation (LSC) and covariance function

When measurements are numerous and dense, most interpolation methods give similar results for interpolated points. When measurements are sparse or only few, however, the assumptions made about the underlying variation of the data and the choice of method can be critical (Burrough and McDonnell, 1998, Chapter 6). Incorporating the concept of randomness, geo-statistical methods of interpolation, i.e., least-squares collocation (LSC) and the *Kriging* method, attempt to optimize spatial variations by using the statistical properties of the measurements. Compared to the deterministic methods, geo-statistical interpolations provide non-unique and flexible output depending on variation assumptions and the choice of essential parameters, which describe the statistical characteristics of the measurements.

Least-squares collocation

Least-squares collocation (LSC) is widely known as an optimal linear estimation method in geodetic modelling for discrete data, which usually consist of signal s and noise ε. As a linear minimum variance unbiased estimation, LSC adjusts parameters, filters noises, and predicts unknown points. Therefore, LSC plays a combination role of adjustment, filtering, and prediction. The advantages of LSC are that it is able to deal with non-homogeneous quantities in its input and output. This method has been comprehensively discussed in geodetic applications by Moritz (1980). However, in this thesis, it will be used only for the purpose of interpolation, which also is known as least-squares interpolation.

$$\hat{z} = C_{zs}(C_{ss} + C_{\varepsilon\varepsilon})^{-1} s, \tag{4.24}$$

where matrix C is the covariance matrix. Therefore, C_{ss} and $C_{\varepsilon\varepsilon}$ are the auto-covariance matrices of s and ε, respectively, and C_{zs} is the cross-covariance matrix between s and the interpolated signal z.

Least-squares interpolation assumes that signal s and noise ε are uncorrelated. Therefore, the error variance of $\hat{z}$ can be propagated from the covariance matrices:

$$E_{\hat{z}\hat{z}} = C_{zz} - C_{zs}(C_{ss} + C_{\varepsilon\varepsilon})^{-1} C_{sz}. \tag{4.25}$$

The prerequisite in least-squares collocation, however, is the availability or the determination of the covariance function, which will be discussed next.

Covariance function

The covariance function plays an important role in LSC. The parameters of covariance function depend on the characteristics of geopotential observables. In geodetic applications, the covariance function is usually assumed to be homogeneous (average over the whole sphere) and isotropic (average over all azimuths) (Moritz, 1980). Under these assumptions, the analytical expression for the covariance function will be a function of spherical distance ψ only. There are two ways to get the covariance function.

The first way is the use of a global analytical covariance model. It is normally expanded in a series of *Legendre* polynomials:

$$C(\psi) = \sum_{l=0}^{\infty} C_l P_l(\cos\psi), \tag{4.26}$$

with C_l the degree variance model, and P_l the *Legendre* polynomial of degree l. One way to obtain the degree variance coefficients C_l is from existing models, such as the *Tscherning-Rapp* model. This model is derived by considering potential coefficients to degree $l = 20$, and updated values of the point anomaly variance (1 795 mGa1^2), the 1° block variance (920 mGa1^2), and the 5° block variance (302 mGa1^2) (Tscherning and Rapp, 1974). The corresponding analytical covariance function for the disturbing potential based on the *Tscherning-Rapp* model is given as follows:

$$\begin{aligned} C_2^{VV} &= 7.6\,\mathrm{mGal}^2 \cdot r_s\, r_z && \text{for } l = 2 \\ C_l^{VV} &= \left(\frac{GM}{R}\right)^2 \left(\frac{R^2}{r_s r_z}\right)^{l+1} t^{l+2} \frac{A}{(l-1)(l-2)(l+B)} && \text{for } l \geq 3, \end{aligned} \tag{4.27}$$

where $t = ({R_B}/{R})^2 = 0.999617$, R_B the radius of the *Bjerhammar* sphere smaller than R, $A = 425.28\,\mathrm{mGal}^2$, and $B = 24$.

The covariance function can be propagated from one geo-potential functional to another one. The covariance propagation law of the degree variance is written in the following equation:

$$C_l^{f_1 f_1} = (\beta_l^{f_1})^2\, C_l, \text{and} \tag{4.28}$$

$$C_l^{f_1 f_2} = \beta_l^{f_1}\, \beta_l^{f_2}\, C_l. \tag{4.29}$$

where f_1 and f_2 are two isotropic geo-potential functionals, and β is a specific coefficient with the combination of a dimensioning factor "Dim," an upward continuation term R/r with a specific power, and the corresponding eigenvalue λ_l for degree l. As an example, some β coefficients are listed in Table 4.1.

Based on the transition coefficient β, the degree variance of a specific isotropic geo-potential functional f can be derived from the given disturbing potential degree variance C_l^{VV} by

$$C_l^{ff} = \left(\frac{\beta_l^f}{\beta_l^V}\right)^2 C_l^{VV}. \tag{4.30}$$

Table 4.1: Coefficients of geo-potential observables in covariance propagation

	Dim	$\left(\frac{R}{r}\right)$	λ_l	β_l
V	$\frac{GM}{R}$	$l+1$	1	$\frac{GM}{R}\left(\frac{R}{r}\right)^{l+1}$
V_r	$\frac{GM}{R^2}$	$l+3$	$-(l+1)$	$-(l+1)\frac{GM}{R^2}\left(\frac{R}{r}\right)^{l+2}$
Δg	$\frac{GM}{R^2}$	$l+2$	$(l-1)$	$(l-1)\frac{GM}{R^2}\left(\frac{R}{r}\right)^{l+2}$
V_{rr}	$\frac{GM}{R^3}$	$l+3$	$(l+1)(l+2)$	$(l+1)(l+2)\frac{GM}{R^3}\left(\frac{R}{r}\right)^{l+3}$

In addition to the analytical global covariance model, the variance coefficient C_l can also be estimated empirically from the observations. After plotting a 1D empirical covariance function as a function of the spherical distances, the analytical covariance function can be estimated optimally by a least-squares adjustment (Rummel, 1991); see Figure 4.12. Assuming that the variance model is truncated at degree L, the linear relation is achieved:

$$\begin{bmatrix} C(\psi_1) \\ C(\psi_2) \\ \vdots \\ C(\psi_n) \end{bmatrix} = \begin{bmatrix} P_1(\cos\psi_1) & P_2(\cos\psi_1) & \cdots & P_n(\cos\psi_1) \\ P_1(\cos\psi_2) & P_2(\cos\psi_2) & \cdots & P_n(\cos\psi_2) \\ \vdots & \vdots & \ddots & \vdots \\ P_1(\cos\psi_L) & P_2(\cos\psi_L) & \cdots & P_n(\cos\psi_L) \end{bmatrix} \begin{bmatrix} C_1 \\ C_2 \\ \cdots \\ C_L \end{bmatrix},$$

with n the number of covariance.

The second group of covariance models are the local analytical models. One example is the Gaussian covariance function, defined as follows:

$$C(\rho) = 2C_0 e^{-\rho^2/\xi^2}. \tag{4.31}$$

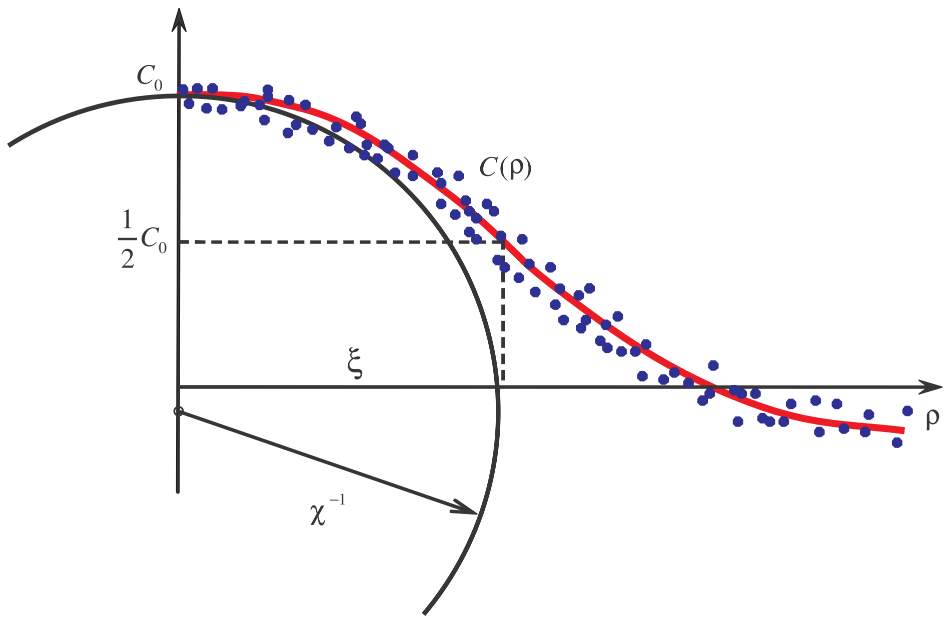

Figure 4.12: **Essential parameters of covariance function in LSC**

There are three essential parameters involved in the local covariance function: the variance C_0, the correlation length ξ, and the curvature parameter χ. C_0 is the value of the covariance function $C(\rho)$ for $\rho = 0$ and the correlation length ξ is the value of the argument for which $C(\rho)$ has decreased to half its value at $\rho = 0$, i.e., $C(\xi) = \frac{1}{2}C_0$ (Moritz, 1980). In equation (4.31), the two parameters C_0 and ξ have to be empirically estimated from the variance histogram of the observations using a least-squares adjustment similar to the procedure mentioned above. The third parameter χ can be determined empirically from the gradient variance G_0 (Moritz, 1980):

$$\chi = \frac{\xi^2 G_0}{C_0}. \tag{4.32}$$

The gradient variance G_0 is defined as either the variance of any horizontal gradient or equivalently half of the variance of the vertical gradient:

$$G_0 = \left.\frac{\partial^2 C}{\partial x^2}\right|_{\rho=0} = \left.\frac{\partial^2 C}{\partial y^2}\right|_{\rho=0} = \frac{1}{2}\left.\frac{\partial^2 C}{\partial z^2}\right|_{\rho=0} \tag{4.33}$$

4.4.3 Semi-variogram and *Kriging*

Semi-variogram

The *Kriging* method was originally developed as an optimal interpolation method by the South African mining engineer, *D. G. Krige*, for usage in the mining industry. It employs the concept of a regionalized variable, which is defined in a way between a truly random variable and one that is completely deterministic. The size, shape, orientation, and spatial arrangement of samples are the supporting factors for regionalized variables. Any changes in these parameters affect the underlying characteristics of the variables. The basic geostatistical measure of the degree of spatial dependence between observations is the semi-variogram $\gamma(h)$, which is defined as follows:

$$\gamma(h) = \frac{1}{2n}\sum_{i=1}^{n}[s(x_i) - s(x_i + h)]^2, \tag{4.34}$$

where n is the number of pairs of samples of the given values s separated by the distance h. A plot of $\gamma(h)$ as a function of h is known as the experimental semi-variogram $\hat{\gamma}(h)$ (Figure 4.13), which provides some useful information for interpolation, optimizing, sampling, and determining spatial patterns. Three important parameters in the semi-variogram are the nugget C_0, range a, and sill C_1. The normally used analytical models include, but are not limited to, the spherical model, exponential model, Gaussian model, and linear model, listed below (Burrough and McDonnell, 1998, Chapter 6):

- spherical model

$$\gamma(h) = \begin{cases} C_0 + C_1\left[\left(\frac{3h}{2a}\right) - \frac{1}{2}\left(\frac{h}{a}\right)^3\right] & 0 < h < a \\ C_0 + C_1 & h \geq a \end{cases}$$

- exponential model

$$\gamma(h) = \begin{cases} C_0 + C_1\left[1 - e^{\left(-\frac{h}{a}\right)}\right] & 0 < h < a \\ C_0 + C_1 & h \geq a \end{cases}$$

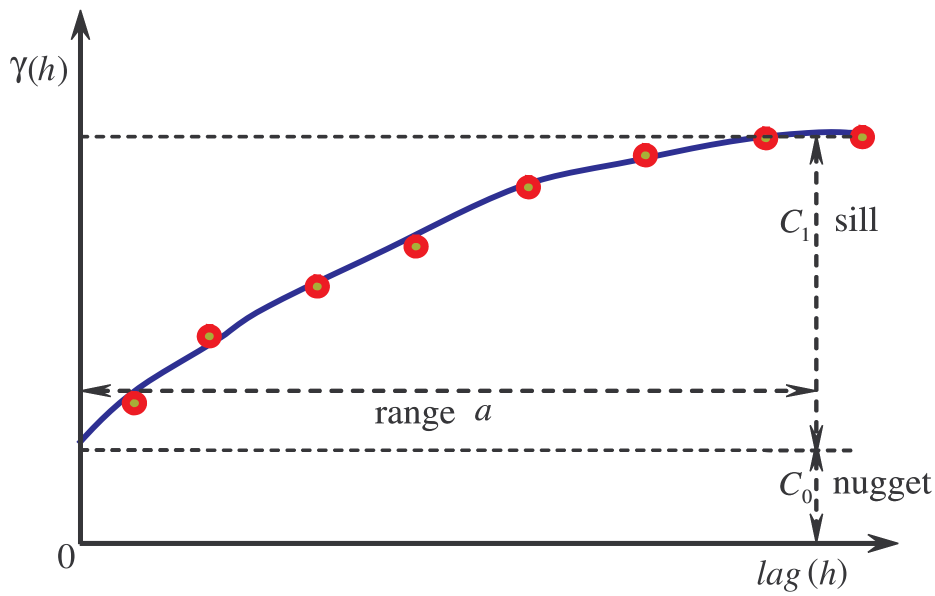

Figure 4.13: Empirical semi-variogram modelling in *Kriging*

- Gaussian model

$$\gamma(h) = \begin{cases} C_0 + C_1 \left[1 - e^{\left(-\frac{h^2}{a^2}\right)}\right] & 0 < h < a \\ C_0 + C_1 & h \geq a \end{cases}$$

- linear model

$$\gamma(h) = \begin{cases} C_0 + bh & 0 < h < a \\ C_0 + C_1 & h \geq a \end{cases}$$

where b is the slope of the line.

For a specific geo-potential data set, the three parameters (nugget C_0, range a, and sill C_1) in the analytical models above are normally unknown. Therefore, they have to be empirically fitted from the experimental semi-variogram cloud by a weighted least-squares adjustment.

In least-squares adjustment, the design matrix consists of the partial derivatives with respect to three unknown parameters, and the weights are proportional to the reciprocal of squares of distances, e.g., $\propto \frac{1}{h^2}$ (Cressie, 1985; Jian et al., 1996).

The *Akaike* information criterion (AIC) is applied to determine which one is the best fitted semi-variogram model. The estimate of this criterion is defined as follows:

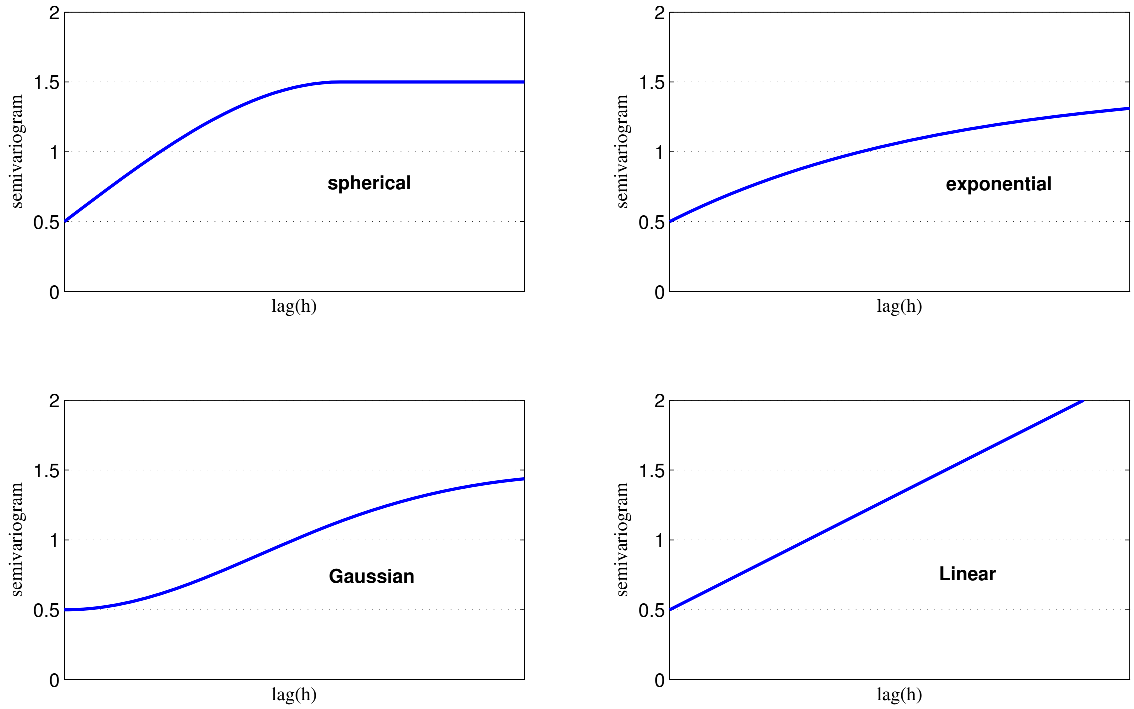

Figure 4.14: **Examples of several semi-variogram models in *Kriging***

$$\text{AIC} = n \ln\left(\frac{R_m}{n}\right) + 2p, \tag{4.35}$$

where n is the number of points in the experimental semi-variogram cloud, p is the number of parameters in the model and R_m is the sum of the square of the weighted difference. The one with the smallest AIC value is selected as the best model (Olea, 1999, Chapter 5).

Kriging interpolation

Based on the generalized linear regression algorithm, the *Kriging* method makes use of the knowledge of the semi-variogram from regionalized variables to estimate the functional values at unknown locations. The generalized interpolation equation for the *Kriging* method is written as follows:

$$z(x,y) = \sum_{i=1}^{n} \zeta_i s(x_i, y_i), \tag{4.36}$$

with the weights factor $\sum_{i=1}^{n} \zeta_i = 1$ as a constraint.

Depending on the way of estimating the weight factor ζ from the experimental semi-variogram cloud, the classical types of *Kriging* are simple *Kriging*, ordinary *Kriging*, and universal *Kriging*, to list a few.

Assuming no trend in the observations, the weights in simple *Kriging* can be estimated in a matrix form as

$$\begin{aligned}
\begin{bmatrix} \zeta_1 \\ \zeta_2 \\ \vdots \\ \zeta_n \end{bmatrix} &= \begin{bmatrix} \gamma(d_{11}) & \gamma(d_{12}) & \cdots & \gamma(d_{1n}) \\ \gamma(d_{21}) & \gamma(d_{22}) & \cdots & \gamma(d_{2n}) \\ \vdots & \vdots & \ddots & \vdots \\ \gamma(d_{n1}) & \gamma(d_{n2}) & \cdots & \gamma(d_{nn}) \end{bmatrix}^{-1} \begin{bmatrix} \gamma(d_{01}) \\ \gamma(d_{02}) \\ \cdots \\ \gamma(d_{0n}) \end{bmatrix} \\
\Phi &= \Upsilon^{-1} D, \qquad (4.37)
\end{aligned}$$

where the subscript “0” is the index of the unknown point to be interpolated.

The corresponding interpolation error variance at the estimated point “0” can be calculated by

$$\sigma_0^2 = D^{\mathrm{T}} \Upsilon^{-1} D. \qquad (4.38)$$

The second one is ordinary *Kriging*. It assumes that there is a constant trend to be estimated in the observations:

$$\begin{aligned}
\begin{bmatrix} \zeta_1 \\ \zeta_2 \\ \vdots \\ \zeta_n \\ -\varphi \end{bmatrix} &= \begin{bmatrix} \gamma(d_{11}) & \gamma(d_{12}) & \cdots & \gamma(d_{1n}) & 1 \\ \gamma(d_{21}) & \gamma(d_{22}) & \cdots & \gamma(d_{2n}) & 1 \\ \vdots & \vdots & \ddots & \vdots & \vdots \\ \gamma(d_{n1}) & \gamma(d_{n2}) & \cdots & \gamma(d_{nn}) & 1 \\ 1 & 1 & 1 & 1 & 0 \end{bmatrix}^{-1} \begin{bmatrix} \gamma(d_{01}) \\ \gamma(d_{02}) \\ \cdots \\ \gamma(d_{0n}) \\ 1 \end{bmatrix} \\
\Phi &= \Upsilon^{-1} D, \qquad (4.39)
\end{aligned}$$

where the parameter φ is a *Lagrange* multiplier required for the minimalization of the error variances at the unknown point “0.” The *Lagrange* multiplier, an additional unknown, measures the sensitivity of the solution to the constraint. Correspondingly, the error variances of the interpolated point can be estimated by Equation (4.38).

The third one is universal *Kriging*, which tries to find an estimator as a linear trend as follows:

$$
\begin{bmatrix} \zeta_1 \\ \zeta_2 \\ \vdots \\ \zeta_n \\ -\varphi_0 \\ -\varphi_1 \\ -\varphi_2 \end{bmatrix}
=
\begin{bmatrix}
\gamma(d_{11}) & \gamma(d_{12}) & \cdots & \gamma(d_{1n}) & 1 & x_1 & y_1 \\
\gamma(d_{21}) & \gamma(d_{22}) & \cdots & \gamma(d_{2n}) & 1 & x_2 & y_2 \\
\vdots & \vdots & \ddots & \vdots & \vdots & \vdots & \vdots \\
\gamma(d_{n1}) & \gamma(d_{n2}) & \cdots & \gamma(d_{nn}) & 1 & x_n & y_n \\
1 & 1 & 1 & 1 & 0 & 0 & 0 \\
x_1 & x_2 & \vdots & x_n & 0 & 0 & 0 \\
y_1 & y_2 & \vdots & y_n & 0 & 0 & 0
\end{bmatrix}^{-1}
\begin{bmatrix} \gamma(d_{01}) \\ \gamma(d_{02}) \\ \cdots \\ \gamma(d_{0n}) \\ 1 \\ x_0 \\ y_0 \end{bmatrix}
$$

$$
\Phi = \Upsilon^{-1} D, \tag{4.40}
$$

The error variances by universal *Kriging* also can be estimated by Equation (4.38).

4.4.4 Relation between LSC and *Kriging*

Kriging and LSC are two geo-statistical interpolation methods. However, they normally have their particular usefulness in different communities, i.e., geodetic and geological respectively. Dermanis (1984) showed that they are equivalent to each other with an unknown mean function. Since the covariance function C and the semi-variogram γ are defined in a lag (h) domain, for a statistically stationary process, the semi-variogram $\gamma(h)$ is related to the covariance function, $C(h)$, as follows (Herzfeld, 1992):

$$
\gamma(h) = C(0) - C(h). \tag{4.41}
$$

4.4.5 Comparison of different interpolation methods

The mathematical backgrounds and derivations of all aforementioned interpolation methods, i.e., bi-linear, spline, LSC, and *Kriging*, are not new. However, their applications and comparisons in the context of processing satellite observations are new. All approaches have been employed to interpolate a grid on the nominal torus from the filtered and reduced spaceborne gravimetry observations. In order to compare their performances, several scenarios have been studied, which is demonstrated in the flow chart in Figure 4.15. The idea is to compare the interpolated values with the values calculated from the reference gravity field model on the same torus grid. The model of LSC with observation errors is used,

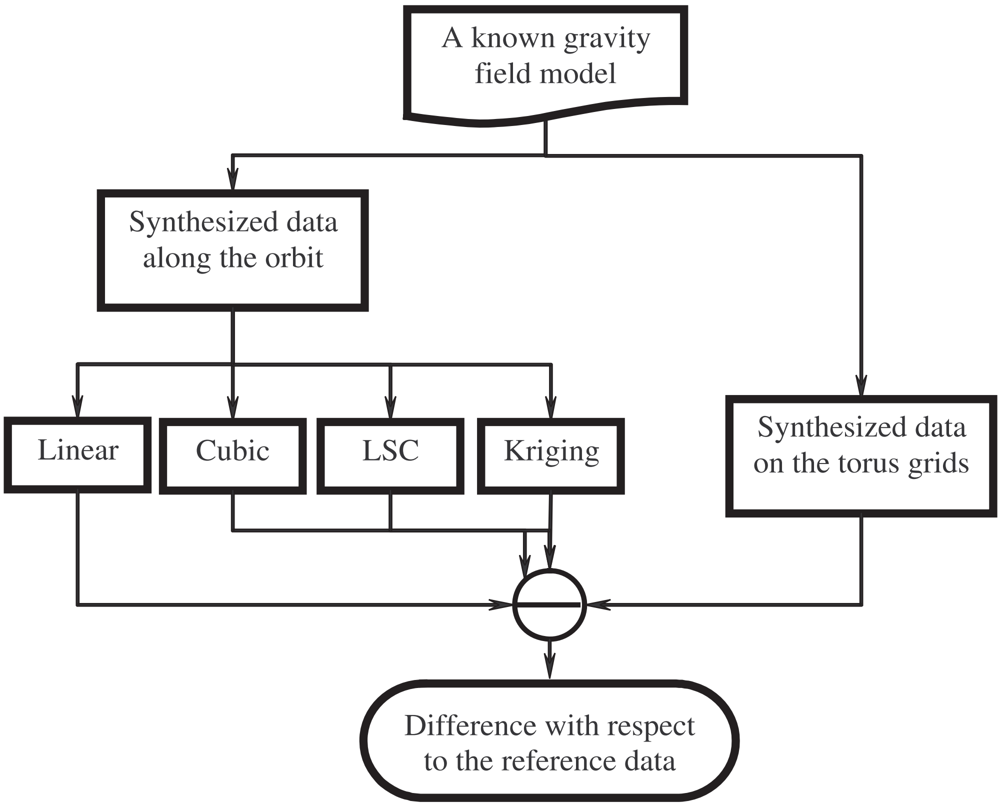

Figure 4.15: Calculating flow chart of the investigation of interpolation methods

where the covariance function is a global covariance model in terms of a series of *Legendre* polynomials (Equation 4.26). The degree coefficients C_l are estimated empirically by taking the average values of the degree coefficients of each projected orbital track on the torus (Figure 4.16). In addition, ordinary *Kriging* with the analytical spherical model is chosen to interpolate the grid and remove a constant trend if there is one among observations. The parameters in the spherical model of semi-variogram are estimated empirically using the same track-wise determination approach also. Note that all distances involved in the geo-statistical interpolation methods are determined on the basis of a sphere. The spherical distance between two points can be calculate dy the cosine law:

$$d_{12} = \arccos(\sin\phi_1 \sin\phi_2 + \cos\phi_1 \cos\phi_2 \cos(\lambda_2 - \lambda_1)); \tag{4.42}$$

Several aspects, such as interpolation accuracy, requirement of computational time and memory storage, ability of spatial analysis, error propagation, and practical implementa-

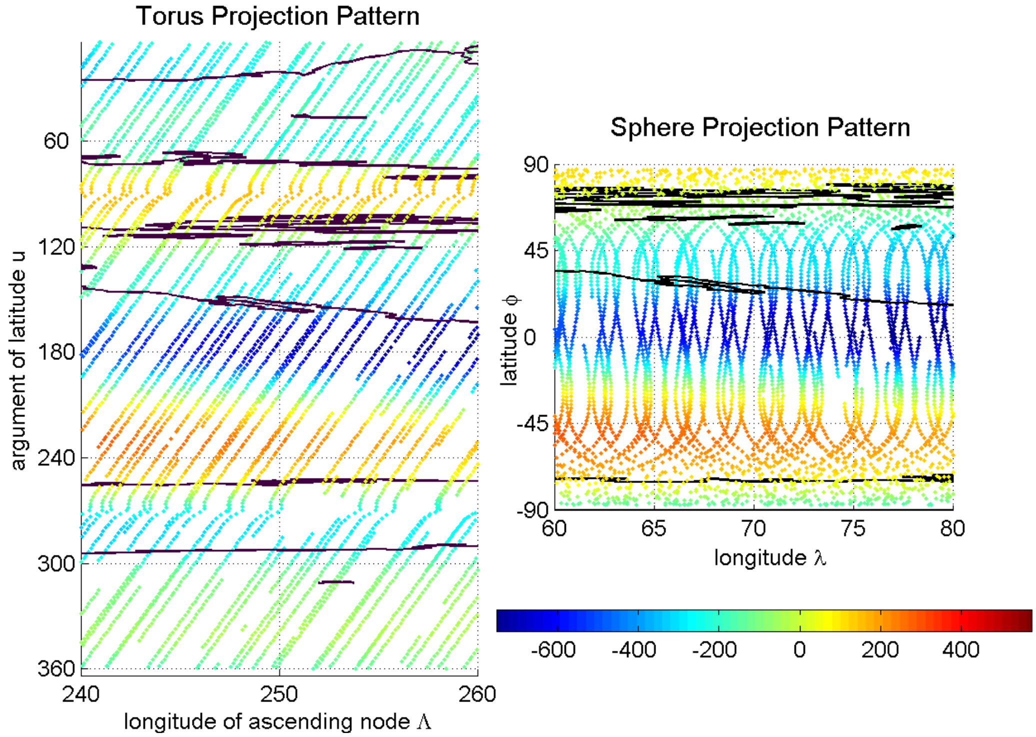

Figure 4.16: Regional orbital geometry of disturbing potential projected on the torus and the sphere

tion, are considered as the evaluation factors.

Scenario I. In the first test, taking the spherical harmonic coefficients from the GGM02S gravity field model as the reference input, one month noiseless disturbing potential data with a sampling increment of 30 s are synthesized along a CHAMP-like nominal orbit with a constant height ($h = 450$ km) and a constant inclination ($I = 87.5°$). A regional orbital geometry of the disturbing potential data is projected on both the sphere and the torus in Figure 4.16. Interpolation methods are applied to generate a regular $2° \times 2°$ grid on the nominal torus. The essential parameters in the covariance function of least-squares collocation and parameters in the semi-variogram of *Kriging* are fitted empirically by least squares adjustment in Figure 4.17. The coefficients of the *Legendre* polynomials of the covariance model (curve in red) are determined up to $l = 20$ in Equation (4.26). The variance C_0 is around 5.0×10^4, and the correlation length ξ is about 0.5. The complementary curve in green is the corresponding semi-variogram calculated from the empirical covariance by Equation (4.41). In Figure 4.17(b), the fitted semi-variogram spherical model (curve in

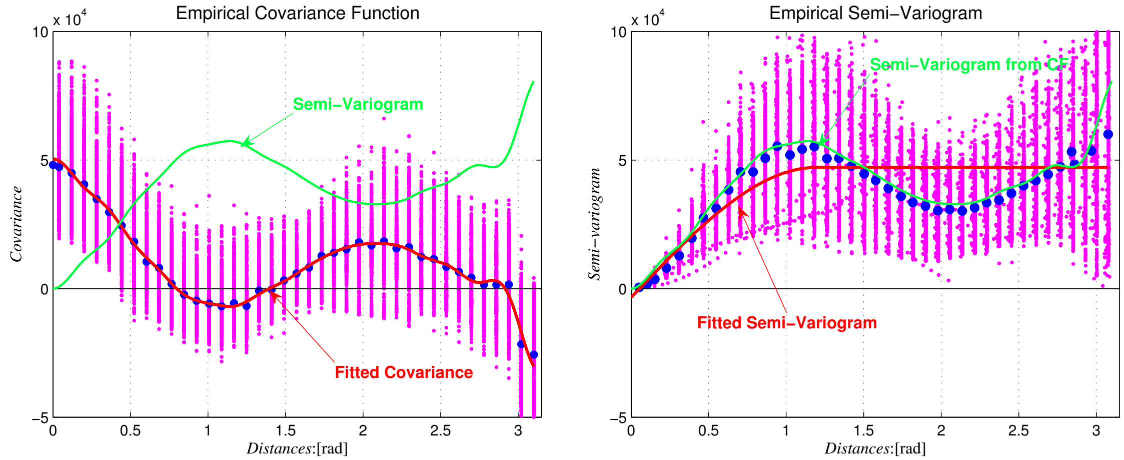

(a) Empirical determination of covariance function (b) Empirical determination of semi-variogram

Figure 4.17: Empirical determination of covariance function and semi-variogram for the disturbing potential data

red) has a nugget $C_0 = 0.0$, a sill $C_1 = 5.0 \times 10^4$, and a sill of 1.5. The modelled curve shows a similar pattern with the one derived from the empirical covariance model (curve in green). The gridding results by the four interpolation methods are compared with the synthesized values on the same grid using the GGM02S gravity field model; see the gravity field synthesis Section 4.3.2.

The differences of the interpolation results on the grid with respect to the synthesized values can be treated as an external accuracy analysis. Figure 4.18 shows that the spline method performs better than the linear method and the geo-statistical methods generally give better results than the deterministic methods. *Kriging* gives the most homogeneous output. Figure 4.18 also shows that the interpolated points with bigger values of the differences are at the areas with large gravity gradients, e.g., mountain chains, and trenches. Since there are no polar gaps in the torus domain; See Figure 4.10(b), the interpolated values on the polar areas do not have large differences. Quantitative numbers of the external accuracy for interpolation methods are summarized in Table 4.2. It states that *Kriging* provides the smallest STD values. However, the expense of LSC and *Kriging* is the computational time because the essential parameters in the covariance function or semi-variogram have to be empirically estimated, and the point-wise interpolation in LSC and *Kriging* does not employ a fast calculating algorithm.

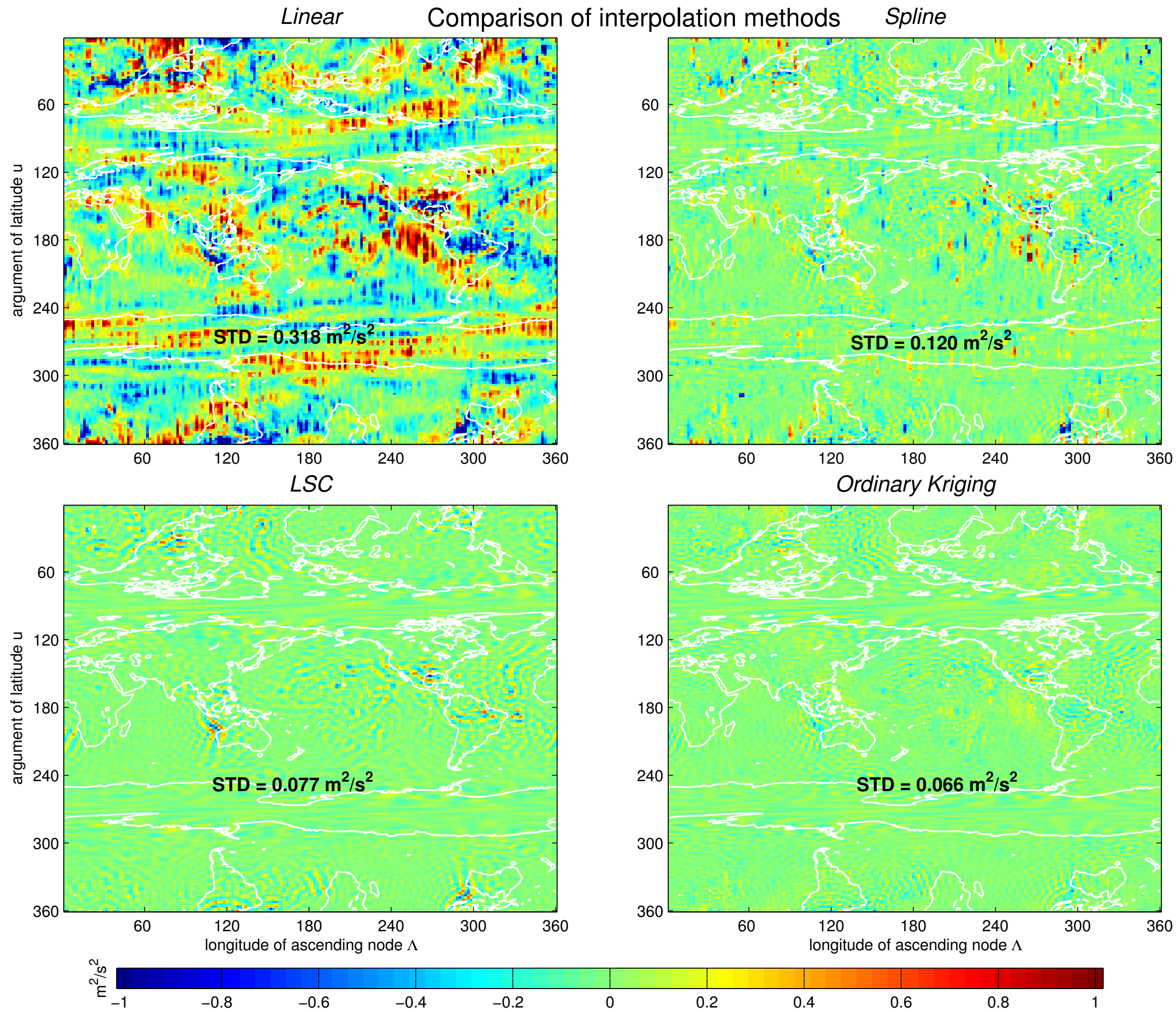

Figure 4.18: Comparison of interpolation methods for the disturbing potential data, the GGM02S model as reference

As discussed before, only the geo-statistical interpolation methods, i.e., LSC and *Kriging*, can provide the error information for the interpolation results by applying the covariance function or semi-variogram propagation law. This accuracy measure can be treated as an analysis of the internal accuracy. Since LSC and *Kriging* employ a point by point interpolating procedure in this thesis, the correlation among the interpolated points can be neglected. Therefore, the variance for each interpolated point can be plotted in Figure 4.19.

It clearly shows that the internal accuracy is related to the geographical locations of the interpolated points and the points in the polar areas have more accurate results. Two bands with smaller interpolating variances in LSC and *Kriging* are located at the polar areas on

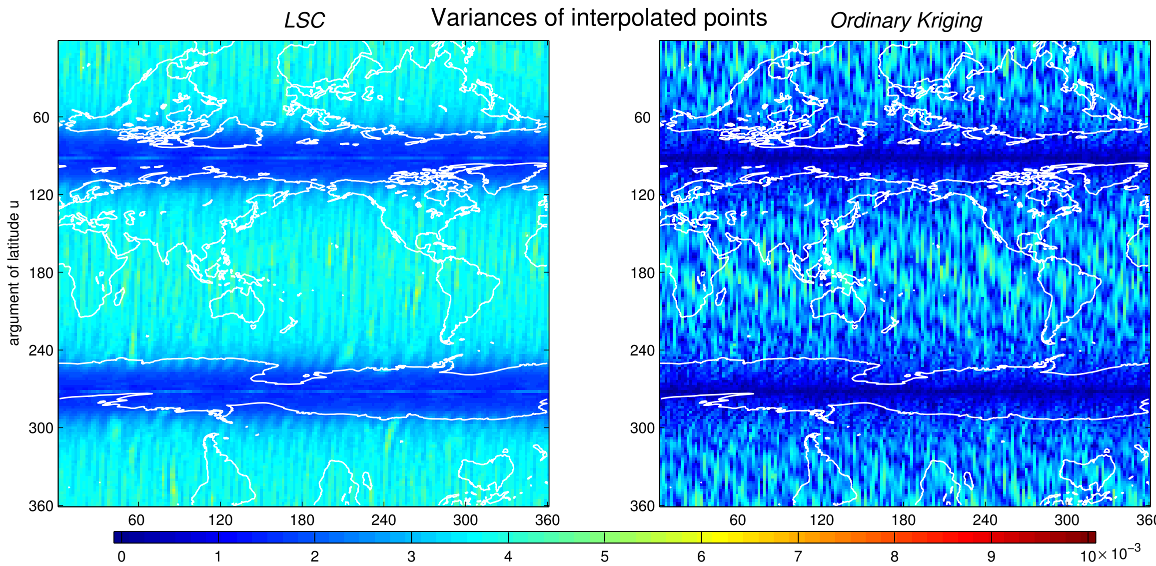

Figure 4.19: **Variances of the interpolated points for the disturbing potential data by LSC and *Kriging***

Table 4.2: **Comparison of interpolation methods in scenario I: disturbing potential V**

method	mean m^2/s^2	std m^2/s^2	time s
Linear	3.5×10^{-4}	0.318	3.6
Spline	0.6×10^{-4}	0.120	4.4
LSC	2.0×10^{-4}	0.077	3328
Kriging	0.5×10^{-4}	0.060	3760

the corresponding spherical projection. The reason for the bands is that in the spherical domain the observations in the polar areas have a much denser data distribution compared to the ones at the lower latitudes.

Scenario II. Choosing the OSU91A gravity field model as the known input, the V_{zz} gravity gradient tensor component with a sampling frequency of 0.2 Hz has been synthesized along with a GOCE-like nominal orbit with a constant height ($h = 246$ km) and a constant inclination ($I = 96.6°$). Interpolation methods are employed to create a regular $1° \times 1°$ grid on the nominal torus. The empirical covariance model in a series of *Legendre* polynomials

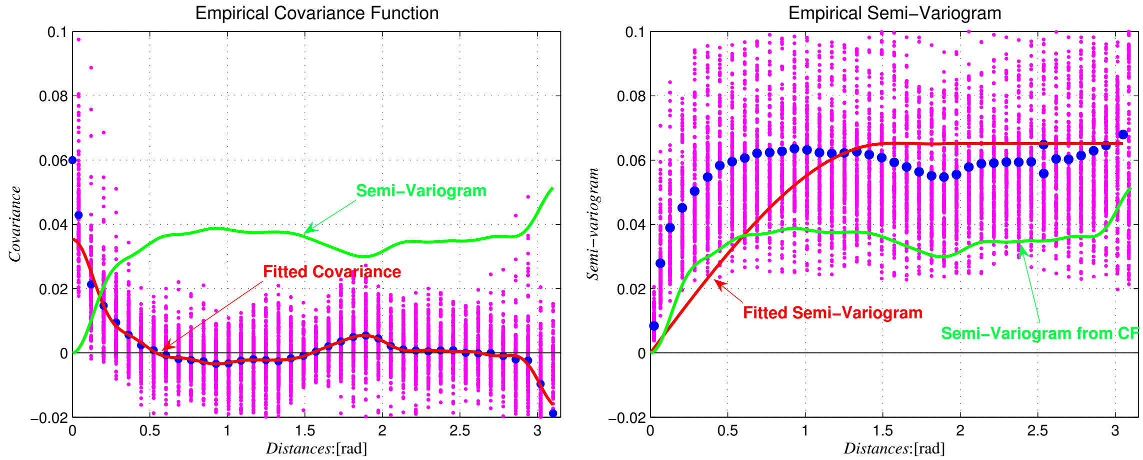

(a) Empirical determination of covariance function (b) Empirical determination of semi-variogram

Figure 4.20: Empirical determination of covariance function and semi-variogram for the V_{zz} gravity gradient tensor data

is determined in Figure 4.20(a), where the variance C_0 is 0.038, and the correlation length ξ is about 0.15. The spherical semi-variogram model is fitted empirically in Figure 4.20(b) with the nugget $C_0 = 0.0$, the sill $C_1 = 0.06$, and the range $a = 1.0$, and it has the similar pattern of the one (curve in green) calculated from the covariance model.

Figure 4.21 shows the interpolated results, which are the differences compared with the synthesized values using the OSU91A gravity field model. The corresponding quantitative numbers of the external accuracy for each interpolation method are summarized in Table 4.3. Again, the interpolated points with bigger differences are the ones at the areas with large gradients, and *Kriging* provides the most homogeneous output with the smallest STD values among the four results but it uses the longest computational time. In addition, the differences in the polar areas show a trend along the longitude direction, especially in the LSC results. These values may consequently cause a nearly ill-conditioned problem in least-squares adjustment, which will be discussed in Section 5.4.

Neglecting the correlations among the interpolated points, the variance of each point can be plotted in Figure 4.22. Although the 96.°6 inclination causes two 6.°6 gaps in the polar areas on the spherical domain, the interpolated points these areas still have smaller variances because of the number of observations.

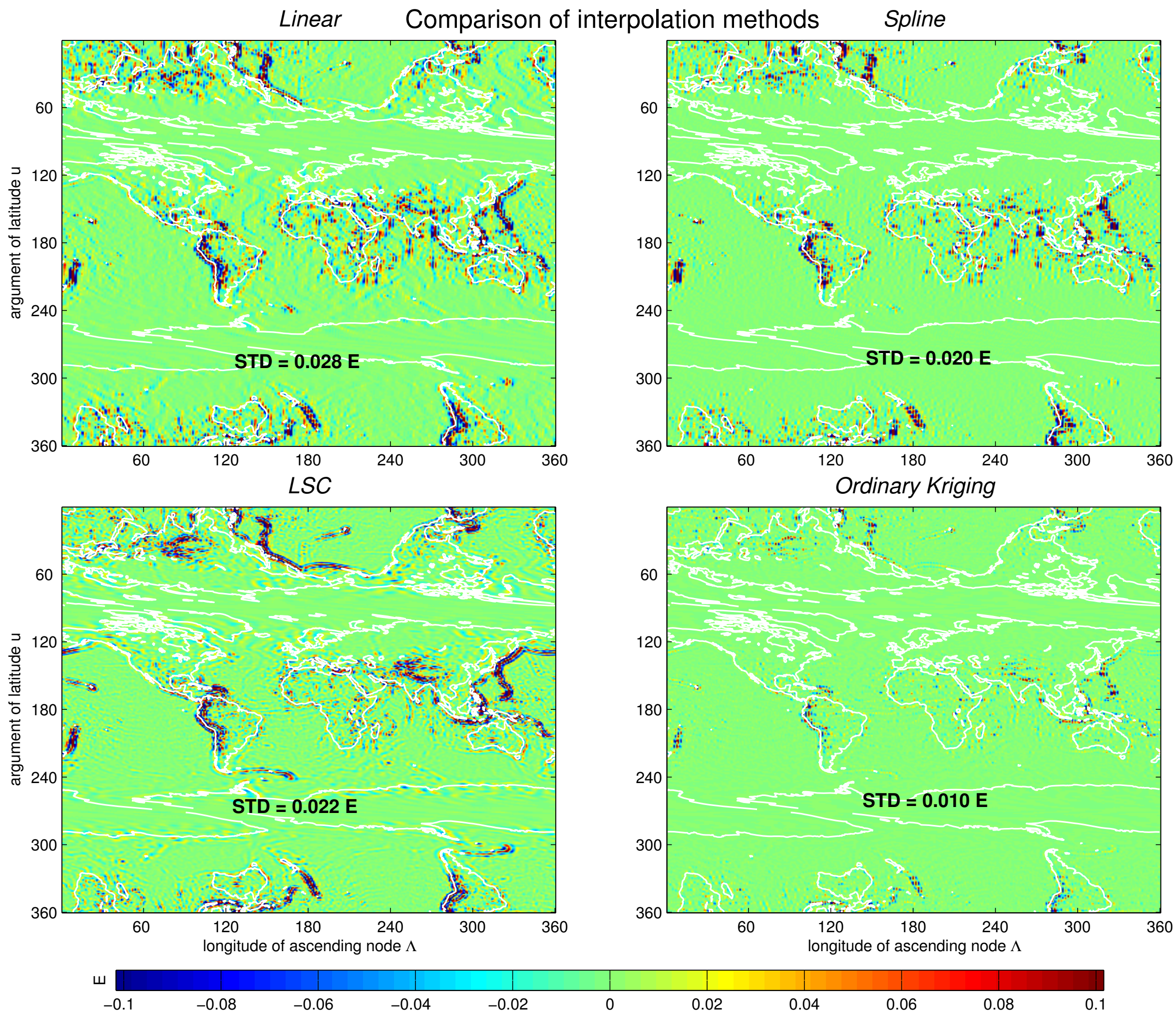

Figure 4.21: Comparison of interpolation methods for the V_{zz} gravity gradient tensor data, the OSU91A model as reference

Scenario III. The tested geo-potential functionals in the first and second examples are the disturbing potential V and the V_{zz} gravity gradient tensor component, respectively. They are all isotropic quantities over the sphere. In the third example, an anisotropic geo-potential functional, which is the cross-track gravity gradient tensor component V_{yy}, is tested. The observations are simulated along a GOCE-like nominal orbit with a constant height ($h = 246\,\text{km}$) and a constant inclination ($I = 96.6°$). A $1° \times 1°$ grid is interpolated on the nominal torus. The *Legendre* polynomials coefficients in the covariance model are determined empirically in Figure 4.23(a) with the variance $C_0 = 0.018$, and the correlation length $\xi = 0.15$. The spherical model of semi-variogram is fitted empirically in Figure

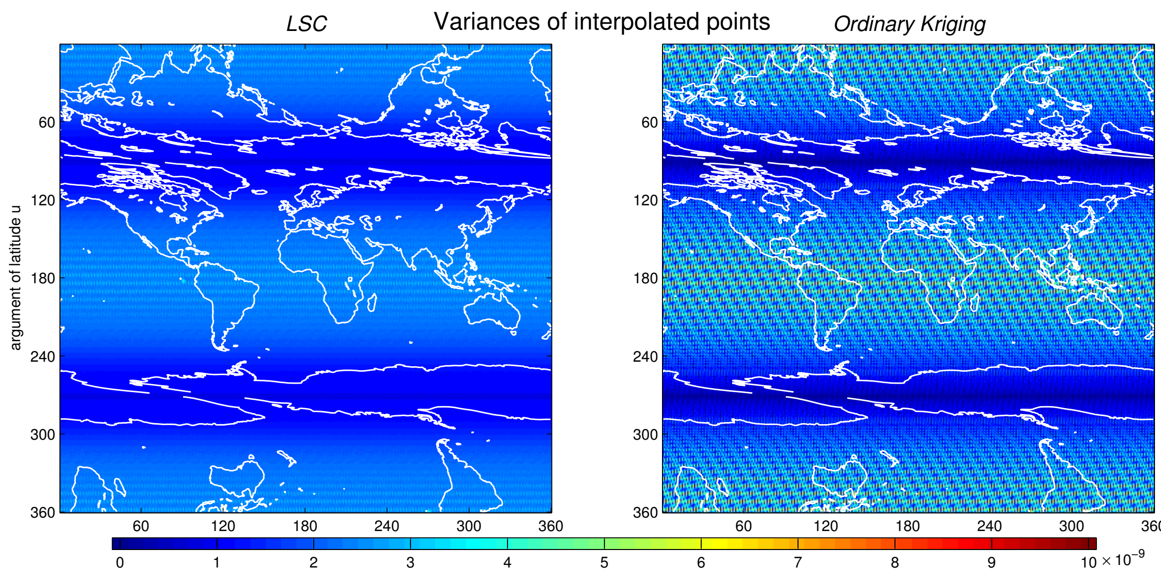

Figure 4.22: Variances of the interpolated points for the V_{zz} gravity gradient tensor data by LSC and *Kriging*

Table 4.3: Comparison of interpolation methods in scenario II: V_{zz} gravity gradient tensor component

method	mean E	std E	time s
Linear	1.3×10^{-5}	0.028	9.5
Spline	0.4×10^{-5}	0.020	11.0
LSC	0.1×10^{-5}	0.022	13280.0
Kriging	0.2×10^{-5}	0.010	14588.6

4.23(b), where the nugget C_0 is 0.0, the sill C_1 is around 0.02, and the range is about 1.2. Again, the fitted semi-variogram model has the similar pattern of the one (curve in green) calculated from the covariance model.

Compared to the reference values on the same grid, the deterministic spline method achieves the best interpolation results (Figure 4.24). The LSC and *Kriging*, which make use of the empirically determined parameters, give worse results. However, the plot by the LSC using the *Tscherning-Rapp* model as covariance function gives the worst results. Therefore, LSC with an analytical covariance function may not be suitable for interpolating

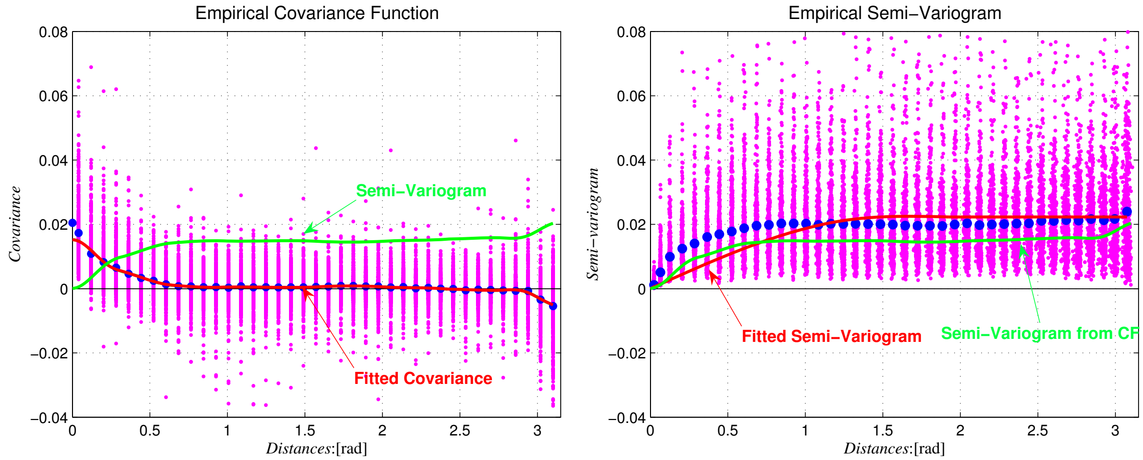

(a) Empirical determination of covariance function (b) Empirical determination of semi-variogram

Figure 4.23: Empirical determination of covariance function and semi-variogram for the V_{yy} gravity gradient tensor data

Table 4.4: Comparison of interpolation methods in scenario III: V_{yy} gravity gradient tensor component

method	mean E	std E	time s
Spline	1.5×10^{-4}	0.027	49.2.0
Empirical LSC	1.0×10^{-4}	0.055	15387.9
Global LSC	0.01	0.902	17263.2
Kriging	2.5×10^{-4}	0.044	16752.6

the anisotropic observables because of the isotropic assumption in the covariance function. As an alternative solution, the spline method should be employed in the interpolations of the anisotropic observations.

In addition, similar to the V_{zz} results in the second scenario, the trend along the longitude direction in the polar areas are more clear in this example. An oscillation in the lower orders of the spherical harmonics solution is expected and regularization has to be applied; see Sections 5.4 and 6.2.4.

The characteristics of the interpolation methods are summarized in Table (4.5) by considering the comparison aspects.

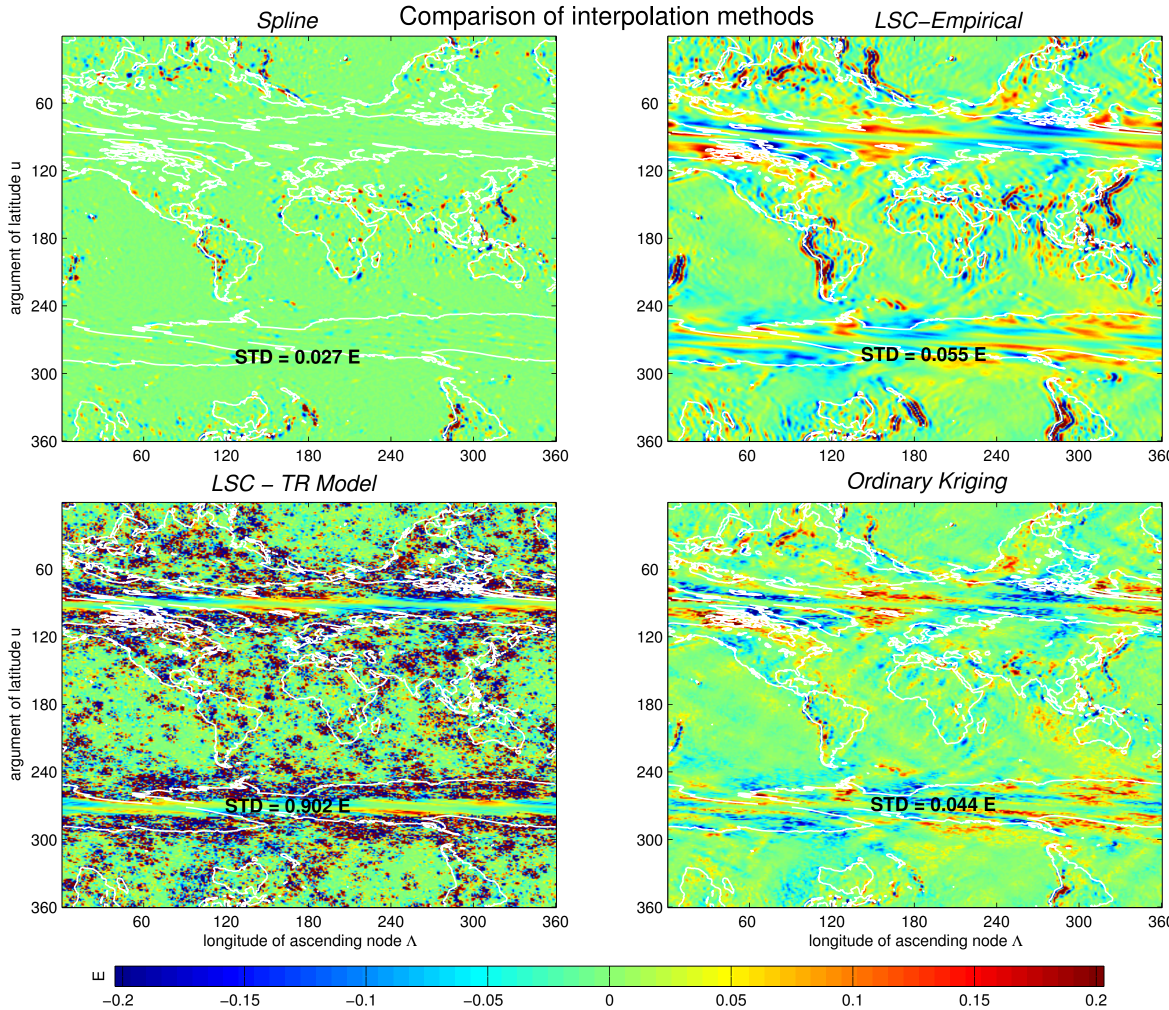

Figure 4.24: Comparison of interpolation methods for anisotropic observable V_{yy}, the OSU91A model as reference

Based on the three interpolation tests carried out above, the following conclusions can be drawn on the suitability of different interpolation methods:

- In general, geo-statistical approaches, i.e., LSC and *Kriging*, provide a better results in terms of mean and STD of differences than the deterministic approaches of the bi-linear and spline interpolation.

- Geo-statistical approaches are able to propagate error information by covariance functions or semi-variogram information, while deterministic approaches cannot.

- However, their excessive computational time and storage requirements will be a considerable problem when dealing with observations in a huge data set.

- ▶ Another characteristic is that both the covariance function and the semi-variogram are data dependent, therefore, statistical approaches have to empirically determine either the covariance function or the semi-variogram model from the actual sampled data set before interpolation.

- ▶ LSC is not suitable for interpolating anisotropic observables because the covariance models are always derived on the basis of an isotropic operator assumption. The spline method is therefore an alternative solution.

Table 4.5: Characteristics of different interpolation methods

Method	isotropic	anisotropic	time	spatial analysis	isotropic assumption	error information
Bi-linear	worst	worse	fast	no	no	no
Spline	worse	best	fast	no	no	no
LSC	better	worst	slow	covariance function	yes	yes
Kriging	best	better	slow	semi-variogram	no	yes

4.5 Aliasing problems

The word "aliasing" comes from signal processing. Aliasing is actually a type of distortion that occurs when recording high frequency signals with a low sampling rate. Therefore, the *Nyquist* theorem states that the maximum resolvable frequency f_{max} in the signal is one-half of the sampling rate f_s

$$f_{\mathrm{max}} \leq \frac{f_{\mathrm{s}}}{2}, \tag{4.43}$$

where $f_{\mathrm{s}}/2$ is the *Nyquist* frequency.

Gravity field spherical harmonic determination from spaceborne gravimetry is affected by aliasing. In the geodetic application, the *Nyquist* theorem can be expressed in a temporal or spatial domain (Sections 4.5.1 and 4.5.2). Aliasing problems also can be caused by the following reasons (Weigelt, 2006):

- ▶ omission errors because of missing information (Section 4.5.3),
- ▶ overlaps of signal sampling in different domains (Section 4.5.4), and
- ▶ special ground track geometry caused by the satellite orbital decays (Section 4.5.5).

4.5.1 *Nyquist* theorem in the spatial domain

Equation (4.43) shows the *Nyquist* theorem from a frequency perspective. By taking the reciprocal value of the frequency, the *Nyquist* theorem can be expressed in a spatial domain. For a specific repeat orbit with N_e (number of nodal days) and N_o (number of revolutions) in the spatial domain, the equatorial distance between two neighboring tracks is treated as a measure of the spatial resolution. Around the equator, the highest wave-number is the maximum resolvable degree L. The *Nyquist* theorem is met in the spatial domain, if $L \leq N_o/2$ (Sneeuw, 2000b; Pail and Plank, 2003). Therefore, when one tries to recover the gravity field beyond the maximum degree L, the information in the higher wave-number part might be aliased because of missing information, and the lower wave-number part might be contaminated by the aliasing effect.

Interpolation is required in the torus-based semi-analytical approach because of the application of the FFT technique on the grid. The interpolation gridding on the nominal torus is actually a re-sampling procedure in the spatial domain. The maximum grid size d_{max} on the torus ($360^\circ \times 360^\circ$) is dependent on the maximum resolvable degree L (the maximum frequency) and can be determined by the spatial *Nyquist* theorem as follows:

$$\begin{aligned} L &\leq \frac{360^\circ}{2d_{max}} \\ \Rightarrow d_{max} &\leq \frac{360^\circ}{2L} \end{aligned} \tag{4.44}$$

For instance, if the maximum resolvable degree $L = 90$, the size of the grids should be at most $2^\circ \times 2^\circ$. Otherwise, it is impossible to recover the corresponding spherical harmonic coefficients up to $L = 90$.

4.5.2 Aliasing and de-aliasing in the temporal domain

Gravity field satellite missions sense not only static gravitational fields but also tides and other temporal gravity field signals, including gravitational perturbations as a result of mass redistributions of the ground water, atmosphere, ocean, and the solid Earth. These high frequency signals (hourly to monthly) cannot be recovered and will alias into the low frequency signals. The way of solving this problem is to treat these temporal gravity changes as systematic effects and remove them from the observations by a de-aliasing step using currently available models before determining the Earth's gravity field (Wahr et al., 1998; Knudsen, 2003).

Thompson et al. (2004) studied the impact of short period, non-tidal temporal mass variability in the atmosphere, ocean, and continental hydrology on gravity field determination from the GRACE mission. They showed that de-aliasing done with approximate models gave a significant reduction in the aliasing errors for the mid-degrees and higher. Abrikosov et al. (2006) recommended using the data from geophysical models and from monthly GRACE gravity field solutions to diminish the aliasing effects in GOCE measurements. However, the errors in the de-aliasing models produce mismodelling and also have an aliasing effect on the monthly gravity field. This was studied for GRACE by Han et al. (2004) and for GOCE by Han et al. (2006). In this thesis, a monthly gravity field solution from both the CHAMP and GRACE missions is the basic unit for the observations to be recovered. By taking an average of multiple monthly solutions in a period of almost two years (Table 2.3), it is hoped that the mismodelling effects will be reduced.

4.5.3 Omission errors

As explained in Section 4.1.1, omission errors are caused by the truncation of the spherical harmonics. This truncation may lead to an aliasing problem in the gravity field recovery. If the maximum resolvable degree is truncated at L, the omitted higher degrees might be aliased in the truncated solution. Therefore, the signals at low degrees are contaminated. As an example, the noiseless gravity gradient tensor data along the radial direction V_{zz} are synthesized on a regular torus ($u \times \Lambda$ domain) at the orbital height. The input gravity field model is EGM96 and the maximum degree used is $L = 150$. The torus-based approach is employed to recover the gravity field for the maximum resolvable degree $L = 120$ and

$L = 150$, respectively. Taking the original EGM96 model as a reference, the corresponding error representation, degree RMSE in Equation (4.5), is plotted in Figure 4.25.

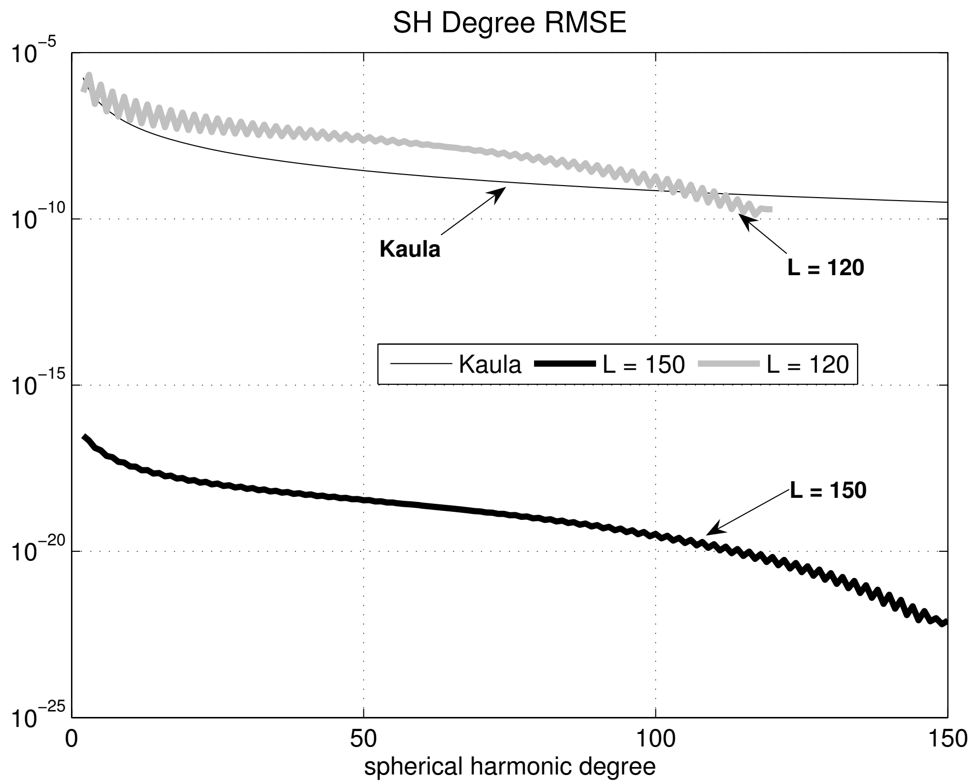

Figure 4.25: Degree RMSE in the aliasing problems caused by omission errors

Theoretically, since the synthesized values on the torus grid are noiseless in this example, gravity field determination should be affected only by the numerical round-off errors. Compared with the input gravity field, the degree RMSE should be very small, which is shown as the degree RMSE curve of the $L = 150$ solution (black). However, as a result of the truncation of the high frequencies beyond degree 120 in the $L = 120$ solution (gray), the omission error causes an aliasing problem and the accuracy is several orders of magnitude worse than the full recovery in the $L = 150$ solution. The degree RMSE curve exceeds the boundary signal curve calculated by *Kaula*'s rule of thumb.

In this research, in order to avoid the aliasing problems caused by omission errors, the high frequency components beyond the maximum resolvable degree L are removed from a reference gravity field before solving the spherical harmonics. Jekeli (1996) discussed the aliasing problems caused by the omission errors for the case of gridded data and suggested applying a spherical cap average as a de-aliasing filter to make a function band-limited. This type of de-aliasing filter might be an interesting topic for future work.

4.5.4 Effects of the satellite ground track patterns caused by the orbital geometry

Another possible cause of aliasing problems is the geometric distribution of the observations on the Earth's (or torus) surface. During the mission lifetime, the satellite orbital height will decay because of the non-gravitational perturbation forces, such as air drag and solar radiation pressure. Consequently the ground track pattern will change and with it the data coverage in the projection domain. Figure 4.26 shows different monthly ground track patterns for January 2004 and June 2003 from the CHAMP mission. The satellite occasionally even went through a repeat orbit mode several times at a certain height because of the boosting. The orbit decay and boosting of the CHAMP satellite is shown in Figure 2.4, in which the ground track pattern in June 2003 was going through a near periodic repeat orbit with $N_\mathrm{e}/N_\mathrm{o} = 31/2$.

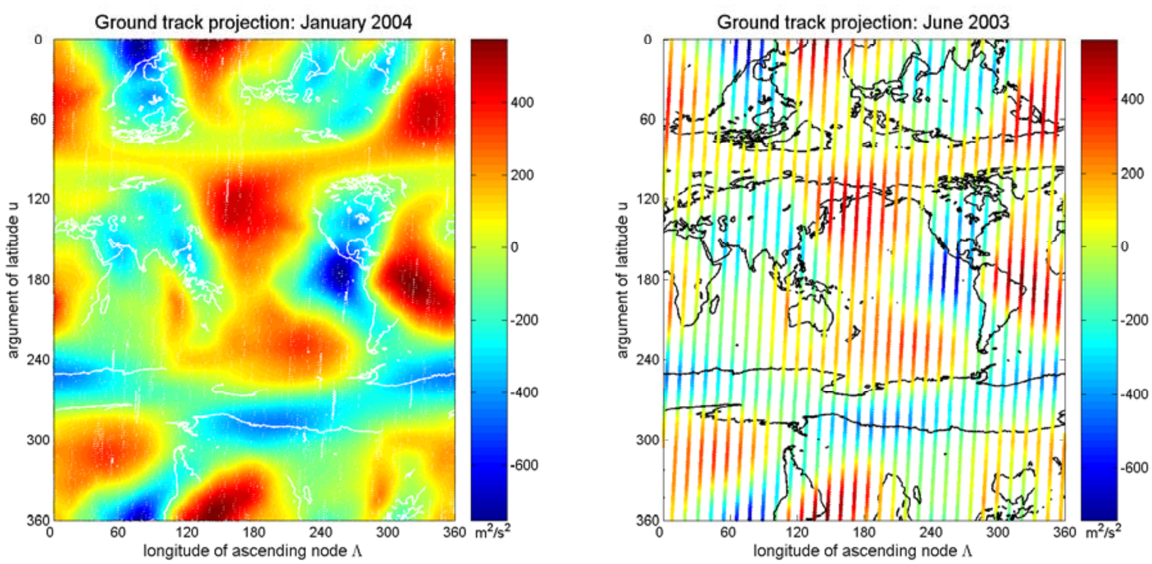

Figure 4.26: **Two typical ground track patterns projected on the torus, January 2004 (left), June 2003 (right)**

Time-variable ground track patterns on the projection domain result in different geometric distributions of observations. Interpolation is mandatory for creating a grid on the

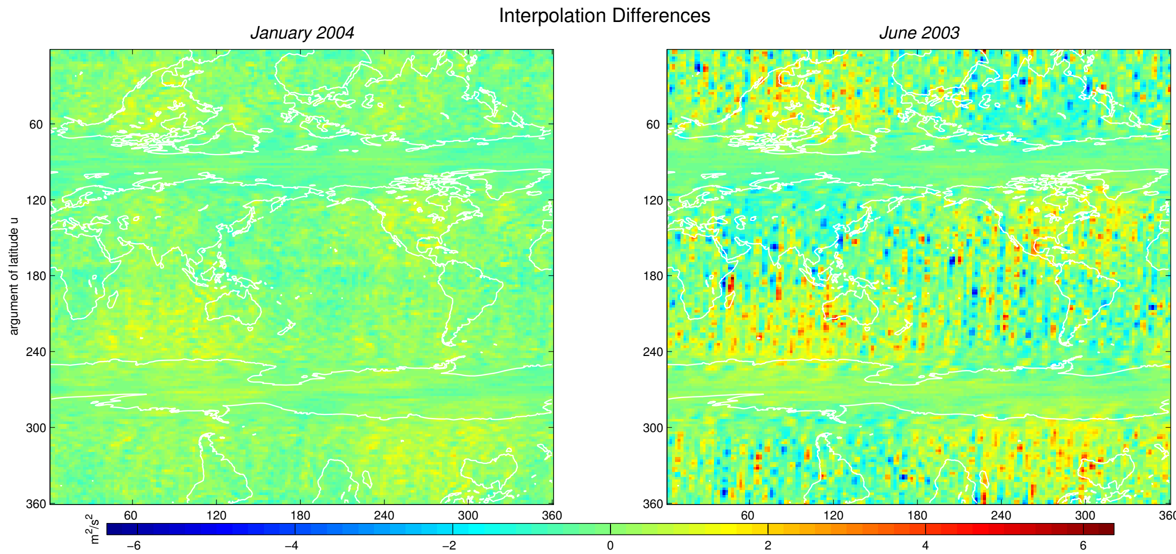

Figure 4.27: **Interpolation difference of January 2004 and June 2003 using LSC with the *Tscherning-Rapp* covariance model**

nominal torus. Least-squares collocation (LSC) with the same covariance function from the *Tscherning-Rapp* model for the disturbing potential is used to interpolate the same $2^\circ \times 2^\circ$ grid for two individual months. The reason of using the *Tscherning-Rapp* model for both two months is to avoid the differences of the covariance function parameters calculated from the empirical determination. The interpolation differences between the gridding results and the synthesized reference values are plotted in Figure 4.27.

Although two individual months employ the same LSC interpolation method with a same type of covariance function, the interpolation differences compared to the reference values are not at the same level. With a good ground track coverage, the month of January 2004 has an interpolation error of $0.38\,\mathrm{m}^2/\mathrm{s}^2$ in STD, while with a repeat orbit pattern, the month of June 2003 degrades with an interpolation error of $0.96\,\mathrm{m}^2/\mathrm{s}^2$ in STD. Different interpolated grids result in different gravity field determination results. Applying the torus-based semi-analytical approach, the monthly solutions can be determined for January 2004 and June 2003. Their corresponding degree RMSE curves compared to a reference field, e.g., the GGSM02S model, are plotted in Figure 4.28. The dashed and solid curves in gray indicate the signal and noise, respectively, of June 2003. The dashed and solid curves in black are for the signal and noise of January 2004, respectively. The cross-over point between the signal and noise curves, where SNR $= 1$, shows the maximum resolvable degree for individual monthly solutions. January 2004 is able to recover the gravity field even up to degree $L = 70$. June 2003 has the cross-over point around degree $l = 50$, and the overall solution is about one order of magnitude worse than the monthly solution from January 2004.

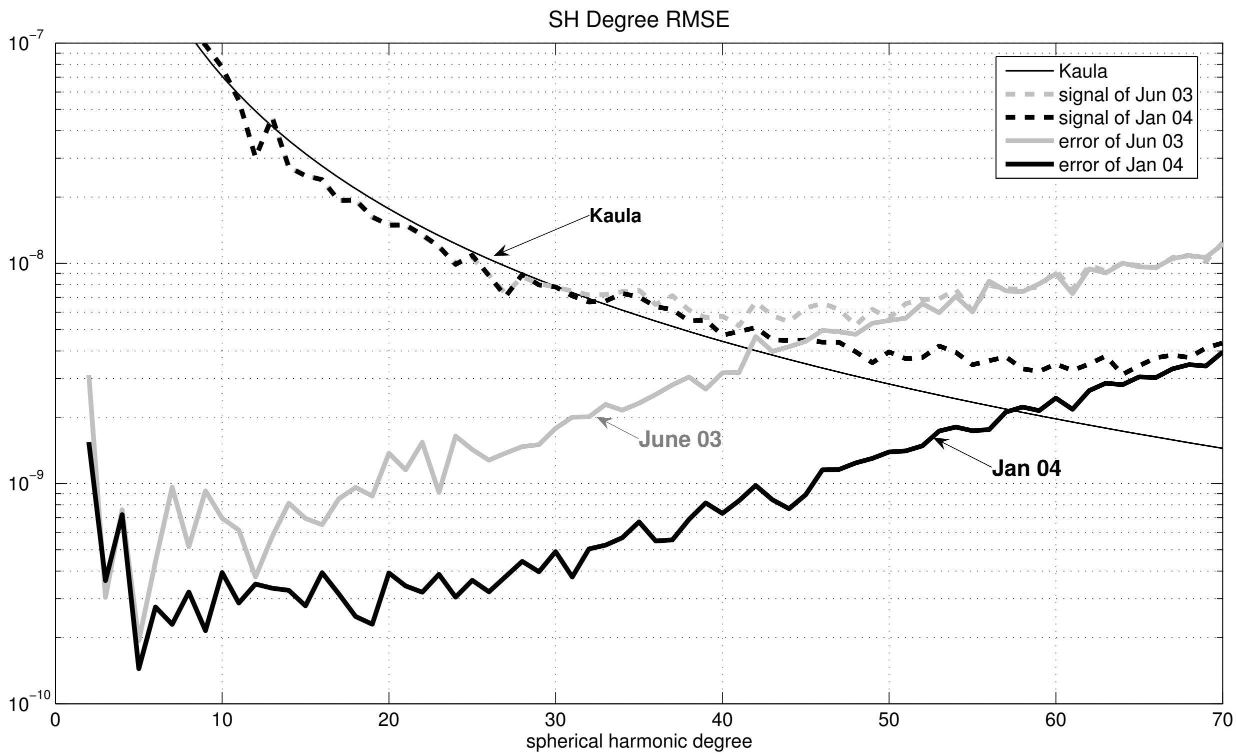

Figure 4.28: Degree RMSE of January 2004 and June 2003 from the CHAMP mission, compared to the GGM02S model

Another perspective to show the aliasing effects caused by the ground track patterns is from the spectral point of view. Choosing the GGM02S gravity field model as reference, differences between the resolved spherical harmonic coefficients and the reference can be plotted in a 2D spectrum Δ_{lm} (Equation 4.2) in Figure 4.29. Compared to the solution from January 2004, the solution from June 2003 has a less accurate spectrum. The accuracy decreases dramatically for the degrees and orders above 30 because the effect of the bad performance in the higher degrees and orders ($l > 50$) aliases into the neighboring lower degrees and orders ($30 < l < 50$).

Similarly, the GRACE mission also suffers from the aliasing problem as a result of the

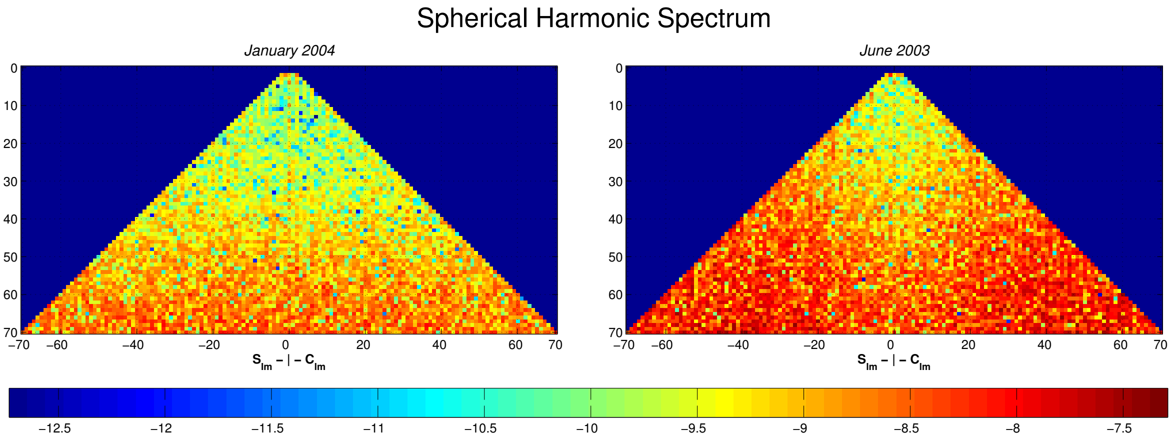

Figure 4.29: Spherical harmonic error spectrum of January 2004 and June 2003 from the CHAMP mission, compared to the GGM02S reference model

orbit decaying. Using a simulated four-weekly disturbing potential data for several repeat orbit scenarios, Yamamoto et al. (2005) investigated the effect of different simulated GRACE orbit decays on the gravity field recovery. In the study, the global standard deviations of the geoid height increases by one order of magnitude and the ground track recovery provides insufficient spatial resolution. Therefore, the gravity field recovery is only up to degree 30 for some specific orbit heights.

Wagner et al. (2006) investigated the same degradation problem of gravity field recovery for one particular monthly solution from real GRACE disturbing potential data. The same conclusion is drawn on the spatial *Nyquist* theorem, namely that gravity field determination from a repeat orbit scenario with resolution of degree L requires the number of orbit revolutions to be greater than $2L$. They recommended that one should avoid the sparse ground tracks for spherical harmonics estimation by changing the repeat patterns of the observations. Figure 4.29 shows that the torus-based approach is therefore an alternative and available choice because interpolation works as a re-sampling tool for the sparse ground track patterns.

4.5.5 Sampling overlaps in different domains

This type of aliasing problem occurs when the orbital frequency in a 2D torus domain ψ_{mk} is transformed to a 1D repeat orbit domain ψ_n, and vice-versa. Sneeuw (2000b) discussed the reasons causing the overlap aliasing problem. The minimum condition avoiding this situation must hold for a repeat orbit with N_e (number of nodal days) and N_o (number of revolutions):

$$L \leq \frac{N_\mathrm{o} + N_\mathrm{e}}{2} - 1. \tag{4.45}$$

This requirement is equivalent to $L \leq N_\mathrm{o}/2$ for a low Earth orbiter (LEO) as discussed before. For instance, in June 2003, the CHAMP satellite was in a repeat orbit scenario with $N_\mathrm{o} = 31$ revolutions in $N_\mathrm{e} = 2$ nodal days. Theoretically, aliasing will occur for the degrees and orders above 15. In one revolution, a point on a torus is sampled twice, which are as much as the samples on a sphere because of ascending and descending arcs on the same point (Figure 4.10). Therefore, the revolutions should be doubled, i.e., $N_\mathrm{o} \times 2 = 62$. An indication of this aliasing phenomenon can be shown in the degree RMSE curve, where the error curve is supposed to cross *Kaula*'s curve around $l = 31$. However, Figure 4.28 demonstrates that the monthly solution from June 2003 is able to resolve the spherical harmonic degrees higher than 31. The reason again is that the interpolation on the torus re-samples the observations and the spatial resolution is therefore changed according to the size of the torus grid.

4.6 Practical implementation of the real-valued FFT technique

The derivations of the FFT technique in Section 3.2.4 are all based on complex-valued expressions for the purpose of compact expression. However, for practical computer programming, real-valued numbers are required. Under this situation, the indices m and k in a *Fourier* series, e.g., in Equation (3.14a), have to be converted to positive integers. This practical issue should be implemented for the real-valued FFT technique application.

Taking the maximum resolvable degree as L, Equation (3.14a) can be re-written in a real-valued expression avoiding the imaginary unit "j":

$$f(u,\Lambda) = \sum_{m=0}^{L} \sum_{k=-L}^{L} A_{mk} \cos(ku + m\Lambda) + B_{mk} \sin(ku + m\Lambda). \tag{4.46}$$

The equation above is still in an implicit format of a 2D *Fourier* series. Since the indices of vectors are always positive integers in the numerical calculation, the index k has to be converted to positive integers. Assuming $0 \leq k \leq L$, Equation (4.46) can be rearranged as a 2D *Fourier* series:

$$\begin{aligned} f(u,\Lambda) = \sum_{m=0}^{L}\sum_{k=0}^{L} \quad & \underbrace{(A_{m,+k}+A_{m,-k})}_{F_1}\cos ku\cos m\Lambda, \\ + \quad & \underbrace{(-A_{m,+k}+A_{m,-k})}_{F_2}\sin ku\sin m\Lambda, \\ + \quad & \underbrace{(B_{m,+k}-B_{m,-k})}_{F_3}\sin ku\cos m\Lambda, \\ + \quad & \underbrace{(B_{m,+k}+B_{m,-k})}_{F_4}\cos ku\sin m\Lambda. \end{aligned} \tag{4.47}$$

The real-valued lumped coefficients A_{mk} and B_{mk} in Equation (4.46) are the combined vectors of $A_{m,\pm k}$ and $B_{m,\pm k}$, respectively, which can be calculated through the *Fourier* coefficients F_1, F_2, F_3, F_4 in Equation (4.47) (Karrer, 2000):

$$\begin{aligned} A_{m,k\in[-L,L]} &= \begin{bmatrix} A_{m,-k} & = \frac{F_1+F_2}{2} \\ A_{m,+k} & = \frac{F_1-F_2}{2} \\ k & \in [0,L] \end{bmatrix}, \\ B_{m,k\in[-L,L]} &= \begin{bmatrix} B_{m,-k} & = \frac{F_3+F_4}{2} \\ B_{m,+k} & = \frac{F_4-F_3}{2} \\ k & \in [0,L] \end{bmatrix}. \end{aligned} \tag{4.48}$$

Equation (4.47) and (4.48) can be applied in both the forward analysis procedure and the backward synthesis procedure when dealing with the real-valued *Fourier* coefficients.

4.7 Summary

THIS chapter has discussed comprehensively the issues involved in the first two major steps of the gravity field recovery procedure, i.e., from the in-situ observations to the 2D lumped coefficients.

A low order ARMA$(8,1)$ filter is designed and tested as a de-nosing tool for the observations contaminated by colored noise, especially for the gravity gradient tensor data. The power spectrum of the noise after filtering is close enough to white noise.

Data reduction uses a multi-parametric *Taylor* expansion series to correct the height and inclination variations. This reduction is essentially important especially for the observables without the normal gravity field removed, because the variation corrections can be over 15 times larger than the disturbing part. The partial derivatives of the observables with respect to height and inclination are presented. By comparing the magnitude of the partial derivatives with the original observation, truncation at the second order is sufficient. The downward/upward corrections along the orbit are calculated by the developed torus-based gravity field synthesis procedure with the corresponding transfer coefficients. A new expression of the first order inclination derivative is derived. The synthesized values can be obtained quickly and easily by making use of the inverse fast *Fourier* transform (IFFT) for the grid data or the numerical vector operation for the scattered data on the nominal torus.

Two groups of interpolation methods, namely the deterministic and geo-statistical approaches, are investigated for creating a grid on the torus. The LSC with observation errors is used and the ordinary *Kriging* is chosen to determine and remove a constant trend if there is one among observations. All the essential parameters are estimated empirically using the track-wise determination. The interpolation results show that for isotropic observables, the geo-statistical approaches, i.e., LSC and *Kriging*, create a more accurate grid than the deterministic approaches of bi-linear and spline interpolation. In addition, the geo-statistical approaches are able to propagate the data errors while the deterministic ones cannot. However, for anisotropic observables, the LSC does not work well because of its intrinsic isotropic assumption. The computational time and the determination of the covariance function or semi-variogram are the limiting factors of LSC and *Kriging* when dealing with a huge date set. Compared to the references values, the interpolation errors (STD values) from the best interpolation results are less than 0.01% for the disturbing potential, 1% for the V_{zz} gravity gradient tensor component, and 3% for the anisotropic V_{yy} component. A better interpolation technique for the anisotropic observables should be investigated in future work.

According to the *Nyquist* theorem in the spatial domain, a rule is discovered that the increment of the torus grid has to be smaller than $180°/L$. In the temporal domain, oceanographic and hydrologic models can be employed as a de-aliasing tool to remove the high frequency signals in the observations. The aliasing problem also occurs because of the omission errors in the spherical harmonics domain. Therefore, it is recommended that the high frequency components beyond the maximum resolvable degree L are removed from a reference gravity field. In addition, since different ground track patterns yield different data distributions, the high degrees and orders may be aliased in the monthly solution with a repeat orbit mode. Fortunately, this situation is improved in the torus-based approach because interpolation re-samples the spatial resolution when creating a grid with a denser data distribution. The monthly solution from June 2003, which was in a repeat mode of 31 revolutions in 2 nodal days, can reach the maximum degree up to $L = 50$, but this solution is only half an order of magnitude worse than the January 2004 monthly solution with a very dense ground coverage.

The real-valued expression of the 2D FFT technique has been derived for the purpose of programming implementation.

Chapter 5

Determination of spherical harmonic coefficients from lumped coefficients using least-squares adjustment

THIS chapter will focus on the estimation of the spherical harmonic coefficients from the pseudo-observables, the lumped coefficients, using least-squares adjustment. The pocket guide representation (Section 5.1) is a collection of different types of transfer coefficients for different observables from spaceborne gravimetry. With these transfer coefficients, the torus-based approach is able to build a linear mapping function between the spherical harmonic coefficients and any geo-potential functional. Therefore, a typical least-squares adjustment can be applied for this normally over-determined problem. Under the nominal torus assumption, a block-diagonal system for each order m is achieved, and the real-valued expression for the order-wise least-squares adjustment is derived in Section 5.2. The multi-observable model is also introduced in order to obtain an overall solution from the individual monthly solutions. A model of the weight matrix will be developed based on the error PSD model, and the error propagation will be discussed in Section 5.3. Section 5.4 will present the regularization techniques for a nearly ill-conditioned problem of the normal matrix. In addition, the performance of the regularization matrices and the determination of the regularization factors are evaluated in the order-wise least squares adjustment. The determination of the optimal weighting factor in the combined solutions from SST and SGG will be addressed in Section 5.5. A torus-based iteration scheme is developed to improve the estimation by compensating for various approximations and assumptions (Section 5.6).

5.1 Pocket guide – transfer coefficient representations

After completing the first two steps of gravity field determination using the torus-based approach, which have been extensively discussed in Chapter 4, the lumped-coefficients A_{mk} are obtained as the pseudo-observables from an interpolated regular grid on the nominal torus by the FFT technique. The next step is to estimate the spherical harmonic coefficients from the lumped coefficients. The linear mapping factor between these two domains is the transfer coefficient, H^f_{lmk}. Spatially, it is a representation between a sphere and a torus (Figure 3.4). As discussed in Section 3.2.4, the torus-based semi-analytical approach is a very handy and flexible tool for dealing with any geo-potential functional, if the corresponding transfer coefficient is available. Without any additional derivation and computation, the only item that needs to be changed in the flow chart of Figure 3.5 is the design matrix of the linear system, which consists of the transfer coefficient.

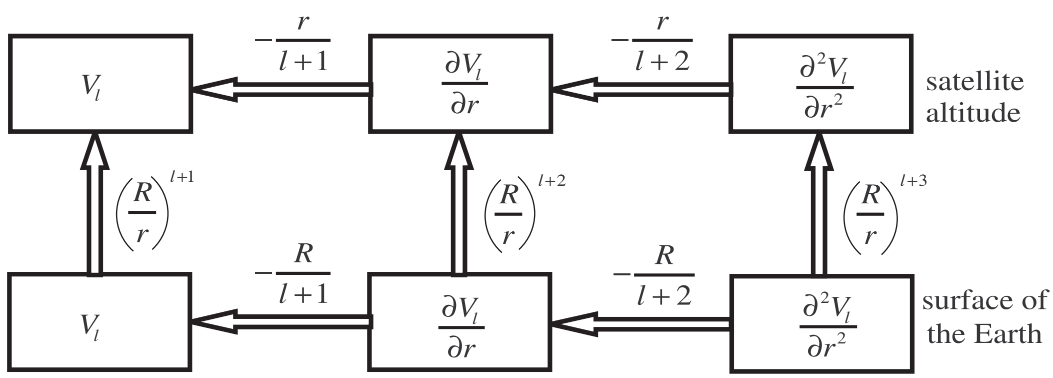

Figure 5.1: The *Meissl* Scheme

The purpose of PG is to establish a complete collection of corresponding transfer coefficients for all relevant geo-potential functionals. The phrase "pocket guide" in physical geodesy came from Rummel (1991). Sneeuw (2000b) extended its meaning and denoted H^f_{lmk} as the collection of different types of the transfer coefficients to dynamic satellite geodesy. The traditional way to connect different observables is using the *Meissl* scheme as shown in Figure 5.1 (Meissl, 1971; Rummel, 1979) and the extended *Meissl* scheme (Rummel and van Gelderen, 1995). However, PG is different from the traditional *Meissl* scheme. The latter scheme presents the spectral characteristics of the first and second order derivatives of a geo-potential functional as eigenvalues of a linear operator. The *Meissl* scheme and the extended *Meissl* scheme stay in only one spectral domain, i.e., either the spherical harmonic or the Fourier domain, and they make use only of the spherical harmonic degree l information. Conversely, a transfer coefficient in PG links these two domains (Sneeuw, 2000b). Consequently, it is not only a function of the degree l, but also a function of the order m and the third index k. Therefore, the transfer coefficient cannot be considered as an eigenvalue of a linear operator as in the case of the *Meissl* scheme.

There are two ways to derive the transfer coefficient: the differentiation technique and the orbital perturbation theory. The linearized homogeneous *Hill* equations with no perturbation forces on the right hand side of Equation (5.1) should be employed to establish a dynamical model of the satellite motion (Hill, 1878). In addition, Xu et al. (2004) derived a non-trivial analytical solution for a set of non-homogeneous *Hill* equations in the context of the J_2 perturbation force.

$$\begin{cases} \ddot{x} + 2n\dot{z} = 0 \\ \ddot{y} + n^2 y = 0 \\ \ddot{z} - 2n\dot{x} - 3n^2 z = 0 \end{cases} \tag{5.1}$$

with x the along-track, y the cross-track, and z the radial direction in the local satellite coordinate system (Figure 3.2). The mean motion of the orbit n comes from *Kepler*'s third law:

$$n = \frac{GM}{r^3}. \tag{5.2}$$

GRACE-type line-of-sight (LOS) gradiometry. The technique of satellite-to-satellite tracking in low-low mode (SST-ll) from the GRACE satellite mission provides very precise inter-satellite range measurements with the K-band ranging system (Section 2.2). The transfer coefficient H^{ρ}_{lmk} for the range observable between the two satellites can be expressed as a combination of the orbit perturbation transfer coefficients $H^{\Delta x}_{lmk}$ and $H^{\Delta z}_{lmk}$ in the local system (Sneeuw, 2000b):

$$H^{\rho}_{lmk} = 2j\cos\eta\sin(\eta\beta_{mk}H^{\Delta x}_{lmk}) + 2j\sin\eta\cos(\eta\beta_{mk}H^{\Delta z}_{lmk}), \tag{5.3a}$$

$$H^{\Delta x}_{lmk} = R\left(\frac{R}{r}\right)^{l-1}\left[j\frac{2(l+1)\beta_{mk} - k(\beta^2_{mk}+3)}{\beta^2_{mk}(\beta^2_{mk}-1)}\right]\bar{F}_{lmk}(I), \tag{5.3b}$$

$$H^{\Delta z}_{lmk} = R\left(\frac{R}{r}\right)^{l-1}\left[\frac{(l+1)\beta_{mk} - 2k}{\beta_{mk}(\beta^2_{mk}-1)}\right]\bar{F}_{lmk}(I), \tag{5.3c}$$

where η is the half angle of the separation between the two satellites connecting to the center of the Earth (for a baseline of 220 km like the GRACE, $\eta \approx 1°$), and β_{mk} is the normalized orbital frequency with the unit of cycles per revolutions (CPR), i.e., $\beta_{mk} = \dot{\psi}_{mk}/n$.

The transfer coefficient of the range observable H^{ρ}_{lmk} is independent of the cross-track component $H^{\Delta y}_{lmk}$, but it carries on the resonances from both $H^{\Delta x}_{lmk}$ and $H^{\Delta z}_{lmk}$ when $\beta_{mk} = 0, \pm 1$. A resonance with an infinite value will destroy the linear system between the lumped coefficients and the spherical harmonic coefficients. The LOS gradiometry can avoid this problem by making use of the ratio between the range and range acceleration in some approximations.

In the GRACE-type SST-ll mission, the twin satellites fly along the same orbit with different mean anomalies. The relation among the inter-satellite range, range rate, and range acceleration is demonstrated in Figure 5.2, and the mathematical equations are derived as follows (Rummel et al., 1978):

$$\rho = \rho \cdot e, \tag{5.4a}$$

$$\dot{\rho} = \dot{\rho} \cdot e, \tag{5.4b}$$

$$\ddot{\rho} = \rho \cdot e + \frac{1}{\rho}(\dot{\rho} \cdot \dot{\rho} - \dot{\rho}^2), \tag{5.4c}$$

where e is the unit vector, which can be calculated from the baseline:

$$e = \frac{\rho}{|\rho|}. \tag{5.5}$$

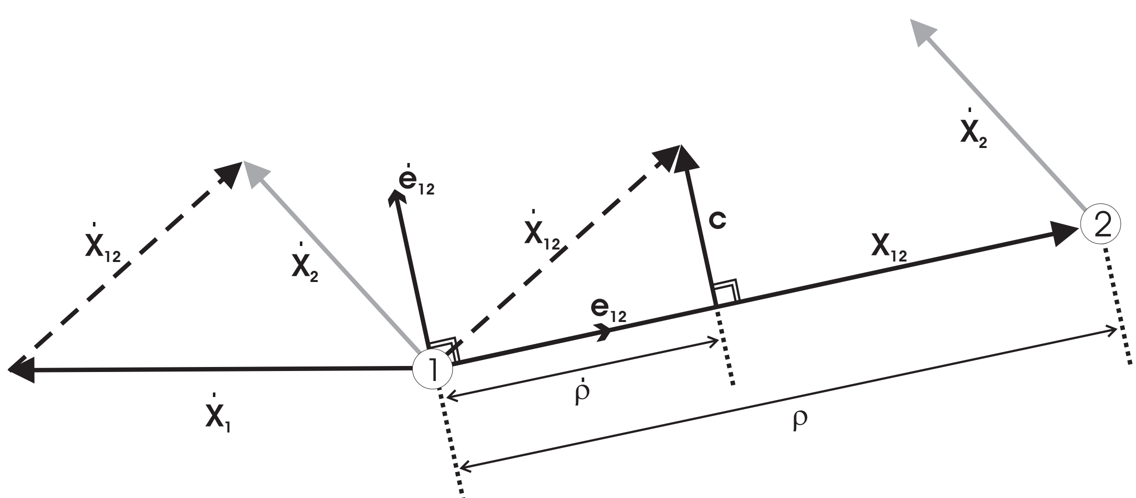

Figure 5.2: Concept of the GRACE-type LOS gradiometry (Rummel et al., 1978)

Under a small angle approximation and some numerical simplifications, Sneeuw (2000b) verified theoretically that the ratio between inter-satellite range and range acceleration $\frac{\ddot{\rho}}{\rho}$ could be interpreted as LOS gravity gradiometry. This combined observable resembles the V_{xx} gravity gradient tensor along-track component with a different scale. Therefore, the approximated transfer coefficient for this GRACE-type LOS gradiometry is very similar to the transfer coefficient of V_{xx} in Equation (5.7a), namely.

$$\frac{H_{lmk}^{\ddot{\rho}}}{\rho} \approx \frac{GM}{R^3}\left(\frac{R}{r}\right)^{l+3}[l-1-k^2]\bar{F}_{lmk}(I). \tag{5.6}$$

Gravity gradient tensors. Since gravity field determination from the GOCE mission comes from processing the gravity gradient tensor data, the corresponding transfer coefficients describing all components of the gravity gradient tensor are given by Sneeuw (2000b) as follows:

$$V_{xx} : H_{lmk}^{xx} = \frac{GM}{R^3}\left(\frac{R}{r}\right)^{l+3}[-(k^2+l+1)]\bar{F}_{lmk}(I), \tag{5.7a}$$

$$V_{yy} : H_{lmk}^{yy} = \frac{GM}{R^3}\left(\frac{R}{r}\right)^{l+3}[k^2-(l+1)^2]\bar{F}_{lmk}(I), \tag{5.7b}$$

$$V_{zz} : H_{lmk}^{zz} = \frac{GM}{R^3}\left(\frac{R}{r}\right)^{l+3}[(l+1)(l+2)]\bar{F}_{lmk}(I), \tag{5.7c}$$

$$V_{xy} : H_{lmk}^{xy} = \frac{GM}{R^3}\left(\frac{R}{r}\right)^{l+3}[jk]\bar{F}_{lmk}^{*}(I), \tag{5.7d}$$

$$V_{xz} : H_{lmk}^{xz} = \frac{GM}{R^3}\left(\frac{R}{r}\right)^{l+3}[-jk(l+2)]\bar{F}_{lmk}(I), \tag{5.7e}$$

$$V_{yz} : H_{lmk}^{yz} = \frac{GM}{R^3}\left(\frac{R}{r}\right)^{l+3}[-(l+2)]\bar{F}_{lmk}^{*}(I), \tag{5.7f}$$

The orientations of x, y, and z axes in the local satellite system are as defined above.

Satellite formation flying (SFF). Serving as a reliable, low cost alternative to the "one satellite does all" approach, the satellite formation flying technology is primarily concerned with the maintenance of the relative location among many satellites (Hughes and Norris, 2002). Simultaneous and redundant measurements from multiple formation flying vehicles provide substantial benefits, such as configuration, resolution, and robustness (Leitner et al., 2002). The GRACE satellite mission is designed as a type of formation flying. For the relative orbit, the two identical satellites were placed in the same orbit with different mean anomalies. Such a configuration is referred to as a leader-follower flying formation. However, this leader-follower configuration is sensitive only along the line-of-sight direction. The weakness in the cross-track direction may cause an aliasing problem in the inter-satellite range observable because of mismodelling. A multiple-formation configuration can provide a cross-track motion and help in de-aliasing signals because it introduces a seperate information in the cross-track direction (Sneeuw and Schaub, 2005; Sneeuw et al., 2005a).

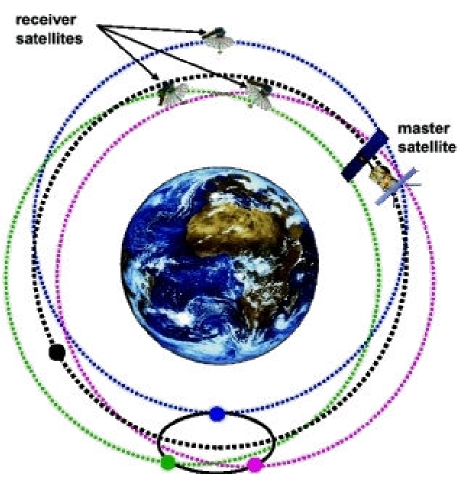

(a) Cartwheel configuration in SAR

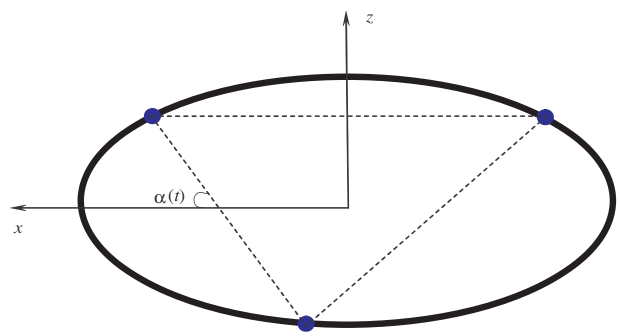

(b) New observable from a cartwheel formation

Figure 5.3: Concept of cartwheel configuration in satellite formation flying

Therefore, the concept of satellite formation flying will probably be employed in future satellite missions, e.g., the SWARM mission (the Earth's magnetic field and environment explorers). It consists of a constellation of three satellites in three different polar orbits (ESA, 2004). Another possible formation is the so-called cartwheel configuration (Figure 5.3(a)), which originated in the synthetic aperture radar (SAR) community (Massonnet, 1999). If such a cartwheel formation of three satellites is designed, a time-variable rotation angle $\alpha(t)$ about the y-axis will be introduced (Sneeuw and Schaub, 2005). Any two satellites are always on the new x'-axis along the triangle edges of the wheel, and the new observable $V_{x'x'}$ can be expressed as follows (Figure 5.3(b)):

$$V_{x'x'} = \cos^2\alpha V_{xx} + 2\cos\alpha\sin\alpha V_{xz} + \sin^2\alpha V_{zz}. \tag{5.8}$$

Since the corresponding transfer coefficient $H_{lmk}^{x'x'}$ for the time-variable along-track component is determined by the combination of the transfer coefficients H_{lmk}^{xx}, H_{lmk}^{xz}, and H_{lmk}^{zz}, this new kind of observable can be used to recover the gravity field by employing the calculating flow chart in Figure 3.5.

5.2 Block-diagonal structured linear system and order-wise least-squares estimation

The transfer coefficients provide a linear relationship between the *Fourier* coefficients (lumped coefficients A_{mk}) and the spherical harmonic coefficients. In addition, this linear system has a block-diagonal structure as a result of the nominal torus assumption (Figure 3.1). Therefore, the spherical harmonic unknowns can be estimated separately by a typical least-squares adjustment for individual orders m.

5.2.1 Block-diagonal system

Under the assumption of a nominal orbit, the transfer coefficients are independent or uncorrelated for the individual orders $m \in [-L, L]$. Thus, for each order m, a corresponding linear system $a = H\kappa$ is yielded in a matrix format, where a is the vector of the lumped-coefficients A_{mk}, H is the design matrix consisting of the transfer coefficients H_{lmk}, and κ is the vector of spherical harmonic coefficients. Because $-L \leq k \leq L$ and $-L \leq m \leq L$, the dimensions of the linear system for a specific order m are demonstrated as follows:

$$\underset{(2L+1)\times 1}{a_m} = \underset{(2L+1)\times(L-|m|+1)}{H_m} \underset{(L-|m|+1)\times 1}{\kappa_m} . \tag{5.9}$$

In the design matrix H, the left upper and lower triangular corners are all zeros when $|k| > l$, because the third index k is in the range of $-l \leq k \leq l$ by definition. In addition, alternating elements are filled with zeros depending on the usage of the inclination function $\bar{F}_{lmk}(I)$ or the cross-track inclination function $\bar{F}_{lmk}^{*}(I)$. For instance, those using $\bar{F}_{lmk}(I)$ are zero for $l-k$ odd, whereas those with $\bar{F}_{lmk}^{*}(I)$ are zero for $l-k$ even. Therefore, a proper even or odd permutation of columns and rows yields two sub-blocks for each order m with a size of $(L+1) \times \frac{1}{2}(L-|m|+1)$. Figure 5.4 shows the structure of the design matrix using an inclination function $\bar{F}_{lmk}(I)$ with $L=20$, $m=0$ and $m=10$, respectively, (a black square means having a value and a white spot means zero).

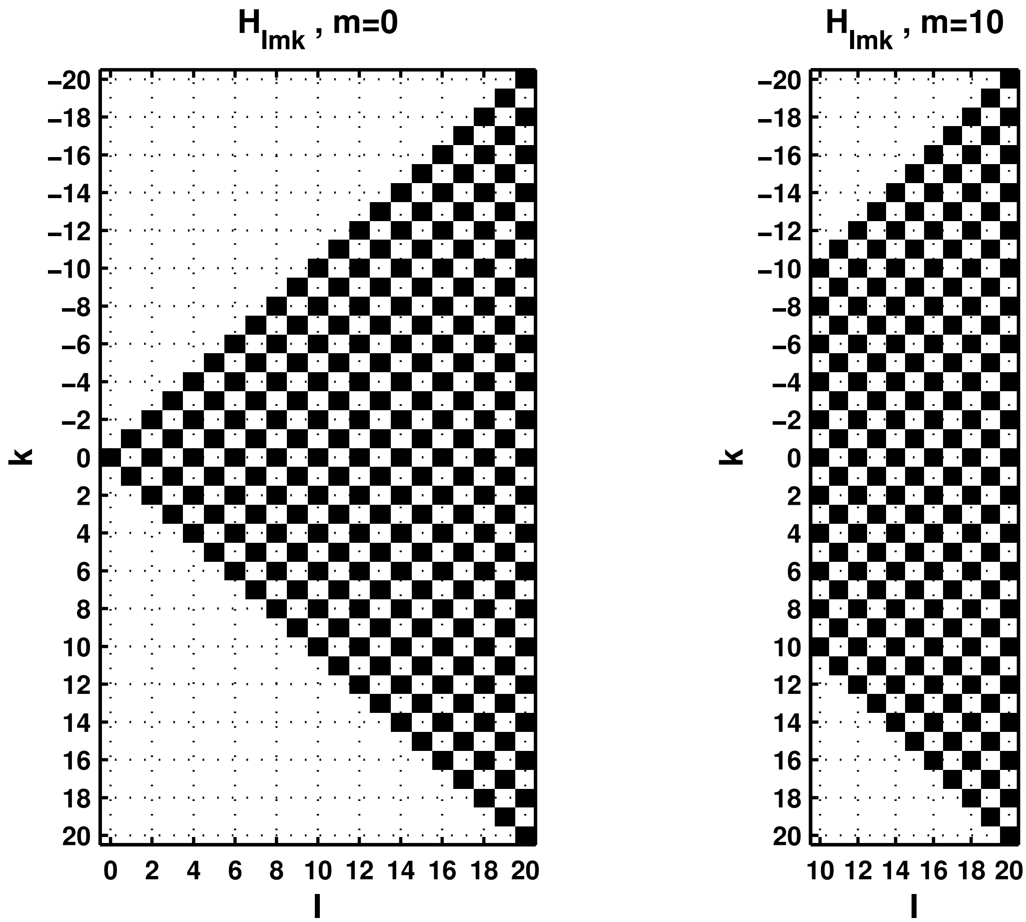

Figure 5.4: The structure of the H matrix for $m=0$ and $m=10$, $L=20$

5.2.2 Order-wise least-squares adjustment

Normally, estimating the spherical harmonic coefficients with $(L+1)^2$ unknowns from the lumped coefficients of $(360/d_{\max})^2$ pseudo observables is an over-determined problem. Since measurements always contain noise, the noise will propagate in the lumped coefficients. The linear system is modified by adding an error vector e:

$$a = H\kappa + e. \tag{5.10}$$

The corresponding stochastic model for the linear system can be written as a standard

Gauss-Markov model:

$$E\{e\} = 0, D\{e\} = Q_0, \tag{5.11}$$

The operators $E\{...\}$ and $D\{...\}$ are the first moment (expectation value) and second moment (variance-covariance matrix or dispersion matrix), respectively. Q_0 is the *a-priori* variance-covariance matrix of the measurements, which comes from observation information, such as the accuracy of the measurements. The best linear unbiased estimation of the unknowns κ with respect to the quadratic minimum of e, i.e., $\min\{e^{\mathrm{T}}Pe\}$, yields the least-squares estimator:

$$\hat{\kappa} = (H^{\mathrm{T}}PH)^{-1}(H^{\mathrm{T}}Pa), \tag{5.12}$$

with the weight matrix $P = Q_0^{-1}$. The matrix $H^{\mathrm{T}}PH$ is known as the normal matrix "N" and the *a-posteriori* variance-covariance matrix is the inverse of the normal matrix:

$$Q_{\hat{\kappa}} = \left(H^{\mathrm{T}}PH\right)^{-1} = N^{-1}. \tag{5.13}$$

Since the linear relationship is established under a block-diagonal structure for each order m, the least-squares estimation will also be applied order-wise. Consequently, all related critical issues discussed below in the context of least-squares estimation, such as the regularization technique and optimal weighting methods, also are implemented separately for individual orders.

5.2.3 Real-valued linear representation

The complex-valued expression of the block-diagonal linear system is very concise for the purpose of derivation. However, a real-valued expression is always preferred for practical numerical implementation. The real-valued coefficients need to take into the consideration the distinction between even or odd $l-m$ and the proper selection of either $\bar{C}_{lm}$ or $\bar{S}_{lm}$. Therefore, the *Fourier* coefficients in the linear system of Equation (3.14b) can be represented by (Schrama, 1989):

$$\left.\begin{matrix} A_{mk} \\ B_{mk} \end{matrix}\right\} = \sum_{l=0}^{L} H_{lmk}^{V} \left\{\begin{matrix} \alpha_{lm} \\ \beta_{lm} \end{matrix}\right. \tag{5.14}$$

in which

$$\alpha_{lm} = \begin{bmatrix} \bar{C}_{lm} \\ -\bar{S}_{lm} \end{bmatrix} \begin{matrix} l-m = \text{even} \\ l-m = \text{odd} \end{matrix} \tag{5.15a}$$

$$\beta_{lm} = \begin{bmatrix} \bar{S}_{lm} \\ \bar{C}_{lm} \end{bmatrix} \begin{matrix} l-m = \text{even} \\ l-m = \text{odd} \end{matrix} \tag{5.15b}$$

If the transfer coefficient makes use of the cross-track inclination function $\bar{F}^{*}_{lmk}(I)$, there is a phase shift of 90° in both α_{lm} and β_{lm}, which means that α_{lm} has to be replaced by β_{lm}, and β_{lm} has to be replaced by $-\alpha_{lm}$. If there is an imaginary unit j involved in the transfer coefficient, the same phase changes and substitutions have to be applied to α_{lm} and β_{lm}. If both the cross-track inclination function $\bar{F}^{*}_{lmk}(I)$ and the imaginary unit j are used in the transfer coefficient, a total phase-shift of 180° occurs. Under this circumstance, α_{lm} is changed to $-\alpha_{lm}$, and β_{lm} is substituted by $-\beta_{lm}$. According to this criterion, the real-valued expressions for gravity gradient tensor components in Equations (5.7d), (5.7e), and (5.7f) have to be changed correspondingly as follows (Rummel et al., 1993; Karrer, 2000):

For the V_{xy} component,

$$\left.\begin{matrix} A_{mk} \\ B_{mk} \end{matrix}\right\} = \sum_{l=0}^{L} H^{xy}_{lmk} \left\{\begin{matrix} -\alpha_{lm} \\ -\beta_{lm} \end{matrix}\right. . \tag{5.16}$$

For the V_{xz} component,

$$\left.\begin{matrix} A_{mk} \\ B_{mk} \end{matrix}\right\} = \sum_{l=0}^{L} H^{xz}_{lmk} \left\{\begin{matrix} \beta_{lm} \\ -\alpha_{lm} \end{matrix}\right. . \tag{5.17}$$

For the V_{yz} component,

$$\left.\begin{matrix} A_{mk} \\ B_{mk} \end{matrix}\right\} = \sum_{l=0}^{L} H^{yz}_{lmk} \left\{\begin{matrix} \beta_{lm} \\ -\alpha_{lm} \end{matrix}\right. . \tag{5.18}$$

5.2.4 Multi-observable model

In this thesis, the basic unit for gravity field determination from spaceborne gravimetry is a monthly solution. Because of the linearity property, the combined overall solution for several months can easily be obtained by a multi-observable model without repeating the previous steps mentioned in Chapter 4, such as data reduction, interpolation, and the FFT. Based on the superposition principle of the normal matrix in least-squares adjustment, this multi-observable model can be employed also for different geo-potential functionals from different satellite missions. For a specific design matrix a_n from either different epochs or different geo-potential functionals, the linear stochastic model in Equation (5.11) can be extended as follows:

$$E\{e_i\} = 0, D\{e_i\} = Q_i,\ i = 1,2...\#\text{months/types}. \tag{5.19}$$

For each set of observables, the corresponding normal matrix N_1 and observation vector C_i can be formed:

$$N_i = {H_i}^{\mathrm{T}} P_i H_i, \tag{5.20}$$

$$C_i = {H_i}^{\mathrm{T}} P_i a_i. \tag{5.21}$$

The overall least squares adjustment can be achieved as a superposition of the individual solutions by the multi-observable model with the overall normal matrix $N = \sum_i N_i$ and observation vector $C = \sum_i C_i$, and the overall *a-posteriori* variance-covariance matrix $Q_{\hat{\kappa}} = N^{-1}$:

$$\bar{\kappa} = \left(\sum_{i=1}^{\#\text{months/types}} ({H_i}^{\mathrm{T}} P_i H_i)\right)^{-1} \left(\sum_{i=1}^{\#\text{months/types}} ({H_i}^{\mathrm{T}} P_i a_i)\right), \tag{5.22}$$

$$= N^{-1} C. \tag{5.23}$$

Since the *a-priori* information in the regularization technique can be treated as one of the data sets in Equation (5.19) in the form of a pseudo-observable, the regularized solution can be incorporated naturally into the multi-observable model (Section 5.4).

The contribution from each observable is considered to have an equal weight in the combined solution of Equation (5.22). As an extended version of the multi-observable model with corresponding relative weighting contributions, the optimal weighting method determines the different weights for different observables to get a better overall solution. This method will be discussed in detail in Section 5.5.

5.3 Development of spectral analysis and error propagation

The *in situ* consecutive measurements can be treated as a time series along an 1D orbit or a 2D torus trajectory. The *a-priori* noise information of the observations should be projected to the pseudo-observable in least-squares adjustment. The error information can be obtained in two ways: the variances of the *in situ* observations and the manufactured instrumental errors. The propagation of the the error information from the *in situ* observations to the pseudo-observable, lumped coefficients, is demonstrated in Figure 5.5.

Variances of the *in situ* observations. The Variances of the *in situ* observations can be expressed in a diagonal matrix format Q_0, which can be used for the analysis of the noise characteristics in Section 4.2. After filtering, a new variance matrix ${Q_0}'$ can be obtained. Since the corrections in data reduction are very small, compared to the original magnitude, the variance matrix Q_1 is considered as same as Q_0 or ${Q_0}'$. After employing geo-statistical interpolation, i.e., least-squares collocation or *Kriging*, the variance-covariance matrix Q_2 can be propagated through covariance function by Equation (4.25) or semi-variogram by Equation (4.38), respectively. The *Fourier* transform converts the covariance function Q_2 to the PSD error model $S(f)$ by Equation 4.12. Then, the error PSD model can be used as an *a-priori* information Q_{mk} for the lumped coefficients in least-squares adjustment. The calculating procedure from $S(f)$ to Q_{mk} will be explained in the second way of error propagation below, because the manufactured instrumental PSD will have exactly the same steps.

Manufactured instrumental error PSD. The second error information is given directly from the manufactured instrumental errors in terms of PSD model $S(f)$. For instance, the onboard sensitive gravity gradiometer of the GOCE mission requires a maximum error PSD level of $S(f) = 3 \times 10^{-3}\,\mathrm{E}/\sqrt{\mathrm{Hz}}$ in the measurement bandwidth (MBW) of $0.005\,\mathrm{Hz} \leq f \leq 0.1\,\mathrm{Hz}$. Outside the MBW, the PSD is specified as a function of the frequency with higher error level (ESA, 1999). The expected spectra of the gravity gradient measurements error

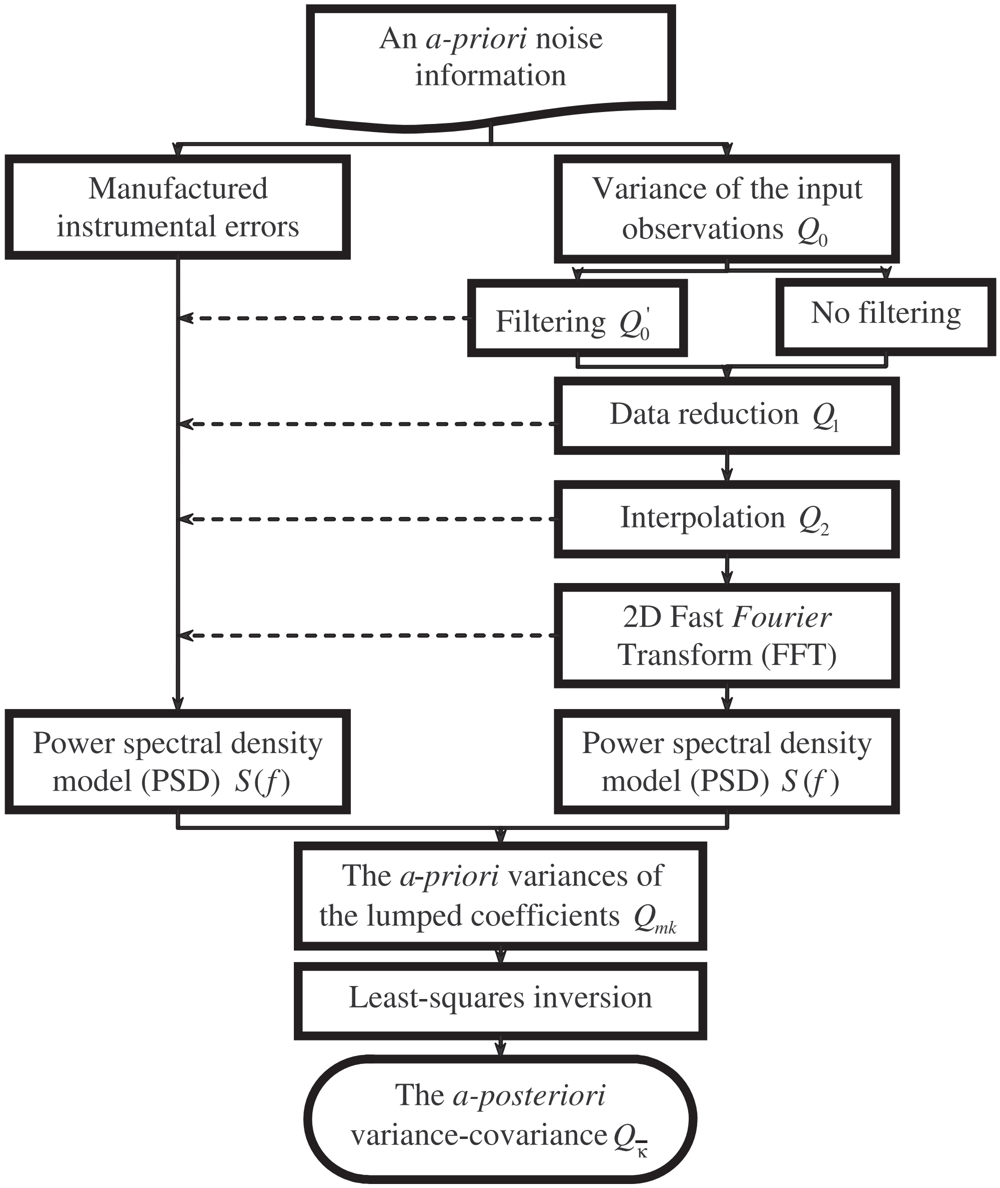

Figure 5.5: **Error propagation from the *in situ* observations to estimated spherical harmonic coefficients**

budget for the GOCE mission has been shown in Figure 2.8.

In this thesis, spectral analysis in least-squares adjustment makes use of the PSD model from the instrumental errors directly, because the implementation is straightforward on the one hand, and on the other hand the error variances of the *in situ* observations are not available for our calculations. Although filtering, reduction, and interpolation will influence the PSD model from instrumental errors (shown in Figure 2.8 with dashed lines), the effects are very small to be neglected because all the calculating procedures are manipulated in a control system with a controlled error budget.

A simplified PSD model for all gravity gradient tensor components is developed under the GOCE error budget, shown in Figure 5.6. The gravity gradient measurements in the MBW of $0.005\,\mathrm{Hz} \leq f \leq 0.1\,\mathrm{Hz}$ have an error spectrum of $3 \times 10^{-3}\,\mathrm{E}/\sqrt{\mathrm{Hz}}$. Outside the MBW, the PSD model is defined as follows:

$$S(f) = \begin{cases} 3 \times 10^{-3} \times 0.005/f & f < 0.005\,\mathrm{Hz}, \\ 3 \times 10^{-3} & 0.005\,\mathrm{Hz} \leq f \leq 0.1\,\mathrm{Hz}, \\ 3 \times 10^{-3} \times (f/0.1)^2 & f > 0.1\,\mathrm{Hz}. \end{cases} \tag{5.24}$$

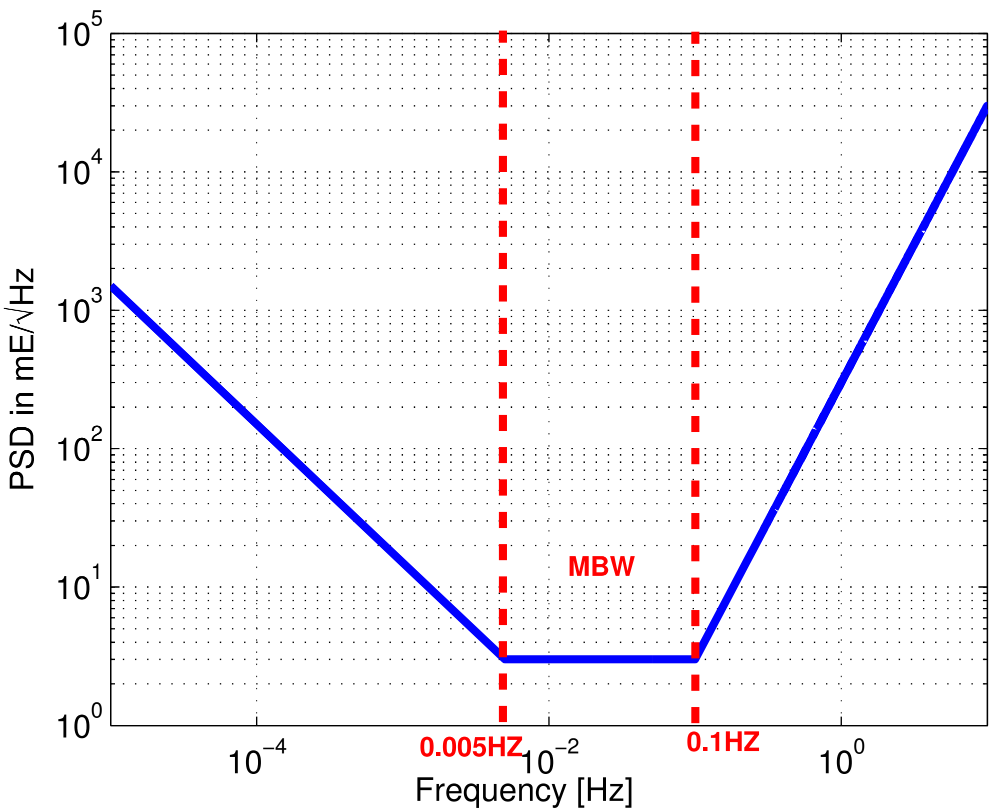

Figure 5.6: A simplified PSD model for the simulated GOCE observations with MBW of $0.005\,\mathrm{Hz} \leq f \leq 0.1\,\mathrm{Hz}$

For a certain spectral line f_{mk} defined by the indices m and k, the corresponding orbital frequency can be expressed by the changes in the orbital coordinates $\dot{u}$ and $\dot{\Lambda}$ in the following equation:

$$f_{mk} = \dot{\psi}_{mk} = k\dot{u} + m\dot{\Lambda}, \quad -L \leq m, k \leq L. \tag{5.25}$$

The precession of the argument of latitude $\dot{u}$ is the sum of the changes of the argument of perigee $\dot{\omega}$ and the mean anomaly $\dot{M}$ (Figure 3.2), because the true anomaly and mean anomaly are the same for a circular orbit (eccentricity $e = 0$). Under the secular perturbation caused by the Earth's oblateness ($J_2 = -C_{2,0}$), the precession $\dot{u}$ can be derived as follows (Kaula, 1966):

$$\dot{u} = \dot{\omega} + \dot{M} = n + \frac{3}{2} n J_2 \left(\frac{R}{r}\right)^2 [4\cos^2 I - 1]. \tag{5.26}$$

As expressed in Equation (3.10), the other orbital frequency argument $\dot{\Lambda}$ is the angular change of the right ascension of the ascending node $\dot{\Omega}$ minus the daily rotation rate $\dot{\text{GAST}} = 2\pi/\text{day}$. The J_2 perturbed $\dot{\Lambda}$ can be derived analytically (Kaula, 1966):

$$\dot{\Lambda} = \dot{\Omega} - \dot{\text{GAST}} = -\frac{3}{2} n J_2 \left(\frac{R}{r}\right)^2 \cos I - \frac{2\pi}{\text{day}}. \tag{5.27}$$

A periodic (repeat) orbit is therefore defined by the orbital frequencies $\dot{u}$ and $\dot{\Lambda}$ when they meet the repeat ratio with a negative sign because $\dot{\Lambda}$ always yields a negative value:

$$-\frac{\dot{u}}{\dot{\Lambda}} = \frac{N_\text{o}}{N_\text{e}}, \tag{5.28}$$

where the number of nodal days N_e and the orbital revolutions N_o have been discussed in Section 3.2.3.

For the specific spectrum $f_{mk} = \dot{\psi}_{mk}$, the corresponding error variance can be obtained by the integration over a tiny frequency band (spectral resolution $\mathrm{d}f$), resulting in the relation between the error variance and the PSD:

$$\sigma_{mk}^2 = S(f_{mk})\mathrm{d}f = \frac{S(f_{mk})}{T}, \tag{5.29}$$

where T is the repeat period for a periodic orbit or the mission duration for a non-periodic orbit (Sneeuw, 2000b).

The error variance σ_{mk}^2 calculated from the PSD with the indices of m and k can be treated as an *a-priori* information for the relevant pseudo-observable with the same indices m and k, the lumped coefficient A_{mk}. Therefore, the error variance goes into the main diagonal element of the weight matrix $P_{mk} = (\sigma^2_{mk})^{-1}$ as a weighting factor for m order-wise least-squares adjustment in Equation (5.12).

$$P = {Q_0}^{-1} = \begin{pmatrix} \sigma^2_{m,-L} & & 0 \\ & \ddots & \\ 0 & & \sigma^2_{m,L} \end{pmatrix}^{-1} . \tag{5.30}$$

Based on the simplified PSD model in Figure 5.6, the main diagonal elements in the weight matrix P for the lumped coefficients with $m = 0$ and $-120 \leq k \leq 120$ can be derived in Figure 5.7.

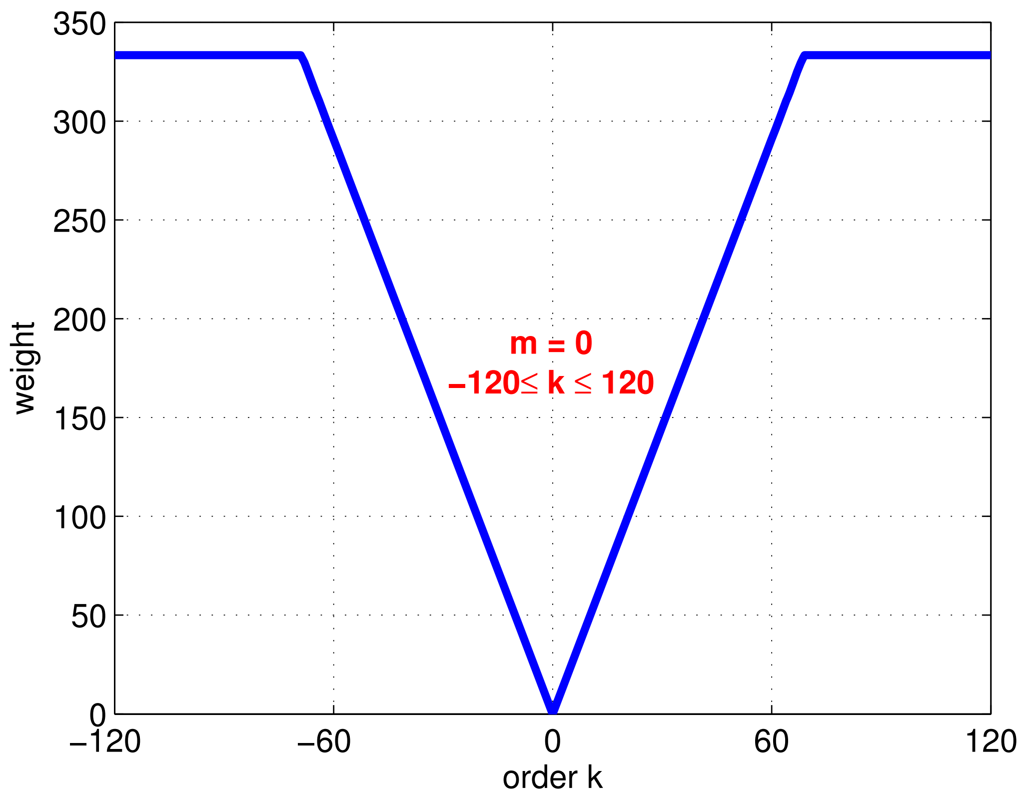

Figure 5.7: The main diagonal elements of the weighting matrix calculated from the simplified PSD model for $m = 0$, $-120 \leq k \leq 120$

By applying the weighted least squares adjustment for the individual orders, the unknown spherical harmonic coefficients can be estimated. The *a-posteriori* error variances and covariances of the coefficients are obtained from the co-factor matrix $Q_{\hat{\kappa}}$ in Equation

(5.13). Since the least squares solution is applied for individual order m, the error variance-covariance matrix cannot be estimated as a fully-populated matrix, and it also shows a block-diagonal structure. This error variance-covariance matrix $Q_{\hat{\kappa}}$ is a basic internal accuracy measure of the least-squares adjustment. In particular, the square root of the main diagonal elements represent the standard deviation σ_{lm} for single coefficients. The full set of σ_{lm} represents the spherical harmonic error spectrum, which can be used to create different error representation measures; see Section 4.1.

As mentioned in the spatial error representations, the expected errors of derived products, e.g., geoid height or gravity anomaly, are of importance for gaining a better understanding of the data quality in the spatial domain. This spatial error information can be obtained by the error propagation law from the *a-posteriori* variance-covariance matrix $Q_{\hat{\kappa}}$ in Equation (5.13) after least-squares adjustment.

5.4 Regularization Techniques

Global gravity field recovery from satellite observations by least-squares adjustment is an inverse problem. For various reasons, such as the polar gaps problem and non-continuous data distribution, the normal matrix in the least-squares inversion is typically ill-conditioned. Sometimes, the observable itself, e.g., a certain single component from the gravity gradient tensor, may contain insufficient information to be inverted to obtain the gravity field (Sneeuw, 2000b). Most importantly, the downward continuation from satellite altitude to the surface of the Earth, which amplifies not only the signal but also the noise, causes instabilities of the normal matrix. Therefore, the traditional gravity field recovery approaches normally have difficulties inverting an unstable normal matrix to estimate the unknown coefficients. The torus-based semi-analytical approach naturally solves some of the problems causing the instability. For instance, the normal matrix in the least-squares adjustment becomes stable, because the polar gaps on the sphere are filled by interpolation, and the irregular data are gridded regularly on a nominal torus surface. However, the interpolation errors and the insufficient information about the observable itself may cause some oscillations in the lower degrees from the spherical harmonics solution. Therefore, it is still important to evaluate regularization methods to solve the numerical ill-conditioned problems in the torus-based semi-analytical approach.

There exist several methods for numerically stabilizing the normal matrix inversion, such as the *Tikhonov* regularization (Tikhonov and Arsenin, 1977), the generalized ridge regression (Xu and Rummel, 1994), the conjugate gradient method (Hansen, 1992), and truncated singular value decomposition (TSVD) (Xu, 1998). An overview of these regularization methods applied to gravity field determination from satellite observations has been presented in Bouman and Koop (1998) and Ditmar et al. (2003b). Theoretically, these regularization methods lead to the same regularized normal equations, and they differ only in how the results are interpreted (Kusche and Klees, 2002). The *Tikhonov* regularization method will be applied in this thesis because the *a-priori* knowledge is normally provided in gravity field determination, which can be incorporated as one additional set of observations in the normal matrix.

5.4.1 *Tikhonov* regularization

The *Tikhonov* regularization minimizes the weighted norm of the errors and weighted norm of the unknowns simultaneously in a hybrid norm:

$$\min\{e^{\mathrm{T}}Pe + \alpha\kappa^{\mathrm{T}}\Re\kappa\}, \tag{5.31}$$

where α is the regularization factor and $\Re$ is a covariance matrix as a constraint.

Based on the minimization criterion, the *Tikhonov* regularization leads to a biased estimator $\hat{\kappa}_\alpha$:

$$\hat{\kappa}_\alpha = (H^{\mathrm{T}}PH + \alpha\Re)^{-1}(H^{\mathrm{T}}Pa) = N_\alpha^{-1}(H^{\mathrm{T}}Pa), \tag{5.32}$$

with N_α the regularized normal matrix.

Therefore, the *a-posteriori* variance-covariance matrix can be obtained as the inverse of the regularized normal matrix:

$$Q_{\hat{\kappa},\alpha} = N_\alpha{}^{-1}. \tag{5.33}$$

5.4.2 Overview of the regularization matrices

Apparently, there are two aspects involved in the *Tikhonov* regularization evaluation. The first aspect is the determination of an appropriate regularization matrix $\Re$ as an *a-priori* knowledge. An overview of a set of regularization matrices and their corresponding physical meanings has been given in Ditmar et al. (2003b).

The unit matrix. The simplest case is using the unit matrix I as the regularization matrix, which is also known as the zero-order *Tikhonov* regularization. This choice leads to a minimization of the disturbing potential near the Earth's surface.

First order and second order *Tikhonov* matrix. By analogy to the zero order *Tikhonov* regularization, the first order *Tikhonov* regularization minimizes the first order derivative of disturbing potential. The corresponding *Tikhonov* matrix is achieved as follows:

$$\Re_{ii} = l(l+1), \tag{5.34}$$

where the off-diagonal elements in the regularization matrix $\Re$ are all zeros.

Similar to the first order *Tikhonov* matrix, the second order *Tikhonov* matrix can be written as

$$\Re_{ii} = l^2(l+1)^2. \tag{5.35}$$

***Kaula*'s rule of thumb.** In gravity field determination, it is common practice to use the *a-priori* knowledge of degree variance models or an existing gravity field model. If the elements of the regularization matrix correspond to the inversion of *Kaula*'s rule of thumb in Equation (4.10), the regularization approach is called *Kaula* regularization:

$$\Re_{ii} = l^4. \tag{5.36}$$

The constant factor of 10^{10} is omitted in the matrix above and it will be incorporated in the regularization parameter α. Because both the second order *Tikhonov* matrix and *Kaula* regularization matrix contain a factor of l^4, these two matrices should have a similar behavior for the purpose of regularization.

5.4.3 Regularization factor determination

The second issue in regularization methods is the optimal determination of the regularization parameter α, which is a trade-off between the accuracy of the estimated parameters and the regularization constraints. A small regularization parameter (equivalent to a small amount of regularization) favors a good approximation to the least-squares solution, but the instability problem may still be not sufficiently reduced. A large regularization parameter constrains the observation noise but makes the solution more biased towards an *a-priori* knowledge. As far as *Tikhonov* regularization is concerned, there exists an estimate for the theoretically optimal value of α based on an *a-posteriori* selection criteria. The optimal factor can be determined by the L-curve criterion, the generalized cross-validation (GCV) method, and the minimum mean square error (MSE) approach, respectively.

Minimum mean square error (MSE). The MSE approach determines the regularization parameter α as the minimized solution of the expected squared norm of the difference between the regularized estimate $\hat{\kappa_\alpha}$ and the true value of κ:

$$\alpha_{mse} : \min E(\|\hat{\kappa}_\alpha - \kappa\|^2). \tag{5.37}$$

Xu (1992) derived the MSE as an estimate of the combination of a variance-covariance matrix $Q_{\hat{\kappa}_\alpha}$ and a squared norm of a bias vector $\mathrm{d}\kappa_\alpha = \hat{\kappa}_\alpha - \kappa$:

$$E(\|\hat{\kappa}_\alpha - \kappa\|^2) = \mathrm{trace}(Q_{\hat{\kappa}_\alpha}) + \mathrm{d}\kappa_\alpha^{\mathrm{T}}\mathrm{d}\kappa_\alpha. \tag{5.38}$$

In practice, it is impossible to compute the bias vector $\mathrm{d}\kappa_\alpha$ compared to the true solution κ, which is unknown. However, it can be obtained approximately by using the following equation:

$$\mathrm{d}\kappa_\alpha^{\mathrm{T}}\mathrm{d}\kappa_\alpha = \|(VH - I)\kappa_\alpha\|^2 \tag{5.39}$$

with $V = (H^{\mathrm{T}}PH + \alpha\Re)^{-1}H^{\mathrm{T}}P$.

The L-curve criterion. The most convenient graphic tool for the regularization factor determination is the so-called L-curve, which is a plot of the residual norm $\|H\kappa_\alpha - a\|$ versus the norm of the regularized solution $\|\hat{\kappa}_\alpha\|$ for all possible values of the regularization parameters. In this way, it clearly displays the compromise between minimizing these two quantities. The L-curve is normally plotted in log-log scale showing a characteristic L-shaped appearance with a distinct corner.

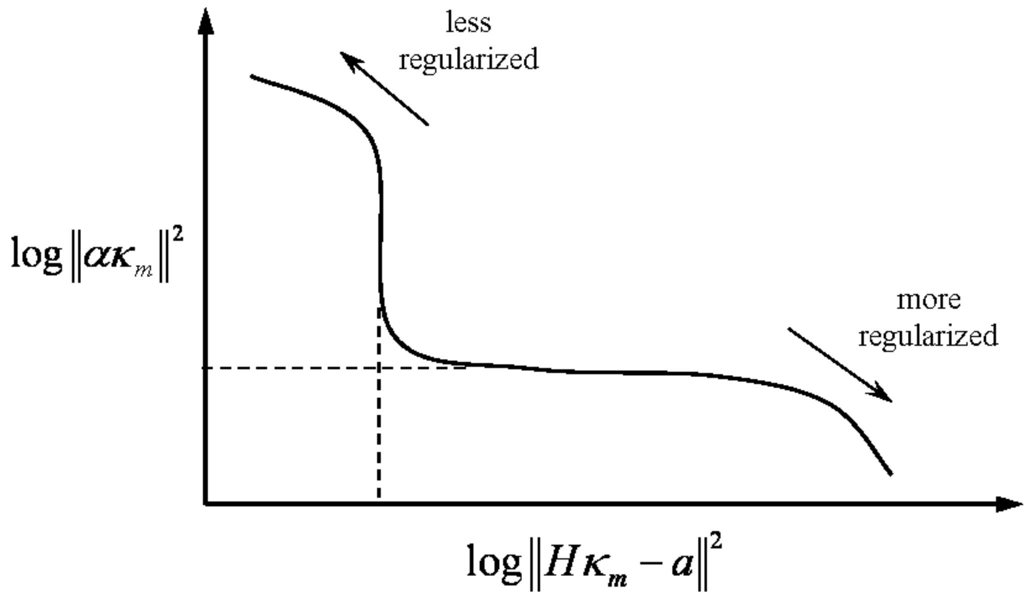

Figure 5.8: A general L-curve in log-log scale (Hansen, 1994)

The corner in the L-curve, which has the maximum curvature of the plot, separates the horizontal and vertical parts of the curve. The corner value is a balance between the residual norm and the norm of the regularized solution. Therefore, it can be used as the approximation of the optimal regularization parameter (Hansen and O'Leary, 1993). The L-curve criterion has been investigated by Kusche and Klees (2002) in the context of gravity field determination from satellite data. In their simulations, the L-curve criterion yields over-smoothed solutions. It should be used with care because of its sensitivity with respect to the choice of the norm of the residuals (Kusche and Klees, 2002).

Generalized cross validation (GCV). The GCV method is based on the statistical consideration that a good value of the regularization parameter should predict well missing data values. It is called the leave-out-one idea. More precisely, if an arbitrary element a_i of the observation vector a is left out, then the corresponding regularized solution should be able to predict this missing observation well (Golub and von Matt, 1997). The regularization factor minimizes the weighted sum of the squares of the residuals divided by a quantity containing the trace of the inversion of the normal matrix. Under this definition, the parameter α_{gcv} is the minimization solution of the GCV function:

$$\alpha_{\text{gcv}} : \min \frac{n\|H\kappa_\alpha - a\|^2}{(\text{trace}(E - Q_\alpha))^2}, \tag{5.40}$$

with n the number of unknowns, E the unit matrix and Q_α the inversion of regularized normal matrix N_α.

By comparing the performance of regularization parameter determination by the L-curve criterion and the GCV method in the context of satellite gravity gradient observations, Kusche and Klees (2002) concluded that the GCV method outperforms the L-curve criterion, because the GCV method provides a good approximation for the optimal regularization parameter, and the L-curve criterion leads to over-smoothed solutions.

5.4.4 Examples of regularization techniques

The application of regularization techniques in the order-wise least-squares adjustment of the torus-based approach has not been done before. Tests should be done to find the best regularization techniques for this adjustment, including choice of regularization matrix and determination of regularization factor. Therefore, the first example compares the performance of different regularization matrices, i.e., the unit matrix, the first and second order *Tikhonov* matrix, and the *Kaula* matrix. Simulated observations of the V_{zz} gravity gradient tensor radial component on the nominal orbit from "GOCE data set I" were processed. The pseudo-observables (the lumped coefficients) were obtained through the first and second steps of the recovery approach (Figure 3.5). Then, the next step is to solve the spherical harmonic coefficients up to degree $L = 120$ of the linear system by weighted least-squares inversion (Section 5.3).

The optimal regularization factors in this example are determined by the MSE method for each individual regularization matrix. The reference gravity field is the OSU91A model. Without regularization (curve in red), the estimated coefficients at low degrees ($l < 60$) have a very large oscillation as shown in Figure 5.9. The oscillation can be caused by either the observable V_{zz} itself having insufficient gravity information or the errors, e.g., observation errors or interpolation errors, in the polar areas; See 4.4.5. This oscillation should be corrected by a proper regularization procedure. The situation is demonstrated also in Figure

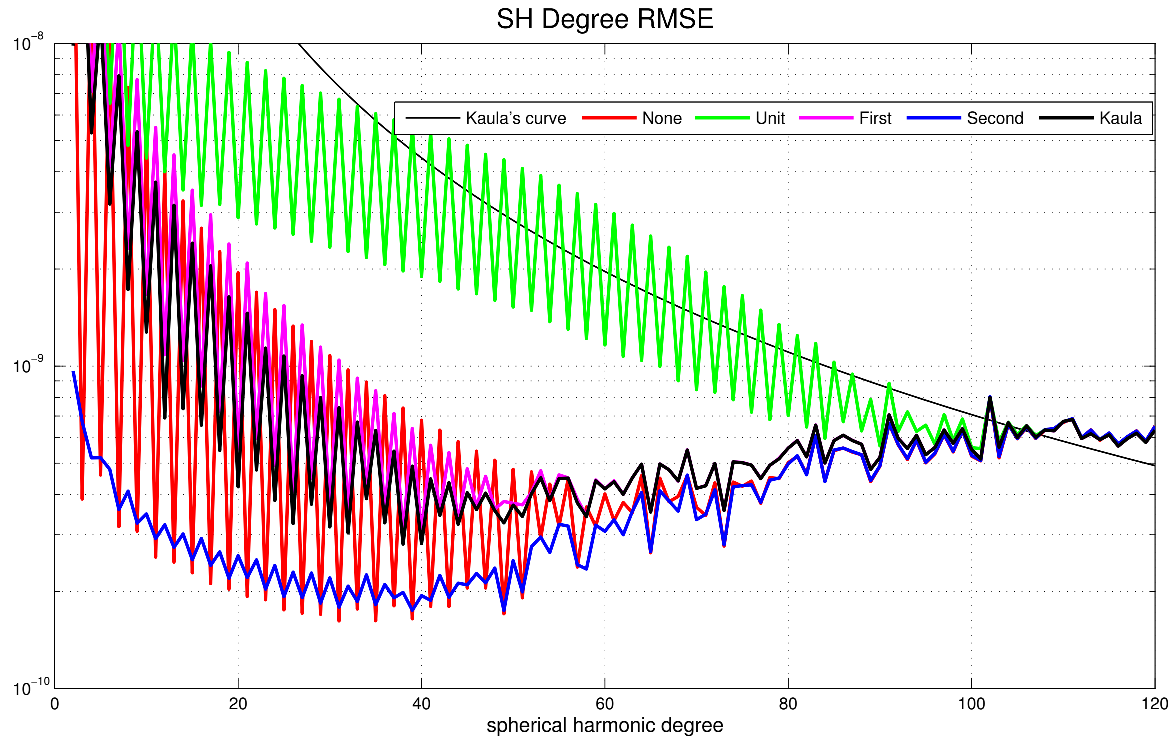

Figure 5.9: Degree RMSE of the regularized solutions by different regularization matrices up to $L = 120$, compared to the OSU91A model

5.10, where the condition numbers of the normal matrix for individual orders are calculated. For orders $m < 8$, the condition numbers before regularization are very big leading to an unstable inversion. By applying regularization, the condition numbers are reduced and the inversion becomes stable. Although the condition numbers of orders $m > 8$ are smaller, regularization still is necessarily applied to reduce the oscillations in the non-regularized solution.

Another demonstration to show the regularization effects is from the spectral perspective. Compared to the OSU91A reference field, the 2D spherical harmonic error spectrum can be calculated by Equation (4.2) and plotted in Figure 5.11. It shows also that the low order coefficients are affected by the instability problem of the order-wise normal matrices. The first order *Tikhonov* matrix regularized solution still has large error spectra in the very low orders, e.g., $m < 8$, however, the regularized solutions by the *Tikhonov* matrix and the *Kaula* regularization matrix reduce the errors in these orders.

In Figure 5.9, the unit regularization matrix (curve in green) gives a worse degree RMSE

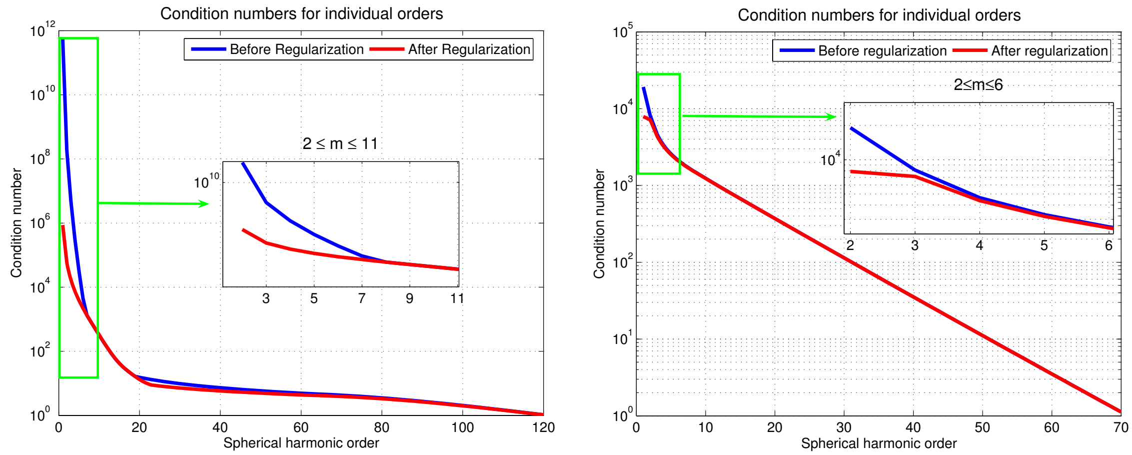

(a) V_{zz} gravity gradient tensor component (b) Disturbing potential V

Figure 5.10: Condition numbers of the normal matrix for individual orders m before and after regularization

curve, while the first order *Tikhonov* matrix (curve in Magenta) and the *Kaula* regularization matrix (curve in black) decrease the oscillation in the low degrees. This indicates that the regularization matrix with information related to the degree l works better for the order-wise estimation. However, none of them provide better results than the non-regularized solution in the high degrees $80 < l < 120$ because the normal matrices are very stable for the orders $80 < m < 120$ (Figure 5.10(a)). Although the second order *Tikhonov* matrix (curve in blue) does not perform better than the non-regularized solution in the low odd degrees $(20 < l < 30)$, it significantly reduces the oscillation and overall gives a better overall result. The RMS values in terms of the geoid height differences for the regularization matrices are compared to the reference model, and summarized in Table 5.1.

Table 5.1: The STD values of the regularized solutions in the evaluation of the regularization matrices up to $L = 120$, compared to the OSU91A model

method	non-regularized	unit	first order *Tikhonov*	second order *Tikhonov*	Kaula
STD (m)	3.00	9.50	2.96	0.38	2.17

Since the spherical harmonic coefficients are estimated by the order-wise least-squares

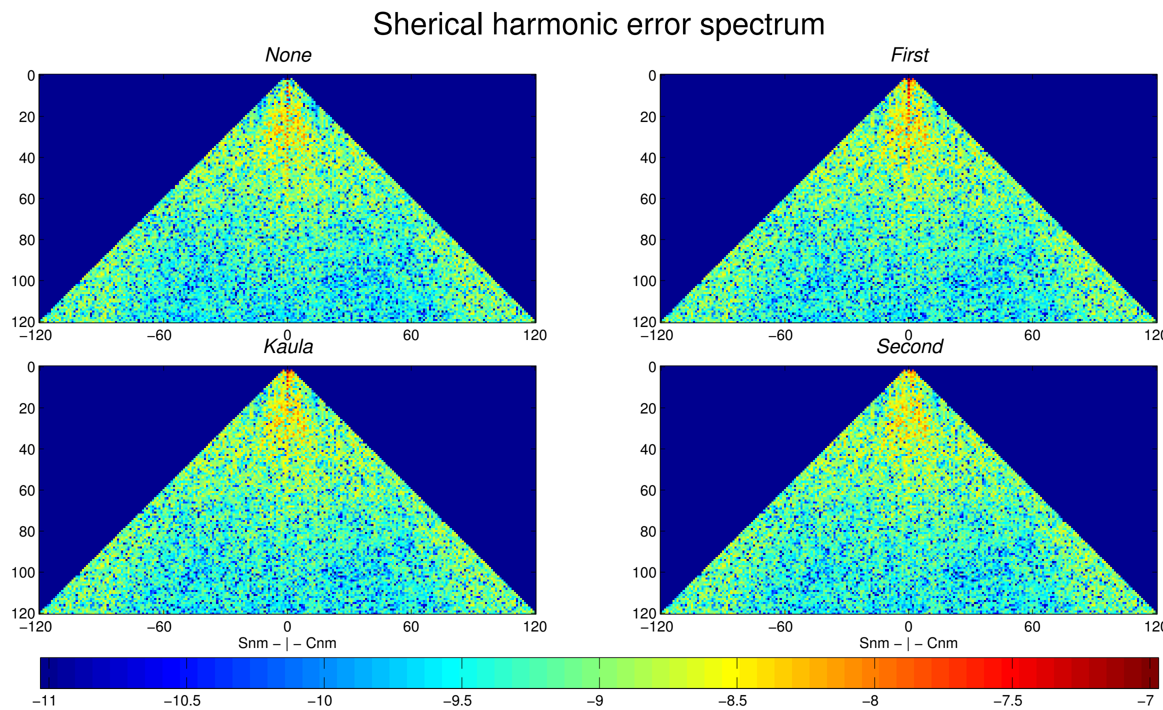

Figure 5.11: Spherical harmonic error spectrum of the regularized solutions by different regularization matrices, compared to the OSU91A reference model

adjustment, the regularization factors are correspondingly calculated for individual orders. Figure 5.12 shows the regularization factor as a function of the order for the second order *Tikhonov* matrix (curve in blue) and the *Kaula* matrix (curve in black). Note that the scales are different on the left for the *Tikhonov* matrix with 10^5 and on the right for the *Kaula* matrix with 10^7. The values of the regularization factor in the second order *Tikhonov* matrix are two order of magnitude smaller than the values in the *Kaula* matrix, which means the *Kaula* matrix regularized solution is more constrained and the choice of the *Kaula* is more sensitive to the nearly ill-conditioned matrix. However, both matrices show a similar pattern of the regularization factor, which is larger at the low degrees and smaller at the high degrees.

The second example compares the performance of the regularization factors computed by different ways, i.e., the MSE approach, the L-curve criterion, and the GCV method, using the same data set mentioned in the first example. Because the second order *Tikhonov* matrix works better than the other regularization constraints (Figure 5.9), it is selected as

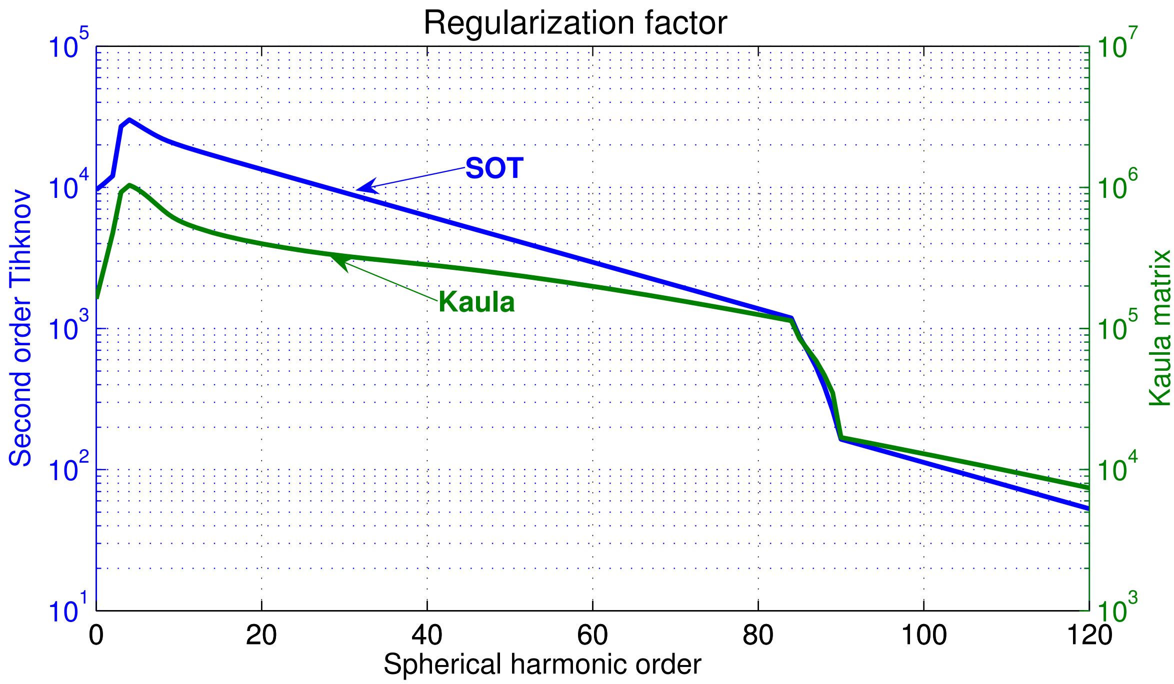

Figure 5.12: Regularization factors of the second-order *Tikhonov* and *Kaula* regularization solutions for individual orders

the regularization matrix for all determination factor approaches in this example. After applying the regularized least-squares adjustment, the degree RMSE curves estimated by different regularization factors are plotted in Figure 5.13.

The regularized solutions all reduce the oscillations of the non-regularized solution in the low degrees. The degree RMSE calculated from the L-curve criterion (curve in magenta), and the GCV method (curve in green) improve the accuracy of every degree, especially for the degrees $20 < l < 50$. However, both solutions still have small oscillations for degrees lower than $l = 10$. Therefore, these two methods do not provide the best overall solution in terms of the STD values, shown in Table 5.2. The MSE solution (curve in blue) shows a smoother degree RMSE curve and provides the best overall solution with the smallest STD value. The curve in black is the solution by fixing the regularization factor as 1×10^4. It is an empirical value from several trial-and-error tests, and it also reduces the oscillation in the non-regularized solution.

Again, the 2D spherical harmonic error spectrum of the regularized solutions from different factor determination methods are calculated by the comparison of the OSU91A ref-

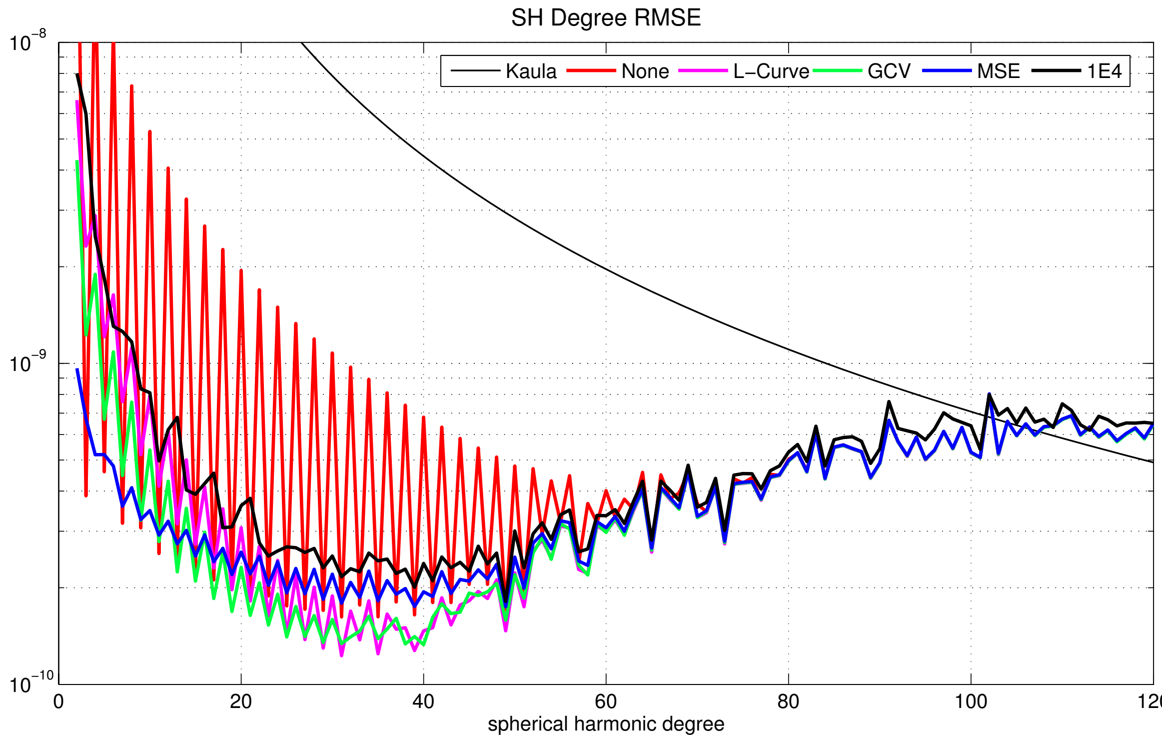

Figure 5.13: Degree RMSE of the regularized solutions by different regularization factor determination methods, compared to the OSU91A model

erence field using Equation (4.2) and plotted in Figure 5.14. The regularized solutions from the MSE approach, the L-curve criterion, and the GCV method have smaller error spectra, compared to the non-regularized solution. The MSE approach regularized solution leads to the smoothest 2D error spectrum.

Therefore, for the processing of the gravity gradient tensor data in Chapter 6, the MSE approach will be preferred to determine the regularization factor in the regularized solution to obtain a better overall solution. The L-curve criterion and GCV method will be the alternative choices for the solutions focusing on $20 < l < L$.

Table 5.2: The STD values of the regularized solutions in the determination of the regularization factor up to $L = 120$, compared to the OSU91A model

method	non-regularized	1×10^4	L-curve	GCV	MSE
STD (m)	3.00	0.57	0.61	0.49	0.38

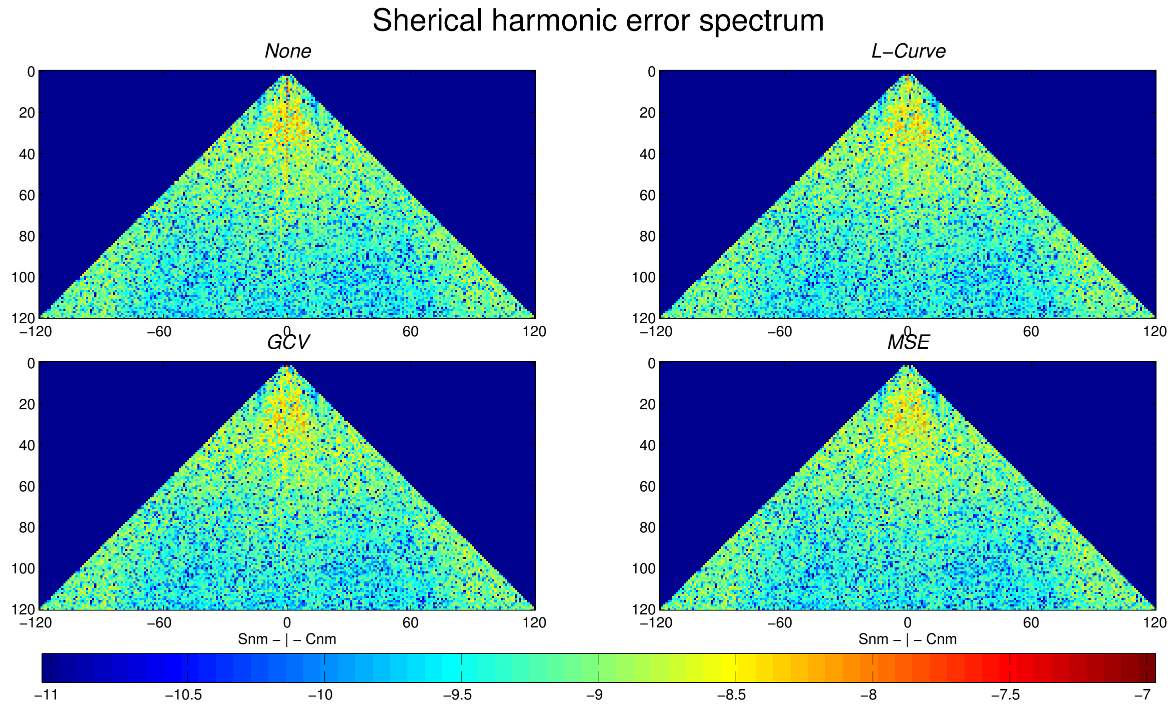

Figure 5.14: Spherical harmonic error spectrum of the regularized solutions by different regularization factor determination methods, compared to the OSU91A reference model

The corresponding regularization factors, which are dependent on the spherical harmonic orders, are plotted in Figure 5.15. The factors determined by the MSE method become smaller for bigger orders. However, these factors are almost two orders of magnitude bigger than the ones from GCV and L-CURVE in the low orders, where the normal matrices need to be regularized. Therefore, the MSE method are more sensitive to the choice of the regularization factors and the corresponding regularized solutions are more constrained. The factors calculated from the L-curve criterion are almost constant except for the very low orders. From $20 < l < 40$, the factors from the GCV method have almost the same values of the L-curve criterion, while in the range of $50 < l < L$, the GCV factors are identical to the MSE approach. The performance of the GCV method explains why it can be the alternative choice for $20 < l < L$.

The final example is studying the regularization techniques on disturbing potential. The data used are the disturbing potential observations in June 2003 from the CHAMP mission; see Section 2.2.2. The CHAMP satellite went through a repeat orbit mode in this month,

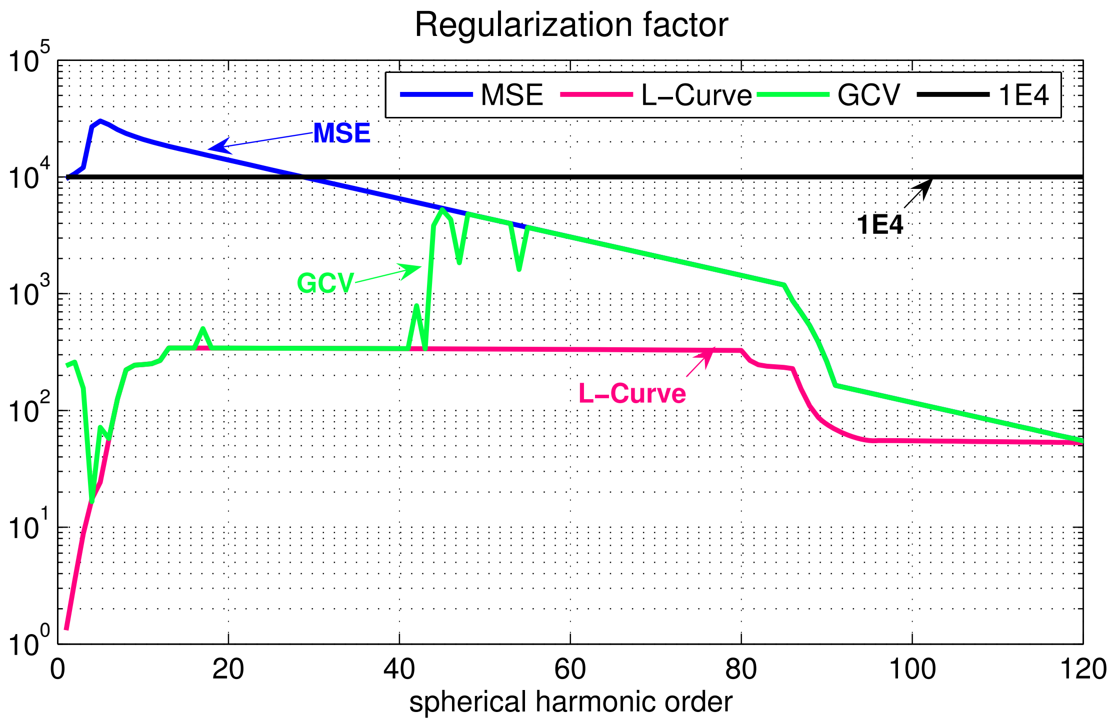

Figure 5.15: **Regularization factors of different regularization factor determination methods for individual orders**

and the non-regularized solution has a very low accuracy; see Section 4.5.4. Therefore, the example tries to test how much the regularized solution can improve the estimation. The spherical harmonic coefficients are estimated up to $L = 70$. Figure 5.16(a) shows the comparisons of the estimated results from the non-regularized (thin black solid line) and regularized solutions (thick gray dashed line). There are almost no differences between these two solutions, which indicates that the normal matrix in this least-squares adjustment is stable. This situation is also demonstrated in Figure 5.10(b), where the condition numbers are almost identical except before and after regularization for orders $m \leq 6$. Figure 5.16(b) is the corresponding regularization factor for the individual degrees. The value of the factor decreases quickly as the degree increases and becomes relatively small for degrees $l > 6$. This example demonstrates that regularization of the disturbing potential data processing is not necessary. There are two reasons for this: on the one hand, the observation errors and interpolation errors are homogeneously distributed (no polar gap problems); on the other hand, the maximum resolvable degree is only around 70 from the CHAMP mission (Weigelt, 2006); see Section 6.2.1.

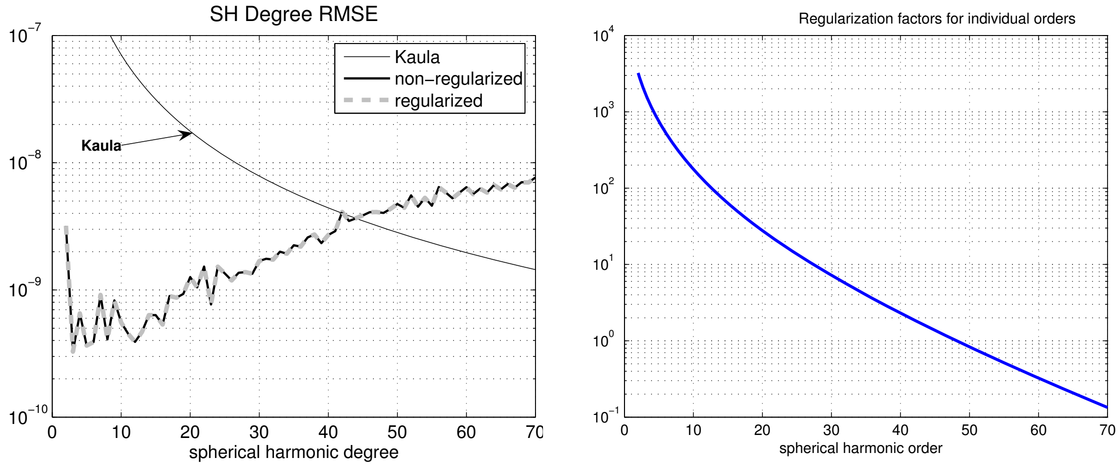

(a) Degree RMSE of the non-regularized and regularized solutions

(b) Regularization factors for different orders

Figure 5.16: Example of regularization technique in the processing of the disturbing potential data

The regularization examples show that proper selection of the regularization matrix and optimal determination of the regularization factor can cope with a near ill-conditioned problem of the normal matrix in least-squares adjustment, especially for the gravity gradient tensor observations. The first example illustrates that a degree-dependent constraint, such as the second order *Tikhonov* matrix or the *Kaula* matrix, works as a better regularization matrix, because it provides constraint information related to spherical harmonic degrees. In the second example, the MSE method, the L-curve criterion, and the GCV approach have been employed to determine the regularization factor. For the particular scenario in the second example, the MSE method and the GCV approach outperform the L-curve criterion and yield better regularized solutions in terms of STD values of geoid height error. This statement is in agreement with the conclusion drawn by Kusche and Klees (2002) on the regularization of gravity field determination from satellite gravity gradients. The last example shows that regularization technique is not necessary for the processing of disturbing potential.

5.5 Optimal weighting methods

Individual gravity field missions cover only certain spatial resolutions because of their practical implementations and prospective target goals. Therefore, the stand-alone solution from SST disturbing potential observations is more sensitive to the low degrees, e.g., $l < 50$, while the SGG tensor better resolves the high frequencies of the Earth's gravity. In order to cover the whole gravity field spectrum, a combined solution is preferred. To achieve this goal, the normal matrices from SST and SGG data are merged in a combined least-squares adjustment.

The multi-observable model in least-squares adjustment is the simplest way to make the combination by adding up the normal matrix from each data set; see Section 5.2.4. However, this merged matrix does not necessarily provide a better solution because the combination does not take the accuracies of different observations into account, especially for the individual orders. Therefore, it is better to determine an optimal weighting factor w_i for each data set based on the observation accuracies. Optimum weighting means to apply the proper weights for the SST and SGG components to get a better solution. Because the normal matrix has an order-wise block diagonal structure, the optimal weighting factor w_i has to be estimated correspondingly for each order m in the least-squares adjustment as well.

The combined SST and SGG least-squares solution with assumed optimal weighting factors w_{SST} and w_{SGG} for a specific order m is given in a general formula as follows:

$$\begin{aligned} \hat{\kappa}_{\mathrm{opt}} &= \left(\sum_i w_i {H_i}^{\mathrm{T}} P_i H_i\right)^{-1} \left(\sum_i w_i {H_i}^{\mathrm{T}} P_i a_i\right) \\ i &= \mathrm{SST}, \mathrm{SGG} \end{aligned} \tag{5.41}$$

Since the optimal weight factors w_{SST} and w_{SGG} are unknown in general, they have to be estimated from the pseudo-observable (the lumped coefficient), in the linear system illustrated in Equation (3.14b). The estimation depends on the *a-priori* accuracies of the given observations. The more accurate a group of observations, the higher the particular weight, and the higher the influence of this group on the parameter estimation. Two approaches for the optimal weight estimation, i.e., the parametric covariance approach and variance components approach, have been studied in the combination of the SST and SGG data by Koch and Kusche (2002) and Pail and Plank (2002), respectively. These two weighting methods are investigated in the following sections.

5.5.1 Parametric covariance approach

The parametric covariance approach originally was developed by Lerch (1989). It is based on a comparison of the parameter differences between the individual solutions and the joint solution, leading to a calibration factor q_i:

$$q_i = \frac{(\hat{\kappa}_i - \hat{\kappa}_{\mathrm{opt}})^{\mathrm{T}}(\hat{\kappa}_i - \hat{\kappa}_{\mathrm{opt}})}{\mathrm{trace}\left[(N_{\mathrm{opt}})^{-1} - (N_i)^{-1}\right]}, \tag{5.42}$$

in which the normal matrices from the combined and from each stand-alone solution are calculated as follows:

$$\begin{aligned} N_{\mathrm{opt}} &= \sum_i w^i {H_i}^{\mathrm{T}} P_i H_i; \\ N_i &= w_i {H_i}^{\mathrm{T}} P_i H_i. \end{aligned} \tag{5.43}$$

Starting with the initial values of $w_i = 1$ for both SST and SGG, the updated weights w_i^* can be obtained iteratively by re-scaling the variances with the calibration factor q_i for each observation group:

$$w_i^* = \frac{w_i}{q_i}. \tag{5.44}$$

Compared with the previous weighting factor w_i, under a threshold criterion, e.g., the relative accuracy between old and updated weights $\frac{|w_i^* - w_i|}{w_i} \leq 10^{-8}$, the calculation will normally converge after a couple of iterations. After the convergence, the final values of the weights w_{SST} and w_{SGG} are introduced into Equation (5.41) to get the optimal joint solution.

5.5.2 Variance components estimation approach

Koch and Kusche (2002) determined the optimal weights by introducing reciprocal values of the estimated variance components, i.e., $w_i = \frac{1}{\hat{\sigma}_i{}^2}$ in Equation (5.41). Starting with the initial value of ${\sigma_i}^2 = 1$ for each group, the *a-posteriori* variance components can be iteratively estimated by

$$\hat{\sigma}_i^{*2} = \frac{{\hat{\varepsilon}_i}^{\mathrm{T}} \hat{\varepsilon}_i}{\tau_i}. \tag{5.45}$$

The residual vector ε_i can be determined by a linear observation system with approximate values of the combined solution $\hat{\kappa}_{\text{opt}}$ as

$$\hat{\varepsilon}_i = H_i \hat{\kappa}_{\text{opt}} - a_i. \tag{5.46}$$

The partial redundancies τ_i for different types of observations can be calculated by

$$\tau_i = (2L+1) - \text{trace}\left(\frac{N_i}{N_{\text{opt}}}\right), \tag{5.47}$$

where $2L+1$ represents the number of observations a for each order m in the linear system Equation (5.10). The normal matrices N_{i} and N_{opt} can be computed in the same way as Equation (5.43).

After calculating the posterior variance components $\hat{\sigma}_i^{*2}$, the updated weighting factors are determined by

$$w_i^* = \frac{w_i}{\hat{\sigma}_i^{*2}}. \tag{5.48}$$

Similar to the procedure in the parametric variance approach, the calculating scheme of the variance component estimation approach also works iteratively. Starting from an initial value of one, the weighting factor for each observation group will normally converge after several iterations to fulfill a certain threshold criterion.

Note that regularization can be employed also in the stand-alone solutions when determining the optimal weights, which will be demonstrated in the complete calculating flow chart in Figure 6.21. Consequently, the combined solution in equation (5.41) can be modified as follows:

$$\hat{\kappa}_{\text{opt}} = \left(\sum_i w_i ({H_i}^{\text{T}} P_i H_i + \alpha_i \Re_i)\right)^{-1} \left(\sum_i w_i {H_i}^{\text{T}} P_i a_i\right). \tag{5.49}$$

with the regularized normal matrices from the combined and from each stand-alone solution:

$$\begin{aligned} N_{\text{opt}} &= \sum_i w^i \left({H_i}^{\text{T}} P_i H_i + \alpha_i \Re_i\right); \\ N_i^{\alpha} &= w_i \left({H_i}^{\text{T}} P_i H_i + \alpha_i \Re_i\right). \end{aligned} \tag{5.50}$$

5.5.3 Examples of the combined solutions from SST and SGG

To compare the determination of the optimal weighting factor by the two aforementioned approaches, two stand-alone solutions from the SST disturbing potential data of the CHAMP mission in January 2003 and the simulated *in situ* gravity gradient tensor V_{zz} data (SGG) from the "GOCE data set I" are merged to obtain a combined solution. Although, in a way, these two data sets are un-combinable because the SST data are measured in the "real world," while the SGG data are generated from a "simulated world." The purpose here is to demonstrate the principles of the two weighting approaches for combining the SST and SGG data (Xu et al., 2006a).

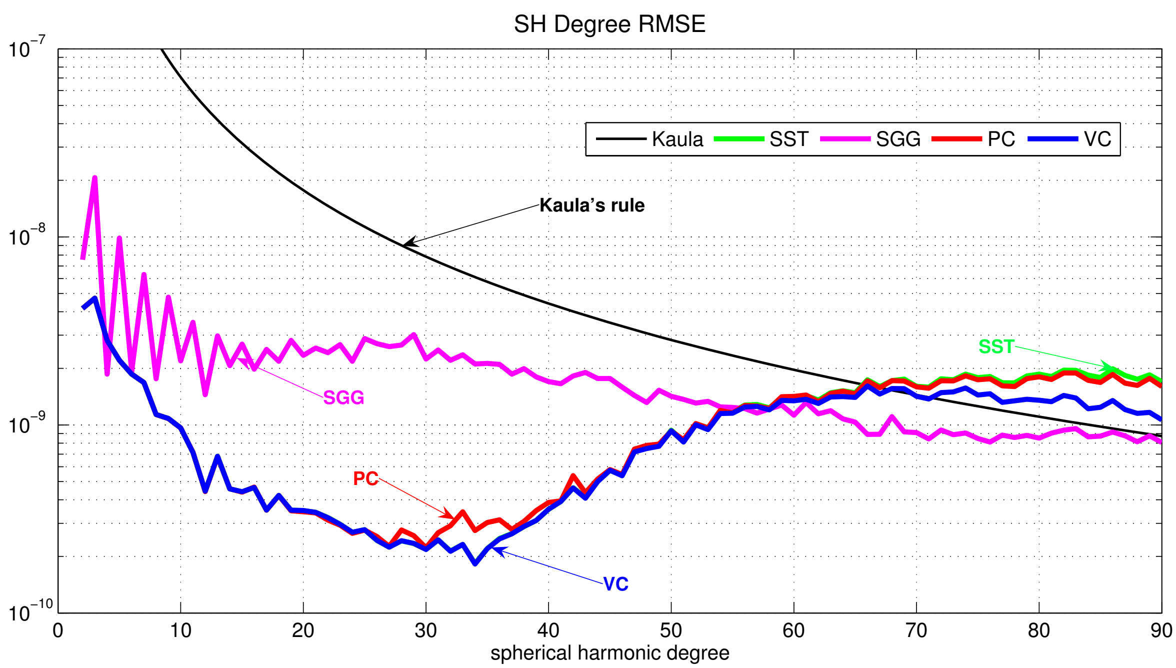

Figure 5.17: Degree RMSE of the stand-alone and combined solution from SST and SGG up to $L = 90$ compared to the GGM02S model

Figure 5.17 shows the degree RMSE cures from two stand-alone solutions and two joint solutions up to degree $L = 90$, where "VC" stands for the variance components approach and "PC" stands for the parametric covariance approach. The reference gravity field for comparison is the GGM02S model. As discussed before, the SST solution (green) better resolves the low degrees and is crossing the *Kaula* curve (black) around $l = 60$ while the SGG solution (magenta) is oscillating in the low degrees, e.g., $l < 40$, and performs better in high degrees. By determining the relative weighting factors for each order m, both joint solutions from PC (red) and VC (blue) merge two stand-alone solutions with better accuracies. In general, PC is very close to the SST-only solution and is influenced by the SGG-only solution only a little. VC yields a better solution. It reduces the oscillations from the SGG-alone solution in the low degrees by adding the information from the SST-only solution, and it moves close to the SGG-alone solution in the high degrees.

For the purpose of reducing the oscillation effect, the optimal weighting methods can therefore be treated as a way of regularization by adding additional information into the normal matrix (Kusche and Klees, 2002).

In order to examine how much each of the SST and SGG sets contributes to the combined solution, the relative weights between these two data sets, i.e., the ratios of w_{SST}/w_{SGG}, for the individual orders m are calculated in a scale of $\log_{10}$ (Figure 5.18). By comparing these two plots, most of the relative weights in PC are contributed by the SST data, while in the estimation by VC, SST dominates the long wavelength parts ($l < 60$), and SGG takes the leading role in the high frequency parts ($l > 60$).

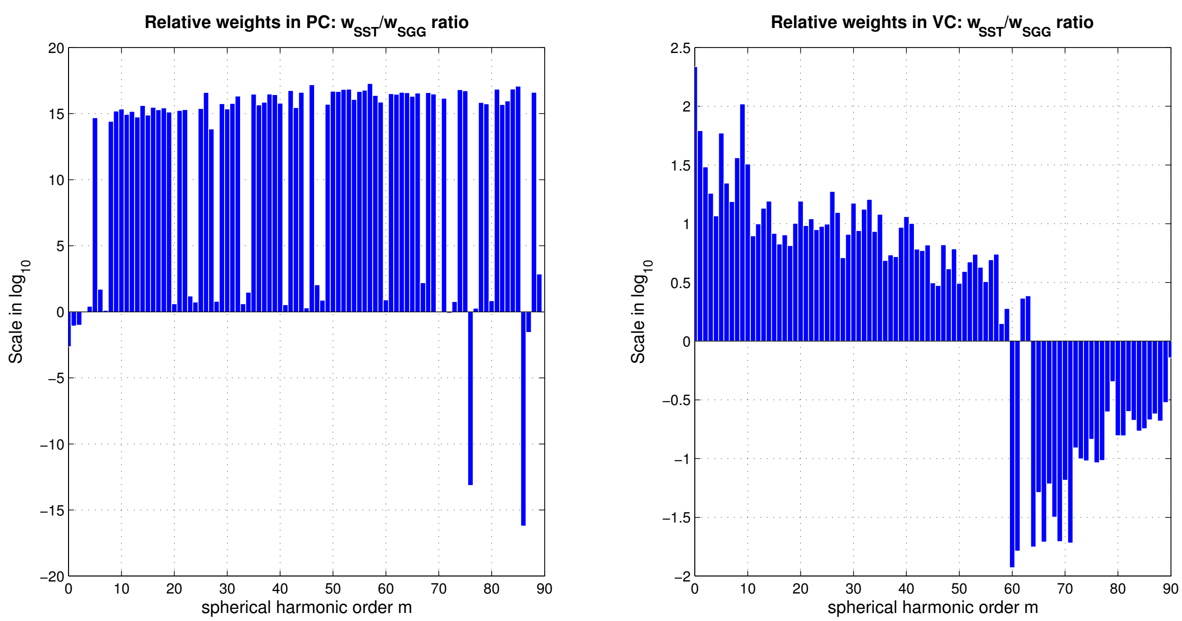

Figure 5.18: Relative weight ratios of individual orders between SST and SGG by PC and VC up to $L = 90$

The quantitative analysis of the standard deviations and the accumulative geoid height

RMS values is summarized in Table (5.3). Together with Figure 5.18, it shows that the estimation by VC works better than PC in terms of the degree RMSE, the relative weight ratios between SST and SGG, and the RMS values of the geoid height differences. The reason is that the denominator q_i in Equation (5.44) is close to zero sometimes, leading the updated weight w_i^* towards infinite and hardly reaching the threshold values. It is consistent with the statement that the PC technique is not designed for calibration of distinct data types where they do not overlap in signal bandwidth by Lemoine et al. (1998).

Table 5.3: Characteristics of the stand-alone and combined solutions from SST and SGG, compared to the GGM02S model

$L = 90$	RMS in [m]	RMS of geoid in [m]
SST	0.739	0.653
SGG	2.365	0.749
PC	0.760	0.634
VC	0.642	0.558

5.6 Updated solutions by an iteration scheme

The fast numerical algorithm of the *Fourier* transform is built under a nominal orbit assumption. In addition, the interpolation on a torus grid introduces interpolation errors. Therefore, the estimated spherical harmonic coefficients certainly do not provide an exact solution from the *in situ* observations. Since the transfer coefficients linearly connect the lumped coefficients and the spherical harmonics, the estimated solution from the initial approximations can be improved and corrected by iteration (Klees et al., 2000).

5.6.1 A developed iteration scheme

A torus-based iteration scheme is developed in Figure 5.19. The key point in the iterative calculations is to update the observations, on the same nominal torus grid, which are now determined by the *i*th latest estimated spherical harmonic coefficients in a synthesis way. There are two ways to reach this goal. The first way is synthesizing a time series of observations along the orbital trajectory; see Section 4.3.2. Then, the interpolation method has to be applied to compute the grid values. The second choice is gravity field synthesis on the torus grid directly. Both orbit synthesis and torus synthesis have their advantages and drawbacks. The former is closer to the original orbit, but interpolation will introduce errors again. Although the latter avoids the additional errors, the direct synthesized grid may not improve the updated solutions because the changes of the grid values are very small.

After the updated grid is available, the difference between these newly computed observations and the old grid observations δgrid^i is used as a new input for the FFT technique to get the corrections of the lumped coefficient, δa^i. The small corrections are treated as a new observation for the order-wise least-squares adjustment, where the design matrix H and the weight matrix P in Equation (5.10) are the same as what they are in the ith solution, and only the observation vector is changed to the new pseudo-observable δa^i.

$$\delta\hat{\kappa}^i = (H^{\mathrm{T}}PH)^{-1}(H^{\mathrm{T}}P\delta a^i), \tag{5.51}$$

After least-squares adjustment, the newly solved spherical harmonics corrections $\delta\hat{\kappa}^i$ in a matrix format, are added to the coefficients that were calculated in the previous solution:

$$\bar{\kappa}^{i+1} = \bar{\kappa}^i + \delta\bar{\kappa}^i. \tag{5.52}$$

The updated estimated spherical harmonic coefficients $\bar{\kappa}^{i+1}$ will yield an improvement of the Earth's gravity field. This procedure is stopped when the gravity field solution converges to insignificant improvement from $\delta\bar{\kappa}^i$.

5.6.2 Examples of iterative solutions

One example to demonstrate the iteration scheme is the iterative monthly solutions of June 2003 from the CHAMP mission. Since the ground track pattern is close to a repeat orbit scenario (Section 4.5.4), the interpolation error is the dominant factor for the spherical harmonic solutions. Iteration is expected to reduce the interpolation error and increase the accuracy of the solution. Particularly with the orbital synthesis in each iteration, the degree RMSE curves for each iterative result are plotted in Figure 5.20. The curve in blue is the RMSE of the original estimated solution. The iterative solutions (dot curve in green) bring the error curves down slowly, especially in the high degrees. The fourth iteration (curve in red) is getting very close to the third one, and the solution is considered convergent.

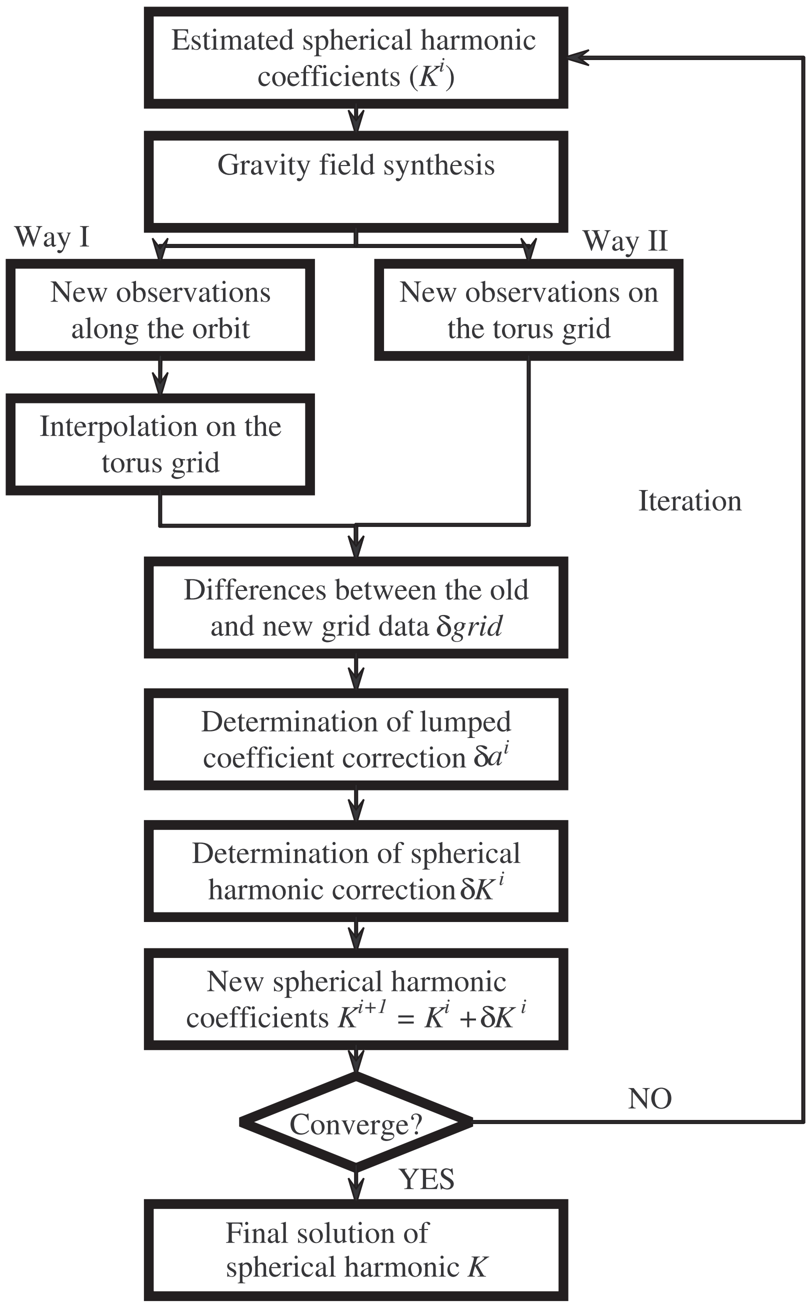

Figure 5.19: Calculating flow chart of the torus-based iteration scheme

5.7 Summary

IN THIS chapter, the final spherical harmonic solutions $\hat{\bar{K}}_{lm}$ have been estimated from the lumped coefficients A_{mk} by the order-wise least-squares adjustment.

The linear mapping factor is the transfer coefficient, whose collections build up the

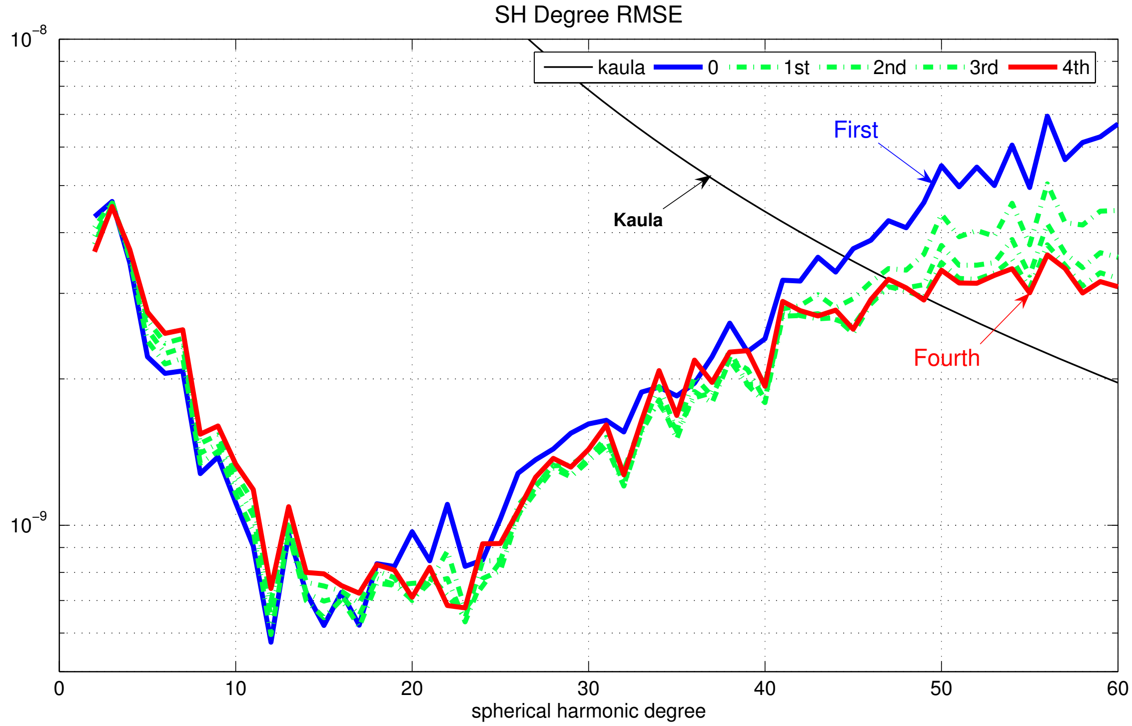

Figure 5.20: Degree RMSE of the four iterative solutions from the CHAMP mission in June 2003, compared to the GGM02S model

PG. The transfer coefficients for gravity gradient tensor components, the GRACE-type LOS gradiometry, and even the future satellite flying formation observables are discussed.

The maximum size of the normal matrix in the order-wise least-squares adjustment is $\frac{1}{2}(L-|m|+1) \times \frac{1}{2}(L-|m|+1)$, which dramatically decreases the computational time and memory requirement. The overall solution is obtained from the monthly solutions by the multi-observable model.

A simplified PSD model is designed based on the GOCE error budget. A weight matrix for a specific observation A_{mk} is developed by calculating the variance from the error PSD according to the corresponding orbital frequency f_{mk}. After least-squares adjustment, the error information of the estimated coefficients can be propagated to spectral and spatial representations by the variance propagation law.

Since an *a-priori* gravity field model is always available, the *Tikhonov* regularization technique is employed for the ill-conditioned problem in gravity field determination. For the first time, the application of regularization techniques in the order-wise least-squares adjustment has been investigated. The regularized solutions from the observable V_{zz} show that a degree-dependent constraint works better as a regularization matrix. In the example of the regularization factor determination, the MSE method and the GCV approach outperform the L-curve criterion and yield better regularized solutions in terms of geoid height error STD values. The MSE method provides the best overall solution, while the GCV approach gives a significant improvement for degrees $20 < l < 40$. The test examples also show that there is no difference between non-regularized and regularized solutions for the disturbing potential data processing, which means the regularization technique is not necessary in this case.

A combined solution with assigned weights for individual SST and SGG solutions has been studied. Both the PC and VC approaches are employed to determine the optimal weighting factors. For the particular example, the latter performs better than the former in terms of the degree RMSE values and the relative weight ratios.

The development of the torus-based iteration scheme focuses on the updated values of the torus grid. The estimated solutions can be improved slightly in the high degrees by the iterative scheme for the compensation of interpolation errors and theoretical approximations, and the estimation will converge after $4-5$ iterations.

Chapter 6

Case studies with simulated and real data from spaceborne gravimetry

THE previous chapters covered the necessary knowledge in sufficient detail for the torus-based semi-analytical approach of gravity field determination. For instance, Chapter 3 presented the mathematical theory and the calculating flow chart, Chapter 4 addressed the critical issues in deriving the lumped coefficients from the *in situ* observations, and Chapter 5 discussed the spherical harmonic coefficients estimation using least-squares adjustment. By means of numerous case studies, this chapter will focus on applying this complete processing procedure to determine the Earth's gravity field from spaceborne gravimetry observations. It is organized into three main sections. For the purpose of assessing the feasibility, flexibility, and efficiency of the torus-based approach, Section 6.1 compares this approach with the direct approach in the context of disturbing potential V and gravity gradient V_{zz} data processing. Several geo-potential observables, i.e., disturbing potential from CHAMP and GRACE, GRACE-type LOS gradiometry, and gravity gradient tensor from GOCE, are processed individually as stand-alone solutions in Section 6.2. Section 6.3 will investigate the combined solutions from different combination scenarios using optimal weighting methods. A complete and comprehensive calculating procedure, including practical considerations at each step, is recommended for gravity field determination.

6.1 Comparison of the direct approach and the torus-based approach

As discussed in the theoretical comparison of different gravity field determination approaches (Section 3.2.5), the direct (brute-force) approach is theoretically the most robust and accurate solution because no assumptions and no approximations are involved. In addition, it is the only method providing a fully populated *a-posteriori* variance-covariance matrix. However, it demands enormous computational time and very high memory storage. The performance comparison between the direct approach and the torus-based semi-analytical approach is carried out in order to show that the latter is an alternative, feasible, and efficient tool for gravity field recovery from spaceborne gravimetry observations.

6.1.1 Disturbing potential V from SST-hl

The first comparison is the processing of the disturbing potential data, which were collected in June 2003 and January 2004 from the CHAMP mission (sampling rate 30 s). The number of measurements is less than 86400 because of missing data. The maximum resolvable degree is taken as $L = 70$.

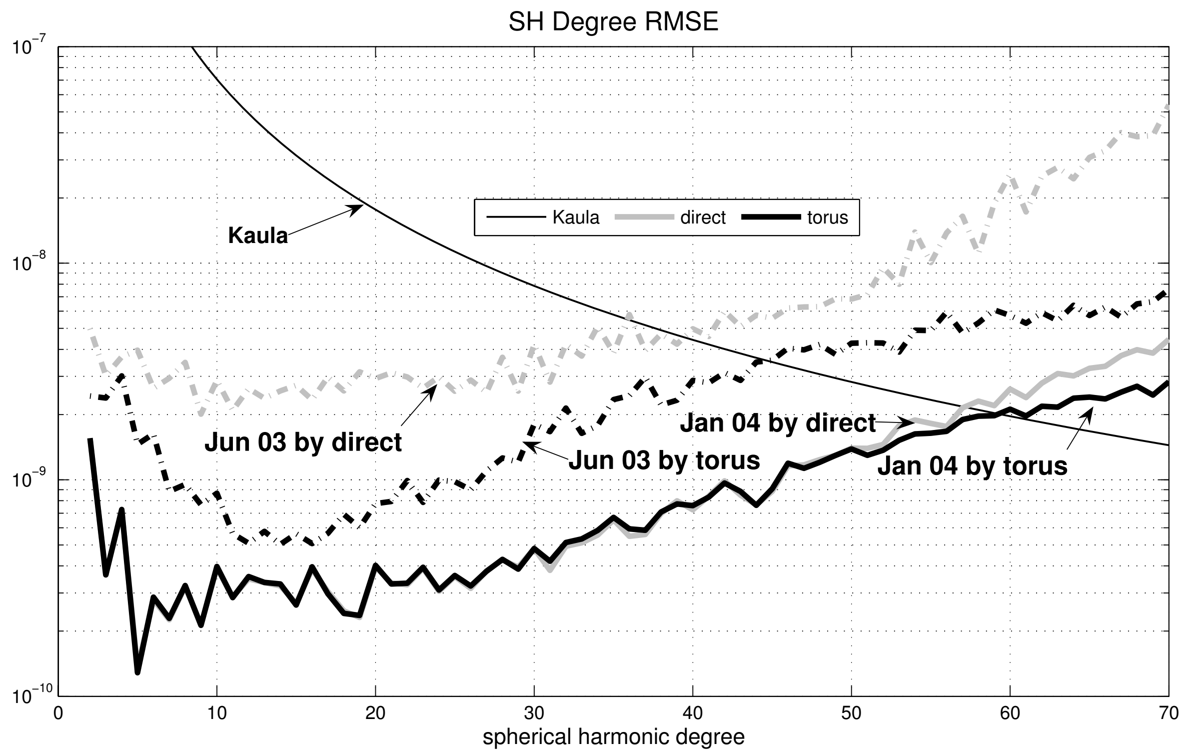

Figure 6.1: Comparison with the direct approach in the processing of the disturbing potential data up to $L = 70$

The direct approach is applied in a torus domain ($u \times \Lambda$) using the spherical harmonic expression in Equation (3.10). Therefore, the design matrix of the linear system consists of the partial derivatives with respect to $\bar{K}_{lm}$ as a function of the orbital parameters u and Λ. The normal matrix is fully populated with a size of $71^2 \times 71^2$. The calculation is processed by a grid computing technique on the "*Westgrid*" system, which combines computer clusters to act as one massive computer. The "*Westgrid*" system operates with a high performance computing, collaboration, and visualization infrastructure (WestGrid website).

4 GB RAM was allocated on the clusters system, and the computational time takes about 72 hours. In contrast, the torus-based semi-analytical approach can run on a standard personal computer (Pentium duo core 2.66 GHz) with a 2 GB RAM memory. The computational time was only about 1 hour because of the point-wise interpolation by the LSC method on a $2^\circ \times 2^\circ$ torus grid. For a consistent comparison, no iterations are applied in the torus-based approach for both months.

The degree RMSE curves of both the direct and the torus-based approaches for June 2003 and January 2004 are plotted in Figure 6.1. The reference gravity field is taken to be the GGM02S gravity field model. For the solution from January 2004 with a good ground track pattern, the torus-based semi-analytical approach is very close to the direct approach. The former even outperforms the latter in the higher degrees, $l > 50$. For the monthly solution from June 2003 with a sparse surface coverage, the torus-based approach had overall an half order of magnitude better performance than the direct approach ($l > 8$). The latter has a problem with a near ill-conditioned normal matrix because of the sparse data distribution, while the former solves this problem by making use of interpolation as a re-sampling tool.

6.1.2 V_{zz} gravity gradient tensor component from SGG

The second example compares the processing of the V_{zz} gravity gradient tensor component data from "GOCE data set I" using the aforementioned two approaches. The number of V_{zz} observations is about $172,800$ as a result of the 30 s sampling rate, and the maximum resolvable degree is chosen as $L = 100$. The normal matrix is fully populated with a size of $101^2 \times 101^2$; therefore, the inversion of the normal matrix requires the full storage of 101^8 elements for the direct approach. Since it is a point-wise calculation, it took about one week (168 hours) on the "*Westgrid*" system to get the complete solution of the spherical harmonic coefficients. By using the torus-based approach, only 4 hours were needed on the personal computer with the specifications mentioned above. The degree RMSE curves compared to the reference OSU91A model are plotted in Figure 6.2. Neither the direct nor the torus-based semi-analytical solutions recovers the Earth's gravity field up to $L = 100$ with a good accuracy. As discussed in Section 5.4, the reason for the lack of accuracy is that one single component from the gravity gradient tensor may contain insufficient in-

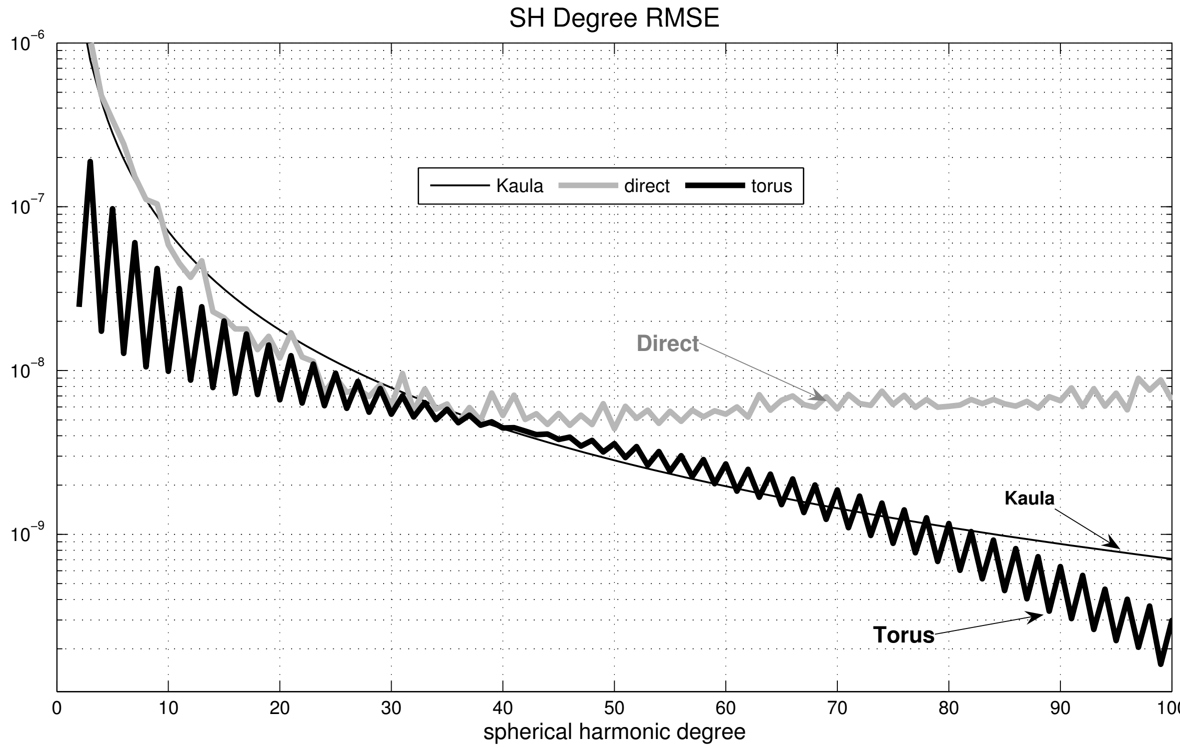

Figure 6.2: Comparison with the direct approach in the processing of the gravity gradient tensor V_{zz} data up to $L = 100$

formation. Therefore, a regularization technique should be applied. However, compared with the non-regularized direct approach, the torus-based approach without regularization achieves almost the same accuracy in the low degrees with some oscillation effects, and it definitely outperforms the direct approach for the higher degrees, e.g., $l > 50$.

Both comparison examples show that gravity field solutions from the torus-based semi-analytical approach are very close to the ones from the direct approach in terms of the level of accuracy. To some extent, the former outperforms the latter, especially in higher degrees. In addition, the torus-based approach takes advantage of smaller memory storage requirement and shorter computational time. Therefore, it is an efficient alternative tool for gravity field determination from spaceborne gravimetry.

6.2 Stand-alone solutions

In this section, different types of observables, i.e., disturbing potential, LOS GRACE-type gradiometry, and gravity gradient tensor components from spaceborne gravimetry will be processed using the torus-based semi-analytical approach. All these data sets have been described in the context of the dedicated satellite missions in Chapter 2.

6.2.1 Processing of the disturbing potential data from the CHAMP mission

Table 6.1: Description of the calculating steps of gravity field determination from the CHAMP and GRACEA&B disturbing potential data

step	disturbing potential from CHAMP	disturbing potential GRACE A&B
maximum degree L	70	70
reference gravity field	GGM02S	GGM02S
normal gravity field	removed	removed
noise filtering	no	no
reduction of h and I	up to 2nd order	up to 2nd order
grid size	$2^\circ \times 2^\circ$	$2^\circ \times 2^\circ$
interpolation method	*Kriging*	*Kriging*
PSD model	no	no
regularization	no	no
optimal weighting	no	no
iteration	no	no

The almost two years of disturbing potential data (from April 2002 to February 2004) in the "CHAMP data set" are divided into groups by a month unit, which contains the first day and the last day of each month. Therefore, a monthly spherical harmonic solution is the basic unit for gravity field determination using the torus-based semi-analytical approach. The data processing for every set of monthly observations follows the same routine illustrated in the calculating flow chart (Figure 3.5), and the corresponding description for each step is shown in the left column of Table 6.1.

The two-year overall solution can be obtained by the multi-observable model without the repetitive processing from the first step because of the linear relationship between the lumped coefficient and the spherical harmonic coefficients (Section 5.2). The combined normal matrix is obtained by making use of equal weights for all monthly normal matrices in Equation (5.22). Figure 6.3 shows the RMS values of geoid height differences compared to the GGM02S reference field for the monthly solutions and the overall solution in the spatial domain.

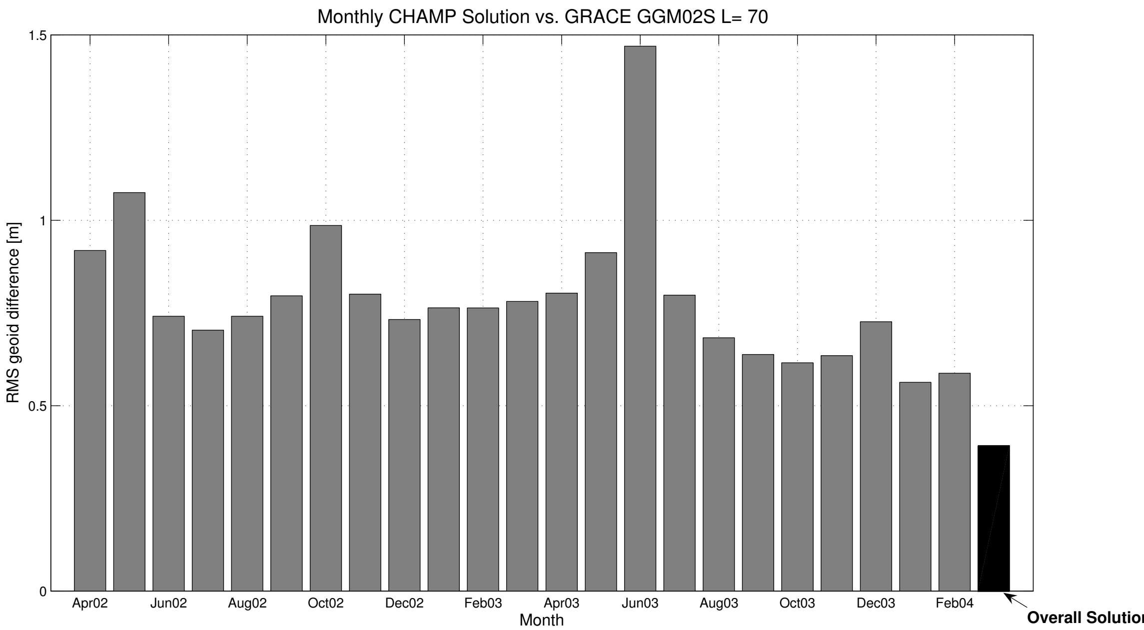

Figure 6.3: RMS in geoid height differences of monthly solutions form the CHAMP mission up to $L = 70$, compared to the GGM02S model

The monthly RMS values in geoid heights vary for different months. Sneeuw et al. (2005b) showed that the CHAMP monthly solutions are not sufficiently accurate to detect monthly time variations in the Earth's gravity field. In addition, Han et al. (2005) concluded that the CHAMP data are able to model only the semi-annual and annual time variable gravity signal in the very low degrees ($l < 3$). Therefore, the variable ground track patterns, which are caused by the changes of the satellite height, may contribute mostly to the accuracy in monthly differences. Consistent with the discussion about the aliasing problems in Section 4.5.4, the month with a good ground coverage has a smaller RMS value (0.56 m for January 2004), while the month with a sparse data distribution as the result of the repeat orbit mode has almost three times worse RMS value (1.50 m for June 2003). Similarly, the monthly solutions from May 2002 and October 2002 have larger RMS values because the satellite orbit is in a near-repeat mode. In addition to the ground track patterns, the quality of the monthly solutions naturally improve with the satellite decay (except for the repeat orbit scenarios) since the sensors onboard are getting closer to the Earth's mass.

The last RMS value bar along the x-axis in Figure 6.3 is the two-year overall solution. Its RMS value is only 0.38 m, and it is more accurate than any monthly solutions because the more observations available, the more homogeneous and dense the data distribution. However, the accuracy is not improved dramatically. The reason is that, on the one hand, the CHAMP mission is limited to solving the gravity field up to $L = 70$ (Weigelt, 2006). On the other hand, the overall solution is based on an equal contribution from the individual monthly solutions. The latter problem can be improved by optimal weighting approaches, which will be discussed in the combined solutions in Section 6.3.

Choosing the GGM02S model as reference, the other two relative error representations of the monthly solutions and the overall solution are the degree RMSE curves and the cumulative geoid height curves, which are shown in Figure 6.4(a) and Figure 6.4(b), respectively.

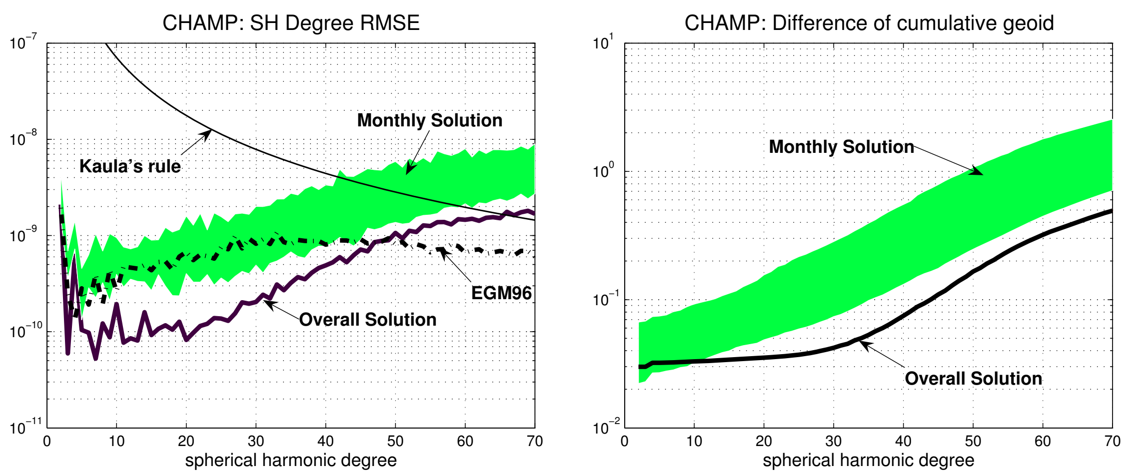

(a) Degree RMSE

(b) Cumulative geoid height error

Figure 6.4: Error representations of the CHAMP monthly and overall solutions

The spread areas in the figures are bounded by the best and the worst monthly solutions, and the (solid) curve in black is the two-year overall solution. Figure 6.4(a) shows that in the low degrees $l < 31$, the overall solution is a half order of magnitude better than the best monthly solution and one order of magnitude better than the worst monthly solution. In the higher degrees, it is close to the best monthly solution but it is still better than the worst monthly solution by one order of magnitude. Figure 6.4(b) shows that the differences in geoid height errors accumulate very slowly below degree 31. The level of 3 cm accuracy can be reached at degree 31 with a corresponding spatial resolution of 600 km half wavelength; see Equation (2.1). Overall, a decimeter accuracy can be achieved at degree 45 with a half wavelength spatial resolution of 450 km.

In general, the error representations in both the spatial and the spectral domains show that the two-year overall solution from the CHAMP mission improves the accuracy of the spherical harmonics from the monthly solutions up to one order of magnitude in the low degrees up to 70, and it has its most significant impact around degree 31.

6.2.2 Processing of the disturbing potential data from the GRACE mission

Equipped with the GPS receivers onboard, each GRACE satellite combines the concept of the SST-hl technology. Therefore, the two satellites can be treated separately as two CHAMP-like satellites flying in the same orbit. The "GRACE data set III" contains one and half years of disturbing potential data calculated by the energy balance approach for GRACE satellites A & B (Weigelt, 2006). First, the monthly gravity field solutions up to degree $L = 70$ are estimated. Then, the overall solution is obtained by the multi-observables model in Equation (5.20), similar to the procedure in the CHAMP data processing. The right column in Table (6.1) explains how each processing step is considered in gravity field determination. These steps are the same as in the CHAMP disturbing potential data processing.

The RMS values of geoid height differences for GRACEA (in red) and GRACEB (in blue) monthly solutions compared to the GGM02S reference field are shown in Figure 6.5. The corresponding monthly solutions from the CHAMP mission (in green) are plotted in the same figure for the purpose of comparison. Some values are zeros for the GRACEA and GRACEB satellites because of missing measurements in the particular months.

Generally speaking, the GRACEA and GRACEB monthly solutions reach a similar accuracy. The small differences might be caused by the calibration procedure in the energy balance approach when calculating the disturbing potential data (Weigelt, 2006). In particular, the monthly solutions of both satellites in September 2002 have the worst results. The RMS values are 2.75 m and 2.28 m, because both satellites were in a 76/5 repeat orbit

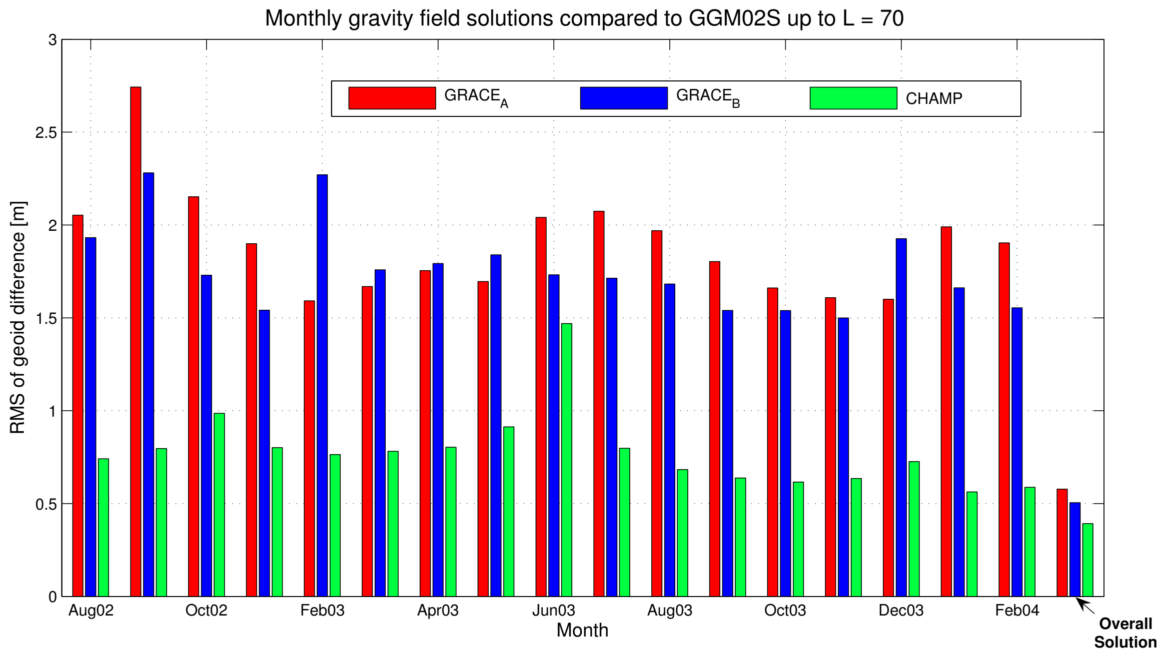

Figure 6.5: **RMS in geoid height differences of monthly solutions from the GRACE A&B satellites up to $L = 70$, compared to the GGM02S model**

mode with a sparse data distribution on the Earth's surface (van den Ameele, 2005). The overall solutions (last bar group) from these two single CHAMP-like satellites are dramatically improved with an accuracy of 0.5 m. However, almost all the GRACEA and GRACEB solutions (monthly and overall) are worse than the CHAMP solutions, because the GRACE satellites are flying in an orbit with a higher altitude. Therefore, they are less sensitive to the gravity field signal as a result of the upward attenuation effect.

Figure 6.6 shows the degree RMSE curves and cumulative geoid height curves of the GRACEA satellite. Similar error representations for the GRACEB satellite are shown in Figure 6.7. In all plots, the areas are bounded by the best and worst monthly solutions, and the black curves show the performance of the overall solutions. The two GRACE satellites achieve a very similar accuracy in both the degree RMSE and the cumulative geoid height. The overall solution combines the monthly solutions with one order of magnitude improvement through the gravity spectrum until the maximum resolvable degree $L = 70$. The cumulative geoid height differences from the overall solution have a stable level of 4 cm below degree $l = 30$. Again, both GRACE satellites have an accuracy degradation compared with the CHAMP satellite as a result of the higher flying altitude.

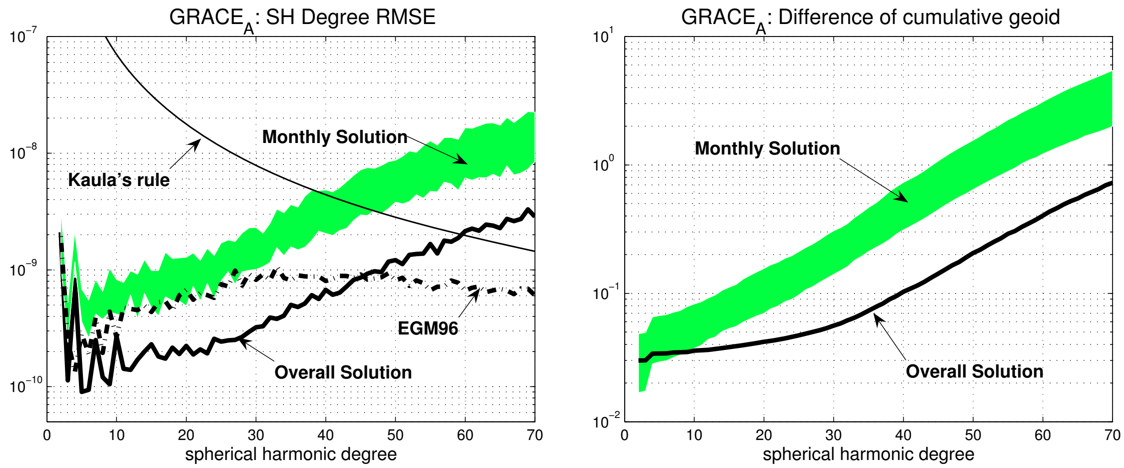

(a) Degree RMSE (b) Cumulative geoid height error

Figure 6.6: Error representations of the GRACEA monthly and overall solutions

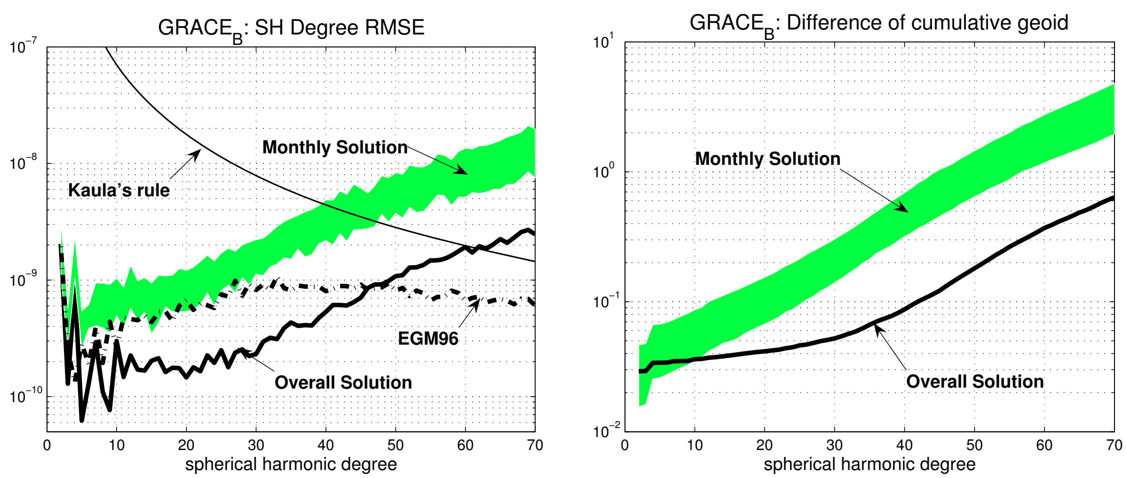

(a) Degree RMSE (b) Cumulative geoid height error

Figure 6.7: Error representations of the GRACEB monthly and overall solutions

6.2.3 Processing of LOS gradiometry data from the GRACE mission

The most important observable from the GRACE mission with the SST-ll technology is the inter-satellite K-band range. Although it is very precise, the corresponding transfer coefficient H^{ρ}_{lmk} has one practical difficulty of the normalized frequency β_{mk} because the resonance occurs at $\beta = 0, \pm 1$ CPR. The resonance will yield an infinite coefficient and destroy the linear relation between the lumped coefficient and the spherical harmonic co-

Table 6.2: Description of the calculating steps of gravity field determination from the GRACE LOS gradiometry data

step	GRACE data set I	GRACE data set II
maximum degree L	120	120
reference gravity field	GGM02S	EGM96
normal gravity field	not removed	not-removed
noise filtering	ARMA(8, 1)	no
reduction of h and I	up to 2nd order	up to 2nd order
grid size	$1^\circ \times 1^\circ$	$1^\circ \times 1^\circ$
interpolation method	*Kriging*	*Kriging*
PSD model	yes	no
regularization matrix	second-order *Tikhonov*	second-order *Tikhonov*
regularization factor	MSE	MSE
optimal weighting	no	no
iteration	no	no

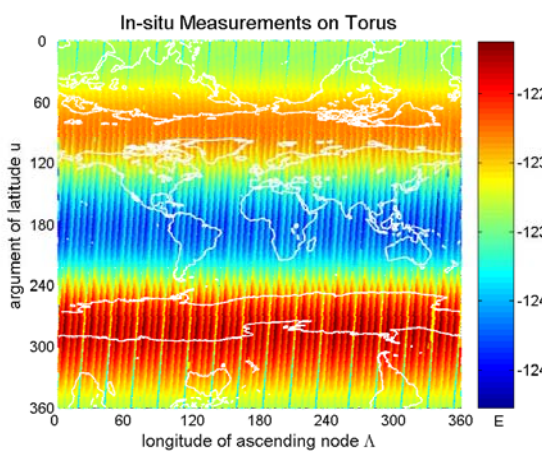

(a) In situ observations at satellite altitude

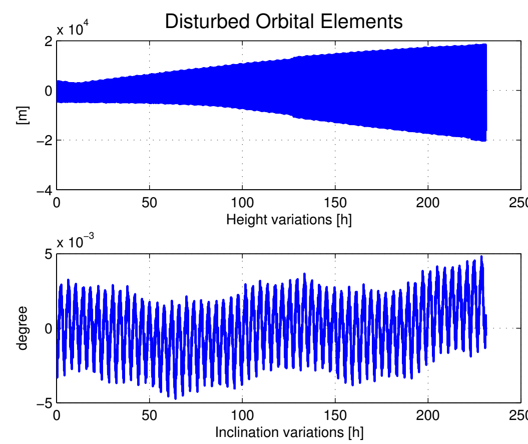

(b) Height and inclination variations

Figure 6.8: In situ LOS gradiometry data derived form the "GRACE data set I"

efficient; see Equation (5.3a). However, the transfer coefficient of the ratio between the range acceleration and range $H_{lmk}^{\frac{\ddot{\rho}}{\rho}}$ is derived in a similar form as the transfer coefficient of the along-track gradiometry observable H_{lmk}^{xx}; see Equation (5.6). The following examples try to study the practical possibility of processing the GRACE-type LOS gradiometry data.

The first example is using the ρ and $\ddot{\rho}$ observations in the "GRACE data set I," which were collected from September 2003 to October 2003. Without removing the normal grav-

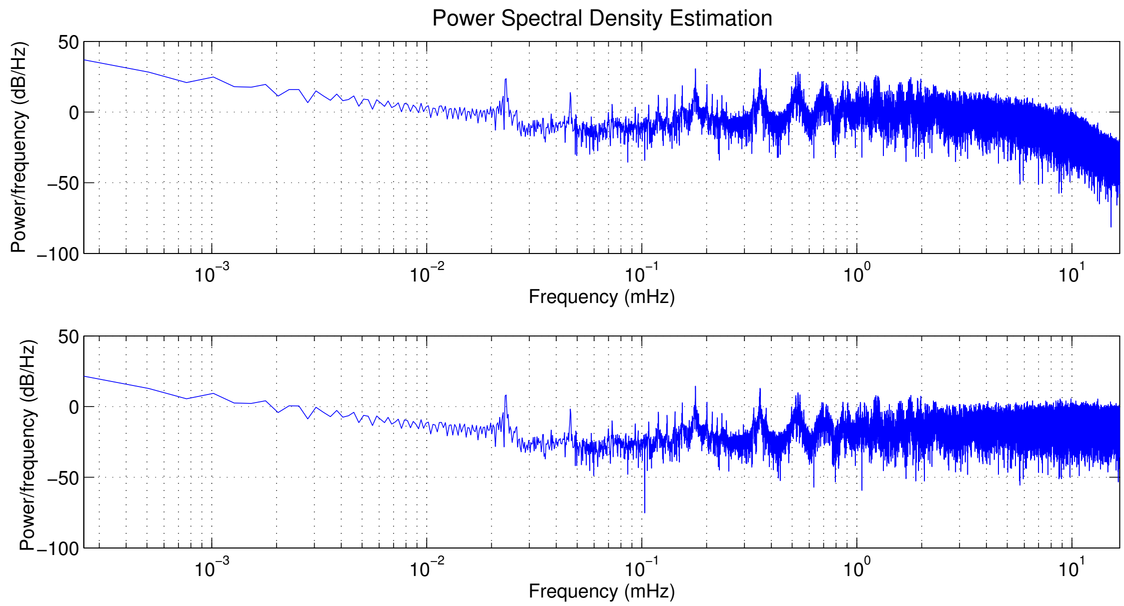

Figure 6.9: Error PSD of the LOS gradiometry observable before (top) and after (bottom) the ARMA filtering

ity field, the *in situ* observations are projected on the torus in Figure 6.8(a). It clearly shows a pattern of striping in the along-track direction, because this GRACE-type gradiometry is sensitive only to the line-of-sight direction.

The error power spectral density (PSD) is plotted in Figure 6.9 top panel for the data pre-processing stage. It shows that there is a slightly decreasing trend in the spectrum. Therefore, an ARMA$(8,1)$ process is employed to filter the trend. The filtered error PSD is flatter among the frequencies (Figure 6.9 bottom panel).

The disturbed *Kepler* elements of height and inclination are plotted in Figure 6.8(b). For the observations without the normal field removed (the even degrees up to $l = 8$), the height and inclination variations have to be reduced to a nominal orbit with constant height and constant inclination by applying a *Taylor* expansion series. As discussed in Section 4.3.2, the height and inclination variation reductions are based on a gravity field synthesis procedure. Taking the OSU91A gravity field model as the input field, the corrections caused by the partial and cross derivatives with respect to height and inclination are easily determined. All corrections are projected on the torus domain in Figure 6.10. It shows that the height corrections are very significant and the patterns are correlated with the locations

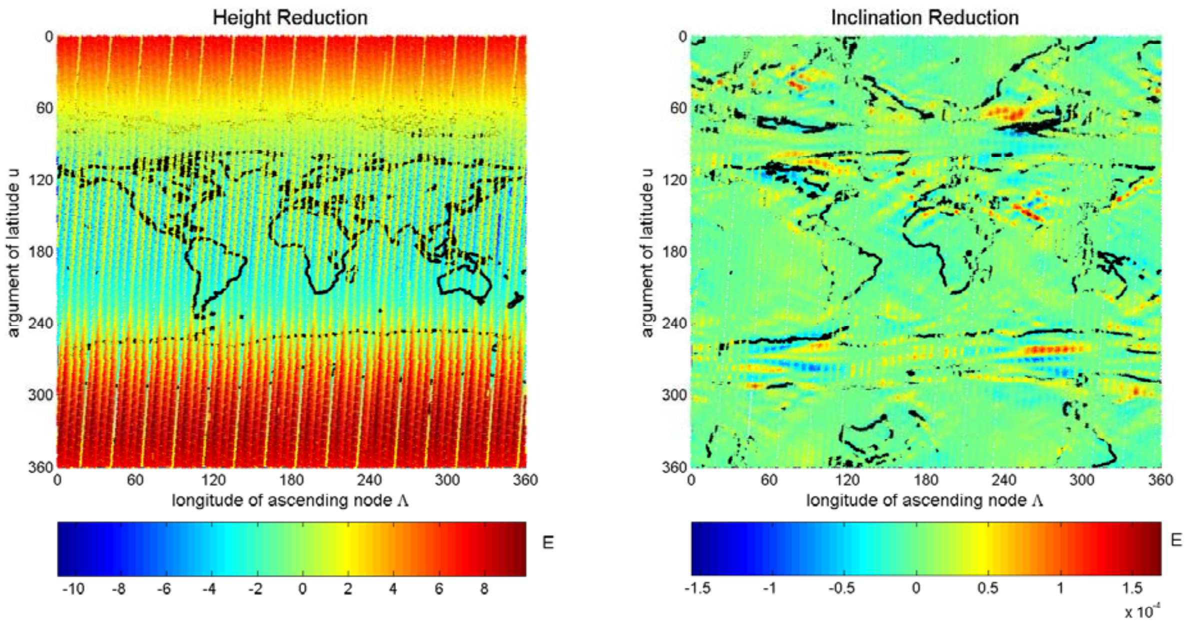

Figure 6.10: Orbital height and inclination corrections for LOS gradiometry

and the ascending/descending arcs. The magnitude of the inclination corrections is very small.

The reduced observations after height and inclination corrections are plotted in the left panel of Figure 6.11. Taking the synthesized orbital values from the GGM02S model as a reference, the right panel of Figure 6.11 shows the difference between the reduced values and the reference on the nominal orbit. After employing the torus-based semi-analytical approach, the accuracy of the gravity field solution in terms of the degree RMSE is shown in Figure 6.12, which is not as good as expected, because even the worst monthly solution from the GRACE disturbing potential data has a relative error of the level of 10^{-9} in the low degrees $l < 30$. On the one hand, the degree RMSE curve is very close to the curve of the signal RMS. Therefore, the maximum resolvable degree is ambiguous, although the two curves cross around degree 70. Compared to the EGM96 gravity field model, on the other hand, the solution from the GRACE-type gradiometry observable is worse than the EGM96 model with an overall degradation of half an order of magnitude. In the low degrees $l < 20$, this degradation even reaches one order of magnitude.

In the first example, the spherical harmonic solution from the real LOS gradiometry data has an unexpectedly low accuracy. The errors in the observations may be responsible for

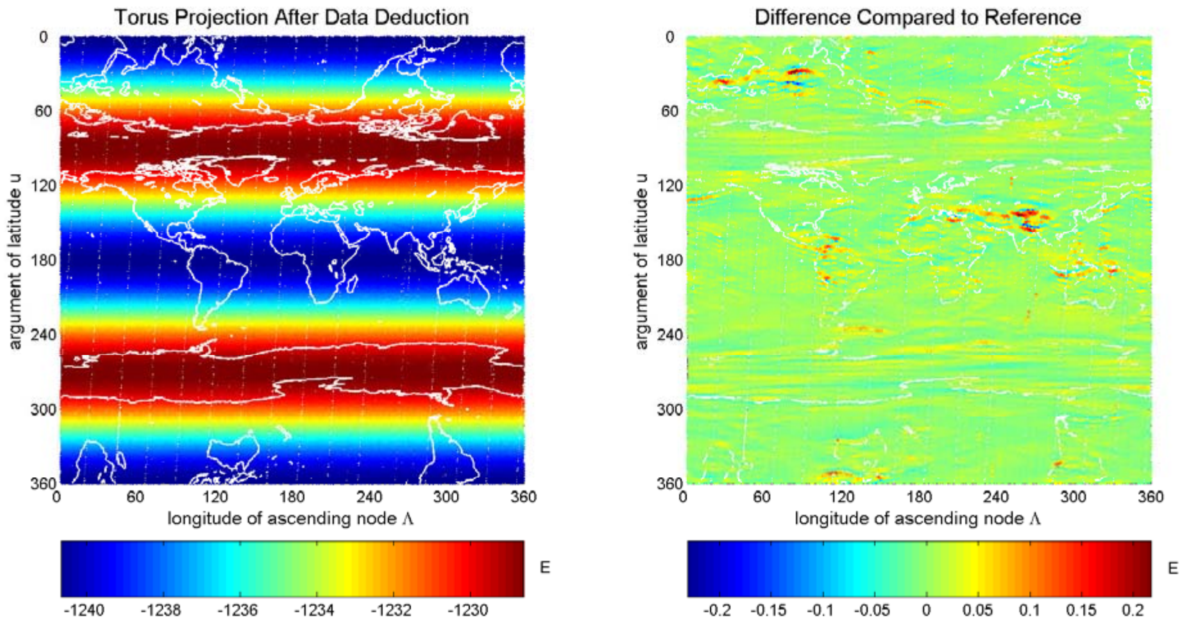

Figure 6.11: LOS gradiometry observations after data reductions and the differences compared to the reference values

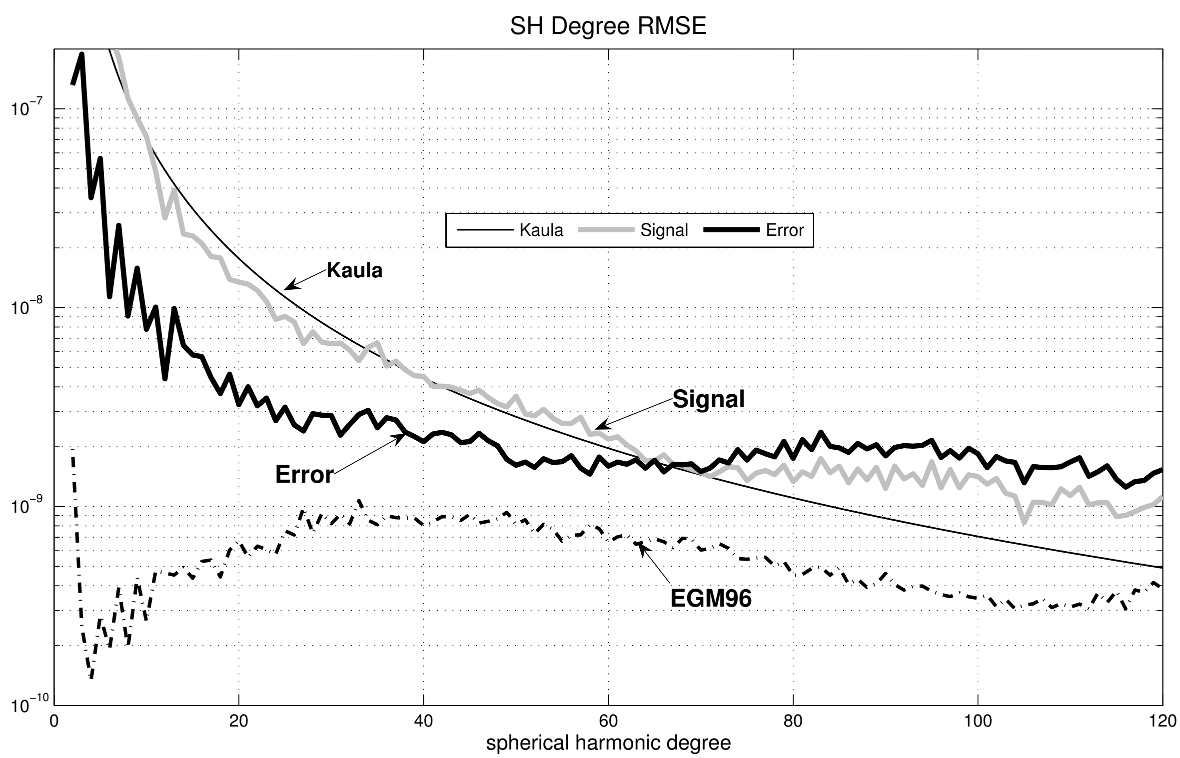

Figure 6.12: Degree RMSE from the LOS gradiometry solutions, compared to the GGM02S model

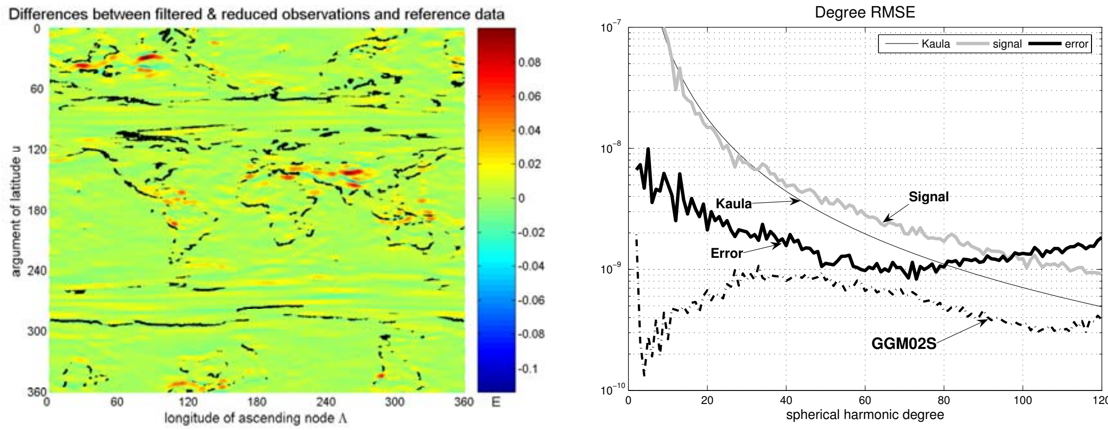

(a) Differences compared to reference data

(b) Degree RMSE

Figure 6.13: Processing of the LOS gradiometry observations from the "GRACE data set II"

this. The second example is trying to validate the GRACE-type LOS gradiometry observable from the simulated and noiseless data using the "GRACE data set II." The inter-satellite range and range acceleration data are not directly provided in this data set, but they can be derived from the simulated errorless measurements, which are position, velocity, and acceleration data without introducing any errors; see Section 5.1. Compared to the reference values synthesized by the input "pseudo-real" gravity field, the EGM96 model, the differences of the GRACE-type LOS gradiometry observable on the nominal orbit are shown in Figure 6.13(a). The spherical harmonic coefficients are estimated by the torus-based semi-analytical approach, and the corresponding degree RMSE compared to the EGM96 model is plotted in Figure 6.13(b).

The degree RMSE curve shows that the errorless observable has a better performance than the real data. However, the error level is still worse than expected.

Both examples demonstrate that the GRACE-type gradiometry observable, which is the ratio between the inter-satellite range and range acceleration, does not provide an accurate enough solution using the torus-based semi-analytical solution. The reason is not the measurement noise but the model itself. The corresponding transfer coefficient $H_{lmk}^{\ddot{\rho}}$ is derived under certain approximations and excluding resonance. Sneeuw (2000b) showed that Equation (5.6) is valid only under the assumption that the baseline is sufficiently small, and β_{mk} in Equation (5.3a) may not be too close to zero. Therefore, a new observable by means of the precise K-band range information has to be found for gravity field determination. Its corresponding transfer coefficient should also be investigated in future work.

6.2.4 Processing of the simulated gravity gradient tensor data from the GOCE mission

Table 6.3: **Description of the calculating steps of gravity field determination from the GOCE gravity gradient tensor data**

step	GOCE data set I	GOCE data set II
maximum degree L	120	120
reference gravity field	OSU91A	EGM96
normal gravity field	removed	not-removed
noise filtering	ARMA$(8,1)$	ARMA$(8,1)$
reduction of h and I	up to 2nd order	up to 2nd order
grid size	$1^\circ \times 1^\circ$	$1^\circ \times 1^\circ$
interpolation method	spline	spline
PSD model	yes	yes
regularization matrix	second-order *Tikhonov*	second-order *Tikhonov*
regularization factor	MSE	MSE
optimal weighting	no	no
iteration	no	no

The input processing observations for the torus-based semi-analytical approach from the GOCE mission are the gravity gradient tensor components V_{ij}. Since the mission is scheduled for launch in spring 2008, only simulated SGG data will be processed in this thesis. The descriptions of both the “GOCE data set I” and “GOCE data set II” have been presented in Chapter 2.

There are only the main-diagonal elements available in the “GOCE data set I.” The original *in situ* simulated observations are corrected by employing the filtering technique and data reductions onto the nominal torus. Compared to the magnitude of the original measurements (1.5 E), where the normal gravity field components are removed, these corrections (0.15 E) reach 10% of the magnitude. *Kriging* is employed to interpolate the torus grid for V_{zz} component. While the spline interpolation is used for V_{xx} and V_{yy} components. In the weighted order-wise least-squares adjustment, the weight for the specific lumped coefficient A_{mk} is calculated based on the simplified PSD model given in Section

5.3. The regularization technique is applied, in which the second-order *Tikhonov* matrix and the MSE method are the selected regularization matrix and optimal factor determination method, respectively. After least-squares adjustment, the degree RMSE curves compared to the OSU91A reference model are plotted in Figure 6.14. Although regularization was applied, all three main diagonal components have high errors at the low degrees $l < 20$, which means that the gravity gradient data have less sensitivity to these degrees. In addition, the V_{yy} component is the worst one with a half order of magnitude degradation compared with the V_{xx} and V_{zz} components because the interpolation errors for the V_{yy} component are larger than the other two components; see Section 4.4.

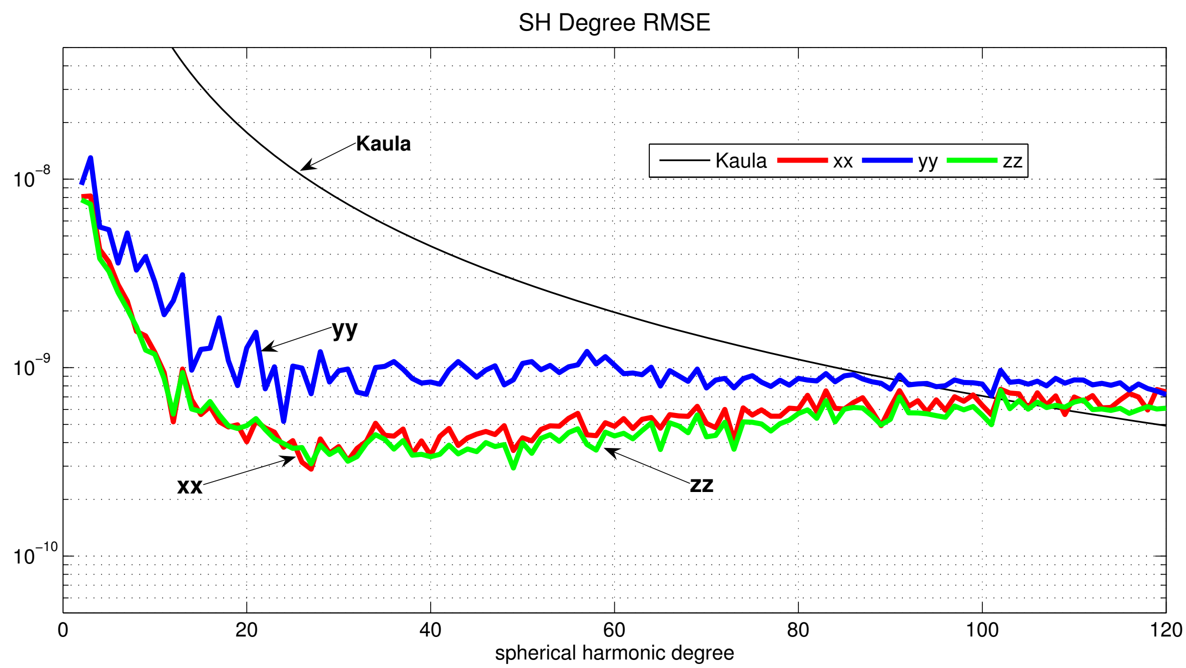

Figure 6.14: Degree RMSE of the gravity gradient tensors from "GOCE data set I," compared to the OSU91A model

A similar procedure is applied to the "GOCE data set II" in the second example. In this case, the reference gravity field is the EGM96 model. The degree RMSE curves for the main diagonal elements are plotted in Figure 6.15. Clearly, the V_{zz} component (bold green) outperforms the other two components, V_{xx} (bold red) and V_{yy} (bold blue), by one order of magnitude. However, all components still have troubles in the low degrees $l < 20$.

The solutions from the simulated gravity gradient tensor data do not give enough accuracy in terms of degree RMSE. One possible reason would be the big interpolation errors;

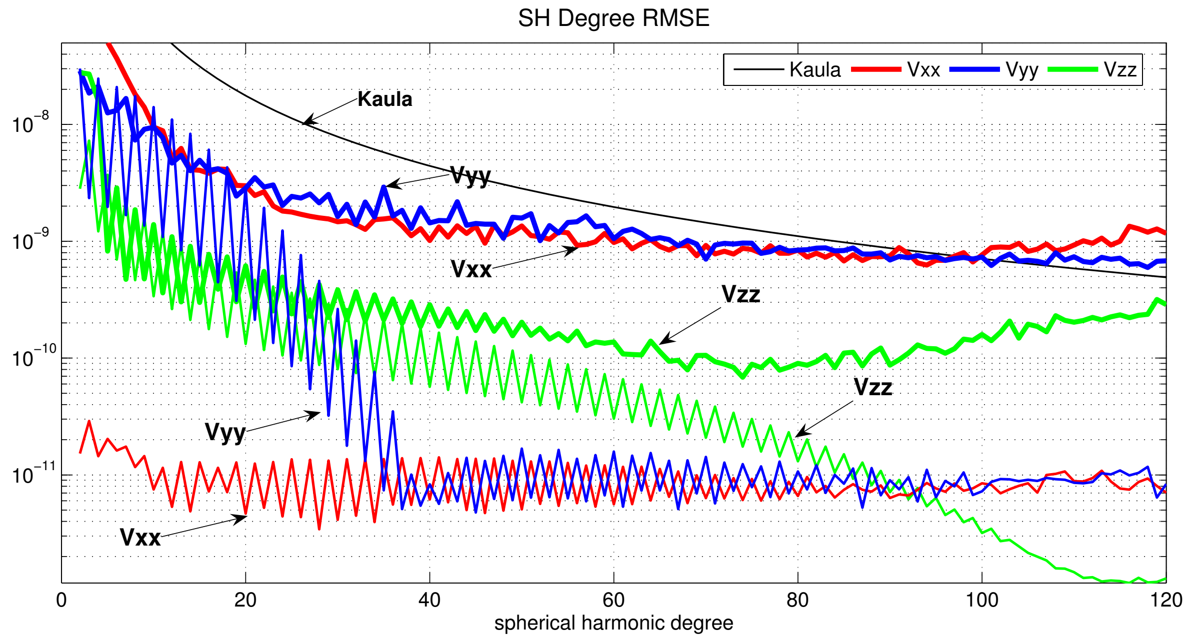

Figure 6.15: Degree RMSE of the gravity gradient tensors from "GOCE data set II," compared to the EGM96 model

for instance, interpolation introduces the errors in V_{yy} component reaching a 3% (STD) level of the original values; see Section 4.4.5. Bouman (2000) used a 3D cubic spline method to achieve the interpolation errors of 1×10^{-5} E (0.01%) with the absolute maxima of 1×10^{-4} E (0.1%). Assuming an error level of 1×10^{-4} E (0.1%) can be achieved for the torus grid, which is one order of magnitude worse than the interpolation errors in Bouman (2000), the solutions of spherical harmonics are plotted in thin curves in Figure 6.15. The new degree RMSE curves show that the accuracies are improved by one or more orders of magnitude better than the solutions estimated from the second example, especially for the degrees $l > 40$.

The two examples of the gravity gradient tensor data processing demonstrate that the V_{yy} component is the weakest component among the main diagonal elements. In addition, interpolation contributes most errors in the estimated solutions. The bigger errors from interpolation, the lower accuracy of the degree RMSE of the spherical harmonics solution. Therefore, a better interpolation method should be investigated.

6.3 Combined solutions

Spaceborne gravimetry provides different types of observables, e.g., disturbing potential from the CHAMP mission (SST data) and gravity gradient tensor from the GOCE mission (SGG data). In addition, the three satellite missions provide the disturbing potential data by the implementation of the SST-hl technique. Currently, both CHAMP and GRACE have the same type of observations for the same period of time. Generally speaking, a solution that combines data from different missions might yield a better solution. In the torus-based semi-analytical approach, the merging can be done by employing a combined model similar to the multi-observable model (Section 5.2.4), where the normal matrices from each observable are merged directly with proper weights. In addition, an optimal weighting factor should be determined based on the observable accuracies. The optimal combination of the same observables from the different satellite missions and the combination of different observables from the same missions are studied next.

6.3.1 Combined solutions by processing the disturbing potential data from the CHAMP and GRACE mission

As demonstrated in the stand-alone examples, a LEO with a lower altitude is more sensitive to the gravity field signal, and the ground track coverage with a denser data distribution has a smaller interpolation error resulting in a better solution. Therefore, the orbital characteristics are the critical aspects for the relative contributing weights among each satellite in the combined solution.

Weighted solutions from the CHAMP mission only

The first scenario is testing the weighted overall solution from the monthly solutions of the CHAMP mission. Two optimal weighting methods discussed in Section 5.5, i.e., the parametric covariance approach (PC) and the variance components approach (VC), are employed to determine the relative weights among different months. These two optimal-weighting solutions are compared to the equal-weighting overall solution achieved by the multi-observable model.

Since different monthly solutions have different accuracies in terms of geoid height differences (Figure 6.3), a better monthly solution should contribute more to the combined

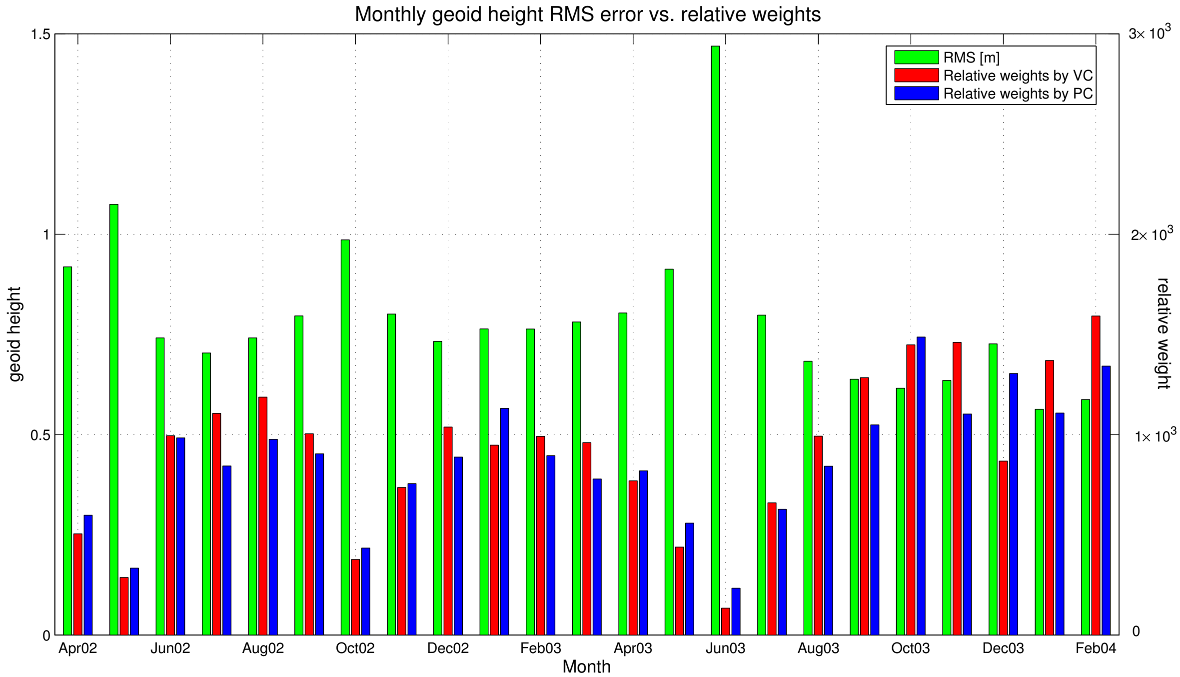

Figure 6.16: RMS in geoid height differences of the combined solution, and relative weights calculated by the PC and VC approaches from the CHAMP mission

solution, while a worse one should contribute less. The results of the contributing relative weights are shown in Figure 6.16, where the bar in blue is the weight (no unit) calculated by PC, the bar in red is calculated from VC, and the bar in green is the RMS values of geoid height differences (in m). As expected, the worst monthly solution from June 2003 has a very small weight in both the PC and VC approaches because of its repeat orbit mode, while a better monthly solution, such as February 2004, has a larger weight and contributes more to the combined solution.

The degree RMSE curves of the estimated spherical harmonic coefficients up to $L = 70$ are plotted in Figure 6.17. It shows that both combined solutions from both the PC and VC approaches are slightly better than the equal-weighting solution. Studying the RMS values in terms of geoid height compared to the GGM02S reference field, we see that the accuracies are improved by 8% for PC (RMS=0.41 m) and 9% for VC (RMS= 0.40 m). The equal-weighting solution has an RMS value of 0.44 m.

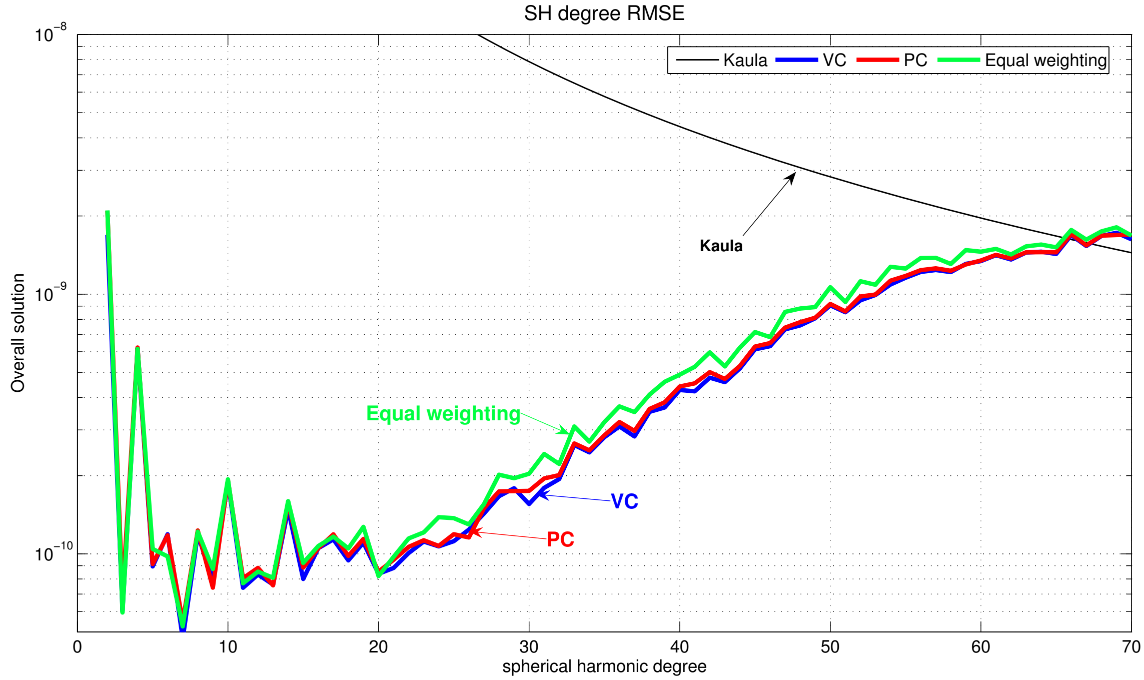

Figure 6.17: Degree RMSE of the combined solution up to $L = 70$ from the CHAMP mission, compared to the GGM02S model

Weighted solutions from both the CHAMP and GRACE missions

The CHAMP, GRACEA, and GRACEB satellites are able to derive the disturbing potential data from the SST position, velocity, and acceleration data for the same period of time; see the principle of the energy balance approach in Chapter 2. These disturbing potential data are combinable and can be merged into a larger data set to achieve a joint spherical harmonic solution in the second testing scenario. Again, both PC and VC approaches are used to determine the weighting factors of the combined solutions.

In the first step, the relative weights are determined among these three satellites to get the weighted monthly solution for each individual month, in which all three satellites have observations available. Next, the overall spherical harmonic solution is achieved by applying the multi-observable model in least-squares adjustment, which means that each weighted monthly solution contributes equally to the overall solution. Figure 6.18 shows the degree RMSE of this combined solution up to $L = 70$. Compared to the equal-weighting overall solution, the combined solution from VC is slightly better. This improvement is expected as a result of more available observation and better data distribution. However, the combined solution from PC is getting worse, which may be caused by improper weights among the three satellites.

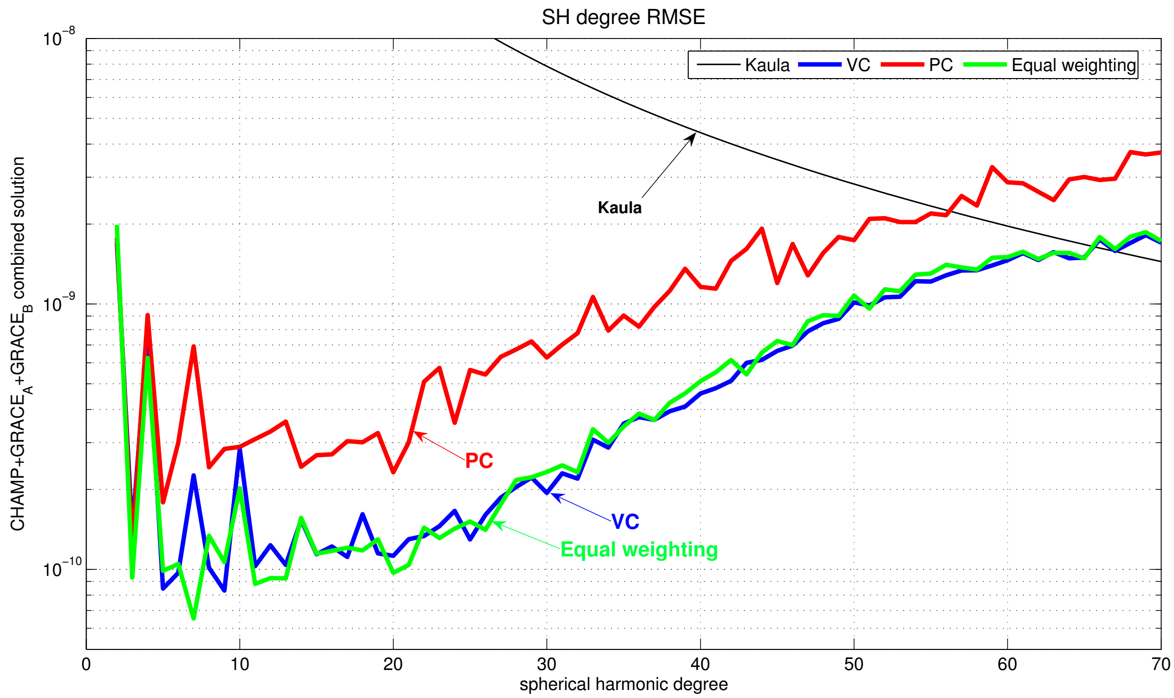

Figure 6.18: Degree RMSE of the combined solutions up to $L = 70$ from the CHAMP, GRACEA, and GRACEB satellites, compared to the GGM02S model

It is also important to study the relative contributions from the CHAMP and GRACE mission. The normalized weights among the three satellites are plotted in Figure 6.19. The weights from the VC approach, which are shown in the right panel, are well distributed. The CHAMP satellite takes a dominant role (relative weights of $0.5 \sim 0.7$ out of 1) for most months. For June 2003, when the CHAMP satellite was in a repeat orbit mode, the GRACE satellites dominated the solution. However, the weights determined by the PC have been contributed more from the GRACE data. Therefore, the weighted solution by PC is closer to the GRACE solution. Compared to the weights calculated by the VC approaches, the PC does not assign the weights correctly for several months, because the calibration factor q_i can be very close to zero in the calculation.

In general, the combined solutions from the processing of the disturbing potential data from both the CHAMP and GRACE missions show that the optimally weighted solutions are slightly better than the equal-weighting solution in most cases. The weights, deter-

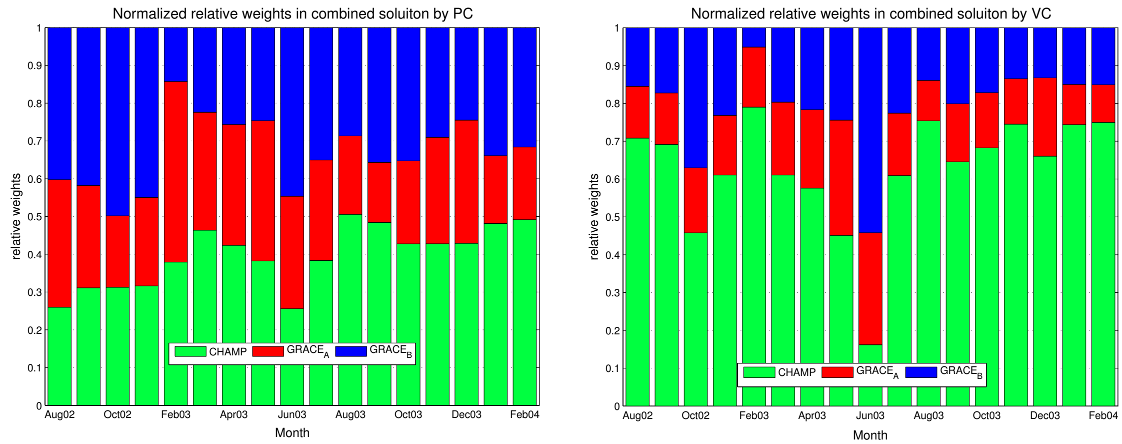

(a) PC

(b) VC

Figure 6.19: Relative weights by the PC and VC methods in the combined solutions from CHAMP, GRACEA, and GRACEB satellites

mined by two optimal weighting approaches (PC and VC), are affected by the individual monthly solutions. However, the PC method may lead to a worse solution as a result of an improper weight distribution. Therefore, the VC approach is preferred to determine the weights among different data sets.

6.3.2 Combined solutions by processing the disturbing potential and gravity gradient tensor data from the GOCE mission

Since the "GOCE data set II" provides the on-board observations in terms of position, velocity, and acceleration data, the disturbing potential data can be derived from these observations using the energy balance approach. Both the SST disturbing potential data and SGG gradient tensor data are calculated and simulated from the same reference field, the EGM96 model. Therefore, they can be combined to determine the gravity field, in which the relative weights are determined by the VC approach (Section 5.5).

The degree RMSE curves of the individual and combined solutions up to $L = 90$ are plotted in Figure 6.20. It shows that the accuracy of the combined solution using the weights takes the advantages of both the stand-alone solutions. The error curve of the combined solution is close to the SST solution in the low degrees and it is dominated by the SGG solution in the high degrees. It also shows that the SST data can be used as a regularization

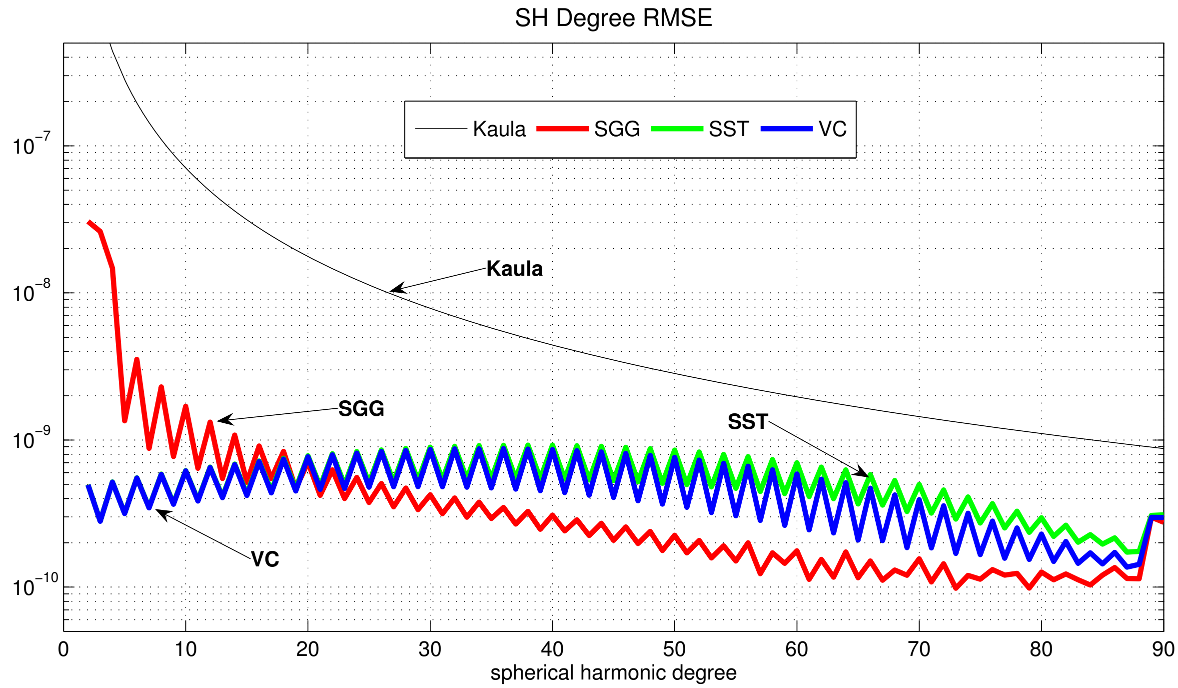

Figure 6.20: **Degree RMSE of the stand-alone and combined solutions up to $L = 90$ from SST and SGG of the "GOCE data set II", compared to the EGM96 model**

constraint for the stand-alone solution from the SGG data because the combined solution with the SST data decreases the oscillations and improves the accuracies in the low degrees ($l < 10$) of the SGG solution.

6.4 Summary

AFTER PROCESSING the disturbing potential data and gravity gradient tensor V_{zz} data using both the direct and the torus-based semi-analytical approaches, it was shown that the latter can reach the same accuracy level as the former. To some extent, the latter even outperforms the former, especially for higher degrees, e.g., $l > 60$.

Making use of the torus-based semi-analytical approach, several spherical harmonics solutions have been estimated from different types of spaceborne gravimetry observations and their combinations. These solutions are categorized into two groups: stand-alone solutions and combined solutions.

Stand-alone solutions

- **Disturbing potential from the CHAMP satellite.** A monthly solution is the basic estimation unit. The accuracies for monthly solutions are different by a half order of magnitude because of the orbital characteristics. The overall solution that is achieved by the multi-observable model outperforms any monthly solutions. For the overall solution, the SNR is equal to one (SNR $= 1$) around $l = 70$, and a decimeter accuracy can be achieved at degree 45 (spatial resolution of 450 km).

- **Disturbing potential from the GRACEA&B satellites.** The GRACEA&B satellites are treated here as two individual CHAMP-like satellites. A similar procedure in the CHAMP data processing is carried out for the disturbing potential data from both GRACE satellites. The monthly solutions from two GRACE satellites also have varying accuracies. The month (September 2002) with a $76/5$ repeat orbit gave the worst solution. However, the two GRACE overall solutions dramatically improve the accuracies of the spherical harmonics up to $L = 70$ by almost a half order of magnitude, compared to the best monthly solution. In general, the GRACEA&B satellites have an accuracy degradation compared with the CHAMP satellite because the higher flying altitude yields lower sensitivity to the gravity field signal.

- **LOS gradiometry from the GRACE satellite.** The ratio between the inter-satellite range and range-rate observations from the GRACE mission is treated as a LOS gradiometry observable. Both real data (noisy) and simulate data (noiseless) are processed. Both spherical harmonic estimations have low accuracies. Since the corresponding transfer coefficient is derived under a very short baseline assumption, the observable $\rho/\ddot{\rho}$ from the GRACE mission ($\rho \approx 220$ km) may not be suitable for gravity field determination using the torus-based approach. A new observable containing very precise range information should be investigated.

- **Gravity gradient tensor from the GOCE satellite.** The three main diagonal elements of the gravity gradient tensor data were processed to estimate the spherical harmonic coefficients up to $L = 120$. All three solutions had difficulties in the low degrees $l < 20$. The V_{zz} component outperforms the other two components, and the V_{yy} component gave the worst solution as a result of large interpolation errors with

3% of the original values. Better solution can be achieved if the interpolation errors are reduced, for instance, to a 0.1% level.

Combined solutions

- **Weighted solutions from the CHAMP satellite only.** As an extended version of the multi-observable model, the monthly solutions are merged by different weighting contributions into the overall solution. Both the PC and VC approaches were used to determine the relative weights among the months optimally. The values of the weights are proportional to the accuracies of the monthly solutions. Therefore, the overall solution is slightly better than the equal-weighted one.

- **Weighted solutions from both the CHAMP and GRACE satellites.** Both the PC and VC were used to determine the relative weights among the CHAMP and two GRACE satellites for each individual month with common observations. The overall solution was achieved by the multi-observable model. The weighted solution by VC was slightly better than the weighted CHAMP solution. However, the PC solution provides a worse solution because it introduces improper weights among the satellites.

- **Combined solutions from SST and SGG of the GOCE satellite.** The simulated SST and SGG data were combined through the optimal weights determined by the VC approach. The combined solution decreases the oscillations and improves the accuracies in the low degrees ($l < 10$) of the SGG stand-alone solution by incorporating the SST information. Therefore, the SST data can be used as a regularization constraint for the SGG data.

Recommended calculating procedure

As a summary of all the aforementioned case studies on gravity field determination by the torus-based semi-analytical approach, a comprehensive calculating flow chart is drawn in Figure 6.21. The purpose of the detailed flow chart is to achieve the best possible estimation of spherical harmonics from satellite observations. Therefore, the determination of the model and essential parameters used in each calculating step is recommended and described in the corresponding block.

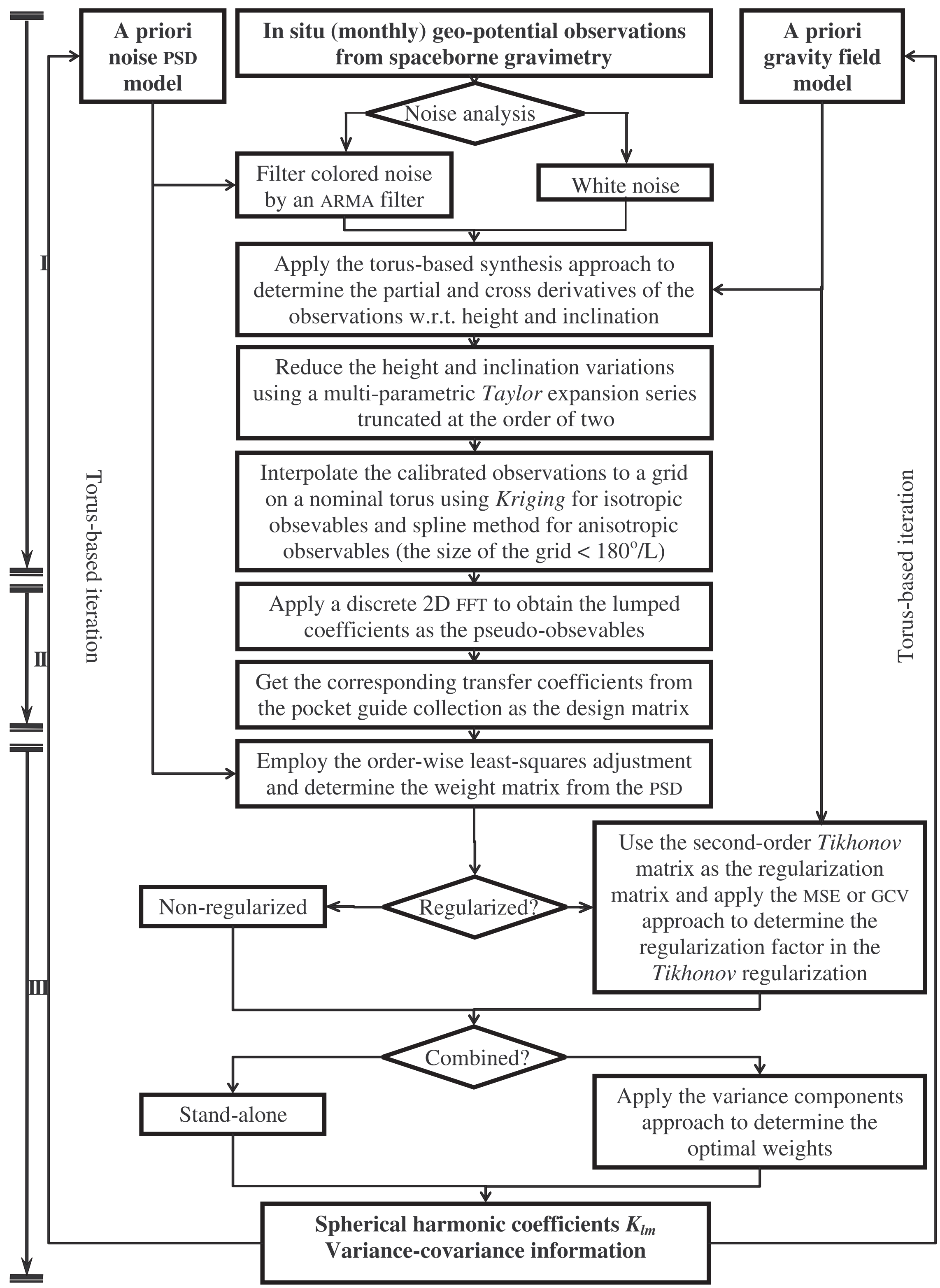

Figure 6.21: **Comprehensive calculating flow chart with the best possible solution of the torus-based semi-analytical approach of gravity field determination from spaceborne gravimetry observations**

Chapter 7

Concluding Remarks

IN THIS final chapter, the major conclusions that can be drawn from this research are presented. The recommendations for future development in this area also are addressed. The major contribution of this thesis is to establish a comprehensive and detailed processing procedure for the torus-based semi-analytical approach in gravity field determination from the spaceborne gravimetry observations. Specifically, the critical issues which are involved in the three main recovery steps have been investigated. Several stand-alone and combined solutions from numerous case studies have been achieved. Many minor improvements and developments have been discussed in the previous chapters, and only the major achievements are addressed in the following conclusions.

7.1 Conclusions

The first part of the conclusions are listed here regarding the contributions of the investigation of the individual calculating steps.

- An ARMA process has been employed to analyze the noise characteristics of the contaminated observations. A specific low order ARMA$(8,1)$ filter has been designed from the ARMASA toolbox and tested for the gravity gradient tensor data with MBW.

- A multi-parametric *Taylor* expansion series has been derived to reduce the height and inclination variations of the *in situ* observations. This reduction is required to obtain the observations on a nominal orbit, especially for those observations without the normal gravity field removed. The expansion series is truncated at the order of two with sufficient accuracy for any observable.

- The torus-based gravity field synthesis procedure is developed as a useful and powerful tool to determine the values of the partial and cross derivatives with respect to height and inclination in the data reductions. A new expression of the inclination derivatives is derived by making use of the cross inclination function only.

- For the isotropic observables, geo-statistical approaches, such as LSC and *Kriging*, create a more accuracy torus grid than deterministic bi-linear and spline interpolations. In addition, the former approaches are able to propagate error information as an internal accuracy assessment through covariance functions or semi-variograms, while the latter approaches cannot. However, the spline interpolation might be a better choice for an anisotropic observable, such as the V_{yy} gravity gradient tensor component.

- Aliasing problems may occur in the spatial/temporal and orbital frequency domains because of the insufficient sampling rate. In particular, the changes of the ground track patterns, which are caused by the orbital height changes, are the major contribution to the different accuracies of the CHAMP monthly solutions. For a repeat orbit, interpolation works as a spatial re-sampling tool by creating a denser grid and improves the sparse distribution situation.

- The collection of transfer coefficients (H_{lmk}) in the PG provides linear relations between the spherical harmonic coefficients ($\bar{K}_{lm}$) and the corresponding lumped coefficients (A_{mk}) for any geo-potential functional.

- Under the assumption of a nominal torus, a block-diagonal structured normal matrix is yielded. Spherical harmonics can therefore be estimated by the order-wise least-squares adjustment. A weight matrix for a specific observation A_{mk} is developed by calculating the variance from the error PSD model. The error information is propagated in both frequency and spatial domains through the error propagation law.

- The *Tikhonov* regularization method is employed in a nearly ill-conditioned problem in the least-squares inversion. A degree-dependent constraint, such as the second order *Tikhonov* matrix, works as a better regularization matrix in the order-wise estimation. In the regularization factor determination, the MSE method and the GCV approach outperform the L-curve criterion, and yield better regularized solutions in terms of geoid height error STD. However, the solutions from the disturbing potential data do not need to be regularized because of the stability of the normal matrix.

- Two optimal weighting determination methods, i.e., PC and VC, have been investigated in the context of combing the SST and SGG data. The combined solution from VC performs better than the one from PC in terms of the degree RMSE and the relative weight ratios.

- A torus-based iteration scheme is developed to compensate the errors introduced by the nominal orbit assumption and interpolation. The iterated solutions slightly improve the high degrees of spherical harmonics.

In addition to the conclusions on the individual steps, the second set of conclusions are drawn based on the numerous case studies.

- The solutions estimated by the torus-based semi-analytical approach can reach the same level of accuracy as the solutions calculated from the direct approach and even outperforms the latter in the high degrees $l > 60$.

- A two-year overall solution from the CHAMP disturbing potential data is achieved by combining the monthly solutions using the multi-observable model. The maximum resolvable degree can reach $l = 70$, and a decimeter geoid accuracy can be achieved at degree 45 (spatial resolution of 450 km).

- The overall solutions from both the GRACEA&B disturbing potential data are obtained by the similar procedure to the one mentioned above. The results are also similar to the CHAMP results. However, the GRACEA&B satellites have an accuracy degradation compared with the CHAMP satellite because of their higher flying altitudes.

- The GRACE-type LOS gradiometry data has been processed from both the real and simulated observations. However, the estimated solutions are not as good as expected. The reason is that the LOS gradiometry observable is derived on the basis of a sufficiently short baseline assumption, while the inter-satellite baseline of GRACE is too long to keep the assumption valid.

- Three main diagonal elements of the gravity gradient tensor data have been used to estimate the spherical harmonic coefficients up to $L = 120$. The V_{zz} component outperforms the other two components, and the V_{yy} component has the worst solution because of its larger interpolation errors. Compared to the reference values, the STD of the interpolation error in V_{yy} reaches 3% of the original values, while it is 1% for the V_{zz} component and 2% for V_{xx}.

- Two types of combined solutions have been investigated. The optimal weights for different observables or data sets are determined by the PC and VC approaches. A solution with a better accuracy has a larger weight. One example is the combination of the disturbing potential data from both CHAMP and GRACE. The solutions estimated by VC outperform the PC and equal-weighted solutions. The example combines the simulated SST and SGG GOCE data shows that the combined solution decreases the oscillations and improves the accuracies in the low degrees ($l < 10$) of the SGG standalone solution by incorporating the SST information.

7.2 Recommendations

Considering the advantages of the torus-based approach and the case studies done in this thesis, it can be recommended to employ this method for gravity field in the following scenarios:

- If one is concerned about computation time and memory storage; for instance, solving on a desktop computer up to maximum degree $L > 200$, e.g., the GOCE mission.
- If one wants to get a quick-look solution to analyze the partial SST and SGG data.
- If one thinks that data interruptions or sparse data distributions might cause a problem with the estimation.
- If one determines the gravity field using the disturbing potential data from CHAMP or GRACE.
- If one wants to combine different observables or data sets to achieve a joint solution.

Naturally, this approach is not an all-purpose gravity field determination approach. It has its intrinsic weaknesses and limitations; for instance, the disturbed orbit is approximated by a nominal orbit and interpolation introduces additional errors. The testing scenarios show that the torus-based approach does not process the GRACE-type LOS data and gravity gradient tensor data with sufficient accuracy. Therefore, the alternative approaches for analyzing the gravity field from satellite observations are recommended.

- The space-wise approach is not influenced by orbit variations, especially the long period errors. Migliaccio et al. (2004) studied an enhanced space-wise simulation dealing with polar gaps effects, gridding effects, and noise propagation for the combined SST and SGG data.

- Ditmar et al. (2003a) developed a modified time-wise approach by "treating the observations as they are." The normal matrix is inverted by a Preconditioned Conjugated Gradient Multiple Adjustment (PCGMA) algorithm (Schuh, 1996). The joint inversion of the simulated SST and SGG GOCE data leads to a geoid model with an RMS error of about 12 cm up to $L = 230$.

- Sharifi (2004) formulated the GRACE-type LOS gradiometry data using the direct approach and solved the spherical harmonics up to degree $L = 120$.

- Despite the problem of computational time, the direct inversion of the full normal matrix is preferred because it provides a full variance-covariance information of the estimated parameters. Pail and Plank (2002) proposed a distributed non-approximative adjustment feasible for simulated GOCE data.

7.3 Future work

ALTHOUGH THE torus-based semi-analytical approach has proven to be an efficient alternative tool for gravity field determination from spaceborne gravimetry, some improvements can still be made. The recommendations for future work are listed as follows:

- The observation errors in the demonstration of the filtering techniques are calculated by taking the differences between the *in situ* observations and the corresponding reference values. In reality, the observation errors are provided in the form of error variances or manufactured instrumental error PSD. Further testing of filtering with these more realistic errors should be carried out.

- ► The interpolation errors for the anisotropic observables are 3% (STD) of the original values. A better interpolation, such as a 3D cubic spline method (Bouman, 2000), has to be investigated.

- ► The implementation of the torus-based approach should be investigated for the precise inter-satellite range and range acceleration data. Thereafter, the time-variable signals from the Earth's gravity field can be detected for geodynamic interpretations.

- ► The GOCE mission is able to provide a gravity field model up to $L = 300$. The application of the torus-based approach on all the GOCE components should be investigated because it will dramatically save computational time and memory storage of the solutions with such a high degree.

- ► SFF (satellite formation flying) will provide new observables with their specific orbiting configurations. The investigation of the corresponding transfer coefficients for data processing should be done.

References

Abrikosov, O., F. Jarecki, J. Muller, S. Petrovic, and P. Schwintzer (2006); The Impact of Temporal Gravity Variations on GOCE Gravity Field Recovery. *Observation of the Earth System from Space*, (edited by J. Flury, R. Rummel, C. Reigber, M. Rothacher, G. Boedecker, and U. Schreiber), pp. 255–269. Springer.

Albertella, A., F. Migliaccio, F. Sansò, and C. Tscherning (2000); The Space-Wise Approach - Overall Scientific Data Strategy. *from Eoetvos to mGal*, (edited by H.Suenkel), pp. 267–279. ESA.

Arabelos, D. and C. C. Tscherning (2001); Improvements in Height Datum Transfer Expected from the GOCE Mission. *Journal of Geodesy*, vol. 75: pp. 308–312.

Balmino, G. (2001); New Space Missions for Mapping the Earth's Gravity Field. *C R Acad Science*, vol. 2 (IV): pp. 1353–1359.

Balmino, G. (2003); Gravity Field Recovery from GRACE: Unique Aspects of the High Precision Inter-Satellite Data and Analysis Methods. *Space Science Reviews*, vol. 108: pp. 47–54. Kluwer Academic Publishers.

Balmino, G., E. J. O. Schrama, and N. Sneeuw (1996); Compatibility of First-Order Circular Orbit Perturbations Theories; Consequences for Cross-Track Inclination Functions. *Journal of Geodesy*, vol. 70: pp. 554–561.

Bouman, J. (2000); *Quality Assessment of Satellite-Based Global Gravity Field Models*. Ph.D. thesis, Netherlands Geodetic Commission, The Netherlands.

Bouman, J. and R. Koop (1998); *Stabilization of Global Gravity Field Solutions by Combining Satellite Gradiometry and Airborne Gravimetry*. Presentation 98, DEOS, Delft University.

Broersen, P. M. T. (2006); *Automatic Autocorrelation and Spectral Analysis*. ISBN: 978-1-84628-328-4. Springer.

Burrough, P. A. and R. A. McDonnell (1998); *Principles of Geographical Information Systems - Spatial Information Systems and Geostatistics*. Oxford University Press. ISBN:0-19-823365-5.

Case, K., G. L. H. Kruizinga, and S.-C. Wu (2004); GRACE Level 1B Data Product User Handbook. *JPL*, vol. 1 (JPL D-22027): pp. 1–32.

Catmull, E. and R. Rom (1974); A Class of Local Interpolating Splines. *Computer Aided Geometric Design*, (edited by R. E. Barnhill and R. Riesenfled), p. pp. 317?26. Academic Press.

CHAMP website (); http://www.gfz-potsdam.de/pb1/op/champ/.

Chao, B. F., V. Dehant, R. S. Gross, R. D. Ray, D. A. Salstein, M. M. Watkins, and C. R. Wilson (2000); Space Geodesy Monitors Mass Transports in Global Geophysical Fluids. *EOS*, vol. 81 (22): pp. 247–250.

Chen, J. L., C. R. Wilson, and B. D. Tapley (2006); Satellite Gravity Measurements Confirm Accelerated Melting of Greenland Ice Sheet. *Science*, vol. 313: pp. 1958–1960.

Colombo, O. L. (1981); *Numerical Methods for Harmonic Analysis on the Sphere*. Report 310, Dept. of Geodetic Science, The Ohio State University, Ohio, USA.

Colombo, O. L. (1984); *The Global Mapping of Gravity with two Satellites*. Publications on Geodesy, New Series 3, Netherlands Geodetic Commission, Delft, Netherlands.

Colombo, O. L. (1986); *Notes on the Mapping of the Gravity Field Using Satellite Data*, vol. 7 of *Lecture Notes in Earth Sciences, Mathematical and Numerical Techniques in Physical Geodesy, Edited by Hans Sünkel*, pp. 264–315. Springer-Verlag.

Colombo, O. L. (1989); *Advanced Techniques for High Resolution Mapping of the Gravitational Field*, vol. 25 of *Theory of Satellite Goedesy and Gravity Field Determination, F. Sansò and R. Rummel (eds.)*, pp. 335–368. Springer-Verlag, Berlin, Germany.

Cressie, N. (1985); Fitting Variogram Models by Weighted Least Squares. *Mathematical Geology*, vol. 17 (5): pp. 563–586.

Dermanis, A. (1984); Kriging and Collocation - A Comparison. *Manuscripta Geodaetica*, vol. 9: pp. 159–167.

Ditmar, P., R. Klees, and F. Kostenko (2003a); Fast and Accurate Computation of Spherical Harmonic Coefficients from Satellite Gravity Gradiometry Data. *Journal of Geodesy*, vol. 76: pp. 690–705.

Ditmar, P., J. Kusche, and R. Klees (2003b); Computation of Spherical Harmonic Coefficients from Gravity Gradiometry Data to be Acquired by the GOCE Satellite: Regularization Issues. *Journal of Geodesy*, vol. 77: pp. 465–477.

ESA, E. (1999); *Gravity Field and Steady-State Ocean Circulation Mission*. Tech. Rep. SP-1233, European Space Agency.

ESA, E. (2004); *Swarm The Earths Magnetic Field and Environment Explorers*. Tech. Rep. SP-1279, European Space Agency.

Fenoglio-Marc, L., J. Kusche, and M. Becker (2006); Mass variation in the Mediterranean Sea from GRACE and its validation by altimetry, steric and hydrologic fields. *Geophysical Research Letters*, vol. 33: p. L19,606.

Fu, L., E. Christensen, C. Yamarone, M. Lefebvre, Y. Menard, M. Dorrer, and P. Esudier (1994); TOPEX/Poseidon Mission Overview. *Journal of Geophysical Research*, vol. 99 (C12): pp. 24,369–24,381.

Gauss, C. F. (1839); *Allgemeine Theorie des Erdmagnetismus*, vol. 5 of *Resultate aus den Beobachtungen des Magnetischen Vereins im Jahre 1838*, pp. 121–139. Gottingen und Leipzig, Gauss and Weber (eds.) edn.

GOCE website (); http://www.esa.int/esaLP/LPgoce.html.

Golub, G. H. and U. von Matt (1997); *Tikhonov Regularization for Large Scale Problems*. Tech. Rep. CS-TR-3829, Standford University.

Gooding, R. H. (1971); Lumped Fifteenth-Order Harmonics in the Geopotential. *Nature, Physical Science*, vol. 231 (25): pp. 168–169.

GRACE website (); http://www.csr.utexas.edu/grace/.

Grenier, Y. (1983); Time-Dependent ARMA Modeling of Nonstationary Signals. *IEEE Transactions on Acoustics, Speech, and Signal Processing*, vol. 31: pp. 899–911.

Han, S. C., C. Jekeli, and C. K. Shum (2004); Time-Variable Aliasing Effects of Ocean Tides, Atmosphere, and Continental Water Mass on Monthly Mean GRACE Gravity Field. *Journal of Geophysical Research*, vol. 109: p. B04,403.

Han, S. C., C. K. Shum, P. Ditmar, P. Visser, C. van Beelen, and E. J. O. Schrama (2006); Aliasing Effect of High-Frequency Mass Variations on GOCE Recovery of the Earth's Gravity Field. *Journal of Geodynamics*, vol. 41 (1-3): pp. 69–76.

Han, S.-C., C. K. Shum, C. Jekeli, A. Braun, Y. Chen, and C.-Y. Kuo (2005); CHAMP Gravity Field Solutions and Geophysical COnstraints Studies. *Earth Observation with CHAMP*.

Hansen, P. C. (1992); Analysis of Discrete Ill-Posed Problems by Means of the L-Curve. *SIAM Review*, vol. 34 (4): pp. 561–580.

Hansen, P. C. (1994); Regularization Tools: A Matlab Package for Analysis and Solution of Discrete Ill-Posed Problems. *Numerical Algorithm*, vol. 6: pp. 1–35.

Hansen, P. C. and D. P. O'Leary (1993); The Use of the L-Curve in the Regularization of Discrete Ill-Posed Problems. *SIAM Journal on Scientific Computing*, vol. 14 (6): pp. 1487–1503.

Heiskanen, W. A. and H. Moritz (1967); *Physical Geodesy*. Freeman, San Francisco.

Herzfeld, U. C. (1992); Least-Squares Collocation, Geophysical Inverse Theory and Geostatistics: A Bird's Eye View. *Geophysical Journal of International*, vol. 111: pp. 237–249.

Hill, D. J. M., E. J. Fletcher, A. O. Moscardini, and T. S. Wilkinson (1990); *Overhauser Patches for Generally Curved Surfaces*, chap. 13, pp. 139–149. E. Horwood, New York.

Hill, G. W. (1878); Researches in the Lunar Theory. *American Journal of Mathematics*, vol. 1: pp. 5–26, 129–147, 245–260.

Hofmann-Wellenhof, B. and H. Moritz (1986); *Introduction to Spectral Analysis*, vol. 7 of *Lecture Notes in Earth Sciences, Mathematical and Numerical Techniques in Physical Geodesy, Edited by Hans Sünkel*, pp. 158–259. Springer-Verlag.

Hughes, M. and S. Norris (2002); *Smaller satellites : bigger business ? concepts, applications & markets for micro/nanosatellites in a new information world*, chap. An Overview of the Technology Satellite of the 21st Century (TechSat 21) Program, pp. 381–382. Springer.

Jekeli, C. (1996); Spherical Harmonic Analysis, Aliasing, and Filtering. *Journal of Geodesy*, vol. 70: pp. 214–223.

Jekeli, C. (1999); The Determination of Gravitational Potential Differences from Satellite-to-Satellite Tracking. *Celestial Mechanics and Dynamical Astronomy*, vol. 75: pp. 85–101. Kluwer Academic Publishers.

Jian, X., R. A. Olea, and Y. S. Yu (1996); Semivariogram Modelling by Weighted Least Squares. *Computers and Geosciences*, vol. 22 (4): pp. 387–397.

Karrer, M. (2000); *Schwerefeldbestimmung aus Satellitengradiometrie - torus-approach*. Master's thesis, Technische Universitat Munchen, Institut fur Astronomische und Physikalische Geodasie.

Kaula, W. M. (1966); *Theory of Satellite Geodesy*. Blaisdell Publishing Company, Waltham Massachusetts.

Kaula, W. M. (1983); Inference of Variations in the Gravity Field from Satellite-to-Satellite Range Rate. *Journal of Geophysical Research*, vol. 88 (B10): pp. 8345–8349.

Klees, R. and P. Broersen (2002); *How to Handle Colored Noise in Large Least-Squares Problems? – Building the Optimal Filter.*. ISSN: 90-407-2348-6. Delft University Press (DUP) Science, The Netherland.

Klees, R., P. Ditmar, and P. Broersen (2003); How to Handle Colored Observation Noise in Large Least-Squares Problems. *Journal of Geodesy*, vol. 76: pp. 629–640.

Klees, R., R. Koop, P. Visser, and J. van den IJssel (2000); Efficient Gravity Field Recovery from GOCE Gravity Gradient Observations. *Journal of Geodesy*, vol. 74: pp. 561–571.

Knudsen, P. (2003); Ocean Tides in GRACE Monthly Averaged Gravity Fields. *Space Science Reviews*, vol. 108: pp. 261–270.

Koch, K. R. and J. Kusche (2002); Regularization of Geopotential Determination from Satellite Data by Variance Components. *Journal of Geodesy*, vol. 76: pp. 259–268.

Koop, R. (1993); *Global Gravity Field Modelling Using Satellite Gravity Gradiometry*. Phd dissertation, Technische Universiteit Delft, Delft, the Netherlands. New Series 38.

Koop, R., P. Visser, J. van den IJssel, and R. Klees (2000); Time-Wise Approach: Detailed Scientific Data Processing Approach. *from Eoetvos to mGal, Final report*, (edited by H.Suenkel), pp. 29–71. ESA.

Kusche, J. and R. Klees (2002); Regularization of Gravity Field Estimation from Satellite Gravity Gradients. *Journal of Geodesy*, vol. 76: pp. 359–368.

Leitner, J., F. Bauer, J. How, M. Moreau, R. Carpenter, and D. Folta (2002); Formation Flight in Space. *GPS world*, vol. 1: pp. 22–31.

Lelgemann, D. and C. Cui (2003); Analytical Versus Numerical Integration in Satellite Geodesy. *Geodesy - The Challenge of the 3rd Millennium*, (edited by F. W. Krumm and V. S. S. (eds.)), pp. 103–109. Springer-Verlag.

Lemoine et al. (1998); *The Development of the Joint NASA GSFC and NIMA Geopotential Model EGM96*. Nasa/tp-1998-206861, NASA Goddard Space Flight Center, Greenbelt, USA.

Lerch, F. J. (1989); *Optimum Data Weighting and Error Calibration for Estimation of Gravitational Parameters*. Technical Memorandum 100737, Goddard Space Flight Center, NASA, Greenbelt, Maryland.

Luthcke, S. B., H. J. Zwally, W. Abdalati, D. D. Rowlands, R. D. Ray, R. S. Nerem, F. G. Lemoine, J. J. McCarthy, and D. S. Chinn (2006); Recent Greenland Ice Mass Loss by Drainage System from Satellite Gravity Observations. *Science*, vol. 314: pp. 1286–1290.

Makhoul, J. (1975); Linear Prediction: A Tutorial Review. *Proceedings of the IEEE*, vol. 63: pp. 561–580.

Massonnet, D. (1999); Capabilities and Limitations of the Interferometric CartWheel. *Proceeding of CEOS-SAR meeting*. ESA-CNES, Toulouse, France.

Meissl, P. (1971); *A Study of Covariance Functions Related to the Earth's Disturbing Potential*. Report 151, Dept. Geodetic Science, The Ohio State University, Columbus, Ohio, USA.

Migliaccio, F., M. Reguzzoni, F. Sansò, and C. C. Tscherning (2004); An Enhanced Space-Wise Simulation for GOCE Data Reduction. *Proceedings of 2nd International* GOCE *User Workshop, "GOCE, The Geoid and Oceanography"*, ESA SP-569. ESA-ESRIN, Frascati, Italy.

Morison, J., J. Wahr, R. Kwok, and C. Peralta-Ferriz (2007); Recent trends in Arctic Ocean mass distribution revealed by GRACE. *Geophysical Research Letters*, vol. 34: p. L07,602.

Moritz, H. (1980); *Advanced Physical Geodesy*. Herbert Wichmann, Karlsruhe, second edn.

O'Keefe, J. (1975); An Application of Jacobi's Integral to the Motion of an Earth Satellite. *The Astronomical Journal*, vol. 68: pp. 266–267.

Olea, R. A. (1999); *Geostatistics for Engineers and Earth Scientists*. Kluwer Academic Publishers, Dordrecht, Netherlands. QE33.2.S82054.

Overhauser, A. W. (1968); *Analytical Definition of Curves and Surfaces by Parabolic Blending*. Tech. rep., Ford Motor Company.

Pail, R., B. Metzler, T. Preimesberger, B. Lackner, and M. Wermuth (2007); GOCE Quick-

Look Gravity Field Analysis in the Framework of HPF. *Proceeding of "The 3rd International GOCE User Workshop"*. ESA-ESRIN, Frascati, Italy.

Pail, R. and G. Plank (2002); Assessment of Three Numerical Solution Strategies for Gravity Field Recovery from GOCE Satellite Gravity Gradiometry Implemented on a Parallel Platform. *Journal of Geodesy*, vol. 76: pp. 462–474.

Pail, R. and G. Plank (2003); Comparison of Numerical Solution Strategies for Gravity Field Recovery from GOCE SGG Observations Implemented on a Parallel Platform. *Advances in Geosciences*, vol. 1 (1): pp. 39–45.

Pail, R. and G. Plank (2004); GOCE Gravity Field Processing Strategy. *Studia Geophysica et Geodaetica*, vol. 48 (2): pp. 289–309.

Pail, R., W. D. Schuh, and M. Wermuth (2005); GOCE Gravity Field Processing. *Gravity, Geoid and Space Missions*, (edited by C. Jekeli, L. Bastos, and J. Fernandes), vol. 129 of *IAG International Symposium*, pp. 36–41. Springer, Porto, Portugal.

Papoulis, A. (1965); *Probability, Random Variables, and Stochastic Processes*. McGraw-Hill.

Preimesberger, T. and R. Pail (2003); GOCE Quick-Look Gravity Solution: Application of the Semi-Analytic Approach in the Case of Data Gaps and Non-Repeat Orbits. *Studia Geophysica et Geodaetica*, vol. 47 (3): pp. 435–453.

Reigber, C. (1989); *Gravity Field Recovery from Satellite Tracking Data*, vol. 25 of *Theory of Satellite Goedesy and Gravity Field Determination, F. Sansò and R. Rummel (eds.)*, pp. 197–234. Springer-Verlag, F. Sansò and R. Rummel edn.

Reigber, C., H. Jochmann, J. Wünsch, S. Petrovic, P. Schwintzer, F. Barthelmes, K.-H. Neumayer, R. König, C. Förste, G. Balmino, R. Biancale, J. M. Lemoine, S. Loyer, and F. Perosanz (2005); *Earth Gravity Field and Seasonal Variability from CHAMP*, pp. 25–30. Earth Observation with CHAMP - Results from Three Years in Orbit. Springer, Berlin, Ch. Reigber and H. Lühr and P. Schwintzer and J. Wickert (eds.) edn.

Rummel, R. (1979); Determination of Short-Wavelength Components of the Gravity Field from Satellite-to-Satellite Tracking or Satellite Gradiometry – An Attempt to an Identification of Problem Areas. *Manuscripta Geodaetica*, vol. 4: pp. 109–148.

Rummel, R. (1986); *Satellite Gradiometry*, vol. 7 of *Lecture Notes in Earth Sciences, Mathematical and Numerical Techniques in Physical Geodesy, Edited by Hans Sünkel*, pp. 318–363. Springer-Verlag.

Rummel, R. (1991); *Physical Geodesy II*. Technische Universiteit Delft, Delft, Netherlands.

Rummel, R., G. Balmino, J. Johannessen, P. Visser, and P. Woodworth (2002); Dedicated Gravity Field Missions - Principles and Aims. *Journal of Geodynamics*, vol. 33: pp. 3–22.

Rummel, R., T. Gruber, and R. Koop (2004); High Level Processing Facility for GOCE: Products and Processing Strategy. *Proceeding of 2nd International GOCE User Workshop "GOCE, The Geoid and Oceanography"*, ESA SP-569. ESA-ESRIN, Frascati, Italy.

Rummel, R., C. Reigber, and K. H. Ilk (1978); The Use of Satellite-to-Satellite Tracking for Gravity Parameter Recovery. *Proceeding of the European Workshop on Space Oceanography*, vol. ESA-SP-137 of *Navigation and Goedynamics*, pp. 16–21. ESA.

Rummel, R. and M. van Gelderen (1995); Meissl Scheme - Spectral Characteristics of Physical Geodesy. *Manuscripta Geodaetica*, vol. 20: pp. 379–385.

Rummel, R., M. van Gelderen, R. Koop, E. Schrama, F. Sansò, M. Brovelli, F. Miggliaccio, and F. Sacerdote (1993); *Spherical Harmonic Analysis of Satellite Gradiometry*. New Series 39, Netherlands Geodetic Commission, the Netherlands.

Schrama, E. J. O. (1989); *The Role of Orbit Errors in Processing of Satellite Altimeter Data*. Publications on Geodesy 33, Netherlands Geodetic Commission.

Schrama, E. J. O. (1990); *Gravity Field Error Analysis: Applications of Global Positioning*

System Receivers and Gradiometers on Low Orbiting Platforms. Technical Memorandum 100769, NASA, Greenbelt, Maryland.

Schuh, W. (2002); *WP2: Improved Modeling of SGG-Data Sets by Advanced Filter Strategies*. Final Report: from E otv os to MilliGal+ 14287/00/NL/DC, ESA/ESTEC, Graz.

Schuh, W.-D. (1996); *Tailored Numerical Solution Strategies for the Global Determination of the Earth's Gravity Field*. Tech. Rep. 81, Mitteilungen der geod Institute der Technischen Universität, Graz, Austria.

Schuh, W.-D. (2003); The Processing of Band-Limited Measurements; Filtering Techniques in the Least Squares Context and in the Presence of Data Gaps. *Space Science Reviews*, vol. 108 (1): pp. 67–78. Kluwer Academic Publishers.

Schwarz, K. P. (1981); *Gravity Induced Position Errors in Airborne Inertial Navigation*. Tech. rep., The Ohio State University, Ohio, USA.

Schwarz, K. P., M. G. Sideris, and R. Forsberg (1987); Orthometric Heights without Levelling. *Journal of Surveying Engineering*, vol. 113 (1): pp. 28–40.

Schwintzer, P., C. Reigber, A. Bode, Z. Kang, S. Y. Zhu, F. H. Massmann, J. C. Raimondo, R. Biancale, G. Balmino, J. M. Lemoine, B. Moynot, J. C. Marty, F. Barlier, and Y. Boudon (1997); Long-Wavelength Global Gravity Field Models: GRIM4-S4, GRIM-C4. *Journal of Geodesy*, vol. 71 (4): pp. 189–209.

Seeber, G. (2003); *Satellite Geodesy*. Walter de Gruyter, second edn.

Sharifi, M. A. (2004); *Satellite Gradiometry Using a Satellite Pair*. Ph.D. thesis, Institute of Geodesy, Stuttgart University.

SID (2000); *GOCE End-to-End Performace Analysis*. Tech. Rep. 12735/98/NL/GD, ESA/ESTEC.

Sneeuw, N. (1992); Representation Coefficients and Their use in Satellite Geodesy. *Manuscripta Geodaetica*, vol. 17: pp. 117–123.

Sneeuw, N. (2000a); Dynamic Satellite Geodesy on the Torus: Block-Diagonality from a Semi-Analytical Approach. *Gravity, Geoid, and Geodynamics 2000*, (edited by M. Sideris), vol. 123, pp. 137–142. IAG, Springer-Verlag.

Sneeuw, N. (2000b); *A Semi-Analytical Approach to Gravity Field Analysis from Satellite Observations*. Dissertation, der Technischen Universität München, Deutsche Geodätische Kommission. Reihe A, Nr. 527.

Sneeuw, N. (2003); *Space-Wise, Time-Wise, Torus and Rosborough Representations in Gravity Field Modelling*, vol. 108 of *Space Science Reviews*, pp. 37–46. Kluwer Academic Publishers, Netherlands.

Sneeuw, N. and R. Bun (1996); Global Spherical Harmonic Computation by two-Dimensional Fourier Methods. *Journal of Geodesy*, vol. 70: pp. 224–232.

Sneeuw, N., J. Flury, and R. Rummel (2005a); Science Requirements on Future Missions and Simulated Mission Scenarios. *Earth, Moon, and Planets*, vol. 94: pp. 113–142.

Sneeuw, N., C. Gerlach, L. Földvráy, T. Gruber, T. Peters, R. Rummel, and D. Švehla (2005b); One Year of Time-Variable CHAMP-only Gravity Field Models Using Kinematic Orbits. *A Window on the Future of Geodesy*, (edited by Sansò), vol. 128, pp. 288–293. IAG, Springer.

Sneeuw, N., C. Gerlach, D. Švehla, and C. Gruber (2003); A First Attempt at Time-Variable Gravity Recovery from CHAMP Using the Energy Balance Approach. *Gravity and Geoid 2002*, (edited by I. N. Tziavos), Proc. 3rd Meeting of the International Gravity and Geoid Commission, pp. 237–242. Thessaloniki, Greece. 960-431-852-7.

Sneeuw, N. and H. Schaub (2005); Satellite Cluster for Future Gravity Field Missions. *Proceeding of Gravity, Geoid and Space Missions (GGSM2004)*. IAG, Springer-Verlag, Porto, Portugal.

Sneeuw, N. and M. van Gelderen (1997); *The Polar Gap*, vol. 65 of *Geodetic Boundary Value Problems in View of the One Centimeter Geoid , Lecture Notes in Earth Sciences , eds. F. Sansò and R. Rummel*, pp. 559–568. Springer-Verlag.

Sneeuw, N., J. vd. IJssel, R. Koop, P. Visser, and C. Gerlach (2002); Validation of Fast Pre-Mission Error Analysis of the GOCE Gradiometry Mission by a Full Gravity Field Recovery Simulation. *Journal of Geodynamics*, vol. 33: pp. 43–52.

Swenson, S. and J. Wahr (2002); Methods for Inferring Regional Surface-Mass Anomalies from Gravity Recovery and Climate Experiment (GRACE) Measurements of Time-Variable Gravity. *Journal of Geophysical Research*, vol. 107 (B9): p. 2193.

Tapley, B., J. Ries, S. Bettadpur, D. Chambers, M. Cheng, F. Condi, B. Gunter, Z. Kang, P. Nagel, R. Pastor, T. Pekker, S. Poole, and F. Wang (2005); GGM02 - An Improved Earth Gravity Field Model from GRACE. *Journal of Geodesy*, vol. 79: pp. 467–478.

Tapley, B. D., S. Bettadpur, J. C. Ries, P. F. Thompson, and M. M. Watkins (2004); GRACE Measurements of Mass Variability in the Earth System. *Science*, vol. 305: pp. 503–505. Www.sciencemag.org.

Thompson, P. F., S. V. Bettadpur, and B. D. Tapley (2004); Impact of short period, non-tidal, temporal mass variability on GRACE gravity estimates. *Geophysical Research Letters*, vol. 31: p. L06,619.

Tikhonov, A. and V. Y. Arsenin (1977); *Solutions of Ill-posed Problems*. John Wiley and Sons.

Tscherning, C., G.Moreaux, A.Albertella, F.Migliaccio, F.Sansò, and D.Arabelo (2000); Detailled Scientific Data Processing using the Space-Wise Approach. *from Eoetvos to mGal, Final report*, (edited by H.Suenkel), 299-304.

Tscherning, C. C. and R. H. Rapp (1974); *Closed Covariance Expressions for Gravity Anomalies, Geoid Undulations, and Deflections of the Vertical Implied by Anomaly Degree Variance Models*. Tech. Rep. 208, Ohi State University.

van den Ameele, J. J. P. (2005); *GRACE Data Processing & Orbit and Groundtrack Analysis*. Intership report, Delft University of Technology, University of Calgary, Calgary, Canada.

Vaníček, P. and E. Krakiwsky (1986); *Geodesy: the concepts, 2nd edition*. North Holland, Amsterdam, Nertherland.

Velicogna, I. and J. Wahr (2006); Measurements of Time-Variable Gravity Show Mass Loss in Antarctica. *Science*, vol. 311: pp. 1754–1756.

Véronneau, M., R. Duval, and J. Huang (2006); A Gravimetric Geoid Model as a Vertical Datum in Canada. *Geomatica*, vol. 60: pp. 165–172.

Visser, P. N. A. M., R. Rummel, G. Balmino, H. Sünkel, J. Johannessen, M. Aguirre, P. Woodworth, C. L. Provost, C. C. Tscherning, and R. Sabadini (2002); *The European Earth Explorer Mission* GOCE*: Impact for the Geosciences*, vol. Ice Sheets, Sea Level and the Dynamic Earth of *Geodynamics Series 29*, pp. 95–107. American Geophysical Union, America.

Wagner, C., D. McAdoo, J. Klokoč, and J. Kostelecký (2006); Degradation of geopotential recovery from short repeat-cycle orbits: application to GRACE monthly fields. *Journal of Geodesy*, vol. 80: pp. 94–103.

Wagner, C. A. (1983); Direct Determination of Gravitational Harmonics from Low-Low GRAVSAT Data. *Journal of Geophysical Research*, vol. 88 (B12): pp. 309–321.

Wagner, C. A. and S. M. Klosko (1977); Gravitational Harmonics from Shallow Resonant Orbits. *Celestial Mechanics and Dynamical Astronomy*, vol. 16: pp. 143–163.

Wahr, J., M. Molenaar, and F. Bryan (1998); Time Variability of the Earth's Gravity Field: Hydrological and Oceanic Effects and Their Possible Detction Using GRACE. *Journal of Geophysical Research*, vol. 103 (B12): pp. 30,205–30,229.

Weigelt, M. (2006); *Global and Local Gravity Field Recovery from Satellite-to-Satellite Tracking*. Ph.D. thesis, Dept. of Geomatics Engineering, University of Calgary.

Wermuth, M., C. Gerlach, D. Švehla, and L. Földváry (2004); Comparison of Different Gravity Field Solution Methods Applied to CHAMP Gravity Field Modeling. *Proceedings of the 1st Workshop on International Gravity Field Research*, (edited by B. Meurers and R. Pail), Zentralanstalt für Meteorologie und Geodynamik, pp. 45–50. Wien.

WestGrid website (); http://www.westgrid.ca.

Xu, C., N. Sneeuw, and M. G. Sideris (2006a); Joint SST and SGG Gravity Field Solutions Using the Torus Approach. *1st International Symposium of the International Gravity Field Service*. IAG, Istanbul, Turkey.

Xu, C., N. Sneeuw, and M. G. Sideris (2006b); The Torus Approach in Spaceborne Gravimetry. *Challenge and Role of Modern Geodesy*, (edited by P. L. Xu), vol. 130. IAG, Springer. Accepted.

Xu, C., R. Tsoi, and N. Sneeuw (2004); Analysis of J2-Perturbed Relative Orbits for Satellite Formation Flying. *Gravity, Geoid and Space Missions (GGSM2004)*, (edited by C. Jekeli, L. Bastos, and J. Fernandes), vol. 129 of *ISBN 3-540-26930-4*, pp. 36–41. IAG, Springer, Porto, Portugal. Www.springeronline.com.

Xu, P. L. (1992); A Generalized Regularization Method with Application in Determination of Potential Fields. *1st Continental Workshops on the Geoid in Europe*. IUGG, Prague.

Xu, P. L. (1998); Truncated SVD Methods for Discrete Linear Ill-Posed Problems. *Geophysical Journal International*, vol. 135: pp. 505–514.

Xu, P. L. and R. Rummel (1991); *A Quality Investigation of Global Vertical Datum Connection*. Tech. rep., Geodetic Commision, the Netherlands.

Xu, P. L. and R. Rummel (1994); Generalized Rridge Regression with Applications in Determination of Potential Fields. *Manuscripta Geodaetica*, vol. 20: pp. 8–20.

Yamamoto, K., T. Otsubo, T. Kubo-oka, and Y. Fukuda (2005); A Simulation Study of Effects of GRACE Orbit Decay on the Gravity Field Recovery. *Earth Planets Space*, vol. 57: pp. 291–295.